Investigating the variability of polar ozone and water vapor in the middle atmosphere and their impacts on the mesospheric dynamics

Inaugural dissertation
of the Faculty of Science,
University of Bern

presented by

Guochun Shi

from Wuwei, China

Supervisor of the doctoral thesis:	PD. Dr. Gunter Stober Institute of Applied Physics

Investigating the variability of polar ozone and water vapor in the middle atmosphere and their impacts on the mesospheric dynamics

Inaugural dissertation
of the Faculty of Science,
University of Bern

presented by

Guochun Shi

from Wuwei, China

Supervisor of the doctoral thesis: PD. Dr. Gunter Stober
Institute of Applied Physics

Accepted by the Faculty of Science.

The Dean:

Bern, 28. April 2025

Prof. Dr. Jean-Louis Reymond

Summary

This thesis is dedicated to investigating the interannual and small-scale variability of ozone and water vapor in the Arctic middle atmosphere using ground-based microwave radiometers GRound-based Ozone MOnitoring System for Campaigns (GROMOS-C) and MIddle Atmospheric WAter vapor RAdiometer for Campaigns (MIAWARA-C), located at Ny-Ålesund, Svalbard (78.99° N, 12° E). These measurements provide continuous observations over an altitude range covering 20 to 75 km, offering valuable insights into atmospheric dynamics and chemical processes by comparing with reanalysis and satellite datasets. Furthermore, by integrating Whole Atmosphere Community Climate Model with thermosphere and ionosphere extension (WACCM-X) model simulations with meteor radar observations, this study examines the radiative effects of ozone and water vapor on mesospheric dynamics. This combined approach enhances our understanding of the complex interactions between radiative forcing, atmospheric waves, and circulation patterns in the Arctic middle atmosphere.

Chapter 1 provides an overview of the structure and dynamics of the Arctic middle atmosphere. It introduces the key large-scale circulation patterns, including the polar vortex, the Brewer-Dobson Circulation (BDC), and Sudden Stratospheric Warming (SSW) events, which play a crucial role in atmospheric variability. The chapter also examines the influence of planetary waves and atmospheric tides on middle atmospheric dynamics. Furthermore, it discusses the role of ozone and water vapor in the Arctic middle atmosphere, emphasizing their interactions with atmospheric circulation and radiative processes. Finally, the chapter presents key measurement techniques and modeling approaches for studying middle atmospheric dynamics and composition.

Chapter 2 describes the datasets used in this study, focusing on ground-based and satellite observations as well as model simulations. It first introduces ground-based microwave measurements, including the principles of microwave remote sensing and the specific instruments GROMOS-C and MIAWARA-C, which provide continuous observations of ozone and water vapor in the Arctic middle atmosphere. Next, it presents integrated ozone and water vapor datasets from Aura Microwave Limb Sounder (MLS), the Modern-Era Retrospective Analysis for Research and Applications (MERRA)-Version 2 reanalysis, and the Specified Dynamics (SD) WACCM-X model, highlighting their relevance for studying atmospheric variability. Finally, the chapter discusses meteor radar observations, effectively capturing tidal activity in the Mesosphere and lower Thermosphere (MLT).

The aim and impact of this thesis are presented in chapter 3, which outlines how the thesis contributes to the broader scientific understanding and the specific role of the project in advancing the study.

Chapter 4 presents ozone and water vapor variability in the polar middle atmosphere observed with ground-based microwave radiometers.

Chapter 5 examines the dynamical and chemical processes in response to polar ozone anomalies during major SSW and early final stratospheric warming events.

Chapter 6 presents new insights into the polar ozone and water vapor, radiative effects, and their connection to the tides in the mesosphere lower thermosphere during major SSW events.

Finally, Chapter 7 summarizes the conclusions of this thesis and provides an outlook on potential future research directions.

Contents

Summary **i**

Table of Contents **iii**

1 The Arctic middle atmosphere **1**
1.1 Structure and dynamics 1
1.1.1 Vertical structure 1
1.1.2 Polar vortex 3
1.1.3 Sudden stratospheric warmings and their impacts 4
1.1.4 Brewer-Dobson circulation 7
1.1.5 Coupling to mesosphere-lower thermosphere 8
1.2 Atmospheric waves 9
1.2.1 Planetary waves 10
1.2.2 Atmospheric tides 11
1.3 Composition and radiative effects 13
1.3.1 Ozone 13
1.3.2 Water vapor 15
1.3.3 Radiative and dynamical effects of ozone and water vapor 17
1.4 Observational and modeling approaches 19
1.4.1 Measurements 19
1.4.2 Models 22

2 Datasets **25**
2.1 Ground-based microwave measurements 25
2.1.1 Microwave radiometry 25
2.1.2 Instruments: GROMOS-C and MIAWARA-C 26
2.2 Integrated ozone and water vapor datasets 30
2.2.1 Aura/MLS 30
2.2.2 MERRA-2 31
2.2.3 WACCM-X 32
2.3 Meteor radars 32

3 Aim and impact of this thesis **35**

4 Interannual variability of ozone and water vapor **37**
4.1 Introduction 37
4.2 Publication 37

5 Ozone anomalies during stratospheric warming events **63**
5.1 Introduction 63
5.2 Publication 63

6 Radiative effect of ozone and water vapor on mesospheric tides **87**
6.1 Introduction 87
6.2 Publication 87

7 Conclusions and Outlook 127

List of publications 143

Acknowledgements 145

Declaration of consent 147

1 The Arctic middle atmosphere

The atmospheric region extending from approximately 10 to 100 km, known as the *middle atmosphere*, has become increasingly recognized with the gradual development of middle atmospheric science. Since the 1950s, understanding of the stratosphere and mesosphere has expanded rapidly, and the importance of this region within the climate system has become evident. As research has progressed, several new stratospheric phenomena have been discovered, such as Quasi-Biennial Oscillation (QBO), SSW, the Antarctic ozone hole, and the impact of large-scale circulation changes on surface weather and patterns.

The Arctic middle atmosphere is crucial in modulating polar and high-latitude climate variability and atmospheric circulation. Characterized by extreme seasonal changes in solar radiation—from continuous darkness in winter to continuous sunlight in summer—the Arctic middle atmosphere exhibits strong temperature gradients that drive large-scale dynamical processes. These include the formation and breakup of the polar vortex, the propagation of planetary and gravity waves, and interactions with atmospheric tides. SSW frequently occurs in the Arctic winter, and can lead to significant disruptions in the polar vortex, influencing weather patterns at lower altitudes in the troposphere and even affecting the higher altitudes in the mesosphere and ionosphere. These phenomena occurring in the Arctic middle atmosphere reveal strong dynamical, chemical, and physical processes due to coupling between the troposphere and the middle atmosphere. Particularly, the impact of the distribution and variations of atmospheric composition in the Arctic middle atmosphere play a critical role in radiative balance and chemical processes, with implications for climate change and long-term atmospheric trends.

Understanding the structure, dynamics, and composition of the middle Arctic atmosphere is fundamental for improving climate models and predicting mesosphere/stratosphere-troposphere interactions. This thesis examines the vertical structure of the atmosphere, large-scale circulation patterns, and the roles of ozone and water vapor in middle atmospheric dynamics. Additionally, it explores observational and modeling capabilities and their implications for mesospheric processes, with a specific focus on the Arctic region.

1.1 Structure and dynamics

1.1.1 Vertical structure

The atmosphere extends from sea level to space and, generally, is in hydrostatic equilibrium under the influence of gravity and buoyancy, with pressure decreasing exponentially with altitude, and density rapidly with altitude. Figure 1.1 presents the mean seasonal temperature and zonal wind profiles above Ny-Ålesund, Svalbard. The Earth's atmosphere is typically divided into the troposphere, stratosphere, mesosphere, and thermosphere based on the vertical temperature gradient characteristics as shown in Figure 1.1a. The upper boundaries of these layers are referred to as the tropopause, stratopause, mesopause, and thermopause, respectively (Mohanakumar, 2008). The altitudes of these boundaries are not fixed but vary slightly with latitude and atmospheric dynamic circulation.

The troposphere is the atmospheric layer where we live, extending from the Earth's surface up to the tropopause. The heat in the troposphere primarily comes from the Earth's thermal radiation, resulting in a negative temperature gradient where temperature decreases with increasing altitude. On average, the atmospheric temperature drops by approximately 0.65°C for every 100 meters of altitude gain. The troposphere contains about 75% of the total atmospheric mass and nearly all atmospheric water vapor. Strong vertical mixing occurs in this layer, and water vapor activity is intense (including the water cycle, cloud formation, precipitation, and storms), making it the primary driver of weather disturbances and climate change (Mak, 2011).

The stratosphere extends upward from the tropopause to approximately an altitude of 50 km at the stratopause, where about 90% of atmospheric ozone is concentrated. This layer contains about one-sixth of the total atmospheric mass. The temperature distribution in the stratosphere is primarily controlled by the photochemical processes of ozone, causing the temperature to increase with altitude. As a result, vertical motion in the stratosphere is very weak, and there is minimal water vapor and particulate matter. Pollutants entering the stratosphere from the troposphere can persist for long periods due to the high stability of this layer, which is characterized mainly by large-scale horizontal motion.

The mesosphere lies between approximately 50 km and 90 km in altitude. In this layer, the heat released by exothermic reactions involving carbon dioxide and other molecules exceeds the heat absorbed from solar radiation by ozone, leading to a decrease in temperature with increasing altitude. The summer mesosphere is the coldest region of the atmosphere (see Figure 1.1a). Similar to the troposphere, the mesosphere has a negative temperature gradient, allowing for high-altitude convection. Additionally, various photochemical reactions occur in this layer, resulting in luminous phenomena such as airglow and auroras. Furthermore, most meteoroids burn up at these altitudes, providing a continuous mass input of meteoric material and dust.

Above the mesosphere is the thermosphere, where atmospheric temperature increases with altitude due to the absorption of high-energy solar radiation by oxygen molecules. This layer experiences intense ultraviolet (UV) solar radiation, leading to strong photodissociation and molecular ionization reactions. As a result, the chemical reaction rates in the thermosphere are extremely high.

The temperature structure in the stratosphere and lower mesosphere is primarily governed by radiative heating and cooling. The large-scale mean zonal wind structure can be interpreted within the framework of thermal equilibrium. Differential radiative heating between the equatorial and polar regions establishes a latitudinal temperature gradient, through thermal wind balance, which drives quasi-geostrophic zonal winds. As shown in Figure 1.1b, these winds exhibit a pronounced seasonal cycle, characterized by eastward (westerly) winds in the

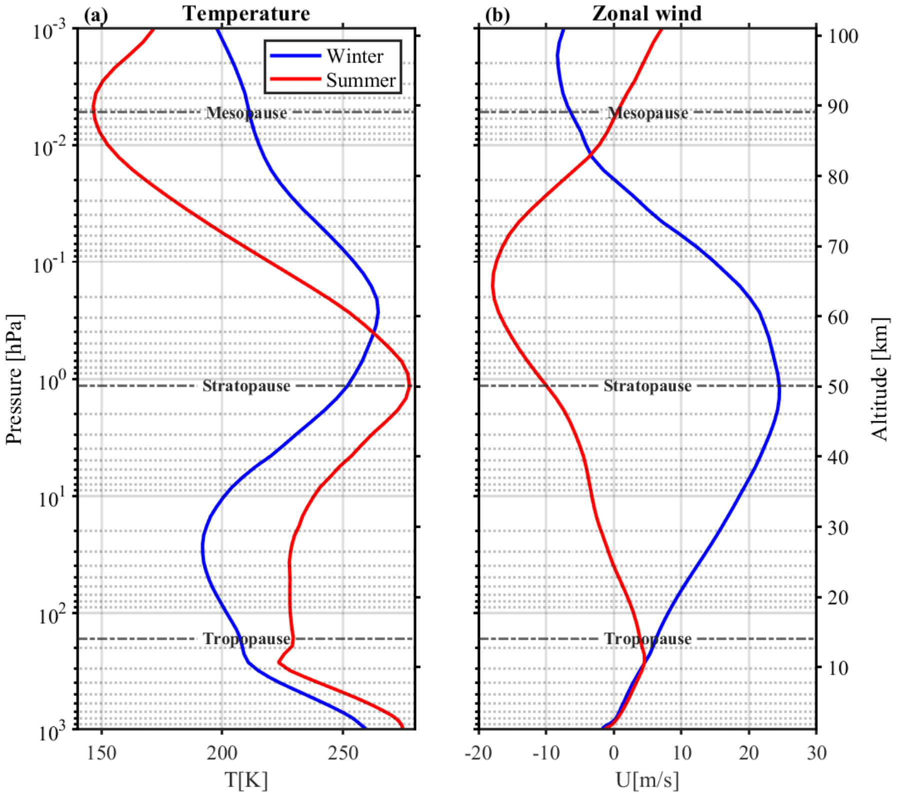

Figure 1.1 Mean seasonal temperature (a) and zonal wind profiles over Ny-Ålesund, Svalbard (78.99° N, 12° E) during boreal winter and summertime. The temperature and wind data are from the WACCM-X(SD) model simulations.

winter hemisphere and westward (easterly) winds in the summer hemisphere. This semiannual reversal occurs near the equinoxes in response to the seasonal variation in solar insolation. The climatological distribution of these zonal wind patterns, as depicted in Figure 1.1b, highlights the seasonal asymmetry in wind direction, particularly at high latitudes.

1.1.2 Polar vortex

The *polar vortex* is a large circumpolar cyclone that forms in the middle atmosphere during the fall, driven by decreased solar insolation at polar latitudes. It is maintained radiatively by the cold temperatures at the pole, which result from the absence of ozone heating during the polar night, and gradually decays during the spring season. The vortex exists in both the Arctic and Antarctic during the winter, but its characteristics and behavior differ significantly between the two hemispheres. The Antarctic polar vortex is generally more stable, stronger, and less prone to disturbances, persisting for a longer duration compared to its Arctic counterpart. In contrast, the Arctic vortex is more variable and susceptible to disruptions. The vortex is occasionally disrupted by the upward propagation of planetary waves from the troposphere, and the amplitude of these waves is larger in the Northern Hemisphere than in the Southern Hemisphere. Extreme disruptions to the vortex are referred to as sudden stratospheric warming events (see subsection 1.1.3). These disruptions result in the vortex being displaced off the pole and, in some cases, even split into two separate cyclones. When this occurs, significant changes

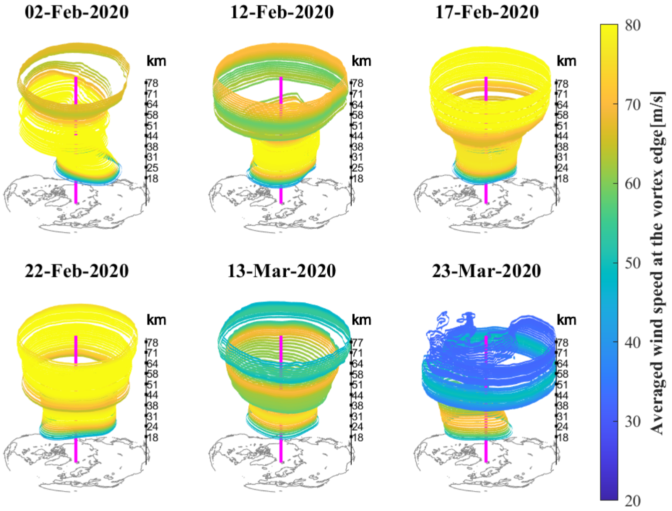

Figure 1.2 Contours of the polar vortex during the winter and spring in 2020. The vertical line is positioned at Ny-Ålesund, Svalbard.

in middle atmosphere chemistry and dynamics are observed, and these changes are linked to tropospheric weather patterns. Figure 1.2 shows the evolution of the polar vortex from the tropopause to the middle mesosphere during the winter and spring seasons of 2020. The polar vortex edge is determined from the European Centre for Medium Range Weather Forecasts (ECMWF) operational data as the geopotential height contour with the largest wind speed at a given pressure level. The edge of the vortex increases with height. Therefore, the polar vortex acts as a transport barrier between polar and midlatitude air masses. Along the edge of the polar vortex, there are strong gradients in both trace gas concentrations and temperature.

The exceptional strength of the stratospheric polar vortex had consequences for winter and early spring weather near the surface and for stratospheric ozone depletion. Due to the unusually weak tropospheric wave activity during winter and reflected waves traveling upward from the troposphere back downward, a cold and strong vortex exists for several months. For example, the extremely low temperatures inside the polar vortex during the winter/spring of 2020 are shown in Figure 1.3. The cold and stable conditions within the polar vortex allow for a large formation of polar stratospheric clouds and subsequent heterogeneous ozone depletion (Lawrence et al., 2020a; Manney, Millán, et al., 2022; Rao and Garfinkel, 2021). Figure 1.4 illustrates the ozone anomaly over the Arctic during the spring of 2020. The observed ozone levels were the lowest ever recorded for this season, indicating that 2019/2020 experienced the most severe ozone depletion potential in the observational record (Lawrence et al., 2020a; Manney, Livesey, et al., 2020).

1.1.3 Sudden stratospheric warmings and their impacts

The winter polar vortex undergoes abrupt disruptions or a sudden weakening, characterized by large and rapid temperature increases, sometimes exceeding 50 K or reversal of westerly winds and a rapid rise in the winter polar stratosphere (approximately 10–50 km). This phenomenon is called a SSW. SSWs are caused by the breaking of planetary-scale waves that propagate upwards from the troposphere. During an SSW, the polar vortex breaks down, accompanied

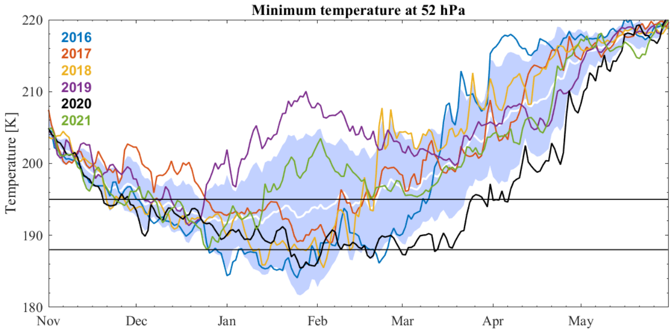

Figure 1.3 Daily time series of 50-hPa minimum temperatures poleward of 40°N. The labeled horizontal black lines represent the approximate formation thresholds for the nitric acid trihydrate (NAT) and ice polar stratospheric cloud (PSC) threshold.

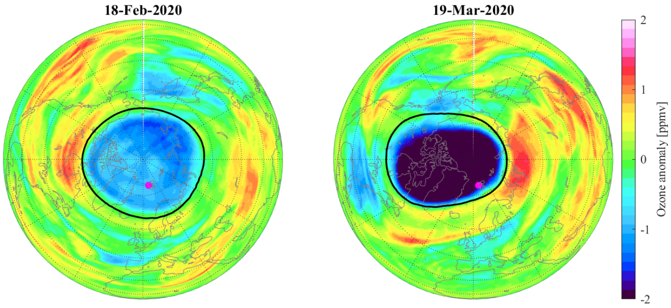

Figure 1.4 Map of Northern Hemisphere ozone volume mixing ratio anomalies during winter and spring 2020, highlighting extreme Arctic ozone depletion in spring. The anomaly is derived by subtracting the 2015–2023 climatological mean ozone volume mixing ratio (VMR) from the 2020 ozone VMR. The black contour represents the polar vortex edge at the 460 K potential temperature level.

by rapid descent and warming of air in polar latitudes, mirrored by ascent and cooling above the warming. These warmings are generally classified into three main categories based on their intensity and impact: *major warming, minor warming, and final warming*. Figure 1.5 shows a specific type of SSW in the Northern Hemisphere. Since the enhanced propagation of planetary waves into the stratosphere is heavily influenced by topography, with the Northern Hemisphere having far more complex terrain than the Southern Hemisphere, planetary waves in the Northern Hemisphere are generally stronger and larger in scale, leading to most SSW events occurring in the Northern Hemisphere, with an average of six events per decade (Rao, Ren, et al., 2018; Yu et al., 2018).

Major warming

Major warming events often occur during mid-winter and are defined by a positive temperature gradient between 60° latitude and the Pole, and a breakdown of the polar vortex, where zonal-mean zonal winds at 60° latitude and the 10 hPa level reverse from westerly to easterly. Furthermore, major warming events are mainly attributed to the split or displacement of the stratospheric polar vortex by the upward propagating planetary waves (Baldwin, Ayarzagüena, et al., 2021; Charlton and Polvani, 2007; Pancheva et al., 2008; Qin et al., 2021). The incisive dynamical perturbations during SSWs have significant effects on stratospheric transport and composition such as ozone and other trace gases anomalies in the distributions of constituents throughout the lower and middle stratosphere (Bahramvash Shams et al., 2022; Cámara et al., 2018; Hong and Reichler, 2021). The effects of major warming events are now recognized to extend well above the stratosphere and can significantly alter the chemistry and dynamics of the mesosphere, thermosphere, and ionosphere. Major warming events lead to mesospheric cooling at high latitudes, as well as a reversal of the zonal mean zonal winds from easterly to westerly, which are primarily due to changes in gravity wave drag (Hoffmann et al., 2007; Limpasuvan et al., 2016; Siskind et al., 2010). Major warming events also influence the tidal variabilities in the MLT. SSWs are often accompanied by an enhancement of migrating semidiurnal tides in the MLT regions after the SSW onset in the mid-latitude and polar latitudes (**vanCaspel_2023_lunar_tide** ; Bhattacharya, Shepherd, and Brown, 2004; Chau et al., 2015; Dutta, Sridharan, and Sinha, 2024; Jacobi et al., 1999; Liu, Janches, et al., 2022; Stober, Baumgarten, et al., 2020; Zhang et al., 2021). Major warming events play an important role in generating variability in the low-latitude and midlatitude ionosphere, with an increase in vertical plasma drifts and electron densities in the morning and a decrease in the afternoon (Baldwin, Ayarzagüena, et al., 2021; Fejer et al., 2011; Goncharenko et al., 2010; Pedatella, Liu, et al., 2012). The downward effect through the induced meridional circulation (Song and Robinson, 2004; Thompson, Furtado, and Shepherd, 2006) and planetary wave absorption and reflection (Shaw, Perlwitz, and Harnik, 2010) contribute to tropospheric response (Domeisen, Sun, and Chen, 2013; Smith and Scott, 2016) and also lead to the surface pressure anomalies (Domeisen, Butler, and Charlton-Perez, 2020).

Minor warming

In contrast, minor warming events during mid-winter are characterized by strong warming of the Arctic stratosphere at 10 hPa and higher levels without a reversal of zonal-mean zonal winds poleward of 60° latitude at 10 hPa. While their immediate impacts are less pronounced than those of major warming events, minor warming events can still influence atmospheric circulation patterns. For instance, the September 2019 Southern Hemisphere minor warming event was associated with significant deceleration of westerly winds and the emergence of easterly anomalies in the subpolar region, extending into the extratropics and tropical stratosphere (Rao, Garfinkel, et al., 2020). During the shifts of the upper stratospheric and mesospheric vortex, the air masses arrive from the midlatitudes, which confirms that the separation of polar and midlatitude air persists during minor warnings (Schranz, Tschanz, et al., 2019). During minor warming events, the deseasoned migrating diurnal tide exhibits a significant short-term increase around the peak warming day across all latitudes, while the deseasoned migrating semidiurnal tide also shows a notable enhancement, indicating a clear tidal response to the warming (Mitra et al., 2023).

Final warming

Final warming events are identified by the criterion that the daily mean zonal-mean zonal winds at 60° latitude and 10 hPa exhibit an easterly flow and remain so continuously for more than 10 consecutive days (Butler and Domeisen, 2021). Final warming events are primarily driven by an increase in shortwave radiation in the polar regions in spring in combination with planetary

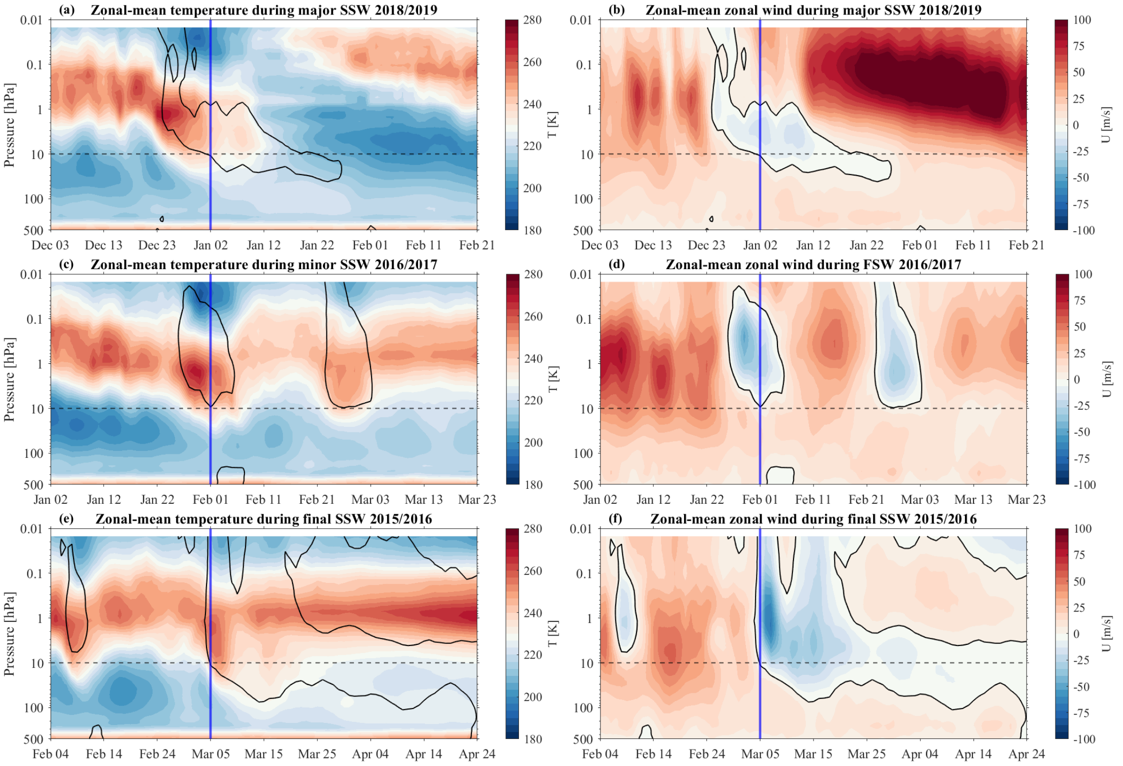

Figure 1.5 Zonal-mean zonal temperature averaged polar region 70° - 90° N (left) and zonal-mean zonal wind at 60°N (right), during major warming, minor warming, and final warming SSW events based on MERRA-2 reanalysis data .

wave forcing (Black and McDaniel, 2007; Friedel, Chiodo, Stenke, Domeisen, and Peter, 2022). While a final SSW occurs every year in both hemispheres, its timing is subject to large interannual variability. In the Arctic, final warming events have been observed from as early as mid-March to as late as the end of May (Hu, Ren, and Xu, 2014), depending on variations in the upward propagation of tropospheric planetary waves, as well as the stratospheric background flow and temperature (Hu, Ren, and Xu, 2014; Salby and Callaghan, 2007; Thiéblemont et al., 2019). The timing of the final SSW has important consequences for both stratospheric and tropospheric climate and sub-seasonal to seasonal predictability (Ayarzagüena and Serrano, 2009; Butler, Charlton-Perez, et al., 2019; Thiéblemont et al., 2019). Final warming events are closely tied to anomalies in stratospheric ozone in the Arctic, for instance, an extremely cold polar vortex with drastic springtime ozone depletion in 2019/2020 (Lawrence et al., 2020b; Matthias, Dörnbrack, and Stober, 2016). Final SSW events leave their fingerprint on the tropospheric circulation through downward coupling by linking the phase changes of the North Atlantic Oscillation (NAO) and Arctic Oscillation (AO), causing surface climate changes (Baldwin, Ayarzagüena, et al., 2021).

1.1.4 Brewer-Dobson circulation

The BDC plays a crucial role in regulating the distribution of ozone in the stratosphere and the exchange of mass between the stratosphere and the troposphere. The strongest ozone production occurs in the equatorial stratosphere due to maximized solar insolation, while the highest ozone concentrations are observed in the polar lower stratosphere. This apparent contradiction was first explained by Brewer (Brewer, 1949) and Dobson (Dobson, 1956), who proposed that a tropical convective motion transports ozone-rich air into the stratosphere, where it is then advected towards the winter pole and descends adiabatically at high latitudes. This meridional circulation, now known as the BDC, is characterized by the upwelling of air masses that can transport tropospheric air deep into the stratosphere. These air masses are then transported horizontally towards high, polar latitudes, where they sink back into the troposphere (Butchart, 2014). The BDC directly affects the temperature of the tropical tropopause and the amount of water vapor entering the stratosphere, which, in turn, influences the surface climate through radiative changes. Furthermore, variations in the stratospheric circulation may influence regional climate and weather patterns.

The BDC is a mechanically forced circulation, with the driving force provided by atmospheric waves such as planetary and synoptic-scale Rossby waves that propagate upwards from the troposphere and break at upper (so-called "critical") levels in the stratosphere (Andrews, Holton, and Leovy, 1987; Holton et al., 1995). When these waves reach their critical levels, they break and deposit momentum into the mean flow, causing a deceleration of the zonal wind. This momentum deposition drives a net poleward transport of air masses, inducing tropical upwelling and high-latitude downwelling. The Coriolis force acts on this poleward flow, modifying the vertical velocity field and leading to the large-scale overturning motion that characterizes the BDC. The BDC influences stratosphere-troposphere coupling, affecting climate and atmospheric composition. The downward transport in the winter hemisphere impacts surface weather, while the tropical upwelling regulates the distribution of stratospheric water vapor and ozone. Understanding this circulation is crucial for predicting long-term changes in atmospheric dynamics, ozone depletion, and climate variability.

Additionally, the pole-to-pole circulation existing in the mesosphere is often referred to as residual circulation or transformed Eulerian mean circulation (Andrews, Holton, and Leovy, 1987; Becker, 2012; Lindzen, 1981; Smith, 2012). Figure 1.6 shows a schematic diagram of the large-scale atmospheric circulation. This circulation in the mesosphere is mainly driven by gravity waves , which results in the summer mesopause temperature up to 100 K below the radiative equilibrium (Becker, 2012; Lindzen, 1981; Smith, 2012). The extreme cold temperatures at the summer mesopause are the result of an upwelling and a corresponding adiabatic cooling of the uplifted air masses in the summer hemisphere and are accompanied by a downwelling in the winter hemisphere.

1.1.5 Coupling to mesosphere-lower thermosphere

The Arctic middle atmosphere, encompassing the stratosphere and mesosphere, plays a critical role in vertical coupling processes that extend into the *mesosphere and lower thermosphere*. While the variability of the middle atmosphere is primarily driven by atmospheric waves propagating upward from the troposphere, recent studies have demonstrated that this coupling is a two-way process, where stratospheric and mesospheric dynamics significantly influence both tropospheric circulation and upper atmospheric variability (Baldwin, Stephenson, et al., 2003; Charlton, Oneill, et al., 2004). In particular, stratosphere-troposphere interactions are crucial for

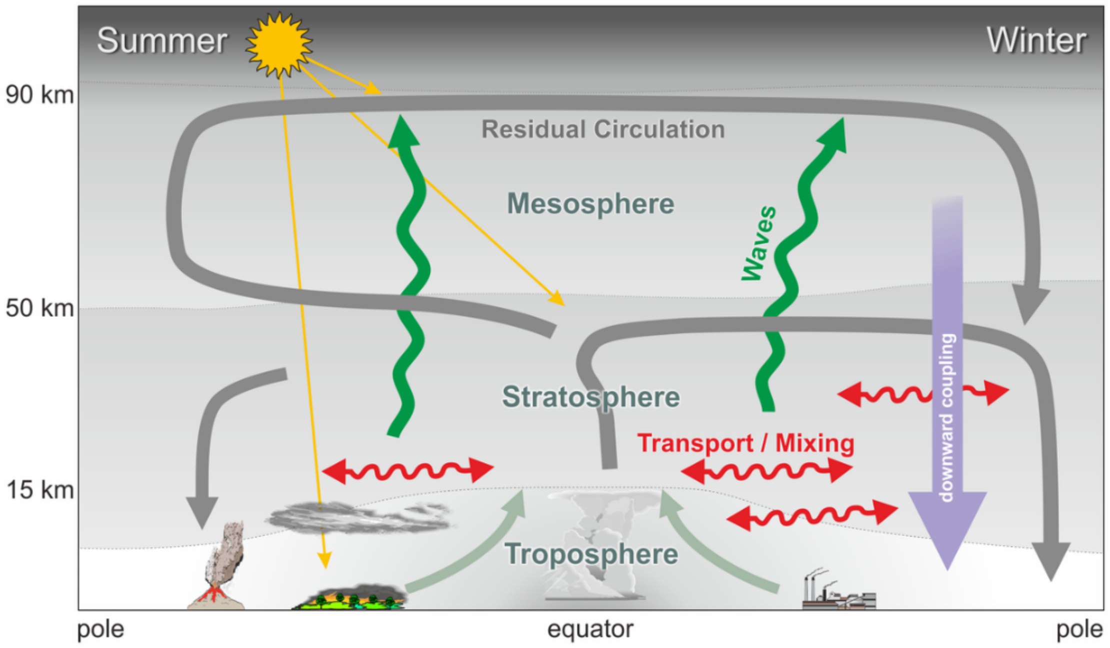

Figure 1.6 Schematic diagram of the global circulation in the stratosphere and mesosphere (Brewer-Dobson circulation) is shown as grey arrows. Upward propagating atmospheric waves, which drive the circulation, are shown as green wavy arrows, and two-way mixing as red arrows.

modulating large-scale weather patterns and improving seasonal forecasts in midlatitude and polar regions (Sigmond et al., 2013).

To better capture these interactions, numerical weather prediction (NWP) and climate models have extended their upper boundaries into the mesosphere and lower thermosphere. However, the scarcity of direct observations at these altitudes remains a major challenge for model development. Without sufficient observational constraints, models rely on parameterizations, artificial damping mechanisms, and sponge layers to approximate middle atmospheric dynamics (Alexander et al., 2010; Kim, Eckermann, and Chun, 2003). The MLT serves as a key transition region for energy and momentum transfer to the upper atmosphere, where planetary, tidal, and gravity waves originating in the troposphere propagate upward, interact nonlinearly, and drive substantial variability in the thermosphere and ionosphere (Alexander et al., 2010; Kim, Eckermann, and Chun, 2003; Liu, 2016). Understanding this vertical coupling across atmospheric layers is essential for accurately modeling energy transport and extreme atmospheric events. Expanding observational datasets and refining model representations of wave-driven interactions will be critical for advancing weather and climate predictions in the Arctic and beyond.

1.2 Atmospheric waves

From the lower to the upper atmosphere, waves and oscillations of various temporal and spatial scales propagate through the atmospheric medium. These waves transport energy and momentum from their source regions to their dissipation regions, where wave breaking and dissipation drive deviations from thermal equilibrium. Wave motions of different scales play a crucial role in the dynamics, physics, and radiative processes of the Arctic middle atmosphere. The following sections provide a brief introduction to the most relevant wave types in the middle atmosphere.

1.2.1 Planetary waves

Planetary waves are large-scale, low-frequency oscillations in the atmosphere due to the Earth's rotation (i.e., the Coriolis effect) and latitudinal temperature gradients. The horizontal scales of *planetary waves* typically span thousands to tens of thousands of kilometers, with zonal wavenumbers 1, 2, and 3. Based on their propagation characteristics and periodicity (Straus and Shukla, 1988), *planetary waves* are generally classified into two types: Quasi-stationary Planetary Waves (QSWs) and Transient Planetary Waves (TPWs).

QSWs are characterized by long periods, typically ranging from several tens of days (Figure 1.7), and appear nearly stationary in the Earth's rotating frame of reference. These waves typically propagate westward relative to the background zonal flow, which is a defining characteristic of *Rossby waves.* Rossby et al., 1939 first derived these waves from the principle of absolute vorticity conservation and demonstrated how the β-effect (i.e., the latitudinal variation of the Coriolis parameter) leads to large-scale atmospheric oscillations, which explains the formation of semi-permanent centers of action such as the Aleutian and Icelandic Lows. These quasi-stationary waves are mainly excited by orographic forcing (e.g., the Himalayas, the Rocky Mountains) and thermal forcing (e.g., land-sea temperature contrasts) (Huang and Gambo, 1982, 1983). Consequently, QSWs are typically more active in the Northern Hemisphere due to their more complex terrain and stronger thermal forcing (Held, Ting, and Wang, 2002). As these waves propagate upward into the stratosphere and mesosphere, they can interact with the polar vortex and trigger major dynamical disturbances such as SSW, subsequently influencing weather and climate patterns in the troposphere.

TPWs are characterized by dominant periodicities of about 2, 5, and 10 days (Madden, 1979; Walterscheid, 1981). These waves are generally excited by mechanisms such as oscillations in background wind, nonlinear wave-wave interactions, and latent heat release in the equatorial atmosphere. They usually reach their peak amplitudes in the MLT and play a significant role in the vertical transport of momentum and energy within these regions (Baldwin and Dunkerton, 2001; Beard et al., 1999; Pancheva, 2001).

QSWs are a key dynamical factor influencing the stratospheric atmosphere. A large number of theoretical, observational, and simulation studies demonstrate that stratospheric QSWs are the result of the upward propagation of QSWs excited in the troposphere (Charney and Drazin, 1990; Charney and Drazin, 1961; Matsuno, 1970; Pogoreltsev et al., 2007). On the one hand, quasi-stationary planetary waves, as long-period disturbances with large spatial scales in the mid-latitude atmosphere, exchange atmospheric composition and heating between the mid-latitude and polar regions of the stratosphere through adiabatic transport. On the other hand, these waves break extensively in the stratosphere and, through wave-mean flow interactions, significantly influence the weather and climate in the stratosphere. Eliassen, 1961 derived the relationships between vertical energy flux, vertical momentum flux, and the mean flow through their study of the vertical propagation of topographic gravity waves, which theoretically explains the vertical propagation of atmospheric waves and their interactions with the mean

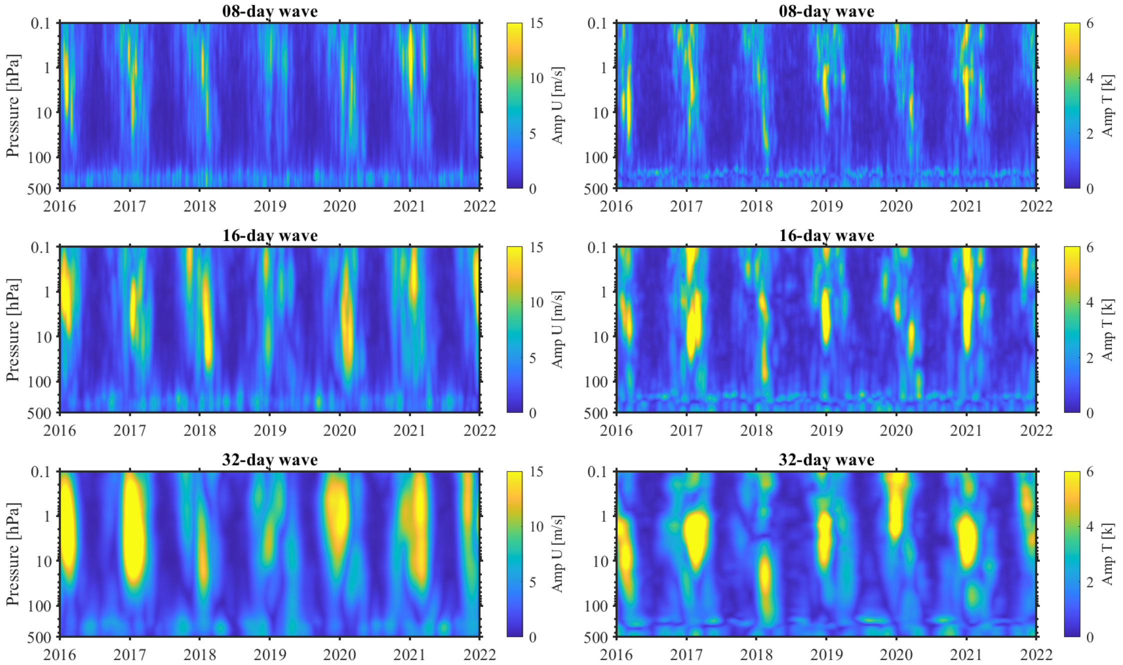

Figure 1.7 Different wave periods derived from zonal wind speed (left) and temperature (right) in the middle atmosphere over Ny-Ålesund, Svalbard (78.99° N, 12° E), based on MERRA-2 reanalysis data from 2016 to 2022.

flow. Momentum and heat transported by Rossby waves can be described by momentum fluxes ($v'u'$) and heat fluxes ($v'\theta'$), with u and v describing the zonal and meridional wind velocities and θ the potential temperature (Andrews, Holton, and Leovy, 1987). The overbars denote zonal averages, while primes indicate the deviation from the zonal mean. Using Eliassen-Palm flux (EPF) and its divergence ($\nabla \cdot F$) to describe the propagation and dissipation of zonally averaged planetary waves (Andrews and McIntyre, 1978; Holton, 1983). In regions with EPF convergence ($\nabla \cdot F < 0$), wave dissipation leads to a deceleration of the zonal flow, and vice versa for regions with EP flux divergence ($\nabla \cdot F > 0$).

Moreover, *planetary waves* can propagate vertically into the middle atmosphere and encounter critical layers, where their phase speed matches the background wind. At these altitudes, the waves undergo breaking, resulting in the deposition of momentum and energy into the mean flow (Matsuno, 1971). This process induces dynamical heating and significantly alters the circulation. The resulting perturbations can destabilize the winter polar vortex and are a primary driver of SSW events (Birner and Albers, 2017; Coy, Eckermann, and Hoppel, 2009; Holton, 1980). Therefore, the propagation and dissipation of *planetary waves* significantly influence the middle atmosphere.

1.2.2 Atmospheric tides

Atmospheric tides are global-scale, periodic oscillations in atmospheric pressure and wind fields primarily driven by the periodic variations in solar thermal radiation and lunar gravitational forcing (Lindzen and Chapman, 1969). Atmospheric tides can be categorized into migrating and non-migrating tides based on their zonal propagation features. Migrating tides always propagate westward with the Sun's apparent motion and exhibit a zonally symmetric structure with constant phase relative to local solar time. They are also referred to as solar tides or sun-synchronous tides. In contrast, non-migrating tides are not sun-synchronous, have different zonal wavenumbers and frequencies, and may propagate eastward or remain stationary. The excitation sources of non-migrating tides are usually related to the differences in solar radiation absorption over land and ocean (Hibbins et al., 2019; Tsuda and Kato, 1989).

The crests and troughs of the zonal structure of migrating tidal waves and the longitudinal distribution of solar radiation strongly reply that migrating tides are primarily driven by solar heating. They typically are driven through three primary mechanisms (Forbes, 1984; Forbes and Garrett, 1979; Hagan, 1996; Hagan, Roble, and Hackney, 2001; Lieberman, Ortland, and Yarosh, 2003; Lindzen and Chapman, 1969): Tropospheric absorption of solar near-infrared radiation by water vapor; Stratospheric ultraviolet absorption by ozone; Thermospheric heating from extreme UV absorption above 100 km altitude. Due to the vertical distribution of water vapor and ozone, the absorption of solar radiation by water vapor decreases with altitude, whereas ozone absorption peaks near 50 km, and the secondary and tertiary ozone layers above this level exhibit a more pronounced seasonal variability.

Tidal waves propagate efficiently upward, relatively small in the lower atmosphere, reaching large amplitudes in the MLT region. Near the surface, tidal winds typically exhibit mean amplitudes of about 2 m/s, while in the MLT region, tidal wind variations can exceed 80 m/s within a few hours as shown in Figure 1.8. When atmospheric tides propagate upward from the lower atmosphere into the middle and upper atmosphere, they are modulated by tropospheric forcing processes near their source regions, including tropical intraseasonal oscillations, QBO, and the Southern Oscillation (Cen et al., 2022; Yang et al., 2018). In addition to being modulated by lower atmospheric activity, tides in the MLT also interact with other large-scale waves (e.g., planetary waves and gravity waves), and with the background zonal-mean flow through nonlinear processes (Forbes and Garrett, 1979; Hagan, Roble, and Hackney, 2001; McLandress, 2002; Riggin and Lieberman, 2013; Yiğit and Medvedev, 2015). These interactions facilitate further energy and momentum exchange, enhancing their influence on the dynamic and physical processes of the middle and upper atmosphere. Furthermore, as tides reach higher altitudes, they may dissipate or break, generating secondary waves and depositing energy and momentum into the mean flow. Through these mechanisms, atmospheric tides serve as one of the primary dynamical drivers of the MLT and upper thermosphere system (Forbes, Zhang, et al., 2008).

Atmospheric tides are fundamental for understanding the dynamics of the atmosphere as a coupled system. Their observation and modeling are therefore crucial for monitoring and predicting atmospheric variability and long-term change (Lindzen, 1971; Lindzen and Chapman, 1969; Volland, 2012). The precise behavior of atmospheric tides on sub-seasonal and local scales remains an active area of research. In particular, the day-to-day variability in amplitude and phase, and the detailed relationships between tidal signatures in temperature and wind fields, as well as the atmospheric composition, are topics of current atmospheric research.

For instance, Baumgarten and Stober (2019) analyzed diurnal and semidiurnal temperature tides using lidar observations and compared their phase characteristics with wind field tides derived from reanalysis data. Additionally, a climatological comparison conducted by Stober,

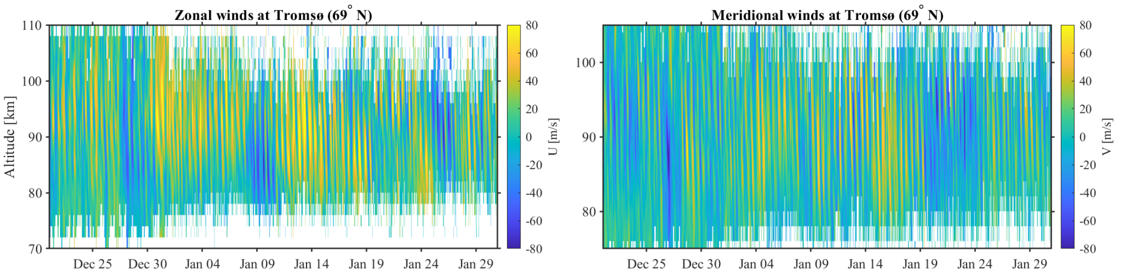

Figure 1.8 Zonal (left) and meridional (right) hourly winds as a function of time and height above polar latitude station at Tromsø (69.58° N, 19.22° E) during the wintertime measured by Meteor radar.

Kuchar, et al., 2021 utilized wind measurements from six meteor radars located at conjugate latitudes to validate mean winds and the representation of diurnal and semidiurnal tides in general circulation models (GCMs). Further, the modulation of tidal amplitudes by trace gas variability during major SSW events has been explored using simulated radiative heating and cooling rates. A detailed analysis of these interactions is presented in chapter 6.

1.3 Composition and radiative effects

1.3.1 Ozone

Ozone (O_3) is classified as an essential climate variable by the World Meteorological Organization (WMO) due to its significant role in atmospheric chemistry and climate regulation. Despite being a minor constituent of the Earth's atmosphere (accounting for less than 0.0001% of its composition), ozone plays a crucial role in absorbing and filtering out harmful UV radiation from the Sun, particularly UV-B and UV-C wavelengths, preventing them from reaching the Earth's surface, consequently enabling and sustaining life in the Earth's biosphere.

Ozone is mostly found in the stratosphere approximately between 20 and 50 km above the surface, a region often referred to as the *stratospheric ozone layer*, where ozone concentration is relatively high with a maximum of 5 ppmv at the polar latitudes in summer (Figure 1.11a). In the stratosphere, it is primarily produced through the photodissociation of molecular oxygen (O) by UV radiation, a process described by the Chapman cycle:

$$O_2 + h\nu \longrightarrow O + O \tag{1.1}$$

$$O + O_2 + M \longrightarrow O_3 + M \tag{1.2}$$

$$O_3 + h\nu \longrightarrow O_2 + O \tag{1.3}$$

$$O_3 + O \longrightarrow O_2 + O_2 \tag{1.4}$$

The formation of O_3 is preceded by the photodissociation of molecular oxygen (O_2), producing atomic oxygen (O) as described in Equation 1.1. Solar UV radiation with wavelengths shorter than 242 nm (UV-C) breaks apart an O_2 molecule into two O atoms. In an exothermic three-body reaction, O subsequently combines with O_2 to form O_3, as shown in Equation 1.2. Here, M acts as an inert collision partner, which can be any atmospheric constituent. The rapid photolysis of O_3 results in the production of O_2 and O, as described in Equation 1.3. Due to the fast exchange between O and O_3, recombination reactions also occur, converting O and O_3 back into O_2 in Equation 1.4. Because of the rapid interchange between O_3 and O, they are often treated together as the odd oxygen (O_X) family.

Chapman's pure-oxygen chemistry, described above, governs the formation and destruction of ozone. In addition, the equilibrium concentration of O_3 is also controlled by catalytic reactions involving specific catalysts, as outlined in the general scheme;

$$\mathrm{O_3 + X \longrightarrow XO + O} \tag{1.5}$$

$$\mathrm{XO + O \longrightarrow X + M} \tag{1.6}$$

$$\mathrm{O_3 + O \longrightarrow 2\,O_2} \tag{1.7}$$

Species that can most efficiently fulfill the role of catalyst X are hydroxyl radicals (OH), nitrogen oxides (NO), and inorganic halogens, which are particularly effective in the destruction of ozone (Bates and Nicolet, 1950). These catalysts play a significant role in ozone depletion, especially in the polar stratosphere, where their abundance and reactivity are enhanced under certain conditions.

To understand changes in O_3 abundance in the atmosphere, it is essential to consider two main processes: (1) the transport of O_3 into or out of the region of interest, and (2) the chemical creation or destruction of O_3. These processes are described by the continuity equation:

$$\frac{d[O_3]}{dt} = \underbrace{\frac{\partial[O_3]}{\partial t} + V \cdot \nabla[O_3]}_{(1)} + \underbrace{S}_{(2)} \tag{1.8}$$

where $[O_3]$ represents the concentration of ozone, V is the wind vector, and S denotes the chemical sources and sinks of ozone. The first two terms on the right-hand side describe the transport of ozone, which is governed by atmospheric dynamics. The third term represents the chemical processes that create or destroy ozone, controlled by atmospheric chemistry. When examining ozone production and loss, it is essential to distinguish between the two factors influencing changes in ozone concentrations, as they can either obscure or mimic each other. The interplay between dynamics and chemistry plays a crucial role in shaping the distribution of atmospheric constituents, and understanding this competition between both is key to accurately interpreting ozone changes (Brasseur and Solomon, 2005).

Ozone is also present in the MLT regions, though at lower concentrations than in the stratosphere. A *secondary ozone layer* forms between 90 and 105 km (Figure 1.9), with a peak concentration driven by UV absorption at much shorter wavelengths (137–200 nm) compared to the *stratospheric ozone layer*, which primarily forms due to the absorption of UV radiation in the 185–242 nm range by molecular oxygen (Smith and Marsh, 2005). The extremely cold temperatures in the mesopause region, combined with the location of the atomic oxygen density maximum, contribute to ozone formation at this altitude. Furthermore, a *tertiary ozone layer* exists between 70 and 75 km (Figure 1.9), characterized by a local maximum that occurs exclusively at high latitudes in the wintertime hemisphere during nighttime (Marsh, Smith, et al., 2001; Smith, Espy, et al., 2018). This nighttime phenomenon results from a significant reduction in ozone destruction by hydrogen radicals under nocturnal conditions (Degenstein et al., 2005; Marsh, Smith, et al., 2001).

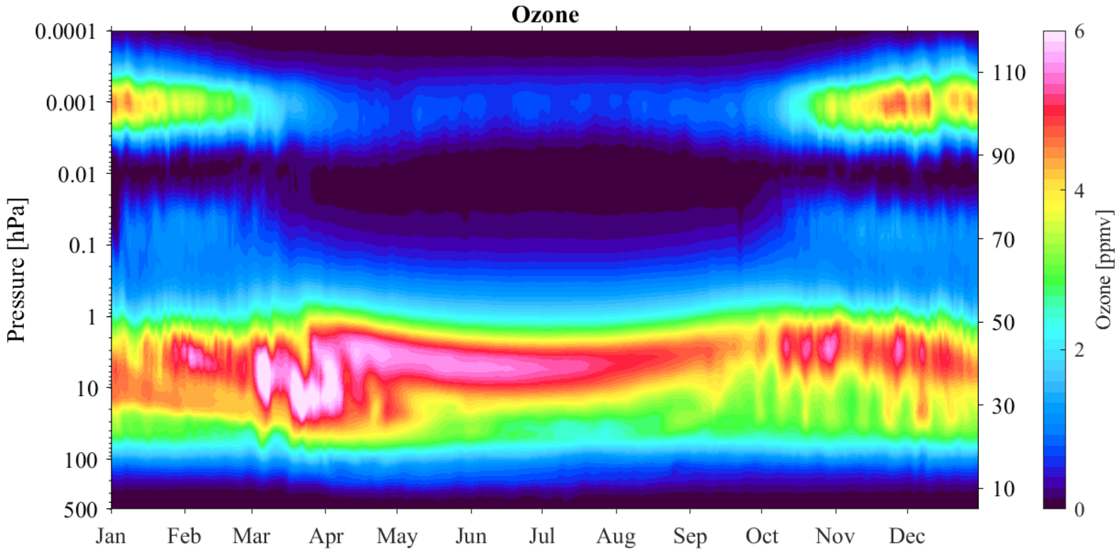

Figure 1.9 Variation of ozone VMR in the Arctic averaged from 70° N to 90° N in 2022 simulated by WACCM-X(SD).

1.3.2 Water vapor

Water vapor (H_2O) is a key trace gas in the middle atmosphere, playing a crucial role in atmospheric chemistry, radiation, and dynamics. Although its concentration is relatively low compared to the troposphere, water vapor in the stratosphere and mesosphere significantly influences climate processes, the ozone layer, and atmospheric circulation. The primary sources of water vapor in the middle atmosphere include:

1. Water vapor enters the middle atmosphere through the cold tropical tropopause, where low temperatures cause most of it to condense and freeze into ice particles before ascending (Fueglistaler et al., 2009; Holton et al., 1995; Nassar et al., 2005).
2. The oxidation of methane (CH_4) generates water vapor within the middle atmosphere (Brasseur and Solomon, 2005; Le Texier, Solomon, and Garcia, 1988):

$$CH_4 + OH \longrightarrow CH_3 + H_2O \tag{1.9}$$

3. Occasional injections from deep convection or volcanic eruptions (Corti et al., 2006; Dessler and Sherwood, 2009; Joshi and Jones, 2009; Manney, Santee, et al., 2023; Xu et al., 2022).

In the stratosphere, water vapor concentration generally increases with altitude due to methane oxidation. However, as altitude increases, photodissociation becomes a significant loss mechanism. Below approximately 70 km, photodissociation is driven by radiation in the Schumann-Runge bands. At higher altitudes, Lyman-α radiation (121.6 nm) dominates the breakdown of water vapor. The balance between production and loss processes typically results in a maximum water vapor concentration near the stratopause - water vapor volume mixing ratio peak of about 7 ppmv near this altitude in the polar region in summer, as seen in Figure 1.11b.

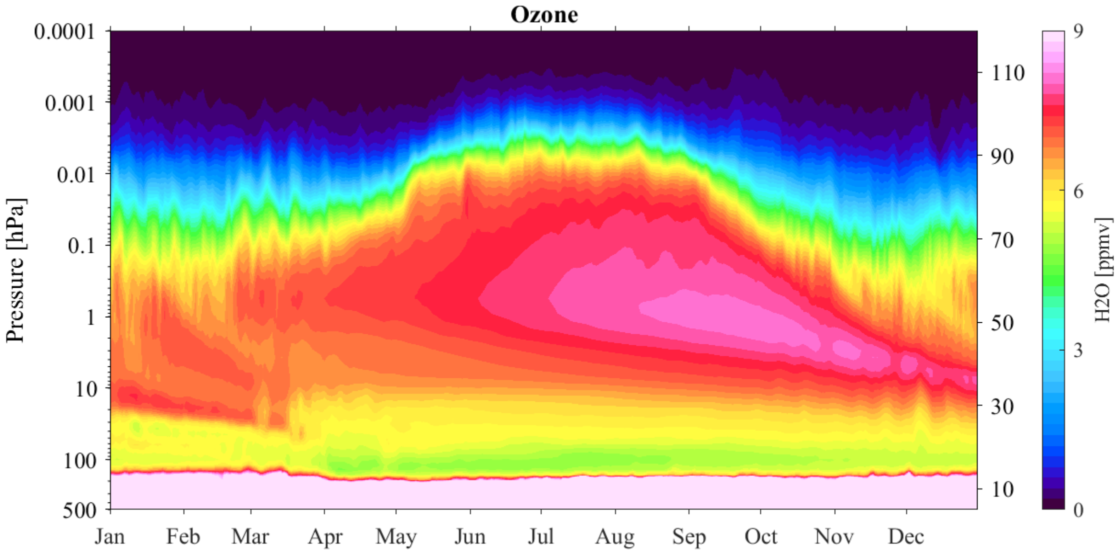

Figure 1.10 Variation of water vapor VMR in the Arctic averaged from 70° N to 90° N in 2022 simulated by WACCM-X(SD).

Above the mesosphere, water vapor concentration generally decreases with altitude due to the absence of additional sources. However, two distinct exceptions disrupt this trend, occurring under specific spatial and temporal conditions. A secondary peak between 65 km and 75 km appears in the tropics around the equinox and in the polar summer. It results from an interplay of dynamics and chemistry during intense solar insolation, involving upwelling winds and autocatalytic water vapor formation from molecular hydrogen (Sonnemann, Grygalashvyly, and Berger, 2005). An additional peak around 82 km in the polar summer arises due to the redistribution of water vapor by sedimenting ice particles associated with noctilucent clouds (NLCs) and polar mesospheric summer echoes (PMSEs) (Summers et al., 2001; Von Zahn and Berger, 2003).

Water vapor is a valuable tracer for studying dynamical processes in the middle atmosphere, as its chemical lifetime and vertical transport timescales are comparable (Brasseur and Solomon, 2005). Its lifetime varies with altitude, ranging from weeks in the upper mesosphere to months in the lower mesosphere. The wave-driven large-scale meridional circulation influences water vapor transport, with upwelling of moist air in summer and subsidence of dry air in winter (Figure 1.10). Water vapor has been widely used to investigate vertical motion in the middle atmosphere, including transport during SSWs, periodicities, and ascent and descent rates (**shi2023**; Bailey et al., 2014; Lee et al., 2011; Orsolini et al., 2010; Scheiben et al., 2012; Schranz, Tschanz, et al., 2019; Tschanz and Kämpfer, 2015). Additionally, water vapor observations can capture well the following large-scale descent inside the newly formed mesospheric vortex. The polar vortex edge acts as a transport barrier, limiting the exchange of chemical species between midlatitudes and polar regions. This leads to strong horizontal gradients in water vapor concentrations across the vortex boundary. At mesospheric altitudes, water vapor levels are generally lower inside the polar vortex than outside, due to the downward transport of dry air from higher altitudes within the vortex core.

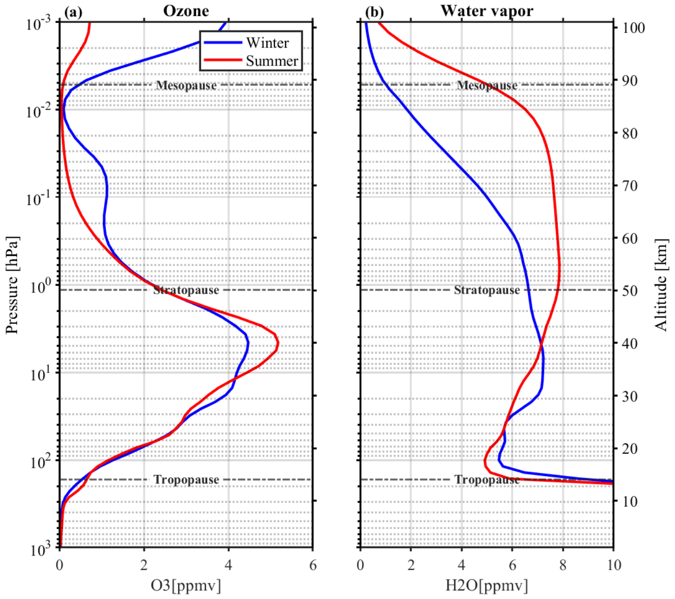

Figure 1.11 Mean seasonal ozone (a) and water vapor VMR profiles over Ny-Ålesund, Svalbard (78.99° N, 12° E) during boreal winter and summertime from WACCM-X(SD) model simulations.

1.3.3 Radiative and dynamical effects of ozone and water vapor

Ozone and water vapor are key trace gases in the Earth's atmosphere, both playing essential roles in sustaining life and regulating the climate. Typical ozone and water vapor profiles from the surface up to 100 km altitude can be seen in Figure 1.11. Stratospheric ozone absorbs harmful UV radiation from the Sun, protecting life on Earth's surface. This absorption also heats the stratosphere, shaping the atmospheric thermal structure. In contrast, tropospheric ozone acts as a pollutant that poses risks to human health but also serves as an oxidizing agent, helping to break down other atmospheric pollutants. Water vapor is one of the most significant greenhouse gases (GHG) in the troposphere, contributing to the greenhouse effect that increases the Earth's mean surface temperature. Additionally, water vapor has a chemical lifetime of the order of months to years in the upper stratosphere and lower mesosphere (Brasseur and Solomon, 2005), making it a valuable tracer for studying large-scale upwelling and downwelling of air masses in the polar mesosphere (Schranz, Tschanz, et al., 2019; Straub, Tschanz, et al., 2012; Tschanz, Straub, et al., 2013).

Both ozone and water vapor are the major contributors to solar heating and terrestrial cooling, thereby influencing Earth's radiation budget and surface climate (Brasseur and Solomon, 2005). In the middle atmosphere, ozone is the dominant absorber, and carbon dioxide is the dominant emitter. Infrared emission by ozone and water vapor, and solar absorption by water vapor, molecular oxygen, carbon dioxide, and nitrogen dioxide play secondary roles (Figure 1.12). The primary source of solar heating in the stratosphere and mesosphere is the absorption of ultraviolet radiation by ozone, while in the lower thermosphere, molecular oxygen plays a dominant role. On the other hand, terrestrial cooling is primarily driven by thermal infrared emission, which is strongly dependent on temperature and the presence of GHG such as carbon dioxide, ozone, and water vapor. These gases regulate the Earth's energy balance by absorbing and re-emitting infrared radiation, influencing atmospheric temperatures and climate dynamics. The presence of GHG, such as carbon dioxide, ozone, and water vapor, absorb and re-emit longwave radiation, acting to cool the stratosphere and mesosphere. Although GHG warm the troposphere by trapping outgoing longwave radiation, some of this re-emitted radiation escapes to space, resulting in overall cooling of the stratosphere. This cooling occurs because the stratosphere is less dense and optically thinner than the troposphere, allowing more infrared radiation to be lost to space.

In the Arctic stratosphere, the highest temperatures occur during the polar summer when continuous solar radiation heats the atmosphere, while the lowest temperatures are observed in winter due to the prolonged absence of sunlight and strong radiative cooling. However, stratospheric temperatures in the Arctic can fluctuate more, leading the ozone and water vapor changes, particularly during extreme events such as SSWs. Exploration of the distinct roles of the radiative and dynamical heating rates during these events can link to the ozone and water vapor VMR variations, whereby the heating/cooling supplied by dynamics is balanced by shortwave radiative heating and longwave radiative cooling. Following a discussion of the approximations and assumptions (Dunkerton, 1978; Solomon et al., 1986), the zonally averaged residual Eulerian thermodynamic equation can be expressed as:

$$\frac{\partial \overline{T}}{\partial t} + \overline{v}^* \frac{\partial \overline{T}}{\partial y} + \overline{\omega}^* (\frac{HN^2}{R} + \frac{\partial \overline{T}}{\partial z}) = \overline{Q} \tag{1.10}$$

where $\overline{T}$ is the zonally averaged deviation from the global mean temperature, $\frac{\partial \overline{T}}{\partial z}$ represents the temperature gradient, and $\frac{HN^2}{R}$ represents the global mean static stability. The net radiative heating rate $\overline{Q}$ (Kiehl and Solomon, 1986; Solomon et al., 1986) accounts for the combined effects of both shortwave and longwave radiative heating. The $\overline{v}^*$ and $\overline{\omega}^*$ are the residual meridional and vertical winds as follows (Andrews, Holton, and Leovy, 1987):

$$M_y = -e^{z/H}(\overline{v'\chi'} - \overline{v'\theta'}/\overline{\theta}_z \overline{\chi}_z) \tag{1.11}$$

$$M_z = -e^{z/H}(\overline{\omega'\chi'} - \overline{v'\theta'}/\overline{\theta}_z \overline{\chi}_y) \tag{1.12}$$

where v and ω are the meridional and vertical winds, θ is the potential temperature, a is the Earth's radius, and φ is the latitude.

The complex interactions within the chemistry-climate system (Figure 1.13) make it challenging to attribute changes in ozone solely to variations in ozone-depleting substance (ODS)s and other influencing factors. For instance, reductions in polar stratospheric ozone due to increased equivalent stratospheric chlorine (ESC) lead to stratospheric cooling, as less UV radiation is absorbed by ozone. This cooling further enhances the effectiveness of ESC by promoting the formation of polar stratospheric clouds. Additionally, rising GHG concentrations contribute to the radiative cooling of the stratosphere while simultaneously strengthening the BDC, which induces adiabatic warming in the polar stratosphere and enhances mixing with lower latitudes.

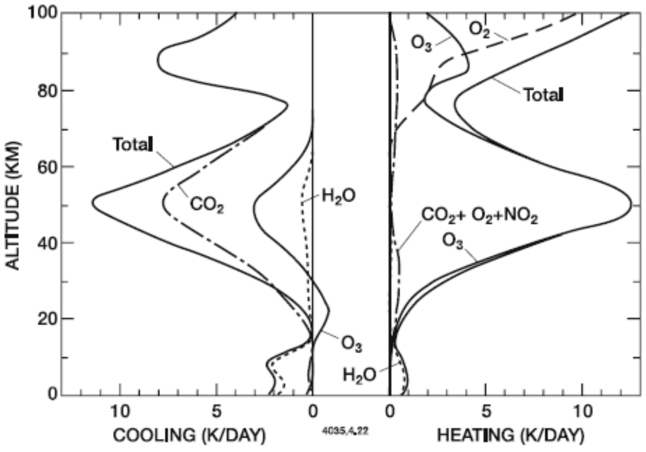

Figure 1.12 Vertical distribution of solar short-wave heating rates by ozone (O_3), molecular oxygen (O_2), Nitrogen Dioxide(NO_2), water vapor (H_2O), carbon dioxide (CO_2), and the terrestrial long-wave cooling rates by CO_2, O_2, and H_2O. This figure is from Brasseur and Solomon, 2005.

1.4 Observational and modeling approaches

The following section provides a comprehensive overview of ozone and water vapor measurements in the middle atmosphere, highlighting key observational techniques, including satellite, ground-based, and in-situ measurements. Additionally, it discusses model simulations used to study their distributions, variability, and underlying physical and chemical processes. The section also examines the strengths and limitations of different measurement approaches and the role of models in interpreting observations and improving our understanding of middle atmospheric dynamics and chemistry.

1.4.1 Measurements

Various techniques are used to measure trace gases in the atmosphere, with the choice of method depending on factors such as altitude range, spatial coverage, and temporal resolution. These techniques can be broadly classified into in situ measurements and remote sensing methods (Figure 1.14). In situ measurements, conducted using instruments on balloons, aircraft, or rockets, provide direct sampling at specific locations. In contrast, remote sensing techniques, including ground-based or satellite measurements rely on the atmospheric emission and absorption of electromagnetic radiation to measure atmospheric trace gases. These methods are governed by the principles of radiative transfer theory.

Balloon-borne techniques (ozonesondes) provide valuable in situ measurements of the vertical distribution of the ozone concentration in the atmosphere but are limited to the lower part of the middle atmosphere, generally reaching altitudes of up to approximately 35 km. Ozonesondes are lightweight and launched in tandem with a radiosonde that also transmits air pressure, temperature, humidity, and wind data to a ground station (Murata et al., 2009; Van Malderen et al., 2021) to investigate atmospheric gravity wave activity (Chane-Ming et al., 2000; Tateno and Sato, 2008). Ultra-thin-film high-altitude balloons that can attain an altitude of about 50 km (Matsuzaka et al., 2000). Precise water vapor measurements above the

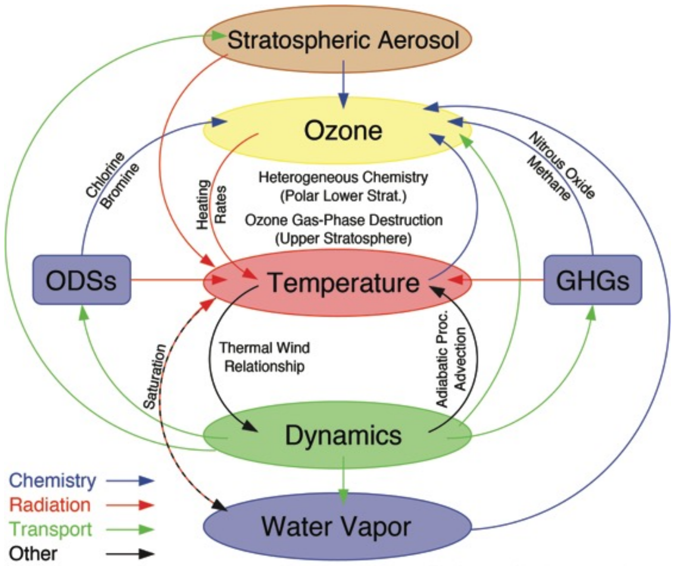

From Chapter 3 of *Scientific Assessment of Ozone Depletion: 2010* (WMO, 2011).

Figure 1.13 Schematic of stratospheric chemistry-climate interactions of ozone and water vapor. Links between elements of the chemistry-climate system are indicated with arrows representing chemistry (blue), radiation (red), transport (green), and other mechanisms (black). This figure is from the WMO report using a simplified picture including feedback processes. Simple and more complex feedback cycles can be constructed following the linking mechanisms.

troposphere can also be collected by in-situ balloon-borne sensors such as Laser Absorption Spectrometers (Graf et al., 2021). Weather balloons are launched once or twice daily from numerous stations worldwide, and their data are widely assimilated into NWP models and reanalysis datasets, such as the MERRA-2. In situ observations are achievable to measure the stratospheric ozone profile through sounding rocket campaigns. Additionally, these rockets have been instrumental in studying atmospheric tides in the middle atmosphere, as demonstrated by (Lindzen and Chapman, 1969; Müllemann and Lübken, 2005), who used repeated rocket soundings to investigate tidal structures. Due to their ability to obtain high-resolution data during both ascent and descent, sounding rockets are also effective in capturing small-scale atmospheric phenomena, such as turbulence in the MLT region (Roberts and Larsen, 2014). Aircraft-based measurements offer high spatial and temporal resolution, complementing balloon and satellite observations. Research aircraft equipped with specialized instruments have been used in various campaigns to investigate stratospheric composition and dynamics. For example, airborne platforms such as NASA's ER-2 and WB-57 aircraft have been employed to study stratospheric ozone variability and transport processes (Anderson et al., 2017). Similarly, in situ water vapor measurements from aircraft missions have contributed to understanding stratosphere-troposphere exchange and the role of water vapor in climate regulation (KLEY, 2000).

Remote exploration of dynamics and composition in the middle atmosphere is challenging due to the region's altitude and the limitations of direct in-situ measurements. The Network for the Detection of Atmospheric Composition Change (NDACC) is a globally coordinated international network comprising over 90 stations that conduct high-precision, long-term measurements of atmospheric composition (De Mazière et al., 2018). NDACC is structured around

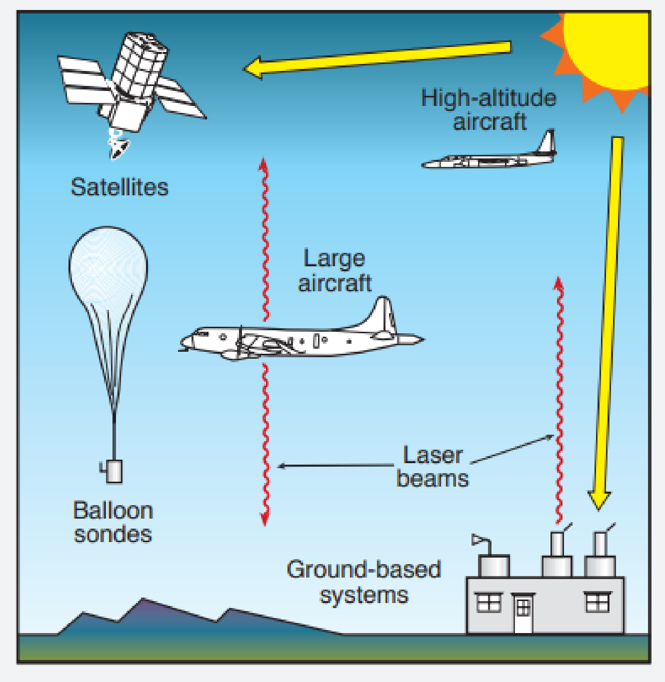

Figure 1.14 Overview of different measurement approaches for atmospheric composition (Salawitch et al., 2019).

categories of ground-based observational techniques (sonde, lidar, microwave radiometers, Fourier Transform Infrared (FTIR), UV-visible Differential Optical Absorption Spectroscopy (DOAS)-type, and Dobson–Brewer spectrometers, as well as spectral UV radiometers), timely cross-cutting themes (ozone, water vapor, measurement strategies, cross-network data integration), satellite measurement systems, and theory and analyses (Figure 1.15):

Ground-based observations play a key role in monitoring middle atmospheric composition. Microwave radiometers (e.g., GROMOS-C and MIAWARA-C) detect emission lines from ozone and water vapor in the microwave spectrum, providing vertical profiles with high time resolution (Fernández, Murk, and Kämpfer, 2015; Schranz, Fernandez, et al., 2018; Straub, Murk, and Kämpfer, 2010). FTIR spectrometers record solar absorption spectra, allowing highly precise and accurate retrieved water vapor profiles (Schneider and Hase, 2009; Wu et al., 2023). The long-term stability of ground-based FTIR measurements makes them valuable for validating satellite-derived water vapor data and model simulations (Bernet et al., 2020; Vigouroux et al., 2008). Lidars and radars provide long-term data for detecting the changes and trends in the middle atmosphere. Differential Absorption Lidar (DIAL) measures ozone concentration profiles with a high vertical resolution, while radars contribute to wind and turbulence measurements that influence water vapor transport (Keckhut et al., 2011; Steinbrecht et al., 2009). Satellite-based instruments offer global coverage of ozone and water vapor distributions. Instruments such as the MLS on Aura, the Sub-Millimeter Radiometer (SMR) on Odin, and FTIR sensors like TROPOspheric Monitoring Instrument (TROPOM) provide continuous observations, capturing key dynamical and chemical processes influencing middle atmospheric composition (Murtagh et al., 2002; Waters et al., 2006). By integrating data from these complementary remote sensing techniques, researchers can better investigate middle atmospheric processes, improve model

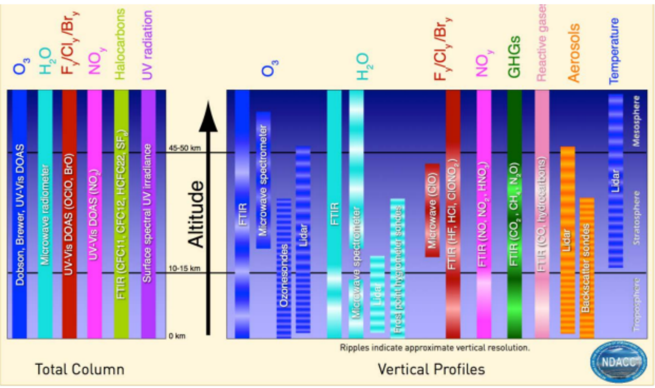

Figure 1.15 NDDACC measurements capabilities, including species and parameters measured, instrumental measurement techniques, and watch measurements approximate vertical resolution (from (De Mazière et al., 2018).

simulations, and enhance our understanding of the role of ozone and water vapor in atmospheric circulation and climate.

1.4.2 Models

Atmospheric models, especially those focused on weather prediction and climate research are mainly concerned with the troposphere and the lower stratosphere. In the last decades, a general trend to elevated model-tops has been observed with models providing data for the middle atmosphere (up to 80 km), and even up to the thermosphere (500 km). How well the modeled quantities agree with measurements in these altitudes is the subject of current research (Blanc et al., 2019; Le Pichon et al., 2015; Rüfenacht, Baumgarten, et al., 2018a).

Global Climate Models (GCMS) and Chemistry-Climate Models (CCMs) are essential tools for investigating dynamics, chemistry, and radiative processes in the stratosphere and mesosphere. A key application of these models is to assess ozone depletion and recovery (Amos et al., 2020), particularly in response to ODSs and climate change. For example, the WACCM, a high-top extension of the Community Earth System Model (CESM), simulates stratospheric ozone trends (Davis et al., 2023; Gettelman et al., 2019), the impact of the QBO (Wang, Hong, et al., 2022), and planetary wave propagation in the middle atmosphere (Lu et al., 2018). Furthermore, WACCM simulations can capture the formation of nighttime secondary ozone layers during major SSW events (Tweedy et al., 2013), and the spatial and temporal structure of tertiary ozone maximum in the polar winter mesosphere (Smith, Espy, et al., 2018).

Models such as MERRA-2 and European Centre for Medium-Range Weather Forecasts (ECMWF) reanalyses datasets assimilate observational data to improve the representation of stratosphere-troposphere exchange and mesospheric dynamics, which influence climate variability and extreme weather events (Wang, Fu, et al., 2023). The Chemistry-Climate Model Initiative (CCMI) has provided multi-model assessments of stratospheric ozone trends and variability, demonstrating how changes in middle atmospheric composition impact surface climate and circulation patterns (Cohen et al., 2021; Garfinkel et al., 2021; Harari et al., 2019).

Chemical Transport Models (CTMs) such as Toulouse Off-line Model of Chemistry And Transport/Single Layer Isentropic Model of Chemistry And Transport (TOMCAT/SLIMCAT) and Goddard Earth Observing System (GEOS)-Chem have been extensively used to study stratospheric ozone and water vapor transport. TOMCAT/SLIMCAT, a 3-dimensional offline model, relies on prescribed meteorological fields to simulate ozone depletion and water vapor variations, particularly in response to dynamical and chemical processes (Chipperfield, 2006). Similarly, GEOS-Chem, driven by reanalysis meteorology, has been widely applied to investigate the transport of tropospheric pollutants into the lower stratosphere and the impact of climate variability on ozone distribution (Bey et al., 2001).

The Chemical Lagrangian Model of the Stratosphere (CLaMS) focuses on small-scale transport and mixing effects that influence ozone and water vapor variability. Studies using CLaMS have demonstrated the importance of isentropic mixing and diabatic descent in shaping polar ozone loss and tropical water vapor variability (McKenna et al., 2002). Additionally, regional-scale models like Icosahedral Nonhydrostatic Model (ICON) and Weather Research and Forecasting Model (WRF) have been employed to investigate gravity wave dynamics, stratospheric intrusions, and mesoscale transport processes (Zängl et al., 2015). These models have provided valuable insights into the fine-scale structure of the middle atmosphere, aiding in the improvement of parameterizations in global models.

2 Datasets

To investigate the variability of middle atmospheric ozone and water vapor in the Arctic, as well as their radiative effects on mesospheric tides, this thesis utilizes ground-based microwave radiometer and meteor radar measurements. Given the complexity of atmospheric processes, it is essential to complement these observations with satellite measurements and reanalysis datasets to achieve a more comprehensive understanding. With continuous advancements in satellite technology and improvements in data assimilation models, an increasing number of atmospheric datasets have become available. The following sections provide a detailed overview of the ground-based measurements and other datasets used in this study.

2.1 Ground-based microwave measurements

2.1.1 Microwave radiometry

Microwave radiometry is a passive remote sensing technique that measures trace gases, temperature, and horizontal winds in the middle atmosphere. It uses radiation in the microwave part of the electromagnetic spectrum from approximately 3 GHz to 3000 GHz, with corresponding wavelengths from 10 cm to 0.1 mm. The principle of microwave radiometry is described in detail for example in Clancy and Muhleman, 1993. Microwave radiometry observes rotational transition lines of atmospheric molecules in the microwave spectrum. It is one of the very few measurement techniques that is sensitive to the middle atmosphere from 30 to 70 km altitude and is also able to provide altitude-resolved profiles in this altitude region. For a long time it has been used to remotely measure the mixing ratio of atmospheric constituents like ozone or water vapor (e.g. Lobsiger, 1987; Nedoluha, Bevilacqua, et al., 1995).

In microwave radiometry, we are interested in the intensity of radiation emitted by a molecule. Molecules that possess an electric or magnetic dipole absorb and emit microwave radiation due to rotational transitions between energetic states. Each molecular species has its own absorption and emission spectrum characterized by molecule-specific spectral lines. The strength of the emitted spectral lines can then be used to derive information about the atmospheric composition.

The shape of the emission lines of oxygen, ozone, and water vapor in the microwave spectrum is determined by the broadening of the central line. A microwave radiometer at the ground measures the pressure and Doppler broadened emission lines, which can be used to infer altitude-resolved profiles of a specific species. The most likely vertical distribution of the species can be inferred with an optimal estimation technique using a radiative transfer model to simulate

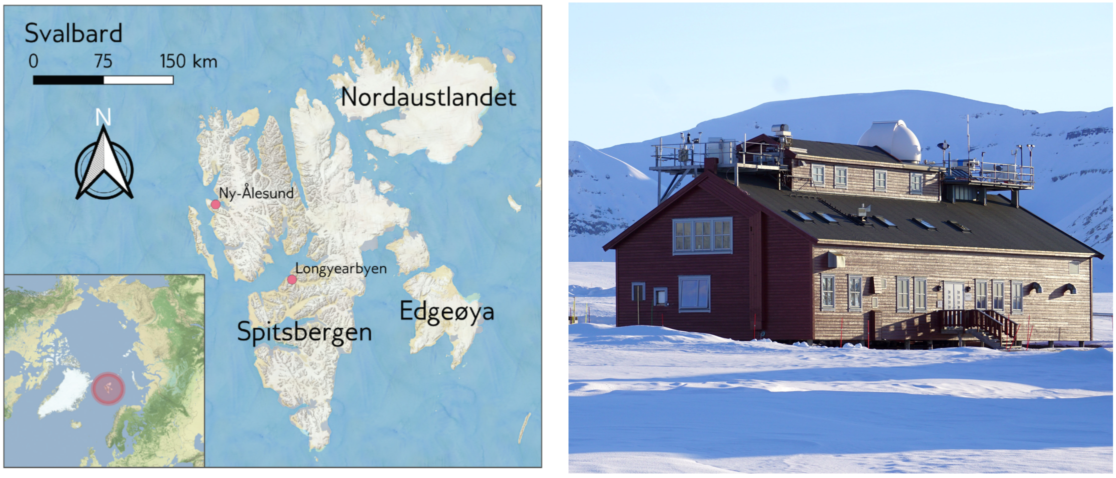

(a) **(b)**

Figure 2.1 The location of Ny-Ålesund is on the island of Spitsbergen in the Svalbard archipelago (a), well within the Arctic Circle (Schön et al., 2022). It serves as a hub for Arctic research, hosting permanent stations from 11 countries and several ground-based atmospheric observatories, including the French-German Alfred Wegener Institute for Polar and Marine Research and the Polar Institute Paul-Émile Victor (AWIPEV) Arctic Research Base (b) from the AWIPEV website. GROMOS-C and MIAWARA-C are located on the roof of this observatory.

the observed spectral line. These models essentially solve the above equations for prescribed atmospheric conditions. In this thesis, the Atmospheric Radiative Transfer Simulator (ARTS) has been used to perform the most radiative transfer calculations. ARTS is an open-source community model focused on the microwave frequency region (Buehler et al., 2018; Eriksson, Buehler, et al., 2011) and includes useful features to simulate the effect of the microwave receiver on the incoming radiation (Eriksson, Ekström, et al., 2006) and is very flexible with regards to the atmosphere definition.

2.1.2 Instruments: GROMOS-C and MIAWARA-C

To improve monitoring of middle atmospheric composition changes in the polar regions and to investigate dynamic and chemical processes in the Arctic, two ground-based microwave radiometers GROMOS-C and MIAWARA-C at Ny-Ålesund, Svalbard (78.99° N, 12° E) have performed the ozone and water vapor measurements since September 2015. Developed by the Institute of Applied Physics (IAP) at the University of Bern, these instruments observe day-to-day, seasonal, annual, and long-term variations in ozone and water vapor in the middle atmosphere, providing valuable insights into polar atmospheric variability and long-term trends.

The location of Ny-Ålesund (see Figure 2.1a) within the Arctic Circle provides a unique viewpoint for atmospheric observations. As one of the northernmost year-round research stations in the world and hosting several research stations from many different countries, it plays a key role in global atmospheric monitoring networks. The location offers a well-maintained infrastructure and minimal local pollution. Research activities at Ny-Ålesund span a wide range of disciplines, including atmospheric science, glaciology, terrestrial ecology, and marine ecosystems, making it ideal for polar-latitude studying the impacts of climate change.

Both GROMOS-C and MIAWARA-C were deployed in September 2015 at the AWIPEV Arctic Research Base in Ny-Ålesund, Svalbard, one of the northernmost permanent research stations in the world (see Figure 2.1b for a view of the observatory). The AWIPEV base, jointly operated by France and Germany, plays a vital role in polar research and contributes to the NDACC—a global network of over 90 stations dedicated to high-quality measurements of atmospheric constituents.

Periods of high optical thickness, especially during rainfall, can introduce substantial noise into the measured spectra, leading to retrieval failures, particularly for ozone measurements from GROMOS-C. Moreover, MIAWARA-C is equipped with an automatic protective lid that closes during precipitation, preventing measurements from being recorded under rainy conditions. However, the clean and dry Arctic air, particularly during winter, often results in relatively low atmospheric opacity, enhancing measurement accuracy.

GROMOS-C

GROMOS-C is an ozone microwave radiometer that measures the ozone emission line at 110.836 GHz (Fernández, Murk, and Kämpfer, 2015). The Microwave Physics group in Bern has specialized in the development of ozone radiometers for several decades (Calisesi et al., 2002; Calisesi, 2003; Moreira et al., 2015). Unlike other instruments, GROMOS-C was designed to be compact, facilitating transport and operation at remote field sites under extreme climate conditions. Additionally, GROMOS-C can switch the frequency of its local oscillator, allowing it to also measure CO at 115 GHz. The instrument is housed externally and is not installed inside a building, ensuring free sight in all cardinal directions. GROMOS-C features two rotating mirrors, enabling observations in all directions. Therefore, GROMOS-C observes subsequently on the four cardinal directions (North, East, South, and West) under an elevation angle of 22° with a sampling time of 4 s (in Figure 2.3a, b). A photograph of GROMOS-C located on the roof of the atmospheric observatory at Ny-Ålesund is shown in Figure 2.2.

Ozone profiles are retrieved from the ozone spectra with ARTS Version 2 (Eriksson, Buehler, et al., 2011) using QPACK (Eriksson, Jiménez, and Buehler, 2005) and according to an optimal estimation algorithm (Rodgers, 2000). The retrieved ozone profiles cover an altitude range of approximately 20-70 km with a time resolution of 2 hours. The retrieved ozone profile agrees well with the convolved MLS profile and has been illustrated (**shi2023**; Fernández, Murk, and Kämpfer, 2015). The averaged ozone time series, calculated from the four cardinal directions, is shown in Figure 2.2c. The measurement response is defined as the area below the averaging kernel for the given altitude and is a measure of the relative contribution of the a priori to the retrieved profile. The area where the measurement response is larger than 0.8 is considered the trustworthy altitude range of the ozone profile. The peak height of the averaging kernels corresponds to the nominal height of the averaging kernel between 50 and 0.1 hPa, and the vertical resolution increases from about 10 to 25 km in this altitude range. The altitude resolution is defined as the full width at half-maximum of the averaging kernel. Zonal and meridional wind profiles are retrieved from ozone spectra measured in the east-west and north-south directions. The retrieval algorithm is described by Hagen et al. (2018) and Rüfenacht, Kämpfer, and Murk (2012). For wind profile retrievals, an integration time of one day is required, and the resulting

Figure 2.2 The ground-based microwave radiometer GROMOS-C at Ny-Ålesund.

profiles cover an altitude range from approximately 75 km down to 60–45 km, depending on tropospheric opacity.

Ozone measurements from GROMOS-C were analyzed to characterize the diurnal ozone cycle, revealing pronounced seasonal variations in the diurnal ozone signal at Ny-Ålesund. In addition, the instrument demonstrated the capability to detect the tertiary ozone maximum above Ny-Ålesund during winter (Schranz, Fernandez, et al., 2018). Over three years, ozone measurements from GROMOS-C were also used to investigate ozone variability associated with both minor and major SSW events. The retrieved ozone profiles were validated through comparisons with Atmospheric Chemistry Experiment – Fourier Transform Spectrometer (ACE-FTS) satellite data, OZone Radiometer for Atmospheric Measurements (OZORAM) ground-based observations, and in situ measurements, showing agreement within 6% relative to SD-WACCM simulations and other observational references (Schranz, Tschanz, et al., 2019).

MIAWARA-C

MIAWARA-C is a water vapor microwave radiometer that measures the rotational transition line of water vapor at 22 GHz (Straub, Murk, and Kämpfer, 2010). The Microwave Physics group has previously built two other 22 GHz water vapor radiometers (De Wachter et al., 2010; Deuber et al., 2005). A photograph of MIAWARA-C, which is also located on the roof of the atmospheric observatory at Ny-Ålesund, is shown in Figure 2.2. The standard measurement cycle of MIAWARA-C is to measure sky East, reference East, sky West, and reference West for about 15 s each. Every 15 minutes, the ambient load is measured for about 2 s, and the sky at 60° elevation is measured for about 15 s. A tipping curve is performed to determine the sky temperature at 60° elevation. Similar to GROMOS-C, MIAWARA-C retrieval is also performed with ARTS Version 2 (Eriksson, Buehler, et al., 2011) and QPACK software (Eriksson, Jiménez, and Buehler, 2005) according to the optimal estimation algorithm (Rodgers, 2000). From the

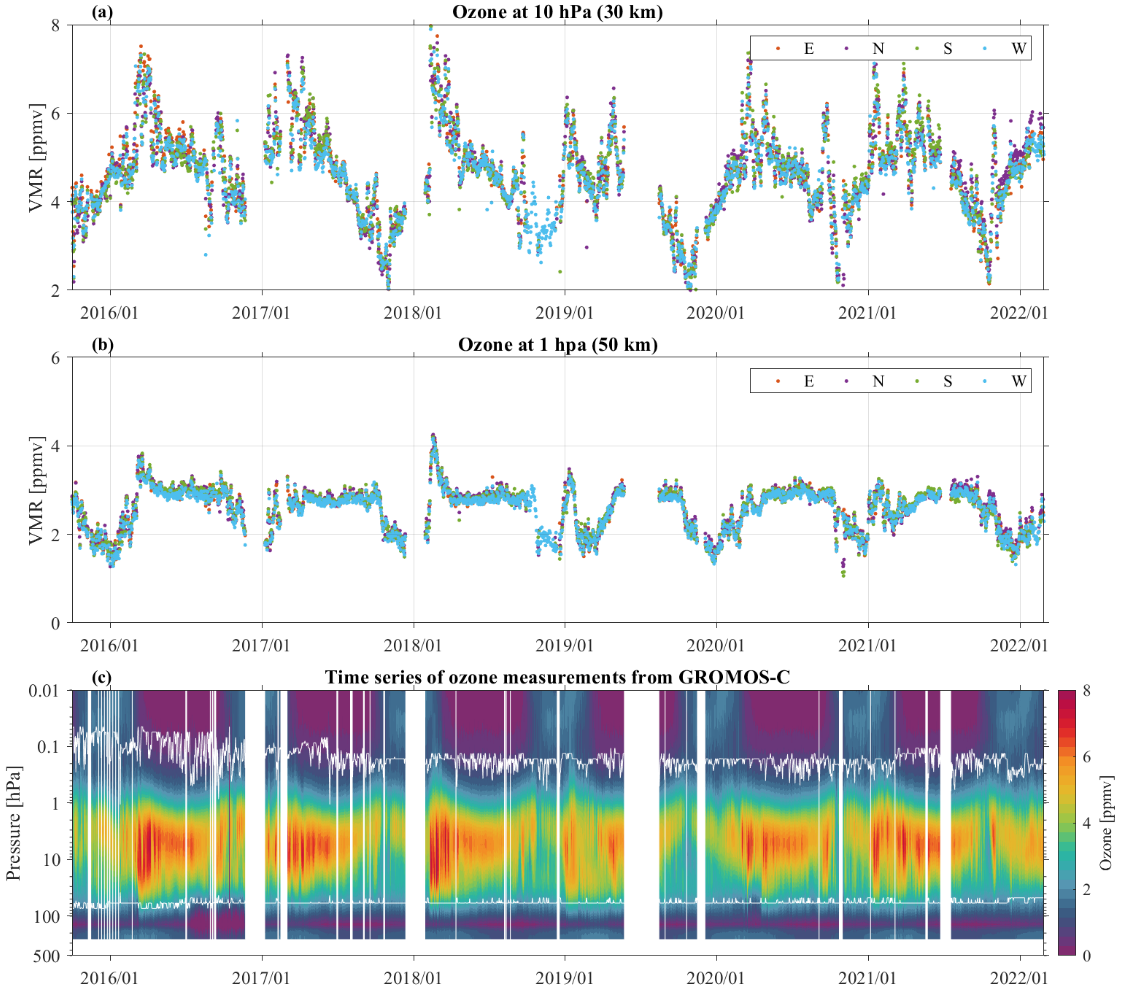

Figure 2.3 GROMOS-C ozone measurements from the four cardinal directions (North, East, South, and West) at two pressure levels: 10 hPa (a) and 50 hPa (b). Panel (c) shows the averaged ozone time series from all four directions.

measured spectra, we retrieve water vapor profiles that cover an altitude range extending from 37 km to 75 km with a time resolution of 2-4 h and a vertical resolution of 12-19 km. A detailed description of the design and the retrieval algorithm can be found in Straub, Murk, and Kämpfer (2010) and Tschanz, Straub, et al. (2013).

Three years of MIAWARA-C measurements were intercompared with satellite, ground-based observations, and models, showing agreement within 5% relative to SD-WACCM simulations and ACE-FTS satellite measurements (Schranz, Tschanz, et al., 2019). Following this validation, water vapor measurements from MIAWARA-C were used to estimate the descent of water vapor within the Arctic polar vortex (Schranz, Hagen, et al., 2020; Schranz, Tschanz, et al., 2019).

Figure 2.4 The ground-based microwave radiometer MIAWARA-C at Ny-Ålesund.

2.2 Integrated ozone and water vapor datasets

2.2.1 Aura/MLS

The MLS is an instrument onboard NASA's EOS-Aura satellite which was launched in 2004 (Waters et al., 2006). The satellite is in a Sun-synchronous orbital altitude of 705 km, with a period of 1.7 hours, and 98 ° inclination. MLS scans the limb in the direction of orbital motion, which gives almost pole-to-pole coverage (82°S to 82°N) with each profile spaced 1.5 degrees or 165 km along the orbit track. The instrument measures thermal microwave signals in the 118, 190, 240, 640, and 2500 GHz regions of the spectrum, with separate microwave receiver and spectrometer assemblies for each region (see in Figure 2.5), which deduce vertical abundance profiles of atmospheric composition, along with temperature, geopotential height, cloud ice amount, and relative humidity according to the "Level 2" retrieval algorithms (Livesey et al., 2018; Read et al., 2006; Schwartz, Read, and Snyder, 2006). These observations are essential for monitoring the stability and recovery of the stratospheric ozone layer, enhancing predictions of climate change and variability, and improving the scientific understanding of global air quality and its long-range transport. In this thesis, the focus is on the measurements of ozone, water vapor, and temperature.

Ozone is retrieved from the 240 GHz spectral band, which provides ozone profiles from approximately 16 km to 86 km altitude (316 – 0.001 hPa), with vertical resolutions ranging from 2.5 to 6 km. Comparisons of MLS ozone with other ozone observations have indicated general agreement at the 5–10% level with stratospheric profiles relative to several other satellites, balloons, aircraft, and ground-based data (Hubert et al., 2016; Nair et al., 2012; Schranz, Tschanz, et al., 2019; Tegtmeier et al., 2013).

Water Vapor is retrieved from the 190 GHz spectral line, which provides water vapor profiles extending from around 10 km to 86 km altitude (316 - 0.00215 hPa). The vertical resolution is about 3.5 km between 316 hPa and 4.64 hPa, and approximately 15 km above 0.1 hPa. The MLS and ground-based measurements and climate models show strong interannual agreement, particularly a clear QBO signature (Kawatani, Lee, and Hamilton, 2014; Nedoluha, Gomez, et al., 2007). When comparing MLS data to the MERRA and MERRA-2 reanalysis

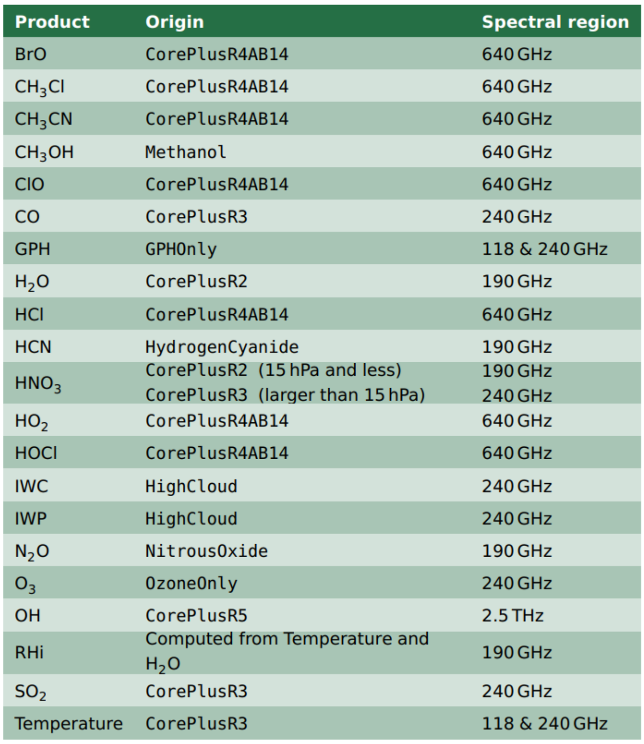

Product	Origin	Spectral region
BrO	`CorePlusR4AB14`	640 GHz
CH_3Cl	`CorePlusR4AB14`	640 GHz
CH_3CN	`CorePlusR4AB14`	640 GHz
CH_3OH	`Methanol`	640 GHz
ClO	`CorePlusR4AB14`	640 GHz
CO	`CorePlusR3`	240 GHz
GPH	`GPHOnly`	118 & 240 GHz
H_2O	`CorePlusR2`	190 GHz
HCl	`CorePlusR4AB14`	640 GHz
HCN	`HydrogenCyanide`	190 GHz
HNO_3	`CorePlusR2` (15 hPa and less) `CorePlusR3` (larger than 15 hPa)	190 GHz 240 GHz
HO_2	`CorePlusR4AB14`	640 GHz
HOCl	`CorePlusR4AB14`	640 GHz
IWC	`HighCloud`	240 GHz
IWP	`HighCloud`	240 GHz
N_2O	`NitrousOxide`	190 GHz
O_3	`OzoneOnly`	240 GHz
OH	`CorePlusR5`	2.5 THz
RHi	Computed from Temperature and H_2O	190 GHz
SO_2	`CorePlusR3`	240 GHz
Temperature	`CorePlusR3`	118 & 240 GHz

Figure 2.5 The origin of each of the standard products from *version 5 Level 2 Data Quality Document.*

datasets show significantly different horizontal transport rates, with MERRA and MERRA-2 being 106% faster in the Northern Hemisphere but 42–45% slower in the Southern Hemisphere compared to MLS (Jiang et al., 2015).

Temperature is derived from radiances measured by the 118 & 240 GHz radiometers. Temperature profiles have a vertical resolution of 3–4 km from 261 hPa to 10 hPa, degrade to 7–8 km at 1–0.1 hPa, 11 km at 0.01 hPa, and to 12 km at 0.0001–0.0002 hPa. MLS observational data with high vertical resolution can quantify temperature trends in the upper stratosphere, particularly above 45 km, which display generally in agreement with other satellite limb instruments (Dubé et al., 2024; Wing et al., 2018). New and updated temperature observations in the middle and upper stratosphere will better understand the multidecadal cooling rate (cooling trend) and more accurately quantify the impact of humanity on the climate.

2.2.2 MERRA-2

The MERRA-2 is NASA's latest global atmospheric reanalysis dataset, developed by the Global Modeling and Assimilation Office (GMAO). It spans from 1980 to the present and provides a consistent and high-resolution record of atmospheric variables for climate and weather research (Waters et al., 2006). Gelaro et al. (2017) provides foundational descriptions of the reanalysis system and its use in climate monitoring. Compared to MERRA, MERRA-2 assimilates a broader range of observational data, including modern satellite measurements, and incorporates significant improvements to the GEOS model and data assimilation system (Gelaro et al., 2017). MERRA-2 enhances the representation of physical processes in the atmosphere, including better treatment of trace gas constituents (e.g., ozone and water vapor), land surface interactions, and cryospheric processes. It has a $0.5° \times 0.625°$ horizontal grid, with 72 hybrid-eta vertical levels extending from the surface up to 0.01 hPa, and a time resolution of 6 hours. The dataset is widely used for studies involving atmospheric composition, dynamics, and climate variability, and is publicly accessible through the *NASA Goddard Earth Sciences Data and Information Services Center* data portal. In this thesis, key applications of MERRA-2 include evaluating variability in stratospheric ozone and water vapor, examining atmospheric transport processes, and validating satellite observations and model simulations such as those from MLS and WACCM-X(SD).

2.2.3 WACCM-X

The WACCM-X is an advanced numerical model developed by the National Center for Atmospheric Research (NCAR) as part of the NCAR framework, which extends from the surface to approximately 500–700 km altitude, thereby covering the entire atmosphere up to the thermosphere and lower ionosphere (Liu, Bardeen, et al., 2018; Pedatella, Chau, et al., 2019). WACCM-X supports coupling to active or prescribed ocean, sea ice, and land components, enabling fully interactive Earth system simulations.

WACCM-X builds upon the physics of WACCM, which itself extends to 145 km and is based on the Community Atmosphere Model (CAM). It includes a detailed interactive chemistry module for major chemical species such as ozone, water vapor, and related trace gases (Garcia et al., 2017; Gettelman et al., 2019; Marsh, Mills, et al., 2013). Key improvements in recent model versions include updates to non-orographic gravity wave drag parameterizations, enhanced representations of SSW events, updated chemical kinetics, and the inclusion of time-varying GHG and ODS (Eyring et al., 2013; Neale et al., 2010; Sander et al., 2010). WACCM-X(SD) is employed for constrained studies. In this configuration, model winds and temperatures from the surface up to 50 km are nudged toward the MERRA-2 reanalysis data, ensuring close agreement with observed meteorological conditions in the troposphere and stratosphere (Gelaro et al., 2017). WACCM-X(SD) sustains the model's full capability in the mesosphere, thermosphere, and ionosphere, making it ideal for investigating vertical coupling processes during events like SSWs or tidal amplification.

The WACCM-X(SD) simulations use a horizontal resolution of 1.9° latitude × 2.5° longitude, with a vertical resolution increasing above 0.96 hPa to better capture upper atmospheric dynamics. The model output includes temperature, winds, trace gases (e.g., O_3, H_2O), and radiative heating/cooling rates with a 3-hourly time resolution.

2.3 Meteor radars

Meteor radars are active remote sensing instruments that detect the backscattered radio signals from meteor trails left by meteoroids as they ablate upon entering Earth's atmosphere. By measuring the Doppler shift of the meteor trail echoes, meteor radars provide high-resolution observations of horizontal wind components (zonal and meridional) in the MLT region. The spatial and temporal resolution of these measurements allows for detailed studies of atmospheric dynamics, including tides and gravity waves, as well as to estimate the gravity wave momentum flux. Meteor radar observations can be used to retrieve the constant phasing of planetary

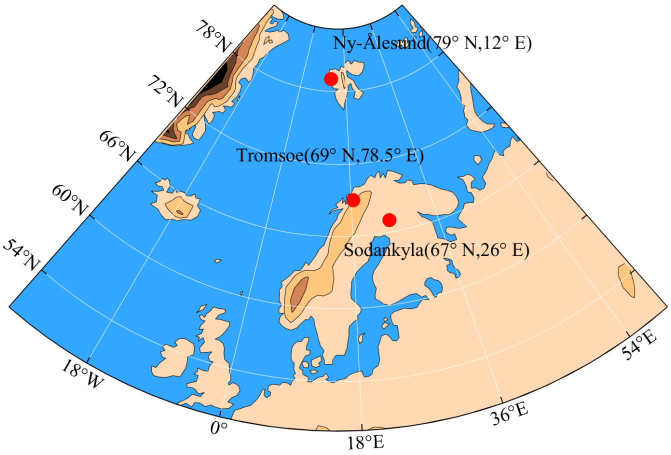

Figure 2.6 Locations of the three high-latitude stations in the Arctic: Svalbard, Tromsø, and Sodankylä.

wave propagation parameters (Stober, Matthias, et al., 2017). By measuring the ambipolar diffusion coefficient, they can also retrieve the temperature field in these altitudes (Stober, Jacobi, et al., 2008). The wind retrieval algorithm builds upon the wind analysis techniques originally introduced by Hocking, Fuller, and Vandepeer, 2001 and Holdsworth, Reid, and Cervera, 2004. The adaptive spectral filter (ASF)2D, as used in (Baumgarten and Stober, 2019; Stober, Baumgarten, et al., 2020), is further optimized to enhance wind estimation accuracy and is employed to estimate the total tidal amplitude and phases.

In this thesis, observational data from three high-latitude stations located at Svalbard (78.99°N, 15.99°E), Tromsø (69.58°N, 19.22°E), and Sodankylä (67.37°N, 26.63°E) (Figure 2.6) are used to calculate the total tides primarily dominated by migrating tidal components. A comprehensive quantification of tidal amplitude variability and co-located tracer variability during SSW events is explored in Chapter 6, by combining observational data with model simulations.

3 Aim and impact of this thesis

The global climate system is likely to remain in a state of accelerated transformation over the next several decades and has profound impacts on global environments and ecosystems. In this context, the middle atmosphere (approximately 20–100 km altitude) has emerged as a key area of focus in atmospheric science. However, observational data for this altitude range remain relatively limited, facing challenges for validating middle atmospheric numerical models and identifying potential long-term trends (Hagen et al., 2018; Rüfenacht, Baumgarten, et al., 2018b). Given a key zone for mass and energy exchange between the stratosphere and mesosphere (Limpasuvan et al., 2016; Shepherd, Beagley, and Fomichev, 2014), the middle atmosphere presents substantial scientific and practical value. Long-term and continuous measurements of wind speed, temperature, density, and atmospheric composition in this region not only help reveal the structure and evolution of the middle atmosphere but also provide essential observational evidence for understanding vertical coupling processes between atmospheric layers. Such data are vital for improving parameterizations in general circulation models, enhancing the accuracy of climate projections, and advancing numerical weather prediction capabilities.

Ozone and water vapor are key constituents of the middle atmosphere. Their distributions and variability are strongly influenced by photochemical processes and solar radiation (Schranz, Fernandez, et al., 2018; Schranz, Tschanz, et al., 2019), and in turn, they affect the atmospheric radiative balance and feedbacks in climate change (Banerjee et al., 2019; Friedel, Chiodo, Stenke, Domeisen, Fueglistaler, et al., 2022; Friedel, Chiodo, Sukhodolov, et al., 2023). Variations in ozone concentration significantly influence atmospheric oxidative capacity and the Earth's radiation budget. Water vapor, due to its relatively long chemical lifetime, serves as an ideal tracer for investigating changes in polar vortex structure, middle atmospheric dynamics, and the impact of SSW events on polar atmospheric conditions. Therefore, long-term and stable monitoring of ozone and water vapor provides new insights to reveal physical and chemical processes in the middle atmosphere, thereby enhancing our understanding of polar middle atmospheric variability.

In this context, the thesis aims to clarify the significance of ground-based microwave measurements of Arctic middle atmospheric ozone and water vapor. Specifically, it intends to highlight how these observations, when compared to satellite and model data, effectively capture diurnal, seasonal, interannual, and long-term variations in polar ozone and water vapor. Additionally, the thesis aims to explore how ozone anomalies at different time scales influence stratospheric and mesospheric dynamics and physical processes. The main questions are addressed:

- Chapter 4: How do interannual and seasonal variations in ozone and water vapor differ between the Northern and Southern Hemispheres, and what are the associated vertical transport velocities of water vapor? Additionally, it investigates how well ground-based radiometers, reanalysis, and satellite data can characterize these differences and improve our understanding of polar atmospheric dynamics.
- Chapter 5: How can observational and numerical simulations quantitatively analyze the dynamical and chemical mechanisms behind polar ozone variations during major warming and final warming SSW events? How do interactions such as horizontal eddy effects, vertical advection, and photochemical processes lead to distinct ozone anomaly patterns and their sustained changes during both types of events?
- Chapter 6: How do diurnal, semidiurnal, and terdiurnal tidal amplitudes in the Arctic MLT vary during and after major SSW events, and what are the roles of dynamical and radiative processes in these variations? How do changes in ozone and water vapor, induced by planetary wave breaking, influence mesospheric tidal variability and their contribution to short-wave heating and long-wave cooling during major SSW events?

4 Interannual variability of ozone and water vapor

4.1 Introduction

Over the past eight years, continuous ground-based microwave radiometer measurements from GROMOS-C and MIAWARA-C have been conducted at (78.99° N, 12° E). We investigate the interannual and seasonal variability of ozone and water vapor at polar latitudes using multi-year ground-based microwave radiometer measurements, in combination with MERRA-2 reanalysis and Aura-MLS satellite data.

In the following publication, we present climatologies for both trace gases and evaluate the consistency across datasets. A hemispheric comparison is conducted by introducing a virtual station at 78.99° S, 12° E, revealing stronger variability in the Northern Hemisphere. Furthermore, we estimate vertical transport velocities of water vapor, offering insights into the residual circulation and polar dynamics linked to the stratospheric polar vortex.

4.2 Publication

The following article has been published in *Atmospheric Chemistry and Physics (ACP).*

Citation: Shi, Guochun, Witali Krochin, Eric Sauvageat, and Gunter Stober. “Ozone and water vapor variability in the polar middle atmosphere observed with ground-based microwave radiometers”. In: *Atmospheric Chemistry and Physics* 23.16 (2023), pp. 9137–9159

DOI: https://acp.copernicus.org/articles/23/9137/2023/

Atmos. Chem. Phys., 23, 9137–9159, 2023
https://doi.org/10.5194/acp-23-9137-2023

Atmospheric Chemistry and Physics
Open Access

Research article

Ozone and water vapor variability in the polar middle atmosphere observed with ground-based microwave radiometers

Guochun Shi[1,2], **Witali Krochin**[1,2], **Eric Sauvageat**[1,2], **and Gunter Stober**[1,2]

[1]Institute of Applied Physics, University of Bern, Bern, Switzerland
[2]Oeschger Center for Climate Change Research, University of Bern, Bern, Switzerland

Correspondence: Guochun Shi (guochun.shi@unibe.ch)

Received: 1 February 2023 – Discussion started: 7 February 2023
Revised: 4 July 2023 – Accepted: 10 July 2023 – Published: 18 August 2023

Abstract. Leveraging continuous ozone and water vapor measurements with the two ground-based radiometers GROMOS-C and MIAWARA-C at Ny-Ålesund, Svalbard (79° N, 12° E) that started in September 2015 and combining MERRA-2 and Aura-MLS datasets, we analyze the interannual behavior and differences in ozone and water vapor and compile climatologies of both trace gases describing the annual variation of ozone and water vapor at polar latitudes. A climatological comparison of the measurements from our ground-based radiometers with reanalysis and satellite data was performed. Overall differences between GROMOS-C and Aura-MLS ozone volume mixing ratio (VMR) climatology are mainly within ±7 % throughout the middle and upper stratosphere and exceed 10 % in the lower mesosphere (1–0.1 hPa) in March and October. For the water vapor climatology, the average 5 % agreement is between MIAWARA-C and Aura-MLS water vapor VMR values throughout the stratosphere and mesosphere (100–0.01 hPa). The comparison to MERRA-2 yields an agreement that reveals discrepancies larger than 50 % above 0.2 hPa depending on the implemented radiative transfer schemes and other model physics. Furthermore, we perform a conjugate latitude comparison by defining a virtual station in the Southern Hemisphere at the geographic coordinate (79° S, 12° E) to investigate interhemispheric differences in the atmospheric compositions. Both trace gases show much more pronounced interannual and seasonal variability in the Northern Hemisphere than in the Southern Hemisphere. We estimate the effective water vapor transport vertical velocities corresponding to upwelling and downwelling periods driven by the residual circulation. In the Northern Hemisphere, the water vapor ascent rate (5 May to 20 June in 2015, 2016, 2017, 2018, and 2021 and 15 April to 31 May in 2019 and 2020) is $3.4 \pm 1.9\,\mathrm{mm\,s^{-1}}$ from MIAWARA-C and $4.6 \pm 1.8\,\mathrm{mm\,s^{-1}}$ from Aura-MLS, and the descent rate (15 September to 31 October in 2015–2021) is $5.0 \pm 1.1\,\mathrm{mm\,s^{-1}}$ from MIAWARA-C and $5.4 \pm 1.5\,\mathrm{mm\,s^{-1}}$ from Aura-MLS at the altitude range of about 50–70 km. The water vapor ascent (15 October to 30 November in 2015–2021) and descent rates (15 March to 30 April in 2015–2021) in the Southern Hemisphere are 5.2 ± 0.8 and $2.6 \pm 1.4\,\mathrm{mm\,s^{-1}}$ from Aura-MLS, respectively. The water vapor transport vertical velocities analysis further reveals a higher variability in the Northern Hemisphere and is suitable to monitor and characterize the evolution of the northern and southern polar dynamics linked to the polar vortex as a function of time and altitude.

1 Introduction

Ozone and water vapor are essential climate variables that play a key role in the radiative balance in the middle atmosphere. Their seasonal and interannual variability is closely coupled to dynamical and chemical processes, which are driven and modulated by atmospheric waves including planetary waves, gravity waves (GWs), and atmospheric tides. These atmospheric waves transport energy and momentum from their source region to the altitudes of their dissipation and thus contribute to the energy balance between different atmospheric layers.

Model results suggest that GWs drive the summer mesopause temperature up to 100 K below the radiative equilibrium (Lindzen, 1981; Smith, 2012; Becker, 2012). The extreme cold temperatures at the summer mesopause are the result of an upwelling and a corresponding adiabatic cooling of the uplifted air masses in the summer hemisphere and are accompanied by a downwelling in the winter hemisphere. The pole-to-pole circulation is often referred to as residual circulation or transformed Eulerian mean circulation (Andrews and Mcintyre, 1976). Another important circulation branch at altitudes lower than the residual circulation is the Brewer–Dobson circulation (BDC) (Brewer, 1949; Dobson, 1956). BDC is a factor in stratospheric ozone and water vapor variability, but, as mentioned later in this paper, polar stratospheric clouds can have significant seasonal impacts on ozone and water vapor abundances in the lower stratosphere. The circulation is fundamentally driven by dissipating waves of tropospheric origin and broadly consists of large-scale tropical ascent and winter pole descent. BDC is much weaker during boreal summer due to the different distribution of land masses and the associated differences in the generation of planetary and GWs between both hemispheres. BDC can govern the entry and distribution of air masses and constituents from the troposphere into and within the stratosphere. The meridional transport of trace gases into the polar cap is controlled by the strength of the polar vortex during polar winter, which is driven by the temperature gradient between the polar cap and the mid-latitudes through the thermal wind balance in the hemispheric winter stratosphere, and the vortex forms an essential barrier separating ozone-rich air at the mid-latitudes from ozone-depleted air within the polar cap. However, planetary waves can disturb the polar vortex and even lead to its breakdown during sudden stratospheric warming events (SSWs) (Matsuno, 1971; Baldwin et al., 2021), which is accompanied by a large-scale intrusion and mixing of air masses from the mid-latitudes towards the high latitudes, helping to recover the ozone volume mixing ratio (VMR) (Schranz et al., 2020). Furthermore, the transition from the winter to the summer circulation is decisively controlled by the presence of the planetary wave activities (Matthias et al., 2021). Previous studies even concluded that dynamical forced transitions have a persistent impact on the circulation lasting several weeks (Baldwin and Dunkerton, 2001). The stratospheric quasi-biennial oscillation (QBO) modulates the Northern Hemisphere wintertime stratospheric polar vortex, resulting in its weakening and shifting (Garfinkel et al., 2012; Zhang et al., 2019). Wang et al. (2022) use reanalysis data and model simulations to demonstrate that the total column ozone and stratospheric ozone (50–10 hPa) anomalies are seasonally dependent and zonally asymmetric in the polar region, and in that work the QBO affects the polar vortex and stratospheric ozone mainly by modifying the wave number 1 activities. Tao et al. (2019) investigate an intercomparison of simulated stratospheric water vapor variations, focusing on the QBO and long-term variability and trends.

Stratospheric ozone observation results largely reflect a distribution that presents significant asymmetry in both hemispheres, with the differences reaching their maximum values in the winter and spring seasons (Shepherd, 2008). Because most ozone is found in the lower stratosphere, the differences in the column ozone distribution explain the asymmetry because of dynamic transport, as well as the interannual variability of ozone in both hemispheres (McConnell and Jin, 2008; Langematz, 2019). Long-term polar ozone observations offer better recognition and predictability of stratospheric ozone trends and an understanding of the attribution of changes. Water vapor has a chemical lifetime on the order of months in the upper stratosphere and lower mesosphere (Brasseur and Solomon, 2005); therefore, it can be used as a tracer to study a large-scale upwelling and downwelling of the air masses in the polar mesosphere. The mesosphere at the high latitudes is characterized by an annual variation with higher water vapor during local summer and lower water vapor during local winter that is mainly determined by the mean vertical transport (Forkman et al., 2005; Lee et al., 2011). Straub et al. (2010) and Schranz et al. (2019) estimate the vertical gradient of water vapor inside of the polar vortex in autumn based on microwave radiometry measurements at polar latitudes. The distribution and variability of ozone and water vapor exhibit a wealth of information on atmospheric circulation.

There are several techniques to obtain ozone and water vapor measurements in the middle atmosphere. The Aura satellite with the Microwave Limb Sounder (MLS) collects global water vapor and ozone profiles among other chemical species with coverage at a fixed local time due to its sun-synchronous orbit (Livesey et al., 2006). Ground-based observations are often performed using Brewer and Dobson instruments (Zuber et al., 2021), which provide very high-quality and high-precision ozone column densities but lack the vertically resolved information. Lidars are providing good vertical resolution to measure ozone (Brinksma et al., 1997; Bernet et al., 2021). The instruments carried with aircraft and balloon-borne instruments including ozonesondes and frost-point hygrometers perform highly vertically resolved measurements of ozone and water vapor in the upper troposphere and lower stratosphere (Zahn et al., 2014; Eckstein et al., 2017). However, there are only a few systems available and the observation time depends on tropospheric weather conditions. At tropospheric altitudes, water vapor can also be retrieved leveraging Raman lidars (Sica and Haefele, 2015, 2016). Precise water vapor measurements above the troposphere can also be collected by in situ balloon-borne sensors such as laser absorption spectrometers (Graf et al., 2021). Ground-based microwave radiometers (MWRs) allow continuous observations under all weather conditions with a time resolution of the order of hours except during rain. MWRs measuring ozone and water vapor are valuable as they complement satellite measurements, are relatively easy to maintain, have long lifetimes (which ensures long and continuous time series covering several decades), and can be operated from different locations with measurements performed autonomously on a campaign basis (Scheiben et al., 2013, 2014). Ground-based microwave radiometry is a reliable technique that performs continuous measurements to monitor the vertical profiles of ozone and water vapor VMR changes to investigate Arctic and Antarctic dynamics from diurnal to interannual timescales.

Here, we present a detailed comparison of ozone and water vapor observed by Aura-MLS at the conjugate latitude station leveraging multiyear ground-based observations from GROMOS-C and MIAWARA-C performed at Ny-Ålesund and Aura-MLS and reanalysis data. We produce and compare the polar regions' multiyear-mean ozone and water vapor climatologies at conjugate latitude stations (Fig. 1). On the one hand, it is intended to provide a well-characterized representation of ozone and water vapor measured by the two instruments and the chemistry differences between both hemispheres concerning climatological behaviors. On the other hand, it provides a source of data for future work, including intercomparison studies and evaluation. Furthermore, we use the water vapor mixing ratio measurements from MIAWARA-C and Aura-MLS observation data to derive the ascent and descent rates. We estimate the strength of upwelling and downwelling in both hemispheres over the polar stations and discuss their interannual variability and the hemispheric differences.

We provide an overview of the datasets in Sect. 2. The time series of ozone and water vapor at conjugate latitude stations in the Northern Hemisphere (NH) and Southern Hemisphere (SH) are presented in Sect. 3. The climatologies of ozone and water vapor are discussed in Sect. 4. The transport of water vapor is discussed in Sect. 5. Sections 6 and 7 present the discussion and conclusions of this study.

2 Instruments and models

In this study, we use ozone and water vapor measurements from our two ground-based MWRs GROMOS-C and MIAWARA-C, which are only available to measure at single locations and are thus representative of a specific geographic location. Both instruments are located at Ny-Ålesund, Svalbard (79° N, 12° E), and have collected continuous data since September 2015. We extract the interannual ozone and water vapor variability between Jan 2015 and July 2022 from MERRA-2 and Aura-MLS over northern and southern polar stations. The corresponding virtual conjugate latitude station (79° S, 12° E) is shown in Fig. 1. In addition, we use temperature observations from Aura-MLS.

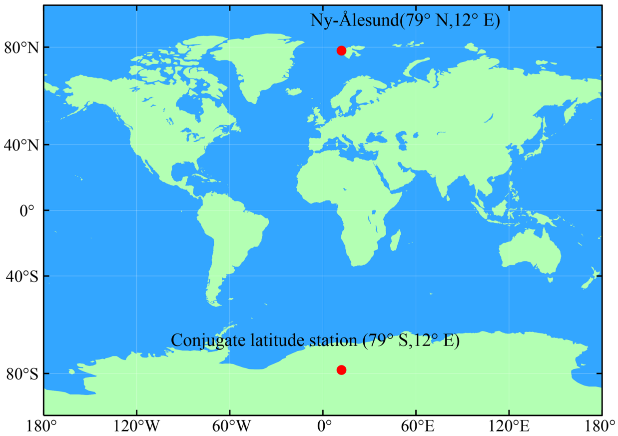

Figure 1. A geographical map indicating the two stations in the northern and southern polar regions. The conjugate latitude station in the Southern Hemisphere is a virtual station for this study. The locations of the stations are indicated with a solid red circle.

2.1 GROMOS-C

GROMOS-C (GRound-based Ozone MOnitoring System for Campaigns) is an ozone MWR measuring the ozone emission line at 110.836 GHz at Ny-Ålesund, Svalbard (79° N, 12° E), which is described in detail in Fernández et al. (2015). It was built by the Institute of Applied Physics (IAP) at the University of Bern. GROMOS-C is very compact, meaning it can be transported and operated at remote field sites under extreme climate conditions. It further can switch the frequency of the local oscillator and measure the 115 GHz carbon monoxide (CO) emission line. The system noise temperature of the instrument is about 1080 K. The optics setup of GROMOS-C has two rotating mirrors such that observations in all four cardinal directions are possible. Therefore, GROMOS-C observes in the four cardinal directions (north, east, south, and west) under an elevation angle of 22° with a sampling time of 4 s. Ozone VMR profiles are retrieved from the ozone spectra with a temporal averaging of 2 h leveraging Atmospheric Radiative Transfer Simulator version-2 (ARTS2; Eriksson et al., 2011) and Qpack2 software (Eriksson et al., 2005) according to the optimal estimation algorithm (Rodgers, 2000). An a priori ozone profile is required for optimal estimation and is taken from an MLS climatology of the years 2004–2013. The sensitive altitude range for this instrument extends from

23 to 70 km. The vertical resolution of ozone profiles is 10–12 km in the stratosphere and increases up to 20 km in the mesosphere as estimated from the width of the averaging kernels. The averaging kernels (AVKs) of GROMOS-C together with its measurement response, errors, and ozone profiles are shown in Appendix A (Fig. A1). In the lower stratosphere, the errors are below 0.3 ppmv and reach above the stratopause values up to 0.4 ppmv. More details about the uncertainty and the AVKs can be found in Fernández et al. (2015).

2.2 MIAWARA-C

MIAWARA-C (MIddle Atmospheric WAter vapor RAdiometer for Campaigns) is a ground-based MWR measuring the pressure-broadened rotational emission line of water vapor at the frequency of 22 GHz. It was also built by the University of Bern and is located at Ny-Ålesund, Svalbard (79° N, 12° E). The MIAWARA-C front end is an uncooled heterodyne receiver with a system noise temperature of 150 K. The antenna is followed by a dual-polarization receiver. The incident radiation is split into vertical and horizontal polarization by an orthomode transducer (OMT) located immediately after the feedhorn. The two polarized signals are processed in the two identical receiver chains and separately analyzed in a fast Fourier transform (FFT) spectrometer model Acqiris AC240. The spectrometer has a 400 MHz bandwidth and a spectral resolution of 30.5 kHz. The standard measurement cycle of MIAWARA-C is to measure sky east, reference east, sky west, and reference west for about 15 s each. Every 15 min the ambient load is measured for about 2 s, and the sky at 60° elevation is measured for about 15 s. A tipping curve is performed to determine the sky temperature at 60° elevation. The difference spectra in the east and west directions and the two polarizations are then calibrated separately with the hot and cold measurements close in time. Similar to GROMOS-C, MIAWARA-C retrieval is also performed with ARTS2 (Eriksson et al., 2011) and QPACK software (Eriksson et al., 2005) according to the optimal estimation algorithm (Rodgers, 2000). An a priori measurement is taken from an MLS climatology of the years 2004–2008. From the measured spectra we retrieve water vapor profiles that cover an altitude range extending from 37 to 75 km with a vertical resolution of 12–19 km and with a time resolution of 2–4 h depending on the opacity of the troposphere. For MIAWARA-C, retrievals are performed with a constant time resolution and with a constant noise of 0.014 K. The AVKs of MIAWARA-C, together with its measurement response, errors, and water vapor profiles, are shown in Appendix A (Fig. A2). In the upper stratosphere, the errors are 0.5 ppmv and increase from 0.5 to 1.5 ppmv in the mesosphere. A detailed design of the instrument and description of the retrieval algorithm can be found in Straub et al. (2010) and Tschanz et al. (2013).

2.3 Aura-MLS

The Microwave Limb Sounder (MLS) is one of the payloads onboard NASA's Earth Observing System (EOS)-Aura satellite, which was launched in 2004 (Waters et al., 2006). The satellite is in a sun-synchronous orbital altitude of 705 km with a period of 1.7 h and 98° inclination. MLS scans the atmospheric limb in the direction of orbital motion, which gives almost pole-to-pole coverage (82° S to 82° N), leading to retrieved profiles at the same latitude every orbit, with a spacing of a 1.5° great circle angle along the suborbital track. Ozone is retrieved from the band of 240 GHz, and water vapor is retrieved from the 183 GHz line. Temperature is derived from radiances measured from the 118 and 240 GHz channels with a vertical resolution between 3 and 6 km (Schwartz et al., 2015b). The estimated temperature single-profile precision is 0.5–1.2 K from 100 to 0.001 hPa. MLS provides ozone profiles (version 5) from 12 to 80 km altitude with a vertical resolution of 2.5–6 km (Schwartz et al., 2015a) and water vapor profiles (version 5) from 10 to 90 km with a vertical resolution of 3.5 km from 316 to 4.64 hPa and 15 km above 0.1 hPa (Lambert et al., 2015). The estimated ozone single-profile precision varies from 0.2 to 0.4 ppmv from the middle stratosphere to the lower mesosphere. For water vapor, the estimated precision is 0.2–0.3 ppmv in most of the stratosphere and increases to 0.7–0.8 ppmv in the middle mesosphere. It passes at Ny-Ålesund twice a day at around 04:00 and 10:00 UTC. Profiles for comparison are extracted if the location is within ±1.2° latitude and ±6° longitude of either Ny-Ålesund or the defined virtual conjugate latitude station.

2.4 MERRA-2

The Modern-Era Retrospective Analysis for Research and Applications, version 2 (Waters et al., 2006; Gelaro et al., 2017, MERRA-2) is the latest global atmospheric reanalysis produced by the NASA Global Modeling and Assimilation Office (GMAO) from 1980 to the present. MERRA-2 assimilates observation types not available to its predecessor, MERRA, and includes updates to the Goddard Earth Observing System (GEOS) model and analysis scheme so as to provide a viable ongoing climate analysis beyond MERRA's terminus. MERRA-2 provides a regularly gridded, homogeneous record of the global atmosphere and incorporates additional aspects of the climate system including several improvements to the trace gas constituents, land surface representation, and cryospheric processes.

In MERRA-2, methods of analysis, model uncertainties, and observations cause uncertainties (Rienecker et al., 2011). Davis et al. (2017) provides a comprehensive assessment of the MERRA-2 ozone product that relatively clearly shows the vertical distribution of ozone and water vapor in the stratosphere and has the best agreement with stratospheric ozone observations compared to other reanalysis products.

Wargan et al. (2017) identified that ozone in MERRA-2 data were expected to have higher uncertainties in regions of high variability, such as winter high latitudes. The uncertainties are related to the chemistry model ozone bias (Gelaro et al., 2017), which is altitude dependent in MERRA-2. Similar behavior was also found in other GEOS chemistry models (Knowland et al., 2022; Wargan et al., 2023). MERRA-2 stratospheric water vapor is also biased compared to independent observations from Aura-MLS and the Atmospheric Chemistry Experiment-Fourier Transform Spectrometer (ACE-FTS). In this study, we use the ozone and water vapor with 72 model levels from the surface up to 0.01 hPa and a horizontal resolution of 0.5° × 0.625°. The time resolution is 6 h. MERRA-2 products are accessible online through the NASA Goddard Earth Sciences Data Information Services Center (GES DISC).

3 Climatologies of ozone and water vapor

This section examines the ozone and water vapor climatologies over Ny-Ålesund, Svalbard (79° N, 12° E), and the conjugate latitude station (79° S, 12° E) generated from the GROMOS-C, MIAWARA-C, MERRA-2, and Aura-MLS datasets. It is important to evaluate how well GROMOS-C and MIAWARA-C can monitor the ozone and water vapor variability and enhance our understanding of their distribution in the Arctic middle atmosphere. The inherent variability of ozone and water vapor in the middle atmosphere can be displayed better in the resulting climatologies, as measured by the two instruments involved in this study, and provide a crucial source of data for future work including intercomparison studies and model evaluation, assessing ozone depletion, validating satellite observations, and studying climate change.

3.1 Ozone

Figure 2 shows the climatological ozone distribution as a function of pressure and time deduced from GROMOS-C, MERRA-2, and Aura-MLS in both hemispheres. Many features of ozone MWR measurement climatologies are broadly consistent with model and satellite data. Some exceptional maximum values larger than 8 ppmv in MERRA-2 data above 0.1 hPa are described in Sect. 3.

Overall, the ozone profile reveals a characteristic seasonal dependence at polar latitudes. In particular, the altitude of the maximum ozone VMR, as well as its temporal variability, exhibits a seasonality. The peak ozone VMR (approximately 6.5 ppmv) appears in the NH in the late spring, whereas autumn shows the lowest values throughout the course of the year. The maximum observed and reanalysis ozone VMR (approximately 5.5 ppmv) in the SH is 1.0 ppmv smaller than the NH maximum and occurs later in the hemispheric spring season. The primary driver of the hemispheric maximum in ozone VMR is related to circulation processes throughout the stratosphere, including those associated with the BDC, transporting ozone-rich air toward the poles in the winter–spring hemisphere. To be precise, this circulation moves the ozone-rich air from the tropical photochemical source region to high latitudes after the polar vortex broke down and essentially enables the intrusion of ozone-rich air from the midlatitudes into the polar region and the replacement of the ozone-depleted air masses. Another essential feature is that GROMOS-C and Aura-MLS capture the tertiary ozone VMR maximum at the northern polar latitude in the early winter and in late spring at the southern polar latitude. However, the tertiary ozone maximum in GROMOS-C occurs at altitudes close to or even above the limit of 0.8 for the measurement response. MERRA-2 performs poorly when trying to capture the tertiary ozone VMR maximum in both polar latitudes. Due to the complexity of altered dynamics in the polar regions (Wargan et al., 2017) introducing extra uncertainties into numerical models and data assimilation systems, ozone VMRs exhibit dramatic variability (red shading in Fig. 2b, e) in the mesosphere.

From September to November in the Southern Hemisphere, both MERRA-2 and MLS effectively capture the presence of the ozone hole in the lower stratosphere. However, the climatology of ozone in the NH does not reflect a corresponding signature. The annual cycle of ozone at 46 hPa in both hemispheres further reveals this significant feature, as shown in Fig. 3a. MLS exhibits a greater magnitude of ozone depletion compared to MERRA-2. In Fig. 8b, the ozone levels at 3 hPa in the NH follow an annual cycle, with a peak occurring in March and a minimum in October. The SH ozone VMR maintains a constant level of 5 ppmv throughout the summer while experiencing two minimum values in February and October. Furthermore, the ozone VMR in MERRA-2 consistently remains lower than that in MLS except during autumn in the SH. In the mesosphere, there is relatively good agreement between GROMOS-C and MLS, while MERRA-2 exhibits higher variability (Fig. 3c). Both hemispheres have dramatically different seasonal variations and distribution in ozone due to differences in the stratospheric dynamics of the two hemispheres.

3.2 Water vapor

Figure 4 shows the climatology of water vapor vertical and temporal distribution from MIAWARA-C, MERRA-2, and Aura-MLS over both stations (79° S and 79° N) compiled from measurements collected between 2015 and 2021. The annual variation of water vapor with a maximum during hemispheric summer and a minimum during hemispheric winter is clearly visible. During the hemispheric winter, the middle-atmospheric water vapor maximum is shifted down to about 10 hPa, whereas it rises up to the lower mesosphere during the hemispheric summer. The characteristics of water vapor in both hemispheres depend strongly on the mesospheric pole-to-pole circulation, which is an upwelling with

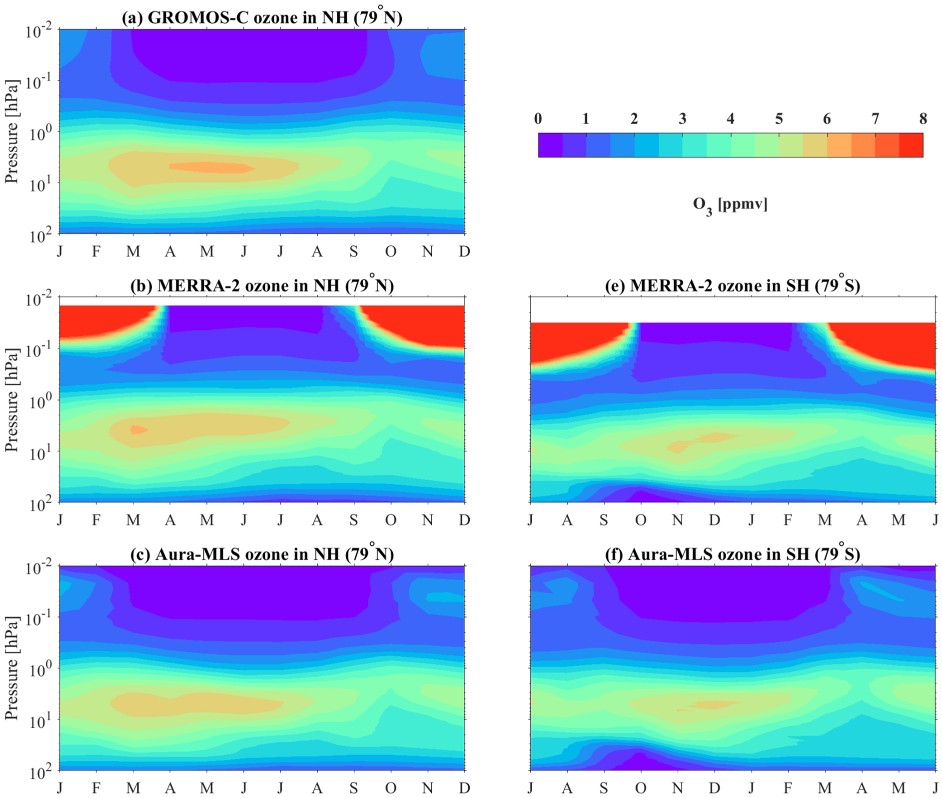

Figure 2. Climatology (2015–2021) of the monthly ozone distribution from GROMOS-C **(a)**, MERRA-2 **(b, e)**, and Aura-MLS **(c, f)** above Ny-Ålesund, Svalbard, in the NH and the conjugate latitude station in the SH. There is no GROMOS-C measurement for ozone in the SH. The *x* axis displays the month.

moist air transporting upwards for the hemispheric summer and a corresponding downward motion with dry air into the stratosphere during the winter (Orsolini et al., 2010). In addition, due to the relatively long photochemical lifetime of water vapor, more water vapor produced by methane oxidation accumulates in summer.

The annual cycle of monthly mean water vapor VMR at three separate pressure levels (3, 0.3, and 0.02 hPa) in both hemispheres can be seen in Fig. 5. Water vapor VMR appears at a maximum in October in both hemispheres in the stratosphere (3 hPa) due to the oxidation of methane. Due to photodissociation caused by solar Lyman-alpha radiation acting as a sink and the amount of water vapor being in equilibrium between different photochemical processes and vertical transport, water vapor is more smooth, with nearly constant mixing ratios from winter to spring in the NH. In the mesosphere (0.3 and 0.02 hPa), water vapor gradient variations can be found during hemispheric spring and summer. The gradient at 0.02 hPa is steeper than at 0.3 hPa from April to July in the NH (from November to January in the SH). Furthermore, the positive gradient is weaker, but the time of increase lasts longer and shows an extreme negative gradient in the hemispheric autumn. In both hemispheres, the seasonal behavior of water vapor is almost symmetric at 0.02 hPa and has a slight asymmetry at 0.3 hPa. At 0.02 hPa the maximum value of the water vapor mixing ratio persists for 1 month, and at 0.3 hPa the decrease in water vapor is not visible until September in the NH (March in the SH), but it then appears with a steep gradient.

3.3 Relative differences

In the two ground-based radiometer measurements from GROMOS-C and MIAWARA-C, the aforementioned seasonal behavior in their ozone and water vapor distributions display very similar patterns to Aura-MLS and MERRA-2. However, there are distinct differences between the datasets. To quantitatively assess the consistency of the ozone and water vapor climatologies from GROMOS-C and MIAWARA-C, the relative differences (RDs) of ozone and water vapor VMR between the ground-based MWRs and the two other data sets are calculated using the following expression:

$$\mathrm{RD} = \frac{(\varphi)_{\mathrm{radiometer}} - (\varphi)_{\mathrm{dataset}}}{(\varphi)_{\mathrm{dataset}}} \cdot 100\,\%, \tag{1}$$

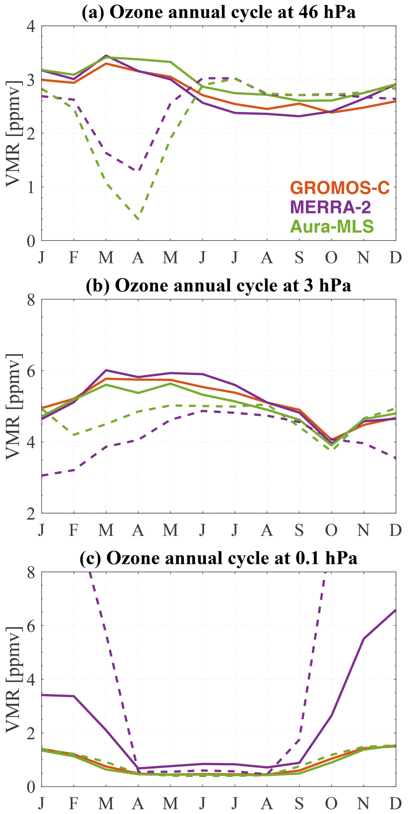

Figure 3. The annual cycles of monthly ozone VMR from GROMOS-C, MERRA-2, and Aura-MLS at 46 hPa **(a)**, 3 hPa **(b)**, and 0.1 hPa **(c)**. Solid lines represent Ny-Ålesund in the NH, and dashed lines represent the conjugate latitude station in the SH. Each month is averaged for the years 2015–2021. The months on the axes are adjusted accordingly for the SH.

where φ represents either ozone or water vapor VMR. Before evaluating the differences in climatology between MWRs and MERRA-2 and Aura-MLS, each MERRA-2 and Aura-MLS profile is convolved with the averaging kernels of MWRs. The convolution is performed according to the following expression:

$$\boldsymbol{x}_{\mathrm{conv}} = \boldsymbol{x}_{\mathrm{a}} - \mathbf{A}(\boldsymbol{x}_{\mathrm{a}} - \boldsymbol{x}), \tag{2}$$

where $\boldsymbol{x}_{\mathrm{conv}}$ is the convolved profile, $\boldsymbol{x}_{\mathrm{a}}$ is the a priori profile, $\mathbf{A}$ is the averaging kernel matrix, and $\boldsymbol{x}$ is the high-resolution profile of MERRA-2 and Aura-MLS.

Figure 6 shows the relative differences of ozone and water vapor climatologies from GROMOS-C and MIAWARA-C with respect to average convolved MERRA-2 and Aura-MLS. In Fig. 6a, the largest negative RD is larger than 50 % above 0.2 hPa in winter and spring because of the high bias of model ozone chemistry in the mesosphere in MERRA-2 (Wargan et al., 2023). GROMOS-C shows relatively good agreement with MERRA-2 in the lower and middle stratosphere (50–5 hPa), with RDs smaller than ±5 %, but includes a low RD with magnitudes greater than 10 % in the upper stratosphere in autumn. GROMOS-C and Aura-MLS agree well, with RDs mainly within ±7 % throughout the middle and upper stratosphere, and exceed positive RD 10 % in the lower mesosphere (1–0.1 hPa) in March and October (Fig. 6b).

The RD between MIAWARA-C and MERRA-2 is larger than 50 % throughout the late autumn to spring months above 0.2 hPa in Fig. 6c. Simultaneously, MERRA-2 underestimates water vapor VMR at all altitudes due to the lack of assimilated observation to constrain the water vapor reanalyses in the polar mesosphere and also in part due to the methane oxidation parameterization being disabled in the GEOS Composition Forecast model (Davis et al., 2017; Knowland et al., 2022). The MIAWARA-C agrees with MERRA-2 within 7 % in the stratosphere and lower mesosphere (about 100–0.3 hPa). MIAWARA-C and Aura-MLS show relatively good agreement, with RDs within 5 % throughout the stratosphere and lower mesosphere (approximately 100–0.02 hPa) in Fig. 6d. Furthermore, MIAWARA-C exhibits a negative RD within 8 % above the lower mesosphere (around 0.1–0.01 hPa). Additionally, we found a wet bias of 5 %–7 % between 100 and 1 hPa for MIAWARA-C measurements in each season. The wet bias becomes noticeable between July and November, primarily attributed to variations in instrument performance and, to a certain extent, the dynamic effects causing an elevation in water vapor levels within the stratosphere (as seen in Fig. 8a).

Note that the RD between ground-based MWRs and Aura-MLS is in part the Aura-MLS ozone and water vapor profile sampling (as mentioned in Sect. 2.3) and the measurement geometry, leading to seasonal variations in the polar ozone and water vapor distribution. Furthermore, the diurnal cycle in the ozone and water vapor has not been explicitly accounted for in the GROMOS-C and MIAWARA-C measurements. Neglecting the diurnal cycle potentially contributes to positive RDs between MWR measurement and other data sets in the upper stratosphere and lower mesosphere. Overall, GROMOS-C and MIAWARA-C are valuable to monitor the distribution of stratospheric ozone and mesospheric water vapor at the polar latitudes, respectively, which gives us more details to investigate their long-term variability, sources, and trend.

4 Time series of ozone and water vapor

4.1 Ny-Ålesund, Svalbard (79° N, 12° E) in the NH

The time series of daily ozone for GROMOS-C, MERRA-2, and Aura-MLS at Ny-Ålesund, Svalbard (79° N, 12° E), extending from 2015 to 2021 are shown in Fig. 7. The ozone daily profiles measured with GROMOS-C cover a pressure range of 100–0.03 hPa, which corresponds to about 16–70 km. The horizontal upper and lower white lines indicate the bounds of the trustworthy pressure range where the mea-

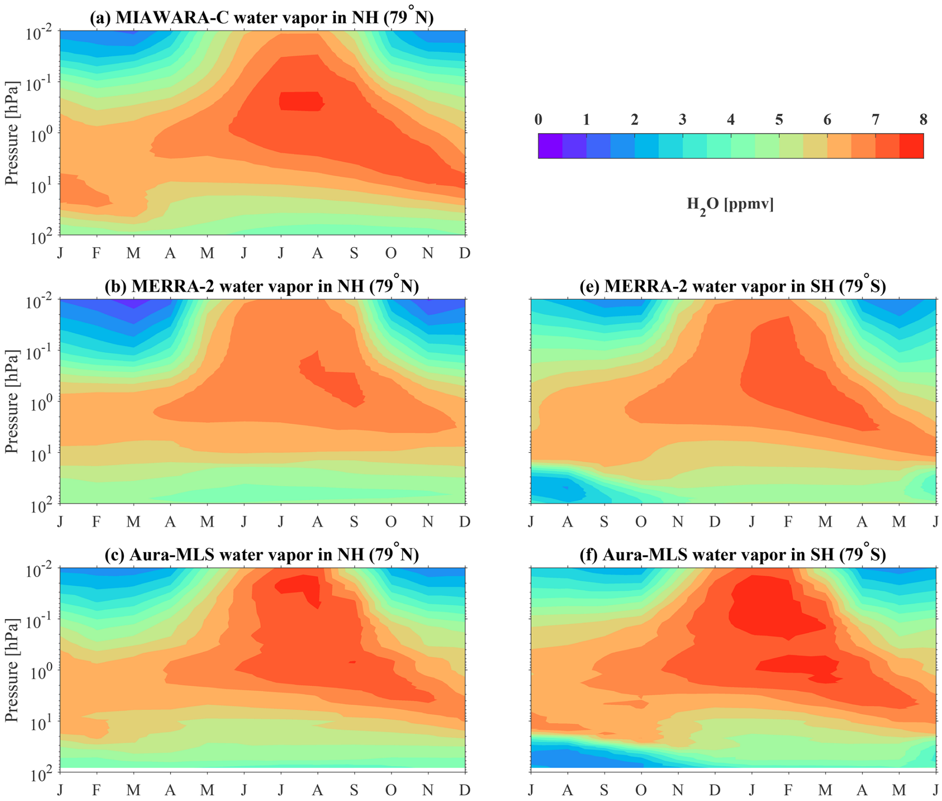

Figure 4. Climatology (2015–2021) of the water vapor monthly distribution from MIAWARA-C **(a)**, MERRA-2 **(b, e)**, and Aura-MLS **(c, f)** above Ny-Ålesund, Svalbard, in the NH and the conjugate latitude station in the SH. There is no MIAWARA-C measurement for water vapor in the SH.

surement response is larger than 0.8, meaning that the measured spectrum contributes more than 80 % to the retrieved profile. The measurement data gaps are that GROMOS-C measured CO for about 2 months during winter 2017/2018 and the spectrometer had a hardware problem during winter 2016/2017 and summer 2019.

Figure 7 reveals the annual ozone cycle with higher ozone VMR in summer (about 6 ppmv) than in winter (about 4.5 ppmv) at about 5 hPa (≈ 35 km). The GROMOS-C ozone VMR time series together with MERRA-2 and Aura-MLS at about 5 hPa smoothed by a 30 d running mean is shown in Appendix B (Fig. B1a). We can see that all three datasets are able to capture the annual ozone variations well in the stratosphere. Stratospheric ozone largely follows the annual cycle of solar irradiation and is produced through the Chapman cycle; more specifically, ozone VMR is mainly dominated by photochemical production in the summer months in the Arctic middle atmosphere.

In late winter and spring, the stratospheric ozone's higher variability is largely associated with the stratospheric polar vortex. Figure 7 shows the ozone VMR starting to increase up to the maximum value of about 8 ppmv for some of the years in the stratosphere when the polar vortex is disturbed or weakened by the planetary waves leading to the formation of SSWs. It shows that the planetary wave activity results in meridional transport of the ozone-rich air from the subtropics towards the pole and significantly perturbed the distribution of ozone. For example, the polar vortex split and shifted away from Ny-Ålesund, and ozone VMR reached about 7 ppmv during the winter 2018/2019 SSW (Schranz et al., 2020). In some years, the polar vortex is stable and strong over Ny-Ålesund, and ozone VMR sustains smaller values. At the end of the winter 2019/2020 season, the stratosphere featured an extremely strong and cold polar vortex, resulting in low stratospheric ozone in the polar regions (Lawrence et al., 2020; Inness et al., 2020). During late winter and early spring, stratospheric ozone decreases rapidly when the vortex passes over Ny-Ålesund.

Marsh et al. (2001) and Smith et al. (2009, 2018) investigate the tertiary ozone maximum in the winter middle mesosphere at high latitudes based on the models and observations. In this study, GROMOS-C and Aura-MLS present the seasonal tertiary ozone layer at 0.03–0.02 hPa (about 70–75 km) in winter months, but the tertiary ozone VMRs have higher values of 15 %–20 % in MERRA-2 (as shown the red shading in Fig. 7b). The red shading originates from the un-

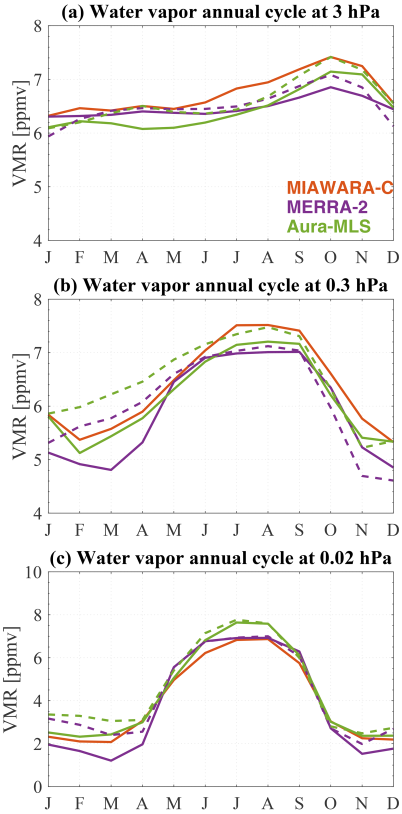

Figure 5. The annual cycles of monthly ozone VMR from GROMOS-C, MERRA-2, and Aura-MLS at 3 hPa **(a)**, 0.3 hPa **(b)**, and 0.02 hPa **(c)**. Solid lines represent Ny-Ålesund in the NH, and dashed lines represent the conjugate latitude station in the SH. Each month is averaged for the years 2015–2021. The month on the axes is adjusted accordingly for the SH.

certainties in the MERRA-2 product, which are expected to be magnified at high latitudes in winter and spring when the variability is increased compared to other seasons (Wargan et al., 2017). The anomalous atmospheric dynamics, displaced or split polar vortex, and hemispherically asymmetric conditions during SSWs may cause complexity and additional uncertainties in the estimation of ozone flux and transport terms. Figure 7 shows the consistencies of GROMOS-C with both MERRA-2 and Aura-MLS datasets in the time series of ozone below 1 hPa. A clear annual cycle in the stratosphere is well captured by all datasets, and the higher variability of ozone in winter and spring seasons is clearly visible. Remarkably, the annual variation in MERRA-2 ozone is significantly different from the observed variation throughout the mesosphere above 1 hPa.

Figure 8 shows the time series of daily water vapor VMR from MIAWARA-C, MERRA-2, and Aura-MLS at Ny-Ålesund, Svalbard (79° N, 12° E), for the period 2015–2021. MIAWARA-C continuously measures water vapor profiles which cover a pressure range from 5–0.02 hPa corresponding to about 37–75 km. The horizontal upper and lower white lines again indicate the bounds of the trustworthy pressure range where the measurement response is larger than 0.8.

The most evident feature of water vapor is its annual cycle with higher mixing ratios during local summertime and lower mixing ratios during local wintertime throughout the middle atmosphere. This seasonal behavior is mainly driven by the upward and downward branches of the mesospheric residual circulation. As shown in Appendix B (Fig. B1a), water vapor VMR has a maximum of about 7.5 ppmv in summer and a minimum of about 3.5 ppmv in winter at 0.1 hPa (approximately 60 km). Due to the air subsidence inside the polar vortex from autumn to winter, water vapor VMR reaches the maximum at 10 hPa.

In some years, such as 2020, water vapor exhibits a larger variability in late winter and spring. The variation of water vapor is mainly affected by the occurrence of a major SSW which interrupts the polar vortex; after that point, the vortex recovers, and the lower mesospheric water vapor content increases and is accompanied by a decrease in the stratosphere, corresponding to the water vapor vertical profile in the regions outside of the polar vortex (Schranz et al., 2019, 2020). In general, in MIAWARA-C the annually varying mesospheric distribution of water vapor agrees well with reanalysis data and satellite observations. However, there are notable differences at the polar latitudes in the water vapor VMR compared to MERRA-2 throughout the stratosphere and the mesosphere. While MERRA-2 shows a tendency to lower water vapor VMR compared to MIAWARA-C and MLS observations, the seasonal variations of similar amplitude do show reasonably good agreement with the observations. This tendency is likely related to the lack of assimilated observations and known deficiencies in the representation of stratospheric transport (Davis et al., 2017) in the reanalysis data.

4.2 The conjugate latitude station (79° S, 12° E) in the SH

Figures 9 and 10 show time series of ozone and water vapor VMR from MERRA-2 and Aura-MLS at the conjugate latitude station (79° S, 12° E) for the 2015–2021 period, respectively. For comparison purposes, the conjugate latitude station results are lagged by 6 months relative to those for Ny-Ålesund. Both stations exhibit annual cycles of ozone, while the conjugate latitude station shows an ozone VMR maximum of about 6 ppmv in summer and a minimum of about 4 ppmv in winter at about 5 hPa, as shown in Appendix B (Fig. B1b).

Compared to the interannual ozone variability at Ny-Ålesund, the results from the conjugate latitude station are less variable throughout the spring in the stratosphere. Compared to the NH, the planetary wave activity is much weaker in the SH, where a minimum in the ozone mixing ratios prevails over the polar latitudes during the late winter and

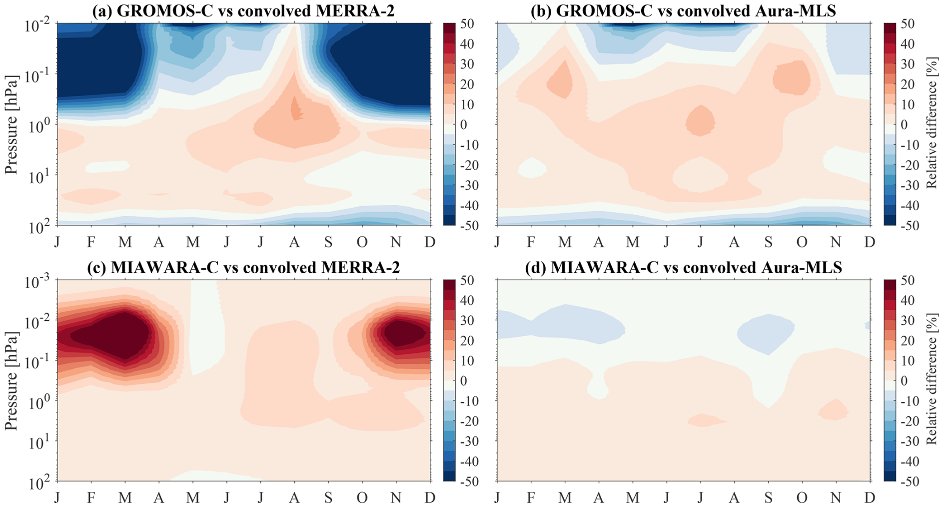

Figure 6. Monthly distributions of ozone and water vapor relative differences between ground-based MWRs and data sets: **(a, c)** MERRA-2 and **(b, d)** Aura-MLS.

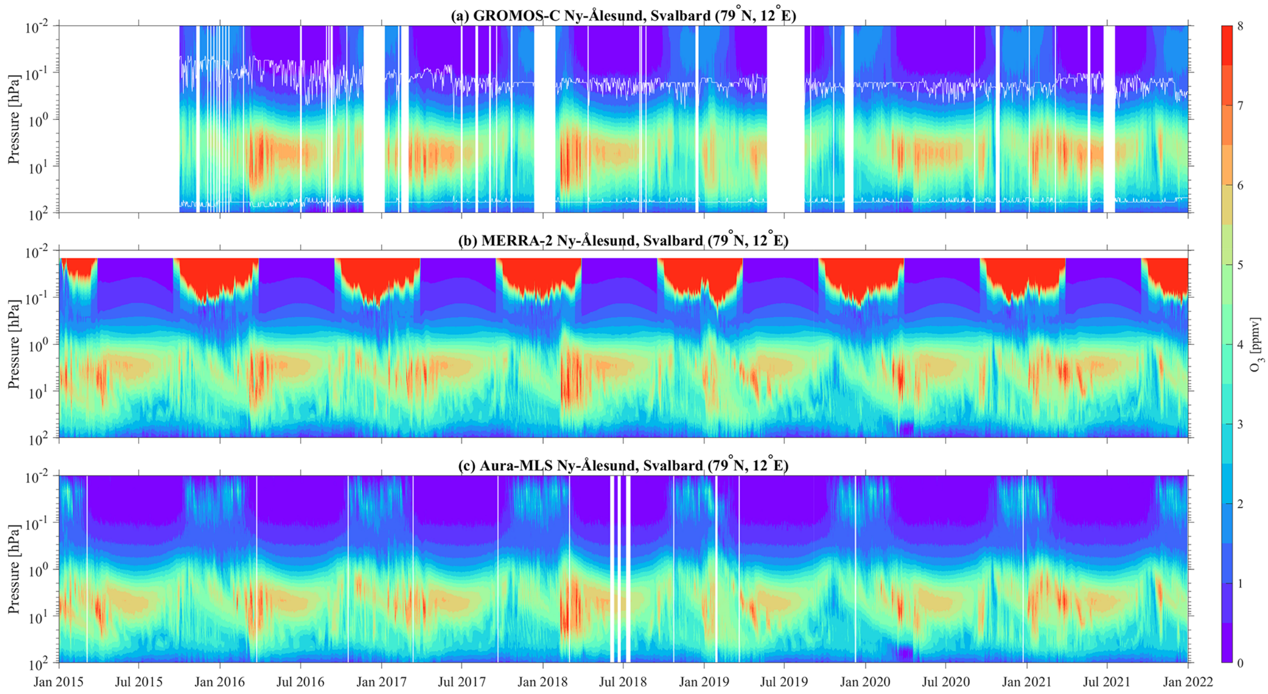

Figure 7. Time series of daily ozone VMR as a function of pressure over Ny-Ålesund, Svalbard (79° N, 12° E), for the 2015–2021 period. Panels show ozone VMR from **(a)** GROMOS-C measurements, **(b)** MERRA-2 reanalysis data, and **(c)** MLS satellite observations. The vertical white lines represent the data gaps caused by the hardware and measurement problems. The horizontal upper and lower white lines indicate a measurement response of 0.8 in panel **(a)**.

spring. There is a dominance of an isolated and stable polar vortex which inhibits the meridional ozone transport to the South Pole throughout the annual cycle, and the formation of polar stratospheric clouds promotes the production of chemically active chlorine and bromine, leading to catalytic ozone depletion in the lower stratosphere. This process is reflected well in the MLS observations and MERRA-2 data for September and October at the conjugate latitude station. Figure 10 presents the water vapor annual cycle with higher mixing ratios during local wintertime and lower mix-

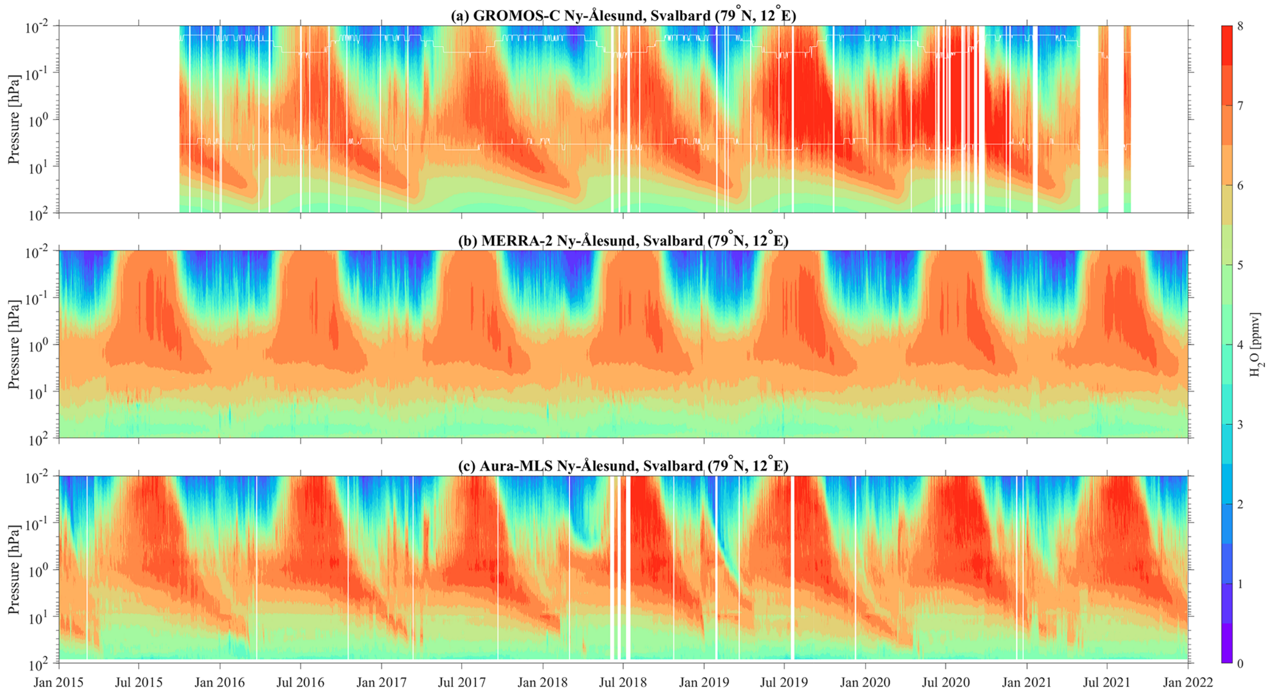

Figure 8. Time series of water vapor VMR as a function of pressure over Ny-Ålesund, Svalbard (79° N, 12° E), for the 2015–2021 period. Panels show ozone VMR from **(a)** MIAWARA-C measurements, **(b)** MERRA-2 reanalysis, and **(c)** MLS satellite observations. The vertical white lines represent the data gaps caused by the hardware and measurement problems. The horizontal upper and lower white lines indicate a measurement response of 0.8 in panel **(a)**.

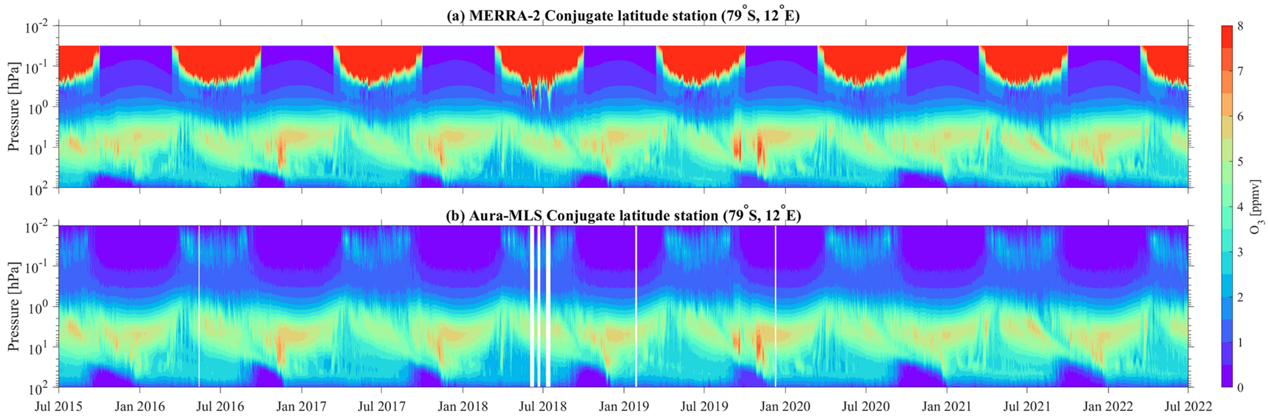

Figure 9. The same as Fig. 7 (without GROMOS-C measurements) but for the SH at the conjugate latitude station (79° S, 12° E).

ing ratios during local summertime over the conjugate latitude station. Furthermore, polar stratospheric cloud particles can sediment with considerable velocities and irreversibly remove water and nitric acid, resulting in a substantial reduction in water vapor VMR at the lower stratosphere during the southern polar winter and early spring (Waibel et al., 1999; Tritscher et al., 2021). After September, the water vapor VMR increases again as the polar stratospheric cloud influence reduces.

While MERRA-2 generally does an excellent job at reproducing the variability of stratospheric ozone and water vapor, it fails in the mesosphere as discussed in previous sections and also underestimates the vertical extent of the ozone hole, which appears to end at lower altitudes (larger pressures) in MERRA-2 than in MLS. This is also reflected in water vapor, where MERRA-2 fails to reproduce the vertical layering (e.g., July 2015 or July 2017) and underestimates the area of dehydration. Since the reanalysis is less constrained when it

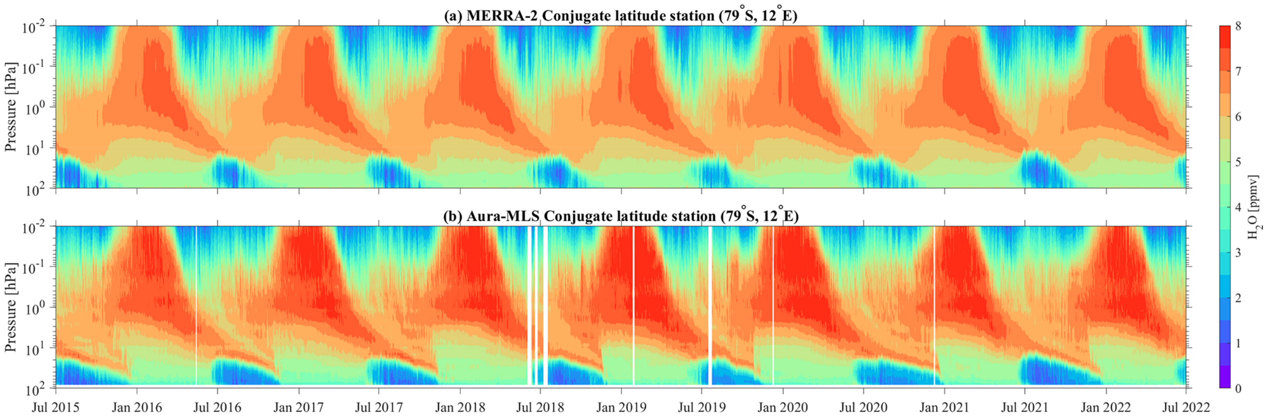

Figure 10. The same as Fig. 8 (without MIAWARA-C measurements) but for the SH at the conjugate latitude station (79° S, 12° E).

is assimilated (Davis et al., 2017; Shangguan et al., 2019), this behavior can be seen in MERRA-2 when it is compared to observations. It further demonstrates that ozone and water vapor in the NH will continue to be available from ground-based MWR observations; however, the detailed information about the SH winter as shown here for the "conjugate latitude" will be lost after the end of the last three limb sounders, such as Aura-MLS, which is still observing.

5 Dynamics and transport of water vapor

Water vapor is widely used as a tracer to investigate the dynamics of transport processes in the Arctic middle atmosphere (Lossow et al., 2009; Straub et al., 2012; Tschanz et al., 2013; Schranz et al., 2019, 2020). The chemical lifetime of water vapor is on the order of years in the lower stratosphere, months in the lower mesosphere, and weeks in the upper mesosphere (Brasseur and Solomon, 2005). Water vapor mixing ratios display different dynamical features depending on the altitude ranges because of different vertical gradients of water vapor VMR above and below its peak in the upper stratosphere. The water vapor mixing ratio is assumed to be constant for a month and a half, and the vertical velocity of air can be estimated.

The time periods of the year when water vapor VMR increases and decreases with altitude (in the upper stratosphere and lower mesosphere) measured from MIAWARA-C and Aura-MLS over both Ny-Ålesund and the conjugate latitude station are well covered in this study. We will denote the period with a stable high water vapor mixing ratio as the hemispheric summer and the positive and negative transition periods as the upwelling and downwelling branches, respectively. With the northern and southern hemispheric water vapor measurements, we calculate the effective ascent and descent rates as derived from a linear regression fit to different water vapor mixing ratio isopleths (5.5, 6.0, and 6.5 ppmv). For instance, the ascent and descent rates from 6.5 ppmv water vapor isopleth are shown in Figs. 11 and 12).

The time period of many years of descent rate from 15 September to 31 October in the altitude range of about 50–70 km is well presented in Fig. 11 (the first and third rows). This is an estimated result and not a quantitative calculation of the water vapor descent since the water vapor dynamic and chemical reactions not directly related to descent may also affect the polar water vapor changes. However, the effect of dynamic processes such as planetary wave disturbance is relatively obvious to estimate the ascent rate. As shown in Fig. 11 (second and fourth rows), the time period of 5 years (2015, 2016, 2017, 2018, and 2021) of ascent rate starts from 5 May to 20 June, and in another 2 years (2019 and 2020) the starting time for the increase of water vapor happens earlier by approximately 20 d (from 15 April). In 2019 and 2020, MIAWARA-C and Aura-MLS observe the return of the water vapor mixing ratio to pre-winter values in mid-April, and the moist air is lifted to greater altitudes in early May. The starting time of the ascent rate in 2019 and 2020 is about 3 weeks earlier than that in other years, which is caused by several processes. The planetary waves displace the polar vortex above Ny-Ålesund, and water-vapor-rich air is transported into the upper stratosphere; furthermore, the maximum water vapor mixing ratio is re-established at an altitude of about 55 km. Wave breaking and mixing above the strongest vortex level tends to reduce the tracer gradient (Lee et al., 2011), leading to an increase in the water vapor mixing ratios. In addition, photochemical processes from solar radiation can also contribute to the accumulation of water vapor in the springtime at the stratopause altitude (Brasseur and Solomon, 2005).

In the SH, the time period of each year of the ascent rate is relatively consistent from 15 October to 30 November in the upper stratosphere and mesosphere (Fig. 12). The descent rate of water vapor from 15 March to 30 April in the SH appears to be similar for each of the 7 years,

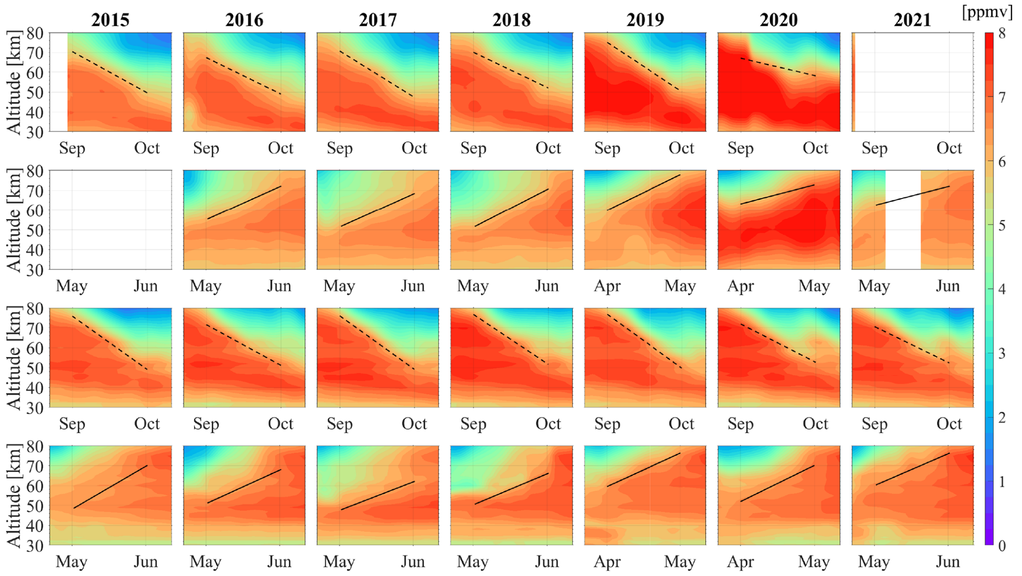

Figure 11. Time–altitude plots of mean water vapor VMR from MIAWARA-C (first and second rows) and Aura-MLS (third and fourth rows) over Ny-Ålesund, Svalbard (79° N, 12° E), in the NH. The data have been smoothed by a 20 d Gaussian. The dashed and solid black lines indicate the descent and ascent rates of water vapor as derived from a linear regression fit to the 6.5 ppmv isopleth of water vapor VMR, respectively. There are no data for MIAWARA-C from May to June 2015 and from September to October 2021.

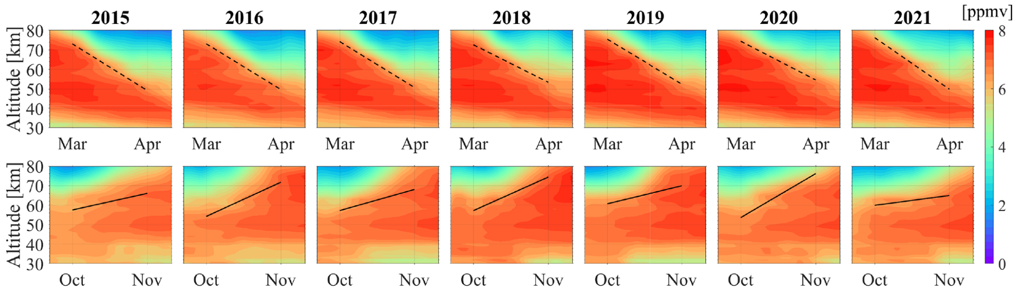

Figure 12. The same as Fig. 11 (without GROMOS-C measurements) but for the conjugate latitude station (79° S, 12° E) in the SH.

likely due to the higher stability and strength of the southern polar vortex. Figure 13 shows the annual variability of effective ascent and descent rates in the SH and NH during a given time period. In contrast to the NH, the southern hemispheric rate exhibits less interannual variability and an approximately consistent variation with the rates corresponding to the different isopleths, illustrating the qualitative agreement in different years in the effective vertical rates for the transition periods in the SH. The uncertainties for the ascent and descent rates of airflow over northern and southern polar latitude stations are depicted by error bars in Fig. 13. Effective ascent and descent rates estimated from water vapor measurements are very significant. Table 1 gives a more quantitative perspective to compare the vertical movement of air in both hemispheres. In the NH, the average vertical velocities are $3.4 \pm 1.9\,\mathrm{mm\,s^{-1}}$ from MIAWARA-C and $4.6 \pm 1.8\,\mathrm{mm\,s^{-1}}$ from Aura-MLS for upwelling from spring to summer and $5.0 \pm 1.1\,\mathrm{mm\,s^{-1}}$ from MIAWARA-C and $5.4 \pm 1.5\,\mathrm{mm\,s^{-1}}$ from Aura-MLS for downwelling from summer to autumn. During the transition from winter to spring, the vertical velocity is $5.2 \pm 0.8\,\mathrm{mm\,s^{-1}}$ for downwelling and $2.6 \pm 1.4\,\mathrm{mm\,s^{-1}}$ for upwelling from autumn to winter calculated by Aura-MLS in the SH. Table 1 shows a stronger upwelling branch in the NH polar summer mesosphere as compared to the SH, and this is accompanied by a stronger downwelling branch towards the SH winter in the polar region. In general, these results assess the ability to derive middle atmospheric ascent and descent rates from water vapor measurements at polar latitudes and further provide evidence for the higher variability in the NH than in the SH.

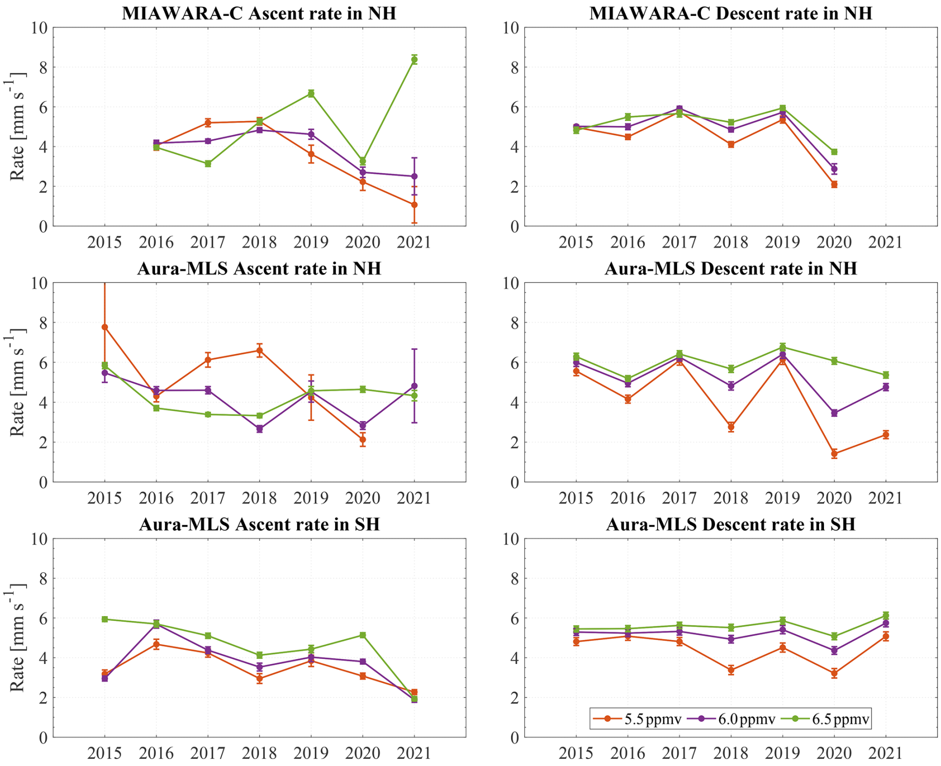

Figure 13. Interannual variability of the effective ascent and descent rates over both Ny-Ålesund, Svalbard (79° N, 12° E), and the conjugate latitude station (79° S, 12° E) estimated from the linear regression fit to the 5.5, 6.0, and 6.5 ppmv isopleths of water vapor VMR from MIAWARA-C and Aura-MLS. Bars indicate the uncertainties in the ascent and descent rates based on the MIAWARA-C and Aura-MLS observations.

Table 1. Comparison of the mean values and standard deviations (SDs) of ascent and descent rates from MIAWARA-C and Aura-MLS in both hemispheres. The mean is computed for the rates from 5.5, 6.0, and 6.5 ppmv isopleths (as shown in Fig. 13).

Ascent rate ($\mathrm{mm\,s^{-1}}$)	NH (mean ± SD)	SH (mean ± SD)
MIAWARA-C	3.4 ± 1.9	–
Aura-MLS	4.6 ± 1.8	2.6 ± 1.4
Descent rate ($\mathrm{mm\,s^{-1}}$)	NH (mean ± SD)	SH (mean ± SD)
MIAWARA-C	5.0 ± 1.1	–
Aura-MLS	5.4 ± 1.5	5.2 ± 0.8

6 Discussion

Continuous observations of essential climate variables such as ozone and water vapor are important for investigating the radiative balance of the atmosphere. Interhemispheric and interannual differences shed light on ozone and water vapor natural variability due to transport and photochemistry. Ground-based measurements such as those performed by GROMOS-C and MIAWARA-C provide a high-resolution and continuous data set of these trace gases at remote locations such as Ny-Ålesund. A comparison to the Aura-MLS satellite data exhibits excellent agreement throughout all altitudes in the stratosphere with GROMOS-C and the upper stratosphere and lower mesosphere with MIAWARA-C. The climatologies of Aura-MLS and the MWRs agree within ±10 % during the year. However, a climatological comparison to the reanalysis data MERRA-2 and our ground-based radiometers indicates larger discrepancies above 0.2 hPa. These increased deviations are partially due to the implemented radiative transfer schemes and other model physics used, such as interactive chemistry, which is computationally much more expensive (Gelaro et al., 2017). Furthermore, MERRA-2 includes the MLS observations of temperature and ozone in the 3DVAR data assimilation (Wargan et al., 2017). MLS observations are most important for the mesosphere and are weighted by their precision and accuracy.

The interhemispheric comparison is performed by defining a virtual conjugate latitude station (79° S, 12° E) in the Southern Hemisphere at conjugate geographic coordinates. Although the general seasonal morphology is very similar,

(a) temperature gradient: 60° N minus 80° N

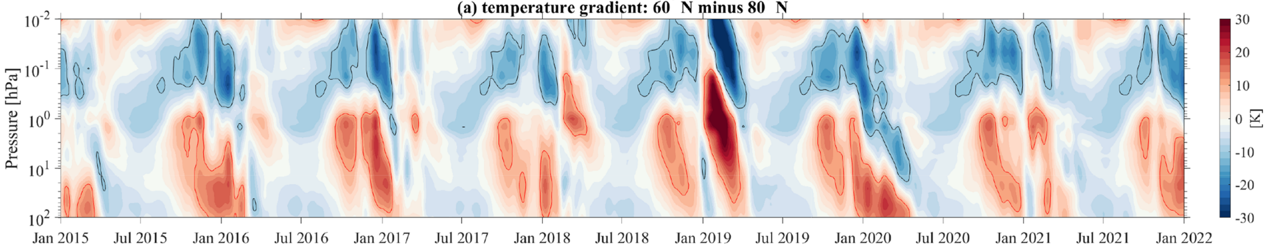

(b) temperature gradient: 60° S minus 80° S

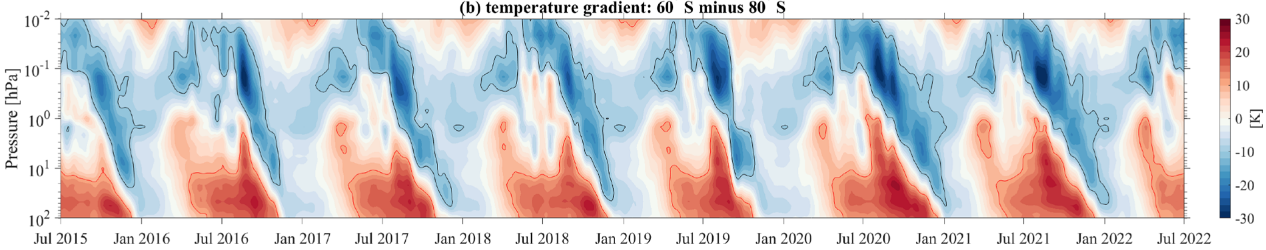

Figure 14. Temperature gradients between the mid-latitudes and polar latitudes in the NH (60 and 80° N) and SH (60 and 80° S). Red and black contours represent positive and negative values (±10 K).

the Northern Hemisphere shows much more variability in the time series of ozone and water vapor. One of the most significant differences is the occurrence of the ozone hole in the Southern Hemisphere towards the end of the winter season below 10 hPa (Solomon et al., 2014). During this time the water vapor VMR measurements also exhibit a minimum due to the formation of polar stratospheric clouds (Flury et al., 2009; Bazhenov, 2019) providing even more favorable conditions for catalytic ozone destruction reactions. In Fig. 14, we present zonally averaged temperature at two conjugate latitudes and compare results between the polar and mid-latitudes from Aura-MLS observations in both hemispheres. The southern polar latitudes appear much colder, by about 20 K, than their northern counterparts, as seen in Appendix C (Fig. C1). Furthermore, the temperature gradient between the mid-latitudes and high latitudes is stronger in the Southern Hemisphere at the stratosphere and thus drives a more stable polar vortex due to the thermal wind balance, which prevents the mixing of ozone-rich air from the low latitudes and mid-latitudes into the polar cap by planetary waves as can often be observed in the Northern Hemisphere (Schranz et al., 2019). There are only a few occasions from 2015 onward where such a stable and cold polar vortex was observed in the Northern Hemisphere, i.e., in 2015/2016 and 2019/2020 in the Arctic winter(Matthias et al., 2016; Lawrence et al., 2020), which can also lead to anomalies in the middle atmospheric dynamics (Stober et al., 2017).

In addition to the strength of the polar vortex, we investigated the strength of the upwelling and downwelling in both hemispheres, which we consider a proxy of the strength of the residual circulation. Water vapor has a longer lifetime than CO at 50–70 km (Brasseur and Solomon, 2005), which makes it a more robust tracer to manifest the vertical motion of air. The effective rates of vertical transport are estimated by using the water vapor measurements following the approach presented by Straub et al. (2010). The vertical velocities are derived under the assumption that other processes, such as chemical reactions, photodissociation, or horizontal advection, are less important. Here we analyze periods around the equinoxes. During this time of the year, the horizontal gradients of temperature between the polar region and the mid-latitudes are minimal or negligible, and thus there is no strong forcing due to horizontal temperature gradients or planetary waves driving the zonal or meridional transport. Furthermore, we only investigated altitudes below typical hydroxyl (OH) layer heights, which also reduces the impact of photodissociation in our estimates (Ryan et al., 2018). We obtained vertical velocities of 3.4 ± 1.9 and $4.6 \pm 1.8\,\mathrm{mm\,s^{-1}}$ for the upwelling towards the northern hemispheric summer and vertical motions of 5.0 ± 1.1 and $5.4 \pm 1.5\,\mathrm{mm\,s^{-1}}$ downwelling during the fall transition. Furthermore, there is rather significant interannual variability in the Northern Hemisphere that is not found above the Antarctic continent. Due to the frequent occurrence of SSWs, the spring transition is more variable in the NH (Matthias et al., 2021). In the Southern Hemisphere, the spring transition towards summer is characterized by $2.6 \pm 1.4\,\mathrm{mm\,s^{-1}}$ vertical velocity, and during the transition from summer to winter a downwelling with $5.2 \pm 0.8\,\mathrm{mm\,s^{-1}}$ vertical velocity is observed. A high variability in NH winter downwelling would imply a high variability of SH summer upwelling, which is indeed observed in Fig. 13. This suggests that the interhemispheric coupling (Körnich and Becker, 2010; Orsolini et al., 2010; Smith et al., 2020) means that disturbances are transmitted from the winter stratosphere to the summer mesosphere in the other hemisphere. However, it is worth noting that there is a lower variability in SH winter downwelling, which corresponds to a higher variability in NH summer upwelling. This observation suggests that the coupling between the winter and summer circulations within each hemisphere is influenced by various factors beyond the interhemispheric exchange. As shown in Fig. 14, with a stronger temperature gradient during SH winter, the polar vortex is relatively stable and well defined, leading to reduced variability in the downward motion of air (downwelling). For instance, the SSW events during the NH winter (Limpasuvan et al., 2016; Schranz et al., 2019, 2020) or increased stratospheric planetary wave activity (de Wit et al., 2015) lead to increased variability in the NH winter stratosphere. Simulations with a GW-resolving model response to the enhanced winter hemisphere Rossby wave activity may lead to both interhemispheric couplings through a downward shift of the GW-driven branch of the residual circulation and increased GW activity at high summer latitudes (Becker and Fritts, 2006). Other observational studies using polar mesospheric clouds and stratospheric reanalysis data exhibited an interhemispheric correlation during the summer months (Karlsson et al., 2007; Espy et al., 2011). More recent model results suggested that the strongest interhemispheric coupling signatures are found between the stratosphere and mesosphere in the opposite hemisphere (Smith et al., 2020).

7 Conclusions

Continuous ground-based measurements of ozone and water vapor remain an essential tool to understand the short and long-term evolution of the middle atmosphere, as well as for the validation and parameterization of atmospheric models. In this study, we present ozone and water vapor measurements from the two ground-based radiometers GROMOS-C and MIAWARA-C located at Ny-Ålesund, Svalbard, collected between 2015 and 2021. The data were compared to observations from MLS onboard the Aura spacecraft as well as reanalysis data MERRA-2. This comparison showed a good agreement for the climatological behavior between the ground-based radiometers and MLS to within almost ±7 % for ozone at about 50–1 hPa and within ±5 % for water vapor at about 100–0.02 hPa. However, we identified pronounced differences between the measurements and the reanalysis data above 0.2 hPa where MERRA-2 deviations up to 50 % were visible. Ground-based observations are going to become more important within the next few years as the satellite instruments such as MLS are going to reach the end of their life and so far there are no adequate replacements in orbit.

By defining a virtual conjugate latitude station in the Southern Hemisphere, we investigated altitude-dependent interhemispheric differences. Both trace gases showed a much higher variability during the northern hemispheric winter driven by planetary wave activity. The Southern Hemisphere was characterized by a more stable polar vortex and colder temperatures in the polar cap that result in more favorable conditions to form polar stratospheric clouds and thus more efficient ozone destruction by catalytic reactions causing the well-known ozone hole. Furthermore, the polar stratospheric cloud formation was accompanied by a reduction in the water vapor VMR at the same altitudes in the lower stratosphere.

We investigated the strength of the residual circulation by estimating the upwelling and downwelling above Ny-Ålesund and the corresponding conjugate latitude station. Typical ascent rates during the summer transition reach values of 3.4–4.6 $\mathrm{mm\,s^{-1}}$, and for the downwelling in the fall transition vertical velocities of 5.0–5.4 $\mathrm{mm\,s^{-1}}$ are inferred. Correspondingly, a vertical velocity of 2.6 $\mathrm{mm\,s^{-1}}$ for the upwelling and 5.2 $\mathrm{mm\,s^{-1}}$ for the downwelling is calculated in the SH. The Northern Hemisphere also reflected a much more pronounced interannual variability compared to the southern polar latitudes. However, there is no strong correlation between upwellings and downwellings in the opposite hemispheres; this is most likely due to dynamic processes such as the QBO or weather patterns that play a role and need to be taken into account. Therefore, long-term ozone and water vapor measurements will create a deeper understanding of the mechanisms that control polar ozone and water vapor variability and predict the future evolution of middle atmospheric ozone and water vapor in climate changes.

Appendix A: Retrieved results of instruments

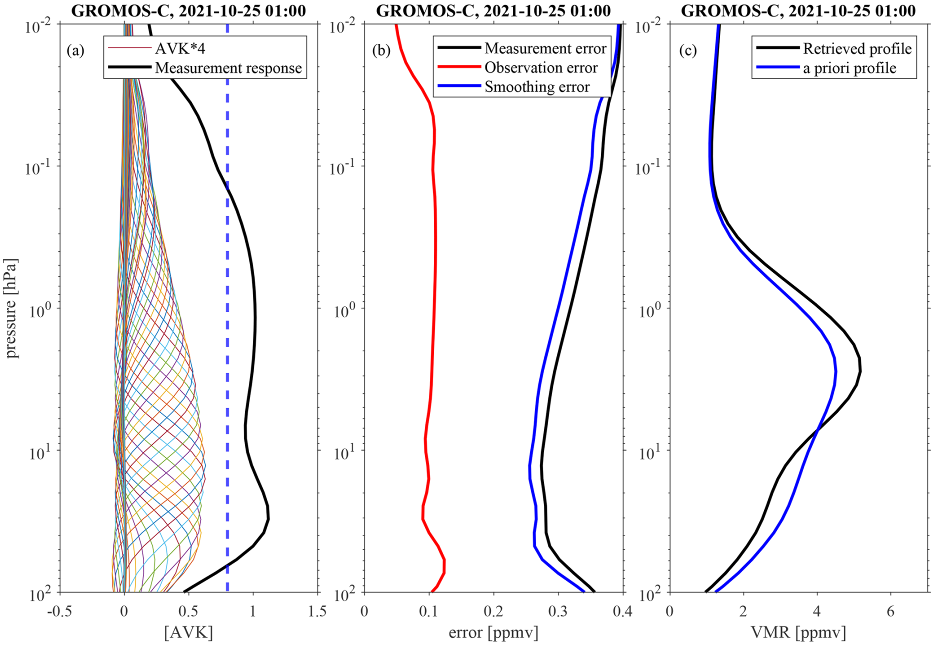

Figure A1. Example of GROMOS-C hourly ozone retrievals on 25 October 2021 around 01:00 UTC. Panel **(a)** shows the averaging kernels together with measurement response; panel **(b)** shows the measurement, smoothing, and observation errors; and panel **(c)** shows the retrieved and a priori ozone profile.

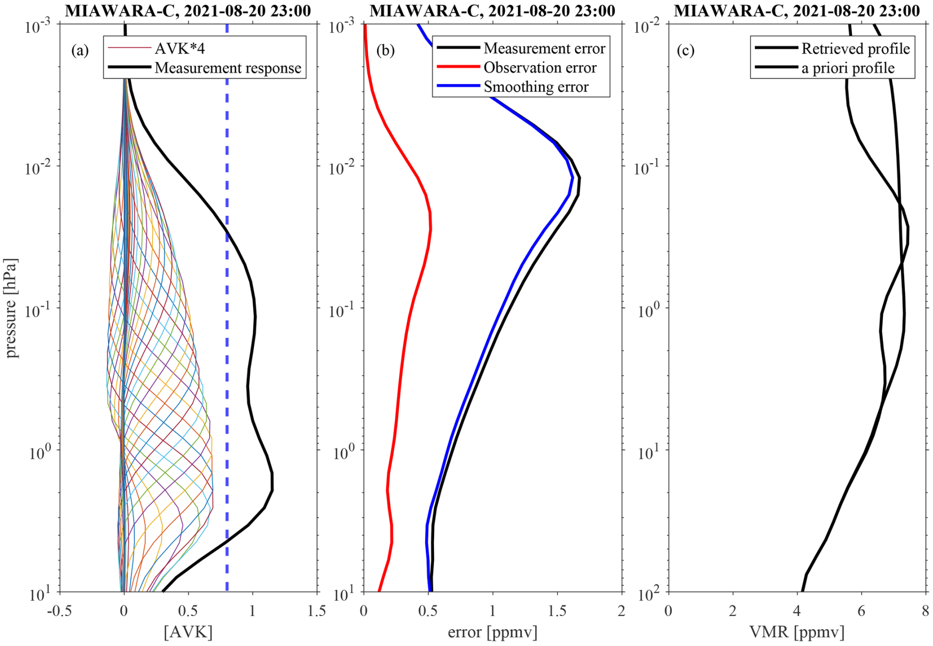

Figure A2. Example of MIAWARA-C hourly water vapor retrievals on 20 August 2021 around 23:00 UTC. Panel **(a)** shows the averaging kernels together with measurement response; panel **(b)** shows the measurement, smoothing, and observation errors; and panel **(c)** shows the retrieved and a priori water vapor profile.

Appendix B: Ozone and water vapor

(a) Ozone at about 5 hPa (~35 km) at Ny-Ålesund, Svalbard (79°N, 12°E)

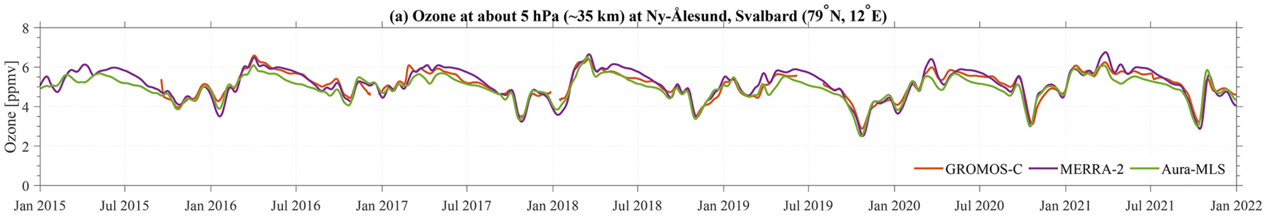

(b) Ozone at about 5 hPa (~35 km) at Conjugate latitude station (79°S, 12°E)

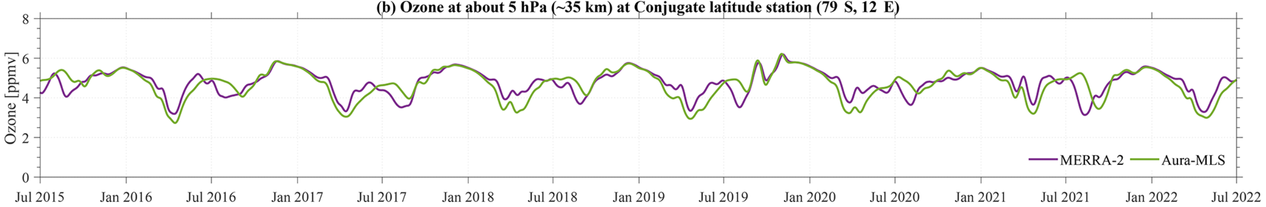

Figure B1. GROMOS-C, MERRA-2, and Aura-MLS ozone VMR time series at about 5 hPa smoothed by a 30 d running mean over Ny-Ålesund, Svalbard (79° N, 12° E), and the conjugate latitude station (79° S, 12° E).

(a) Water vapor at about 0.1 hPa (~60 km) at Ny-Ålesund, Svalbard (79°N, 12°E)

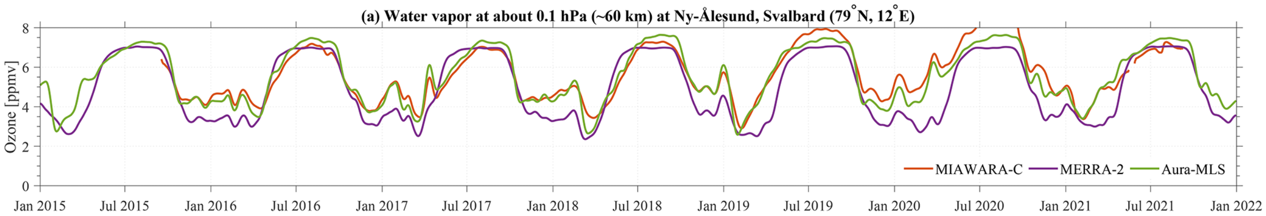

(b) Water vapor at about 0.1 hPa (~60 km) at Conjugate latitude station (79°S, 12°E)

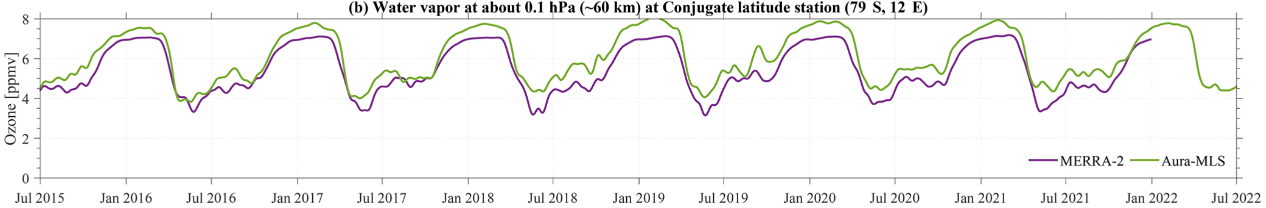

Figure B2. MIAWARA-C, MERRA-2, and Aura-MLS water vapor VMR time series at 0.1 hPa smoothed by a 30 d running mean over Ny-Ålesund, Svalbard (79° N, 12° E), and the conjugate latitude station (79° S, 12° E).

Appendix C: Time series of temperature at mid-latitudes and polar latitudes

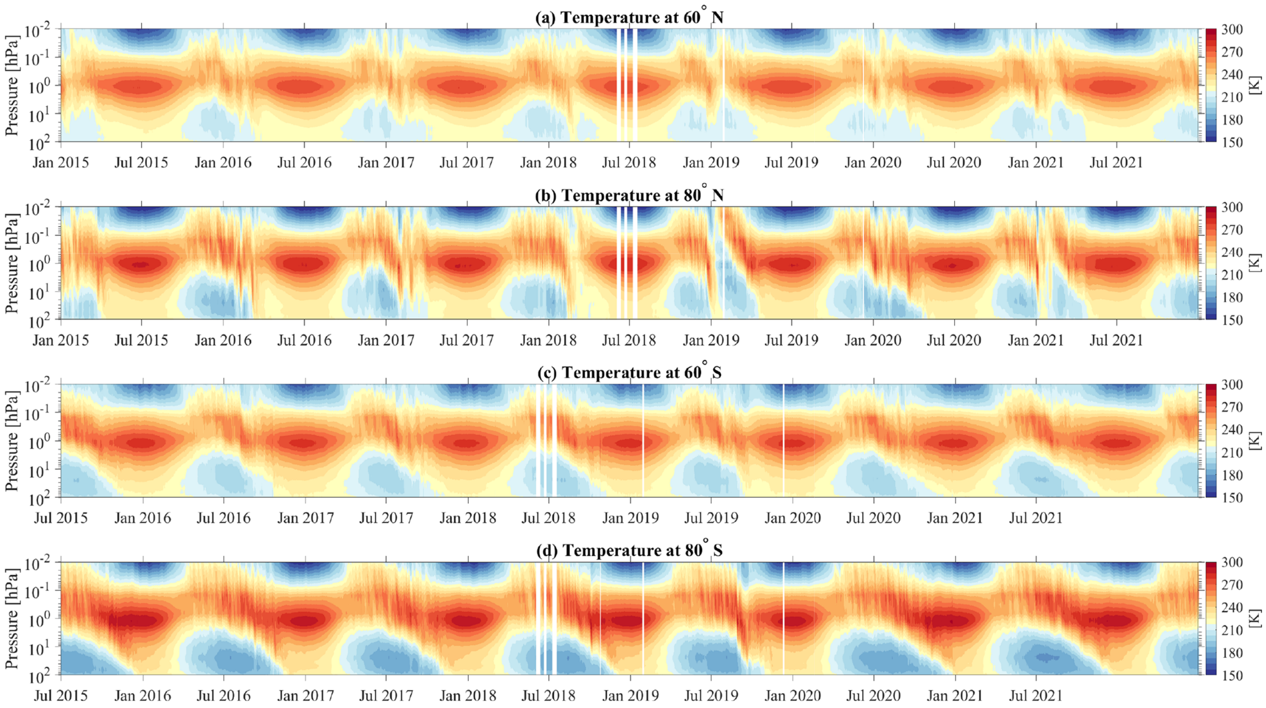

Figure C1. Time series of temperature from Aura-MLS observations as a function of pressure over conjugate polar latitudes (80° N and 80° S) and conjugate mid-latitudes (60° N and 60° S) in both hemispheres.

Data availability. The GROMOS-C and MIAWARA-C level 2 data are provided by the Network for the Detection of Atmospheric Composition Change and are available at https://ndacc.larc.nasa.gov/stations/ny-alesund-norway (Schranz et al., 2020). MLS v5 data are available from the NASA Goddard Space Flight Center Earth Sciences Data and Information Services Center (GES DISC): https://doi.org/10.5067/Aura/MLS/DATA2516 (Schwartz et al., 2020). MERRA-2 data are provided by NASA at the Modeling and Assimilation Data and Information Services Center (MDISC) and are available at the model level at https://doi.org/10.5067/WWQSXQ8IVFW8 (GMAO, 2015a) and the pressure level at https://doi.org/10.5067/QBZ6MG944HW0 (GMAO, 2015b).

Author contributions. GSh was responsible for the ground-based ozone measurements with GROMOS-C, performed the data analysis, and prepared the manuscript. ES provided the Aura-MLS data. WK helped with data analysis. GSt designed the concept of the study and contributed to the interpretation of the results. All of the authors discussed the scientific findings and provided valuable feedback for manuscript editing.

Competing interests. The contact author has declared that none of the authors has any competing interests.

Special issue statement. This article is part of the special issue "Atmospheric ozone and related species in the early 2020s: latest results and trends (ACP/AMT inter-journal SI)". It is not associated with a conference.

Acknowledgements. The authors acknowledge the NASA Global Modeling and assimilation Office (GMAO) for providing the MERRA-2 reanalysis data and the Aura/MLS team for providing the satellite data. We thank the Swiss Polar Institute (SPI), and the Institute of Applied Physics (IAP) supports the development of the GROMOS-C and MIAWARA-C radiometers.

Financial support. This research has been supported by the Swiss National Science Foundation (grant no. 200021-200517/1).

Review statement. This paper was edited by John Plane and reviewed by two anonymous referees.

References

Andrews, D. and Mcintyre, M. E.: Planetary waves in horizontal and vertical shear: The generalized Eliassen-Palm relation and the mean zonal acceleration, J. Atmos. Sci., 33, 2031–2048, 1976.

Baldwin, M. P. and Dunkerton, T. J.: Stratospheric Harbingers of Anomalous Weather Regimes, Science, 294, 581–584, https://doi.org/10.1126/science.1063315, 2001.

Baldwin, M. P., Ayarzagüena, B., Birner, T., Butchart, N., Butler, A. H., Charlton-Perez, A. J., Domeisen, D. I. V., Garfinkel, C. I., Garny, H., Gerber, E. P., Hegglin, M. I., Langematz, U., and Pedatella, N. M.: Sudden Stratospheric Warmings, Rev. Geophys., 59, e2020RG000708, https://doi.org/10.1029/2020RG000708, 2021.

Bazhenov, O.: Increased humidity in the stratosphere as a possible factor of ozone destruction in the Arctic during the spring 2011 using Aura MLS observations, Int. J. Remote Sens., 40, 3448–3460, 2019.

Becker, E.: Dynamical Control of the Middle Atmosphere, Space Sci. Rev., 168, 283–314, https://doi.org/10.1007/s11214-011-9841-5, 2012.

Becker, E. and Fritts, D. C.: Enhanced gravity-wave activity and interhemispheric coupling during the MaCWAVE/MIDAS northern summer program 2002, Ann. Geophys., 24, 1175–1188, https://doi.org/10.5194/angeo-24-1175-2006, 2006.

Bernet, L., Boyd, I., Nedoluha, G., Querel, R., Swart, D., and Hocke, K.: Validation and Trend Analysis of Stratospheric Ozone Data from Ground-Based Observations at Lauder, New Zealand, Remote Sens., 13, 1–15, https://doi.org/10.3390/rs13010109, 2021.

Brasseur, G. P. and Solomon, S.: Composition and chemistry, Aeronomy of the Middle Atmosphere: Chemistry and Physics of the Stratosphere and Mesosphere, 3rd edn., Springer Netherlands, 265–442, 2005.

Brewer, A.: Evidence for a world circulation provided by the measurements of helium and water vapour distribution in the stratosphere, Q. J. Roy. Meteor. Soc., 75, 351–363, 1949.

Brinksma, E. J., Swart, D. P. J., Bergwerff, J. B., Meijer, Y. J., and Ormel, F. T.: RIVM Stratospheric Ozone Lidar at NDSC Station Lauder: Routine Measurements and Validation During the OPAL Campaign, in: Advances in Atmospheric Remote Sensing with Lidar, edited by: Ansmann, A., Neuber, R., Rairoux, P., and Wandinger, U., Springer Berlin Heidelberg, Berlin, Heidelberg, 529–532, 1997.

Davis, S. M., Hegglin, M. I., Fujiwara, M., Dragani, R., Harada, Y., Kobayashi, C., Long, C., Manney, G. L., Nash, E. R., Potter, G. L., Tegtmeier, S., Wang, T., Wargan, K., and Wright, J. S.: Assessment of upper tropospheric and stratospheric water vapor and ozone in reanalyses as part of S-RIP, Atmos. Chem. Phys., 17, 12743–12778, https://doi.org/10.5194/acp-17-12743-2017, 2017.

de Wit, R. J., Hibbins, R. E., Espy, P. J., and Hennum, E. A.: Coupling in the middle atmosphere related to the 2013 major sudden stratospheric warming, Ann. Geophys., 33, 309–319, https://doi.org/10.5194/angeo-33-309-2015, 2015.

Dobson, G. M. B.: Origin and distribution of the polyatomic molecules in the atmosphere, P. Roy. Soc. Lond. A Mat., 236, 187–193, 1956.

Eckstein, J., Ruhnke, R., Zahn, A., Neumaier, M., Kirner, O., and Braesicke, P.: An assessment of the climatological representativeness of IAGOS-CARIBIC trace gas measurements using EMAC model simulations, Atmos. Chem. Phys., 17, 2775–2794, https://doi.org/10.5194/acp-17-2775-2017, 2017.

Eriksson, P., Jiménez, C., and Buehler, S. A.: Qpack, a general tool for instrument simulation and retrieval work, J. Quant. Spectrosc. Ra., 91, 47–64, https://doi.org/10.1016/j.jqsrt.2004.05.050, 2005.

Eriksson, P., Buehler, S., Davis, C., Emde, C., and Lemke, O.: ARTS, the atmospheric radiative transfer simulator, version 2, J. Quant. Spectrosc. Ra., 112, 1551–1558, https://doi.org/10.1016/j.jqsrt.2011.03.001, 2011.

Espy, P. J., Ochoa Fernández, S., Forkman, P., Murtagh, D., and Stegman, J.: The role of the QBO in the inter-hemispheric coupling of summer mesospheric temperatures, Atmos. Chem. Phys., 11, 495–502, https://doi.org/10.5194/acp-11-495-2011, 2011.

Fernandez, S., Murk, A., and Kämpfer, N.: GROMOS-C, a novel ground-based microwave radiometer for ozone measurement campaigns, Atmos. Meas. Tech., 8, 2649–2662, https://doi.org/10.5194/amt-8-2649-2015, 2015.

Flury, T., Hocke, K., Haefele, A., Kämpfer, N., and Lehmann, R.: Ozone depletion, water vapor increase, and PSC generation at midlatitudes by the 2008 major stratospheric warming, J. Geophys. Res.-Atmos., 114, 7903–7914, https://doi.org/10.1029/2009JD011940, 2009.

Forkman, P., Eriksson, P., Murtagh, D., and Espy, P.: Observing the vertical branch of the mesospheric circulation at latitude 60 N using ground-based measurements of CO and H_2O, J. Geophys. Res.-Atmos., 110, D05107, https://doi.org/10.1029/2004JD004916, 2005.

Garfinkel, C. I., Shaw, T. A., Hartmann, D. L., and Waugh, D. W.: Does the Holton–Tan mechanism explain how the quasi-biennial oscillation modulates the Arctic polar vortex?, J. Atmos. Sci., 69, 1713–1733, 2012.

Gelaro, R., McCarty, W., Suárez, M. J., Todling, R., Molod, A., Takacs, L., Randles, C. A., Darmenov, A., Bosilovich, M. G., Reichle, R., Wargan, K., Coy, L., Cullather, R., Draper, C., Akella, S., Buchard, V., Conaty, A., Silva, A. M. da, Gu, W., Kim, G.-K., Koster, R., Lucchesi, R., Merkova, D., Nielsen, J. E., Partyka, G., Pawson, S., Putman, W., Rienecker, M., Schubert, S. D., Sienkiewicz, M., and Zhao, B.: The modern-era retrospective analysis for research and applications, version 2 (MERRA-2), J. Climate, 30, 5419–5454, 2017.

Global Modeling and Assimilation Office (GMAO): MERRA-2 inst3_3d_asm_Nv: 3d,3-Hourly,Instantaneous,Model-Level,Assimilation,Assimilated Meteorological Fields V5.12.4, Greenbelt, MD, USA, Goddard Earth Sciences Data and Information Services Center (GES DISC) [data set], https://doi.org/10.5067/WWQSXQ8IVFW8, 2015a.

Global Modeling and Assimilation Office (GMAO): MERRA-2 inst3_3d_asm_Np: 3d,3-Hourly,Instantaneous,Pressure-Level,Assimilation,Assimilated Meteorological Fields V5.12.4, Greenbelt, MD, USA, Goddard Earth Sciences Data and Information Services Center (GES DISC) [data set], https://doi.org/10.5067/QBZ6MG944HW0, 2015b.

Graf, M., Scheidegger, P., Kupferschmid, A., Looser, H., Peter, T., Dirksen, R., Emmenegger, L., and Tuzson, B.: Compact and lightweight mid-infrared laser spectrometer for balloon-borne water vapor measurements in the UTLS, Atmos. Meas. Tech., 14, 1365–1378, https://doi.org/10.5194/amt-14-1365-2021, 2021.

Inness, A., Chabrillat, S., Flemming, J., Huijnen, V., Langenrock, B., Nicolas, J., Polichtchouk, I., and Razinger, M.: Exceptionally low Arctic stratospheric ozone in spring 2020 as seen in the CAMS reanalysis, J. Geophys. Res.-Atmos., 125, e2020JD033563, https://doi.org/10.1029/2020JD033563, 2020.

Karlsson, B., Körnich, H., and Gumbel, J.: Evidence for interhemispheric stratosphere-mesosphere coupling derived from noctilucent cloud properties, Geophys. Res. Lett., 34, L16806, https://doi.org/10.1029/2007GL030282, 2007.

Knowland, K. E., Keller, C. A., Wales, P. A., Wargan, K., Coy, L., Johnson, M. S., Liu, J., Lucchesi, R. A., Eastham, S. D., Fleming, E., Liang, Q., Leblanc, T., Livesey, N. J., Walker, K. A., Ott, L. E., and Pawson, S.: NASA GEOS Composition Forecast Modeling System GEOS-CF v1.0: Stratospheric Composition, J. Adv. Model. Earth Sy., 14, e2021MS002852, https://doi.org/10.1029/2021MS002852, 2022.

Körnich, H. and Becker, E.: A simple model for the interhemispheric coupling of the middle atmosphere circulation, Adv. Space Res., 45, 661–668, 2010.

Lambert, A., Read, W., and Livesey, N.: MLS/Aura Level 2 Water Vapor (H_2O) Mixing Ratio V004, Greenbelt, MD, USA, Goddard Earth Sciences Data and Information Services Center (GES DISC) [data set], https://doi.org/10.5067/Aura/MLS/DATA2009, 2015.

Langematz, U.: Stratospheric ozone: down and up through the anthropocene, ChemTexts, 5, 1–12, 2019.

Lawrence, Z. D., Perlwitz, J., Butler, A. H., Manney, G. L., Newman, P. A., Lee, S. H., and Nash, E. R.: The remarkably strong Arctic stratospheric polar vortex of winter 2020: Links to record-breaking Arctic oscillation and ozone loss, J. Geophys. Res.-Atmos., 125, e2020JD033271, https://doi.org/10.1029/2020JD033271 2020.

Lee, J. N., Wu, D. L., Manney, G. L., Schwartz, M. J., Lambert, A., Livesey, N. J., Minschwaner, K. R., Pumphrey, H. C., and Read, W. G.: Aura Microwave Limb Sounder observations of the polar middle atmosphere: Dynamics and transport of CO and H_2O, J. Geophys. Res.-Atmos., 116, D05110, https://doi.org/10.1029/2010JD014608, 2011.

Limpasuvan, V., Orsolini, Y. J., Chandran, A., Garcia, R. R., and Smith, A. K.: On the composite response of the MLT to major sudden stratospheric warming events with elevated stratopause, J. Geophys. Res.-Atmos., 121, 4518–4537, 2016.

Lindzen, R. S.: Turbulence and stress owing to gravity wave and tidal breakdown, J. Geophys. Res.-Oceans, 86, 9707–9714, https://doi.org/10.1029/JC086iC10p09707, 1981.

Livesey, N., Van Snyder, W., Read, W., and Wagner, P.: Retrieval algorithms for the EOS Microwave limb sounder (MLS), IEEE T. Geosci. Remote, 44, 1144–1155, https://doi.org/10.1109/TGRS.2006.872327, 2006.

Lossow, S., Khaplanov, M., Gumbel, J., Stegman, J., Witt, G., Dalin, P., Kirkwood, S., Schmidlin, F. J., Fricke, K. H., and Blum, U.: Middle atmospheric water vapour and dynamics in the vicinity of the polar vortex during the Hygrosonde-2 campaign, Atmos. Chem. Phys., 9, 4407–4417, https://doi.org/10.5194/acp-9-4407-2009, 2009.

Marsh, D., Smith, A., Brasseur, G., Kaufmann, M., and Grossmann, K.: The existence of a tertiary ozone maximum in the high-latitude middle mesosphere, Geophys. Res. Lett., 28, 4531–4534, 2001.

Matsuno, T.: A Dynamical Model of the Stratospheric Sudden Warming, J. Atmos. Sci., 28, 1479–1494, https://doi.org/10.1175/1520-0469(1971)028<1479:ADMOTS>2.0.CO;2, 1971.

Matthias, V., Dörnbrack, A., and Stober, G.: The extraordinarily strong and cold polar vortex in the early northern winter 2015/2016, Geophys. Res. Lett., 43, 12287–12294, https://doi.org/10.1002/2016GL071676, 2016.

Matthias, V., Stober, G., Kozlovsky, A., Lester, M., Belova, E., and Kero, J.: Vertical structure of the Arctic spring transition in the middle atmosphere, J. Geophys. Res.-Atmos., 126, e2020JD034353, https://doi.org/10.1029/2020JD034353, 2021.

McConnell, J. C. and Jin, J. J.: Stratospheric ozone chemistry, Atmos.-Ocean, 46, 69–92, 2008.

Orsolini, Y. J., Urban, J., Murtagh, D. P., Lossow, S., and Limpasuvan, V.: Descent from the polar mesosphere and anomalously high stratopause observed in 8 years of water vapor and temperature satellite observations by the Odin Sub-Millimeter Radiometer, J. Geophys. Res.-Atmos., 115, D12305, https://doi.org/10.1029/2009JD013501, 2010.

Rienecker, M. M., Suarez, M. J., Gelaro, R., Todling, R., Bacmeister, J., Liu, E., Bosilovich, M. G., Schubert, S. D., Takacs, L., Kim, G.-K., Bloom, S., Chen, J., Collins, D., Conaty, A., da Silva, A., Gu, W., Joiner, J., Koster, R. D., Lucchesi, R., Molod, A. M., Owens, T., Pawson, S., Pegion, P., Redder, C. R., Reichle, R., Robertson, F. R., Ruddick, A. G., Sienkiewicz, M., and Woollen, J.: MERRA: NASA's modern-era retrospective analysis for research and applications, J. Climate, 24, 3624–3648, https://doi.org/10.1175/JCLI-D-11-00015.1, 2011.

Rodgers, C. D.: Inverse methods for atmospheric sounding: theory and practice, vol. 2, World Scientific Publishing, London, UK, 2000.

Ryan, N. J., Kinnison, D. E., Garcia, R. R., Hoffmann, C. G., Palm, M., Raffalski, U., and Notholt, J.: Assessing the ability to derive rates of polar middle-atmospheric descent using trace gas measurements from remote sensors, Atmos. Chem. Phys., 18, 1457–1474, https://doi.org/10.5194/acp-18-1457-2018, 2018.

Scheiben, D., Schanz, A., Tschanz, B., and Kämpfer, N.: Diurnal variations in middle-atmospheric water vapor by ground-based microwave radiometry, Atmos. Chem. Phys., 13, 6877–6886, https://doi.org/10.5194/acp-13-6877-2013, 2013.

Scheiben, D., Tschanz, B., Hocke, K., Kämpfer, N., Ka, S., and Oh, J. J.: The quasi 16-day wave in mesospheric water vapor during boreal winter 2011/2012, Atmos. Chem. Phys., 14, 6511–6522, https://doi.org/10.5194/acp-14-6511-2014, 2014.

Schranz, F., Tschanz, B., Rüfenacht, R., Hocke, K., Palm, M., and Kämpfer, N.: Investigation of Arctic middle-atmospheric dynamics using 3 years of H_2O and O_3 measurements from microwave radiometers at Ny-Ålesund, Atmos. Chem. Phys., 19, 9927–9947, https://doi.org/10.5194/acp-19-9927-2019, 2019.

Schranz, F., Hagen, J., Stober, G., Hocke, K., Murk, A., and Kämpfer, N.: Small-scale variability of stratospheric ozone during the sudden stratospheric warming 2018/2019 observed at Ny-Ålesund, Svalbard, Atmos. Chem. Phys., 20, 10791–10806, https://doi.org/10.5194/acp-20-10791-2020, 2020 (data available at: https://ndacc.larc.nasa.gov/stations/ny-alesund-norway).

Schwartz, M., Froidevaux, L., Livesey, N., and Read, W.: MLS/Aura Level 2 Ozone (O3) Mixing Ratio V004, Greenbelt, MD, USA, Goddard Earth Sciences Data and Information Services Center (GES DISC) [data set], https://doi.org/10.5067/Aura/MLS/DATA2017, 2015a.

Schwartz, M., Froidevaux, L., Livesey, N., and Read, W.: MLS/Aura Level 2 Temperature V004, Greenbelt, MD, USA, Goddard Earth Sciences Data and Information Services Center (GES DISC) [data set], https://doi.org/10.5067/Aura/MLS/DATA2021, 2015b.

Schwartz, M., Froidevaux, L., Livesey, N., and Read, W.: MLS/Aura Level 2 Ozone (O3) Mixing Ratio V005, Greenbelt, MD, USA, Goddard Earth Sciences Data and Information Services Center (GES DISC) [data set], https://doi.org/10.5067/Aura/MLS/DATA2516, 2020.

Shangguan, M., Wang, W., and Jin, S.: Variability of temperature and ozone in the upper troposphere and lower stratosphere from multi-satellite observations and reanalysis data, Atmos. Chem. Phys., 19, 6659–6679, https://doi.org/10.5194/acp-19-6659-2019, 2019.

Shepherd, T. G.: Dynamics, stratospheric ozone, and climate change, Atmos.-Ocean, 46, 117–138, 2008.

Sica, R. J. and Haefele, A.: Retrieval of temperature from a multiple-channel Rayleigh-scatter lidar using an optimal estimation method, Appl. Opt., 54, 1872–1889, https://doi.org/10.1364/AO.54.001872, 2015.

Sica, R. J. and Haefele, A.: Retrieval of water vapor mixing ratio from a multiple channel Raman-scatter lidar using an optimal estimation method, Appl. Opt., 55, 763–777, https://doi.org/10.1364/AO.55.000763, 2016.

Smith, A., López-Puertas, M., García-Comas, M., and Tukiainen, S.: SABER observations of mesospheric ozone during NH late winter 2002–2009, Geophys. Res. Lett., 36, GL040942, https://doi.org/10.1029/2009GL040942, 2009.

Smith, A. K.: Global Dynamics of the MLT, Surv. Geophys., 33, 1177–1230, https://doi.org/10.1007/s10712-012-9196-9, 2012.

Smith, A. K., Espy, P. J., López-Puertas, M., and Tweedy, O. V.: Spatial and temporal structure of the tertiary ozone maximum in the polar winter mesosphere, J. Geophys. Res.-Atmos., 123, 4373–4389, 2018.

Smith, A. K., Pedatella, N. M., and Mullen, Z. K.: Interhemispheric coupling mechanisms in the middle atmosphere of WACCM6, J. Atmos. Sci., 77, 1101–1118, 2020.

Solomon, S., Haskins, J., Ivy, D. J., and Min, F.: Fundamental differences between Arctic and Antarctic ozone depletion, P. Natl. Acad. Sci. USA, 111, 6220–6225, 2014.

Stober, G., Matthias, V., Jacobi, C., Wilhelm, S., Höffner, J., and Chau, J. L.: Exceptionally strong summer-like zonal wind reversal in the upper mesosphere during winter 2015/16, Ann. Geophys., 35, 711–720, https://doi.org/10.5194/angeo-35-711-2017, 2017.

Straub, C., Murk, A., and Kämpfer, N.: MIAWARA-C, a new ground based water vapor radiometer for measurement campaigns, Atmos. Meas. Tech., 3, 1271–1285, https://doi.org/10.5194/amt-3-1271-2010, 2010.

Straub, C., Tschanz, B., Hocke, K., Kämpfer, N., and Smith, A. K.: Transport of mesospheric H_2O during and after the stratospheric sudden warming of January 2010: observation and simulation, Atmos. Chem. Phys., 12, 5413–5427, https://doi.org/10.5194/acp-12-5413-2012, 2012.

Tao, M., Konopka, P., Ploeger, F., Yan, X., Wright, J. S., Diallo, M., Fueglistaler, S., and Riese, M.: Multitimescale variations in modeled stratospheric water vapor derived from three modern reanalysis products, Atmos. Chem. Phys., 19, 6509–6534, https://doi.org/10.5194/acp-19-6509-2019, 2019.

Tritscher, I., Pitts, M. C., Poole, L. R., Alexander, S. P., Cairo, F., Chipperfield, M. P., Grooß, J.-U., Höpfner, M., Lambert, A., Luo, B., Molleker, S., Orr, A., Salawitch, R., Snels, M., Spang, R., Woiwode, W., and Peter, T.: Polar stratospheric clouds: Satellite observations, processes, and role in ozone depletion, Rev. Geophys., 59, e2020RG000702, https://doi.org/10.1029/2020RG000702, 2021.

Tschanz, B., Straub, C., Scheiben, D., Walker, K. A., Stiller, G. P., and Kämpfer, N.: Validation of middle-atmospheric campaign-based water vapour measured by the ground-based microwave radiometer MIAWARA-C, Atmos. Meas. Tech., 6, 1725–1745, https://doi.org/10.5194/amt-6-1725-2013, 2013.

Waibel, A., Peter, T., Carslaw, K., Oelhaf, H., Wetzel, G., Crutzen, P., Poschl, U., Tsias, A., Reimer, E., and Fischer, H.: Arctic ozone loss due to denitrification, Science, 283, 2064–2069, 1999.

Wang, W., Hong, J., Shangguan, M., Wang, H., Jiang, W., and Zhao, S.: Zonally asymmetric influences of the quasi-biennial oscillation on stratospheric ozone, Atmos. Chem. Phys., 22, 13695–13711, https://doi.org/10.5194/acp-22-13695-2022, 2022.

Wargan, K., Labow, G., Frith, S., Pawson, S., Livesey, N., and Partyka, G.: Evaluation of the ozone fields in NASA's MERRA-2 reanalysis, J. Climate, 30, 2961–2988, https://doi.org/10.1175/JCLI-D-16-0699.1, 2017.

Wargan, K., Weir, B., Manney, G. L., Cohn, S. E., Knowland, K. E., Wales, P. A., and Livesey, N. J.: M2-SCREAM: A stratospheric composition reanalysis of Aura MLS data with MERRA-2 transport, Earth and Space Science, 10, e2022EA002632, https://doi.org/10.1029/2022EA002632, 2023.

Waters, J. W., Froidevaux, L., Harwood, R. S., Jarnot, R. F., Pickett, H. M., Read, W. G., Siegel, P. H., Cofield, R. E., Filipiak, M. J., Flower, D. A., Holden, J. R., Lau, G. K., Livesey, N. J., Manney, G. L., Pumphrey, H. C., Santee, M. L., Wu, D. L., Cuddy, D. T., Lay, R. R., Loo, M. S., Perun, V. S., Schwartz, M. J., Stek, P. C., Thurstans, R. P., Boyles, M. A., Chandra, K. M., Chavez, M. C., Chen, G.-S., Chudasama, B. V., Dodge, R., Fuller, R. A., Girard, M. A., Jiang, J., Jiang, Y., Knosp, B. W., LaBelle, R. C., Lam, J. C., Lee, K., Miller, D., Oswald, J. E., Patel, N. C., Pukala, D. M., Quintero, O., Scaff, D. M., Snyder, W. V., Tope, M. C., Wagner, P. A., and Walch, M. J.: The Earth observing system microwave limb sounder (EOS MLS) on the aura Satellite, IEEE T. Geosci. Remote, 44, 1075–1092, 2006.

Zahn, A., Christner, E., van Velthoven, P., Rauthe-Schöch, A., and Brenninkmeijer, C.: Processes controlling water vapor in the upper troposphere/lowermost stratosphere: An analysis of 8 years of monthly measurements by the IAGOS-CARIBIC observatory, J. Geophys. Res.-Atmos., 119, 11–505, 2014.

Zhang, J., Xie, F., Ma, Z., Zhang, C., Xu, M., Wang, T., and Zhang, R.: Seasonal evolution of the quasi-biennial oscillation impact on the Northern Hemisphere polar vortex in winter, J. Geophys. Res.-Atmos., 124, 12568–12586, 2019.

Zuber, R., Köhler, U., Egli, L., Ribnitzky, M., Steinbrecht, W., and Gröbner, J.: Total ozone column intercomparison of Brewers, Dobsons, and BTS-Solar at Hohenpeißenberg and Davos in 2019/2020, Atmos. Meas. Tech., 14, 4915–4928, https://doi.org/10.5194/amt-14-4915-2021, 2021.

5 Ozone anomalies during stratospheric warming events

5.1 Introduction

The high-resolution daily ozone profile measurements from GROMOS-C are used to investigate ozone anomalies in the Arctic during major SSW and early FSW events. These ground-based observations, MERRA-2 reanalysis, and MLS satellite data facilitate obtaining vertically resolved structures of ozone anomalies relative to compiled climatologies and to assess the consistency across observational and modeled data sources.

Our analysis reveals distinctive ozone anomaly patterns associated with SSW and final stratospheric warming (FSW) events. For SSWs, we observe a consistent sequence of positive ozone anomalies at all altitudes within 30 days of the event onset, followed by descending negative anomalies in the middle stratosphere. In contrast, FSWs exhibit positive anomalies in the lower and middle stratosphere and negative anomalies in the upper stratosphere at onset, which then evolve into the opposite. To further understand the processes driving these anomalies, we apply the ozone continuity equation using MERRA-2 meteorological fields and utilize the ozone tendency diagnostics from MERRA-2. This approach allows us to quantitatively separate the contributions of horizontal eddy transport, vertical advection, and photochemistry. Additionally, we examine variations in total column ozone, linking them to horizontal eddy effects and vertical motion in the lower stratosphere.

5.2 Publication

The following article has been published in *Atmospheric Chemistry and Physics (ACP)*.

Citation: Shi, Guochun, Witali Krochin, Eric Sauvageat, and Gunter Stober. "Ozone anomalies over the polar regions during stratospheric warming events". In: *Atmospheric Chemistry and Physics* 24.17 (2024), pp. 10187–10207

DOI: https://acp.copernicus.org/articles/24/10187/2024/

Atmos. Chem. Phys., 24, 10187–10207, 2024
https://doi.org/10.5194/acp-24-10187-2024

Atmospheric
Chemistry
and Physics
Open Access

Research article

Ozone anomalies over the polar regions during stratospheric warming events

Guochun Shi[1,2], **Witali Krochin**[1,2], **Eric Sauvageat**[3], **and Gunter Stober**[1,2]

[1]Oeschger Center for Climate Change Research, University of Bern, Bern, Switzerland
[2]Institute of Applied Physics, University of Bern, Bern, Switzerland
[3]Federal Office of Meteorology and Climatology, MeteoSwiss, Payerne, Switzerland

Correspondence: Guochun Shi (guochun.shi@unibe.ch)

Received: 9 January 2024 – Discussion started: 8 March 2024
Revised: 10 July 2024 – Accepted: 29 July 2024 – Published: 13 September 2024

Abstract. The impact of major sudden stratospheric warming (SSW) events and early final stratospheric warming (FSW) events on ozone variations in the middle atmosphere in the Arctic is investigated by performing microwave radiometer measurements above Ny-Ålesund, Svalbard (79° N, 12° E), with GROMOS-C (GRound-based Ozone MOnitoring System for Campaigns). The retrieved daily ozone profiles during SSW and FSW events in the stratosphere and lower mesosphere at 20–70 km from microwave observations are cross-compared to MERRA-2 (Modern-Era Retrospective Analysis for Research and Applications, version 2) and MLS (Microwave Limb Sounder). The vertically resolved structures of polar ozone anomalies relative to the climatologies derived from GROMOS-C, MERRA-2, and MLS shed light on the consistent pattern in the evolution of ozone anomalies during both types of events. For SSW events, ozone anomalies are positive at all altitudes within 30 d after onset, followed by negative anomalies descending in the middle stratosphere. However, positive anomalies in the middle and lower stratosphere and negative anomalies in the upper stratosphere at onset are followed by negative anomalies in the middle stratosphere and positive anomalies in the upper stratosphere during FSW events. Here, we compare results by leveraging the ozone continuity equation with meteorological fields from MERRA-2 and directly using MERRA-2 ozone tendency products to quantify the impact of dynamical and chemical processes on ozone anomalies during SSW and FSW events. We document the underlying dynamical and chemical mechanisms that are responsible for the observed ozone anomalies in the entire life cycle of SSW and FSW events. Polar ozone anomalies in the lower and middle stratosphere undergo a rapid and long-lasting increase of more than 1 ppmv close to SSW onset, which is attributed to the dynamical processes of the horizontal eddy effect and vertical advection. The pattern of ozone anomalies for FSW events is associated with the combined effects of dynamical and chemical terms, which reflect the photochemical processes counteracted partially by positive horizontal eddy transport, in particular in the middle stratosphere. In addition, we find that the variability in polar total column ozone (TCO) is associated with horizontal eddy transport and vertical advection of ozone in the lower stratosphere. This study enhances our understanding of the mechanisms that control changes in polar ozone during the life cycle of SSW and FSW events, providing a new aspect of quantitative analysis of dynamical and chemical fields.

Published by Copernicus Publications on behalf of the European Geosciences Union.

1 Introduction

The wintertime polar stratosphere is characterized by a strong, westerly, and cold polar vortex. Due to the different sea–land distributions in the Northern Hemisphere and Southern Hemisphere, large-scale waves with several hundred kilometers of wavelength are generated in the troposphere. These waves propagate upward into the stratosphere, disturbing or weakening the polar vortex and thus affecting the dynamics there (Andrews et al., 1987). The occurrence of sudden stratospheric warming (SSW) events (Charlton and Polvani, 2007; Butler et al., 2015) in midwinter is mainly attributed to the split or displacement of the stratospheric polar vortex by the upward-propagating planetary waves (Holton, 1980; Pancheva et al., 2008; Matthias et al., 2013; Albers and Birner, 2014; Qin et al., 2021; Baldwin et al., 2021). Observed final stratospheric warming (FSW) events (Black and McDaniel, 2007) in early spring depend on variations in the upward propagation of tropospheric planetary waves as well as increasing shortwave radiation in the polar region (Salby and Callaghan, 2007; Sun et al., 2011; Thiéblemont et al., 2019). As the only atmospheric species effectively absorbing ultraviolet solar radiation from about 250 to 300 nm, ozone plays the most important role in the coupling between chemistry, radiation, and dynamical processes in the stratosphere and lower mesosphere. Ozone radiative heating and cooling peak in the stratopause; in the upper mesosphere, heating by oxygen becomes important as well. Therefore, the dynamical fluctuations and chemical reactions of stratospheric ozone in the Arctic are subject to both events (Lubis et al., 2017; Oehrlein et al., 2020; Friedel et al., 2022).

SSW events characterized by abrupt warming and weakening or reversal of the polar wintertime westerly circulation lead to extreme ozone variability at the polar latitudes (Schranz et al., 2019, 2020). de la Cámara et al. (2018b) utilized the Whole Atmosphere Community Climate Model (WACCM) output and European Centre for Medium-Range Weather Forecasts Re-Analysis Interim (ERAI) to do a comprehensive and quantitative analysis of ozone advective transport and mixing in equivalent latitude coordinates during the life cycle of SSW with polar-night jet oscillation and without polar-night jet oscillation. Bahramvash Shams et al. (2022) emphasized the high variability of middle-stratospheric ozone fluctuations and the key role of vertical advection in middle-stratospheric ozone during SSW using MERRA-2 (Modern-Era Retrospective Analysis for Research and Applications, version 2) reanalysis data. Oehrlein et al. (2020) analyzed the responses with and without interactive chemistry versions of WACCM to major SSW events, which resulted in a pattern resembling a more negative North Atlantic Oscillation following midwinter SSW events. Hong and Reichler (2021) examined the changes in ozone in both the Arctic and tropical regions and documented the underlying dynamical mechanisms of the observed changes during the life cycles of SSW and vortex intensification events. In the mesosphere and lower thermosphere (MLT) regions, the evolution of secondary ozone during SSWs is associated with anomalous vertical residual motion due to the wind reversal from the stratosphere up to the mesosphere and is consistent with photochemical equilibrium governing the MLT nighttime ozone based on Specified Dynamics (SD)-WACCM (Tweedy et al., 2013; Smith-Johnsen et al., 2018).

Several case studies of FSW events utilizing a combination of chemistry–climate models and reanalysis data emphasize stratospheric ozone anomalies, which are influenced by the position and strength of the polar vortex and chemical processing to different dynamical conditions. Salby and Callaghan (2007) used a three-dimensional model of dynamics and photochemistry to investigate the enriched polar ozone during springtime through isentropic mixing by planetary waves and eliminated much of the apparent ozone depletion. Thiéblemont et al. (2019) confirmed the timing of FSW affected by ozone and greenhouse gases using coupled chemistry–climate models of WACCM. Lawrence et al. (2020) used MERRA-2 and the Japanese Meteorological Agency's 55-year Reanalysis (JRA-55) to show ozone depletion and total column ozone (TCO) amounts in the Northern Hemisphere polar cap decreasing to the lowest level ever observed in springtime. Hong and Reichler (2021) investigated the persistent loss in Arctic ozone during vortex intensifications, which is dramatically compensated for by sudden warming-like increases after the final warming. Friedel et al. (2022) contrasted results from chemistry–climate models with and without interactive ozone chemistry to quantify the impact of ozone anomalies on the timing of the FSW and its effects on the surface climate. Other studies focused mainly on the dynamical effects of the FSW using ground-based and satellite observations to characterize the transition to the spring and summer circulation in terms of the dynamical or radiative forcing (Matthias et al., 2021) or the tidal amplification of the semidiurnal tide in the aftermath of major SSW events (Stober et al., 2020).

Utilizing the outcomes of ozone continuity equations, we derive the relative contributions of dynamical transport versus chemical processes in determining the polar ozone anomaly behavior observed in SSW and FSW events. In addition, we show that polar ozone anomalies in the lower stratosphere predominantly governed by the horizontal eddy effect and vertical advection transport processes exhibit a strong correlation with polar total column ozone corresponding to both types of events. Overall, our goal is not only to provide a new view of the dynamical and chemical-driven variability in polar ozone anomalies but also to apply it to the validation of coupled chemistry–climate models and other reanalysis data.

The paper is structured as follows. Section 2 describes the data and methods. Section 3 provides the vertically resolved ozone field at polar latitude stations. Section 4 discusses the ozone budget through dynamical and chemical processes and the dynamically controlled polar TCO. Finally, Sect. 5 summarizes and discusses the results.

2 Data and methods

2.1 GROMOS-C (GRound-based Ozone MOnitoring System for Campaigns)

GROMOS-C is an ozone microwave radiometer that has measured the ozone emission line at 110.836 GHz at Ny-Ålesund, Svalbard (79° N, 12° E), since September 2015. It was built by the Institute of Applied Physics at the University of Bern. The radiometer is very compact and is optimized for autonomous operation. Hence, it can be transported and operated at remote field sites under extreme climate conditions. GROMOS-C subsequently observes in the four cardinal directions (north, east, south, and west) at an elevation angle of 22° with a sampling time of 4 s. Ozone volume mixing ratio (VMR) profiles are retrieved from the ozone spectra with a temporal averaging of 2 h by leveraging the Atmospheric Radiative Transfer Simulator version 2 (ARTS2; Eriksson et al., 2011) and Qpack2 software (Eriksson et al., 2005) according to the optimal estimation algorithm (Rodgers, 2000). An a priori ozone profile is required for optimal estimation and is taken from an MLS climatology collected between the years 2004 and 2013. The retrieved 2-hourly ozone profiles have vertical resolutions of 10–12 km in the stratosphere and up to 20 km in the mesosphere and cover a sensitive altitude range of 23–70 km. The averaging kernels (AVKs) of GROMOS-C together with its measurement response, errors, and ozone profiles are shown in Fernandez et al. (2015) and Shi et al. (2023).

2.2 Aura Microwave Limb Sounder (MLS)

NASA's Earth Observing System (EOS) MLS instrument on board the Aura spacecraft measures thermal emissions from the limb of Earth's atmosphere. MLS provides comprehensive measurements of vertical profiles of temperature and 15 chemical species from the upper troposphere to the mesosphere, spanning nearly pole-to-pole coverage from 82° S to 82° N (Waters et al., 2006).

The ozone profile is retrieved using the 240 GHz microwave band, which extends from 261 to 0.0215 hPa for recommended scientific applications. Vertical spacing for these layers is about 1.3 km everywhere below 1 hPa and about 2.7 km at most altitudes above 1 hPa. The vertical resolution of the retrieved ozone profile is reported to be around 3 km, extending from 261 hPa up into the mesosphere (Livesey et al., 2011; Schwartz et al., 2015). The time records for the MLS ozone profiles used in this study are from August 2004 to December 2021 (in the next section, the SSW event in 2003/2004 is not available for analyzing ozone variations from MLS). MLS passes Ny-Ålesund twice a day at around 04:00 and 10:00 UTC. Profiles for comparison are extracted if the location is within ± 1.2° latitude and ±6° longitude of Ny-Ålesund.

2.3 MERRA-2

MERRA-2 (Waters et al., 2006; Gelaro et al., 2017) of the Goddard Earth Observing System-5 (GEOS-5) atmospheric general circulation model (AGCM) is the latest global atmospheric reanalysis produced by NASA's Global Modeling and Assimilation Office (GMAO) from 1980 until the present. A variety of datasets are assimilated into the AGCM to create three-dimensional MERRA-2 ozone datasets with a time resolution of 6 h, although the MERRA-2 fields are provided every 3 h (Wargan et al., 2017; Gelaro et al., 2017). The retrieved ozone profiles from the Solar Backscatter Ultraviolet Radiometer (SBUV, 1980 to 2004) and MLS (since August 2004, down to 177 hPa until 2015, down to 215 hPa after 2015, and up to 0.02 hPa), together with the TCO from SBUV (1980 to 2004) and the Ozone Monitoring Instrument (OMI) (since 2004), are assimilated into MERRA-2 (Gelaro et al., 2017).

MERRA-2 data have been used to study ozone trends, processes, and validations with ozonesondes, microwave radiometers, and satellite observations (Lubis et al., 2017; Albers et al., 2018; Wargan et al., 2018; Schranz et al., 2020; Hong and Reichler, 2021; Bahramvash Shams et al., 2022; Shi et al., 2023). In this study, the ozone dataset from MERRA-2 reanalysis with 72 model levels from the surface to 0.01 hPa, a horizontal resolution of 0.5° × 0.625°, and a time resolution of 3 h will be used. To have the finest possible vertical resolution for comparisons with our microwave measurements, MERRA-2 ozone at the model levels is used to investigate the polar ozone variations in the stratosphere and mesosphere. In addition, meteorological variables such as temperature, eastward and northward winds, and vertical pressure velocity extracted from 42 pressure levels facilitate the calculation of variables such as residual meridional circulation and potential temperature.

As given by Lubis et al. (2017), the MERRA-2 ozone tendency product on 42 pressure levels from the surface up to 0.1 hPa (https://doi.org/10.5067/S0LYTK57786Z) is assimilated with GEOS-5 using the odd-oxygen mixing ratio, qO_x, as its "diagnostic" variable (Bosilovich et al., 2015; Lubis et al., 2017). An odd-oxygen family transport model provides the ozone concentration necessary for solar absorption. Following Bosilovich et al. (2015) and Lubis et al. (2017), the vertically integrated ozone tendency coupling to the layers above and below is given as

$$\left[\frac{\partial \overline{qO_x}}{\partial t}\right]_{\mathrm{TOT}} = \left[-\nabla \cdot \left(\overline{\upsilon qO_x}\right)\right]_{\mathrm{DYN}} + \left[\frac{\partial \overline{qO_x}}{\partial t}\right]_{\mathrm{PHY}} + \left[\frac{\partial \overline{qO_x}}{\partial t}\right]_{\mathrm{ANA}}. \quad (1)$$

This equation consists of four terms describing the total ozone tendency (TOT), which is balanced by the convergence of odd-oxygen mixing ratio products (first term on the right-hand side (DYN) of Eq. 1), the total physics product (PHY) of parameterized production, and loss terms and the total analysis product (ANA) describing the total ozone tendency from the analysis. The derived ozone data products have been validated in the troposphere and stratosphere (Bosilovich et al., 2015). In the mesosphere above 0.1 hPa, the odd-oxygen family starts to be dominated by atomic oxygen rather than ozone and, thus, MERRA-2 results for ozone are no longer representative of the mesosphere for hemispheric winter (Shi et al., 2023), although MLS ozone measurements are assimilated up to 0.02 hPa. Furthermore, the total ozone tendency from physics (PHY) is decomposed into contributions from chemistry (CHM), turbulence (TRB), and moist physics (MST). Given the parameterized ozone chemistry in MERRA-2, the total ozone tendency from chemistry (CHM) is analyzed together with the correcting tendency term (i.e., CHM + ANA). The contributions of turbulence and moist physics are negligible in the stratosphere and are therefore not considered in this analysis.

2.4 Transformed Eulerian mean (TEM) ozone budget

The local changes for atmospheric tracers ($\overline{\chi}$) are investigated using the TEM continuity equation that results from transport processes and chemical sources and sinks as follows (Andrews et al., 1987):

$$\overline{\chi}_{\mathrm{t}} = \underbrace{\left(-\overline{v}^*\overline{\chi}_y - \overline{\omega}^*\overline{\chi}_z + e^{z/H}\nabla\cdot M_y + e^{z/H}\nabla\cdot M_z\right)}_{\overline{\chi}_{\mathrm{dyn}}} + \underbrace{\left(\overline{P}-\overline{L}\right)}_{\overline{S}}, \tag{2}$$

where $\overline{\chi}_{\mathrm{t}}$ is the tracer tendency that denotes transport of the zonal mean tracer volume mixing ratios due to the horizontal and vertical advection by the residual circulation ($\overline{v}^*$, $\overline{\omega}^*$), the horizontal and vertical eddy transport effects are $e^{z/H}\nabla\cdot M_y$ and $e^{z/H}\nabla\cdot M_z$, and $\overline{S}$ is chemical production minus loss ($P-L$). The chemical net is calculated as the residual of the left-hand side minus the sum of the first four terms $\overline{\chi}_{\mathrm{dyn}}$ on the right-hand side of Eq. (2) to better understand the chemical component in the stratosphere. The overbars indicate the zonal means, and the primes denote the departure from the zonal mean. The scale height is represented by an H of 7 km.

The $\overline{v}^*$ and $\overline{\omega}^*$ in Eq. (2) denote the TEM residual meridional and vertical winds defined as

$$\overline{v}^* = \overline{v} - e^{z/H}\partial_z\left(e^{z/H}\overline{v'\theta'}/\overline{\theta}_z\right), \tag{3}$$

$$\overline{\omega}^* = \overline{\omega} + (a\cos\varphi)^{-1}\,\partial_\varphi\left(\cos(\varphi)\overline{v'\theta'}/\overline{\theta}_z\right), \tag{4}$$

where v and ω are the meridional and vertical winds, θ is the potential temperature, a is Earth's radius, and φ is the latitude.

Here, the eddy transport vector $\boldsymbol{M}$ can be decomposed into meridional and vertical components M_y and M_z, respectively (Andrews et al., 1987):

$$M_y = -e^{z/H}\left(\overline{v'\chi'} - \overline{v'\theta'}/\overline{\theta}_z\overline{\chi}_z\right), \tag{5}$$

$$M_z = -e^{z/H}\left(\overline{\omega'\chi'} - \overline{v'\theta'}/\overline{\theta}_z\overline{\chi}_y\right). \tag{6}$$

2.5 Identification of SSW and FSW events

Stratospheric warming events are a crucial stratospheric phenomenon and indicate the vertical coupling of the entire middle atmosphere affecting the mesosphere, stratosphere, and troposphere. Many studies combined temperature increases and wind reversals to detect major SSW events in midwinter (Charlton and Polvani, 2007; Hu et al., 2014; Butler et al., 2015; Butler and Gerber, 2018). One of the most often-used definitions of a major SSW event during wintertime (Charlton and Polvani, 2007) is that zonal-mean zonal winds at 60° N and the 10 hPa level reverse direction from westerly to easterly and that the zonal-mean temperature gradient between 60 and 90° N becomes positive. As shown in Table 1, we identify 10 major SSW events in this study as described in Li et al. (2023). For the FSW events, different studies have analyzed springtime stratospheric zonal winds using single pressure levels at varying latitudes and thresholds (Black and McDaniel, 2007; Byrne et al., 2017; Matthias et al., 2021) as well as multiple pressure levels (Hardiman et al., 2011). We found seven early FSW events (in Table 1) identified by Butler and Domeisen (2021) based on the criterion that the daily mean zonal-mean zonal winds at 60° N latitude and 10 hPa exhibit an easterly flow and remain so continuously for more than 10 consecutive days, as outlined by Butler and Gerber (2018). The SSW and FSW composites will be discussed for the wind and temperature fields and anomalies, which are defined as deviations from the daily seasonal climatology.

3 Meteorological background situations

To examine the ozone anomalies during late winter over the polar latitude station, we summarize some key dynamical quantities of SSW and FSW events. Figure 1 illustrates the pressure–time evolution of the SSW and FSW composite zonal-mean zonal wind (at 60° N) and temperature (70–90° N) in MERRA-2 reanalysis data. Below approximately 0.1 hPa, the westerly wind rapidly weakens – lags by 10 d – and then switches to an easterly wind after the SSW onset (lags by 0 d) at 10 hPa in Fig. 1a. The easterly wind returns after approximately 15 d at 10 hPa. After around 20 d of SSW onset, the wind at 0.1 hPa reverses direction to westerly with a maximum speed of 80 m s^{-1} and stays like this for at least 20 d. The temperature fields undergo alterations in conjunction with the wind field reversal. The SSW onset is character-

Table 1. Dates of the major SSW and early FSW events used for the composite in this study.

Number	Winters	SSW central date	Winters	FSW central date
1	2003/2004	5 January 2004	2004/2005	13 March 2005
2	2005/2006	21 January 2006	2010/2011	4 April 2011
3	2006/2007	24 February 2007	2013/2014	27 March 2014
4	2007/2008	22 February 2008	2014/2015	28 March 2015
5	2008/2009	24 January 2009	2015/2016	5 March 2016
6	2009/2010	9 February 2010	2016/2017	8 April 2017
7	2012/2013	6 January 2013	2019/2020	14 March 2020
8	2017/2018	12 February 2018	–	–
9	2018/2019	2 January 2019	–	–
10	2020/2021	3 January 2021	–	–

ized by the rapid warming in the stratosphere in Fig. 1c, indicating the rapid descent of the stratopause to lower altitudes. In Fig. 1b, the zonal-mean zonal wind at 60° N and 10 hPa during an FSW event is easterly with lags of 50 d until the early summer and does not reverse its direction to westerly. The wind reversal is accompanied by a temperature increase exceeding 280 K after the FSW onset in Fig. 1d. Temperatures in the lower stratosphere also increase greatly, but there is cooling in the upper mesosphere.

Furthermore, we derive anomalies for the relevant physical quantities by subtracting the mean climatology obtained from all years for our composites of SSW and FSW events. Significant anomalies of wind, temperature, and $\overline{\varpi}^*$ extend over nearly the entire pressure range and throughout the life cycle of SSW and FSW as shown in Fig. 2. The strongest negative wind anomalies occur during the first 15 d after the SSW onset and diminish within 20 d in the stratosphere, corresponding to the strongest positive anomalies in the mesosphere occurring between 20 and 50 d after the onset day as shown in Fig. 2a. These changes occur in parallel to rapid stratospheric warming, with the temperature maxima appearing in near-vertical quadrature with the wind anomalies during those 5 d before and after the SSW onset (Fig. 2c). During the recovery phase following the SSW, progressively descending negative anomalies in the stratosphere appear with positive anomalies in the mesosphere, along with the reformation of the "normal" stratopause. The lower mesosphere exhibits negative wind anomalies with lags ranging from −30 to 20 d, with the most pronounced negative values observed at 1 hPa (Fig. 2a). The vertical extent of the zonal wind and temperature anomalies at FSW onset is similar to that of the SSW event, but the magnitude and strength are different. The temperature anomaly at 1 hPa almost vanishes and remains around zero after FSW onset. $\overline{\varpi}^*$ anomalies over the polar regions (70–90° N) as an indicator of wave forcing show more intense downward propagation (blue) and upward propagation (red) during both events. The obvious difference between the two types of events is that strong upwelling starts about 3 weeks earlier at negative lags for SSW events (Fig. 2e). The statistically significant positive anomalies vanish after 15 d, giving way to negative anomalies emerging within 30 d in Fig. 2e. In contrast, FSW events exhibit $\overline{\varpi}^*$ anomalies that remain positive for a duration near 40 d above 1 hPa (Fig. 2f). The lasting $\overline{\varpi}^*$ anomalies after the FSWs at and below 1 hPa are very small though.

4 Local changes over Ny-Ålesund, Svalbard (79° N, 12° E)

Leveraging continuous ozone measurements from the ground-based radiometer GROMOS-C at Ny-Ålesund, Svalbard (79° N, 12° E), and combining MERRA-2 and MLS datasets, we analyze the temporal evolution of ozone and provide more details on the impacts of SSW and FSW events. The main benefit of the ground-based observations is the much higher temporal resolution of 2 h, which permits us to estimate the sampling bias from the MLS satellite, taking data at only two local times. This higher temporal resolution is also sufficient to resolve the daily ozone cycle (Schranz et al., 2018). Figure 3 exhibits the SSW and FSW composite ozone VMR at Ny-Ålesund (79° N, 12° E) as a function of the time lag for an event's central date. The GROMOS-C-measured ozone VMR over Ny-Ålesund is greatly enhanced after an SSW and FSW onset. The results indicate good agreement between MERRA-2 (below 0.1 hPa) and MLS with GROMOS-C observations. However, due to the complexity of altered dynamics in the winter polar regions introducing additional uncertainties into numerical models and data assimilation systems (Wargan et al., 2017), ozone VMRs exhibit dramatic variability (in Fig. 3c, d) in the mesosphere from MERRA-2. Discontinuities in MERRA-2 ozone (Shi et al., 2023) in the mesosphere (0.1–0.01 hPa) have to be taken into account, which is likely associated with the extension of stratospheric chemistry up to the mesosphere. Knowland et al. (2022) discussed the model ozone biases in MERRA-2 due to mesospheric parameterization being disabled in the NASA Goddard Earth Observing System Composition Forecast (GEOS-CF), and the stratospheric chemistry now extends up through the top of the GEOS atmosphere, thus avoiding the need to repeatedly read in produc-

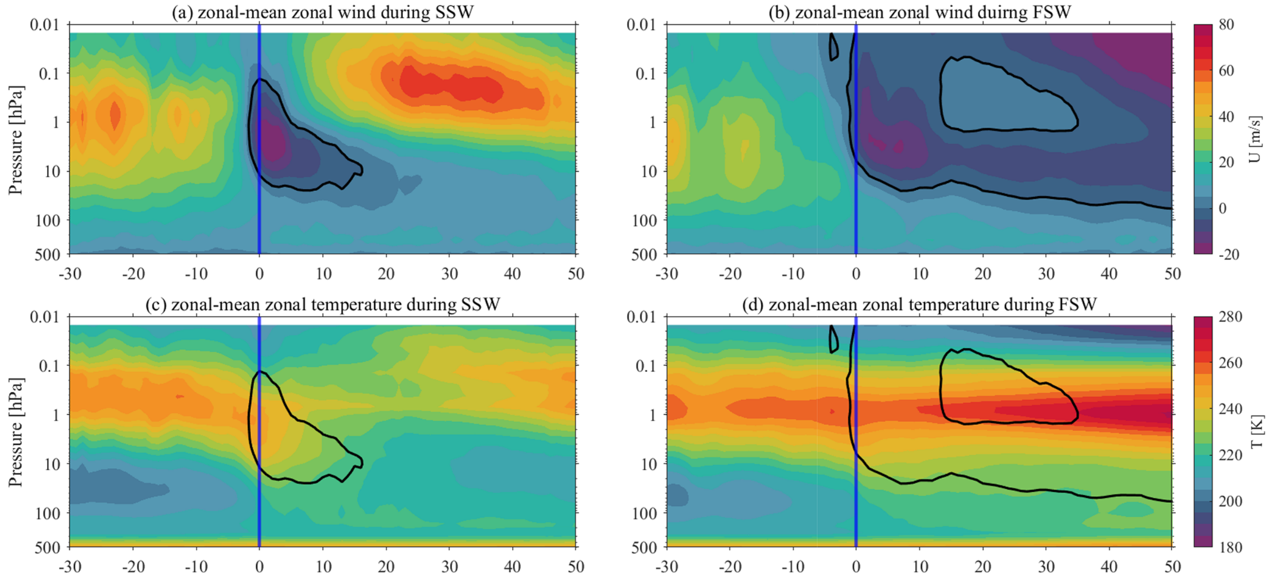

Figure 1. Pressure–time section of the SSW and FSW composite zonal-mean **(a, b)** zonal wind and **(c, d)** temperature from MERRA-2. Time is relative to the SSW and FSW onset on the abscissa. The vertical blue line represents the onset day (day 0). The zero-wind contour is in black.

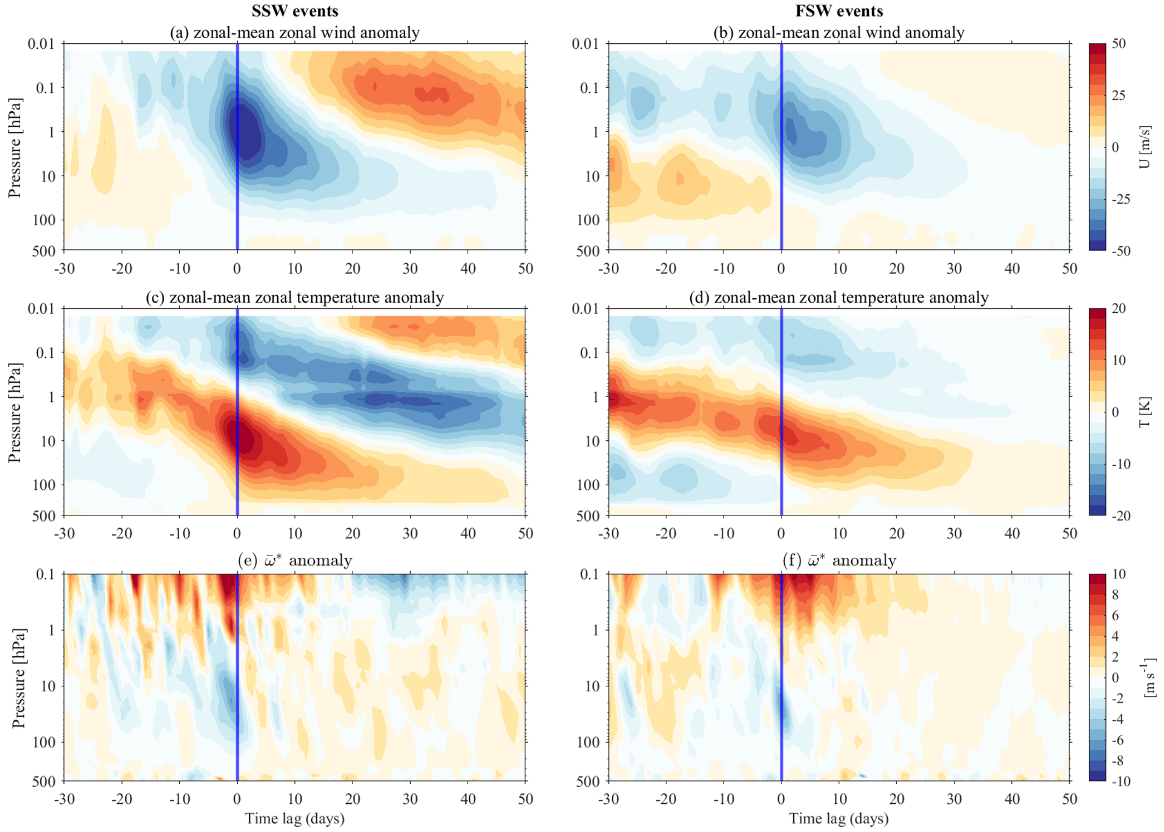

Figure 2. Pressure–time section of the SSW and FSW composite zonal-mean **(a, b)** zonal wind anomalies, **(c, d)** temperature anomalies, and **(e, f)** vertical component of the residual circulation $\overline{\varpi}^*$ anomalies for the averaged polar regions (70–90° N) from MERRA-2.

tion and loss rates. Gelaro et al. (2017) investigated these partially understandable increased deviations using the implemented radiative transfer schemes and other model physics such as interactive chemistry, which is computationally much more expensive. Shi et al. (2023) discussed the climatological deviations of the measurements from the ground-based radiometer GROMOS-C with MERRA-2 and MLS. Otherwise, the presence of much more atomic oxygen compared to ozone in the upper mesosphere could be used to explain the observed large discrepancies above 0.1 hPa when MERRA-2 ozone is compared with MLS and GROMOS-C. Our analysis reveals qualitative agreement in stratospheric ozone between MERRA-2 and observations from the GROMOS-C and MLS instruments during FSW and SSW events. This agreement serves as a robust justification for employing MERRA-2 data to explore the dynamics–chemistry relationship in subsequent steps of our research, providing confidence in the reliability of MERRA-2 ozone data for our analytical purposes.

Figure 4 shows the composite ozone anomalies in GROMOS-C, MERRA-2, and MLS at Ny-Ålesund (79° N, 12° E) as a function of time lag for the SSW and FSW central date. These subplots show very similar behavior despite the variety of datasets and years covered. The strongest positive ozone anomalies of up to 1 ppmv for more than 30 consecutive days after SSW onset in the middle- and upper-stratospheric layers are evident. The positive ozone anomalies persist around 20 d after FSW onset in the middle stratosphere following a negative value of around 0.6 ppmv descending in the upper stratosphere. Otherwise, there is a negative ozone anomaly in the lower stratosphere and upper stratosphere before FSW onset that is stronger than before the onset of the SSW events. Note that the GROMOS-C composite is based on only three SSW and FSW events because the measurement campaign started in September 2015. The anomalies are estimated in terms of the daily climatology (between 2015 and 2022).

5 Dynamical and chemical effects on ozone

5.1 Seasonal cycle of the ozone transport budget

Seasonal changes in ozone tendencies from the eddy effect, advection transport, and chemical loss and production processes based on MERRA-2 reanalysis data for the period 2004–2021 are shown in Fig. 5. The contribution from each term in Eq. (2) is calculated to infer the seasonal cycle of the ozone transport budget in MERRA-2 averaged between 70 and 90° N. The ozone tendency $\overline{\chi}_t$ shows a distinct increase during winter and fall and a decrease during spring and early summer. In Fig. 5b, the horizontal eddy transport exhibits a prominent seasonal cycle, with positive and significantly stronger ozone eddy mixing observed throughout the stratosphere over the entire year, except for the summer months. Vertical eddy transport tends to show a dipole pattern with opposite effects between the middle and upper stratosphere from late fall to early spring in Fig. 5c. This indicates that seasonality in eddy mixing plays a major role in the polar ozone annual cycle. Horizontal advection of ozone is much smaller compared to eddy-mixing and chemical processes as shown in Fig. 5d (an increase of 5 times). However, it has negative effects on the ozone mixing transport in the polar regions. During fall and winter, the vertical advection transport exhibits a pattern comparable to that of the vertical eddy term, yet it demonstrates a tendency towards positive values in the upper stratosphere during summer. Finally, the chemical term is positive during winter in the middle stratosphere. However, the greatest ozone destruction occurs in spring, reaching its maximum in April.

Figure 5g–i show the seasonal cycle of all terms averaged over the latitudes from 70 to 90° N for the pressure levels 10 hPa ($\sim$ 30 km), 3 hPa K ($\sim$ 40 km), and 1 hPa ($\sim$ 50 km). At 10 hPa horizontal eddy transport and net chemical loss nearly balance each other out, particularly from February to June. Vertical eddy transport makes a negative contribution from September to April. Horizontal eddy transport has a large positive contribution of within 0.4 ppmv d^{-1} in March at 3 hPa, corresponding to maximum chemical ozone destruction. However, chemical production starts from October to February and has a peak in January at 3 hPa. Thus, the shape of the ozone seasonal cycle is mainly determined by the seasonally varying eddy-mixing transport and chemical loss and production. At 1 hPa, the chemical term is of crucial relevance, and the seasonal budget of ozone is completely controlled by competing effects of horizontal eddy transport and chemical terms. As a result, the eddy mixing effectively transports ozone into the polar region during winter and spring, where the horizontal eddy transport is so large that it balances a large fraction of the chemical ozone destruction.

Although the chemical term $\overline{S}$ displays the features of a chemical sink and source term, including location and seasonality in Fig. 5, there are differences compared to other methods of calculating ozone loss rates as shown in Fig. 6. We use the output from the chemistry transport model to display the seasonal cycle of TOT, DYN, and CHM based on Eq. (1). TOT shows good agreement in magnitude with the results $\overline{\chi}_t$ from the TEM analysis. The largest discrepancy between $\overline{S}$ and CHM (between DYN and CHM) occurs during the winter months in the middle and upper stratosphere, where the negative (positive) tendency in Eq. (2) is found rather than the positive (negative) tendency found in Eq. (1). It is important to note that the residual term in the TEM equation is shown to be representative of the chemical net production term $\overline{S}$ ($\approx \overline{\chi}_t - \overline{\chi}_{\mathrm{dyn}}$). This is an approximation since it also contains ozone transport due to unresolved waves, such as gravity waves (Plumb, 2002). One of the causes of this discrepancy is that $\overline{S}$ calculations for MERRA-2 rely on the dynamical diagnostic terms in Eq. (2), in particular the effects of irreversible eddy-mixing transport $e^{z/H}\nabla \cdot M$. The horizontal eddy mixing is predominantly influenced by the forc-

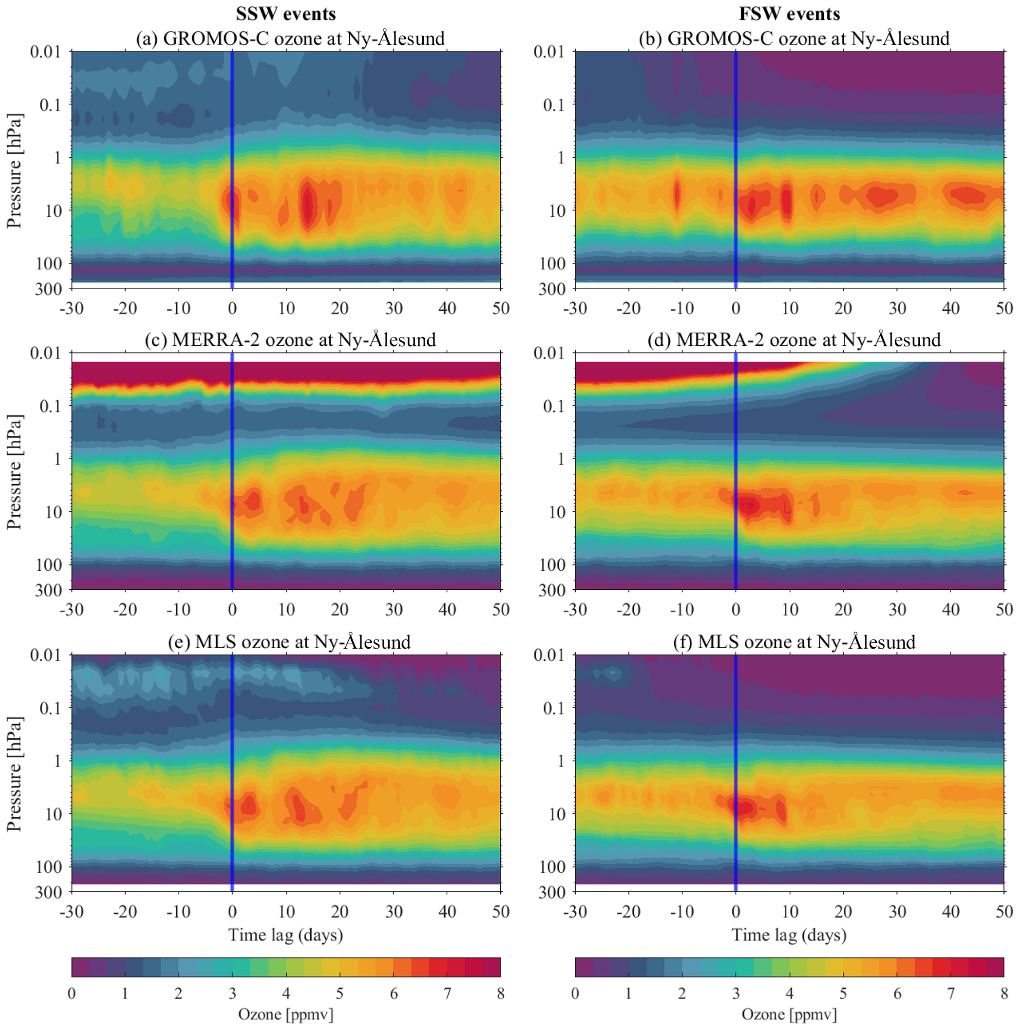

Figure 3. Pressure–time section of SSW and FSW composite ozone VMR from **(a, d)** GROMOS-C, **(b, e)** MERRA-2, and **(c, f)** MLS at Ny-Ålesund (79° N, 12° E).

ing from the breaking of resolved waves (Plumb, 2002). Furthermore, this discrepancy is very pronounced during winter, as shown in Figs. 5f and 6c. Randel et al. (1994) and Minganti et al. (2020) studied the effect of the SSW event on the N_2O TEM budget, which showed more contributions of vertical advection and horizontal eddy mixing to this budget during the SSW event than in the seasonal mean. Thus, we can explain the resulting discrepancy in the ozone TEM budget from the highly frequent occurrence of SSW events in the Northern Hemisphere, which affects the seasonal cycle in climatology in the polar regions. Hence, the discrepancy in the ozone TEM budget can be accounted for by the more frequent occurrence of midwinter SSW events in the Northern Hemisphere, leading to the effects on the ozone TEM budget in the polar regions at the seasonal scale. Determining the ozone transport mechanisms during stratospheric extreme events for better understanding of stratospheric processes and ozone variability in stratospheric chemistry–climate models and better representation in chemistry–climate models therefore has the potential to improve medium-range weather forecasts during high-latitude winter.

5.2 Insights into the ozone budget during SSW and FSW events

A climatological comparison of ozone anomalies throughout the life cycle of SSW and FSW events using MERRA-2 and MLS data provides more details about the dynamical and chemical contributions and temporal evolution of both events. Figure 7 visualizes the composite vertical structure and evolution of ozone anomalies in MERRA-2 and MLS during SSW and FSW events averaged over the polar regions (70–90° N). The vertically resolved ozone VMR (Fig. 7a, c)

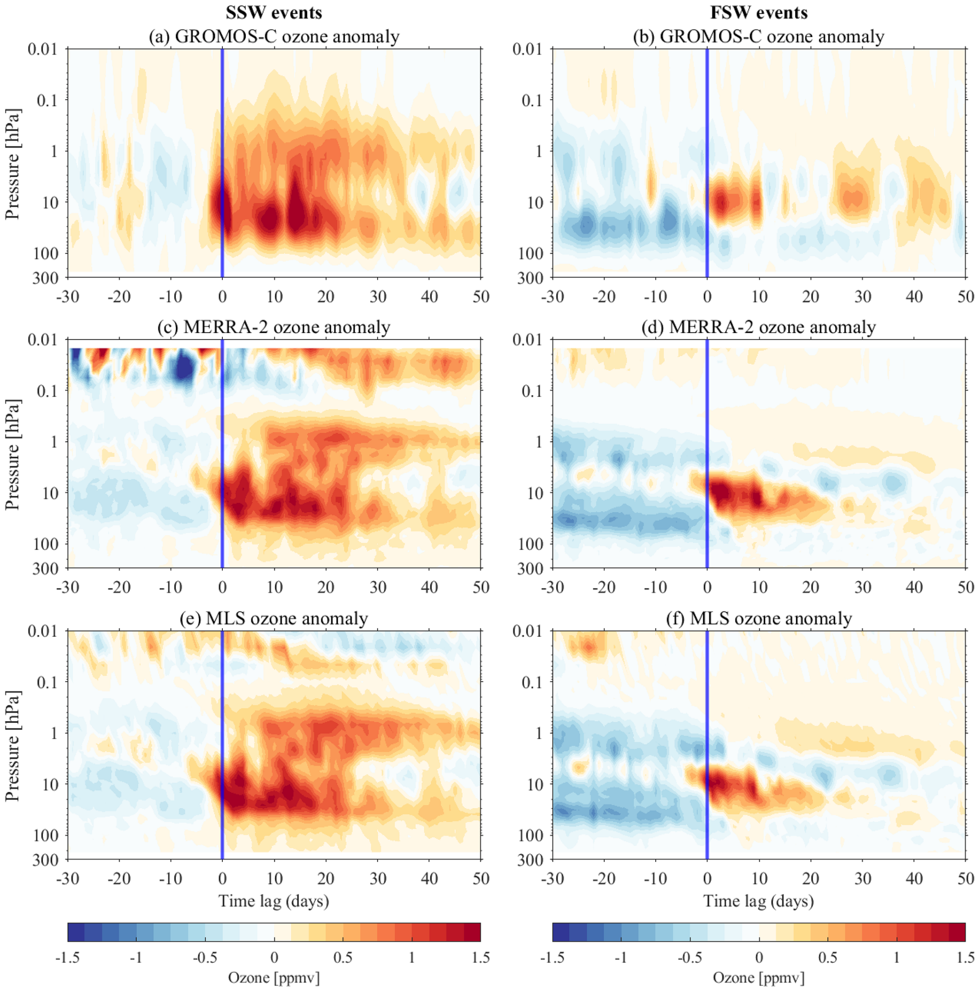

Figure 4. Same as in Fig. 3 but for anomalies at Ny-Ålesund, Svalbard (79° N, 12° E).

shows a more complicated picture during SSW events compared to FSW events (Fig. 7b, d). A weak negative ozone anomaly in the lower and middle stratosphere and a positive ozone anomaly in the upper stratosphere close to the SSW onset are presumably related to the polar stratosphere being dominated by an anomalously strong and cold vortex during this time, leading to reduced transport of ozone-rich air masses into the polar regions. Within the first 20 d following the SSW onset, the ozone VMR anomalies rapidly increase by more than 1 ppmv and persist for up to 50 d until late winter in the middle stratosphere (30–10 hPa). The negative anomalies above 5 hPa exist only briefly at the SSW onset. They are followed by persistent positive anomalies, which tend to reach their maximum value with lags of 20 d in the stratopause and lower mesosphere. During FSW events the ozone anomaly is unusually negative below the 10 hPa level before the onset day, exhibiting a reduced ozone VMR of about −0.8 ppmv from lags of −30 to 0 d compared to the climatology. Above 5 hPa, the negative anomalies persist over the life cycle of FSW events and the altitude of the negative anomaly tends to descend with time after the FSW onset. However, the positive ozone anomalies have a peak in the middle stratosphere at the FSW onset and also persist for about 20 d, propagating downward into the lower stratosphere. The structure of these anomalies differs somewhat from that of SSW events, particularly in the transition from rapidly increasing positive to descending negative anomaly tendencies in the middle to upper stratosphere after FSW onset.

Utilizing the results obtained from vertically integrated ozone tendency and ozone continuity equations, we compare the specific contributions of dynamical and chemical processes to the observed ozone anomaly behavior during SSWs and FSWs. Figures 8 and 9 present the anomalous ozone tendencies averaged between 70 and 90° N during SSW and FSW events, along with their associated dynamical

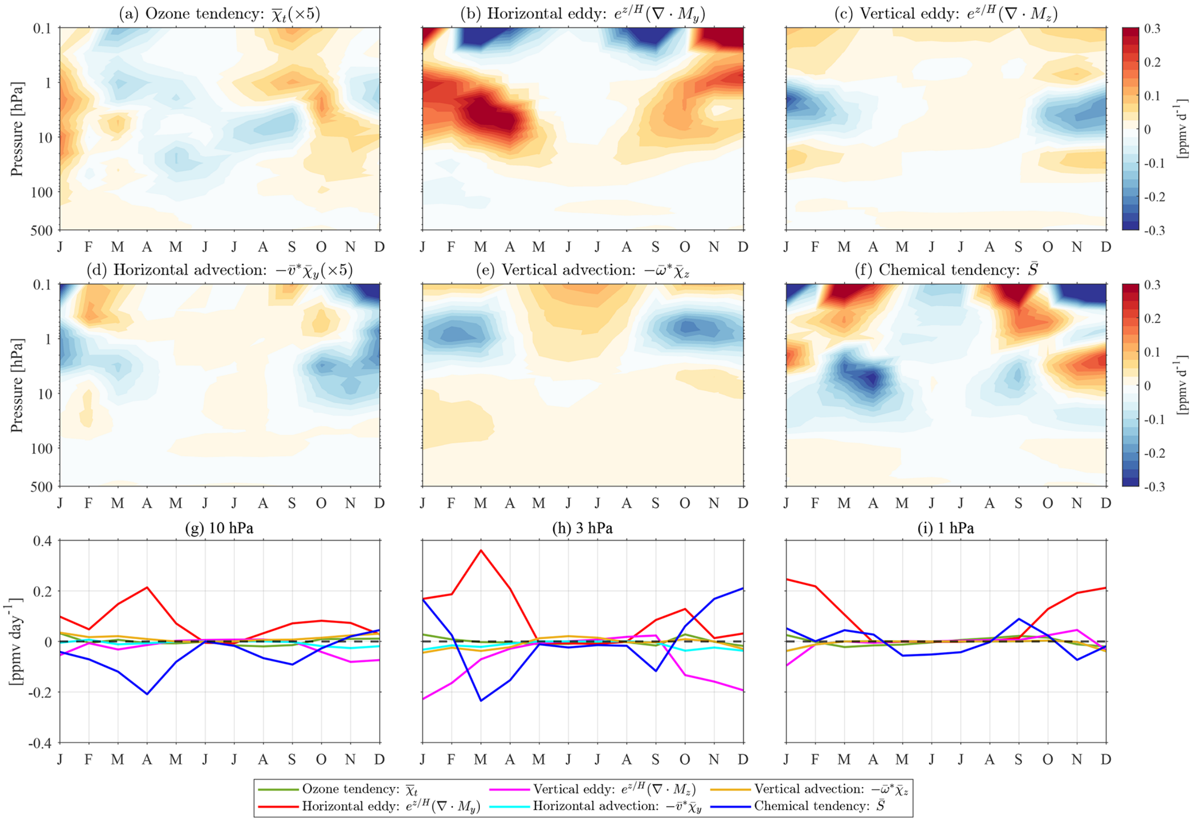

Figure 5. Seasonal cycle of the ozone tendencies as a function of time and pressure from MERRA-2 (period 2004–2021): **(a)** ozone tendency $\overline{\chi}_{\mathrm{t}}$, **(b)** horizontal eddy transport $-\overline{v}^*\overline{\chi}_y$, **(c)** vertical eddy transport $-\overline{\omega}^*\overline{\chi}_z$, **(d)** horizontal advection transport $e^{z/H}\nabla\cdot M_y$, **(e)** vertical advection transport $e^{z/H}\nabla\cdot M_z$, and **(f)** chemical loss and production $\overline{S}$ averaged over the polar regions (70–90° N) based on Eq. (2). The third row is the comparison of each term at different pressure levels: **(g)** 10 hPa, **(h)** 3 hPa, and **(i)** 1 hPa.

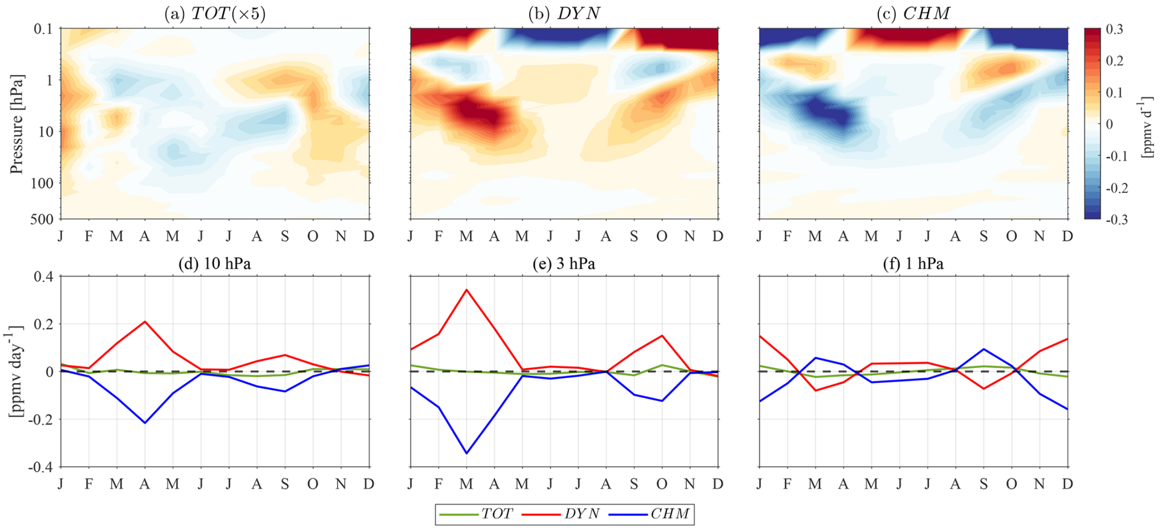

Figure 6. Seasonal cycle of **(a)** TOT, **(b)** the ozone tendency anomaly due to dynamics, and **(c)** the parameterized chemistry averaged over the polar regions (70–90° N) based on Eq. (1). The second row is the comparison of each term at different pressure levels: **(d)** 10 hPa, **(e)** 3 hPa, and **(f)** 1 hPa.

and chemical fields. We have omitted the contributions due to the horizontal advection (not shown) since they are small compared to the other processes. Moreover, we decompose the total ozone tendency into contributions of dynamical and chemical terms in Eq. (1) to infer the sources of transient changes in the polar stratospheric ozone tendency anomalies.

The results indicate pronounced ozone tendency anomalies $\overline{\chi}_t$ primarily between 100 and 10 hPa, starting with a positive ozone tendency anomaly from lag −8 d to the onset day (Fig. 8a). The evolution of the ozone tendency anomaly $\overline{\chi}_t$ is consistent with the TOT anomaly in Fig. 8f. The evolution of the TOT anomaly in the lower and middle stratosphere (between 100 and 1 hPa) is mainly dominated by DYN (Fig. 8g). DYN in the lower and middle stratosphere (100 and 10 hPa) is primarily attributed to the ozone transport via vertical advection (Fig. 8d) and eddy transport effects (Fig. 8b, c). Notably, the dominance of the dynamical term in $\overline{\chi}_t$ or the TOT anomaly in the lower stratosphere during the life cycle of the SSW composite is consistent with the transient changes in vertical residual mean transport (Fig. 2). A strong negative $\overline{\omega}^*$ exists in the polar regions corresponding to the positive $\overline{\chi}_{\mathrm{dyn}}$ and TOT (Fig. A1). An intensified residual circulation significantly weakens or breaks up the polar vortex, hence facilitating poleward ozone transport and resulting in an increase in the ozone VMR (Schranz et al., 2020; Shi et al., 2023; Bahramvash Shams et al., 2022; Harzer et al., 2023).

In the upper stratosphere, there is a notable negative ozone tendency anomaly at the onset of SSW, primarily driven by horizontal eddy and vertical advection. The vertical eddy effect contributes to building up the negative ozone tendency anomaly, while the chemistry term $\overline{S}$ tends to compensate for the ozone tendency anomaly from lag −10 d to the SSW onset day. Conversely, as the vertical eddy effect builds up the ozone tendency anomaly, the chemistry term $\overline{S}$ balances or weakens the ozone tendency anomaly after the SSW onset. Positive vertical eddy transport $e^{z/H}\nabla \cdot M_z$ and negative $\overline{S}$ in the upper stratosphere (between 3 and 1 hPa) from SSW onset day 0 to lag 35 d partially counteract the dynamically induced ozone anomalies through $\overline{S}$ (Fig. 8e). Interestingly, Fig. 8h presents two opposite attributions of CHM before and after SSW onset (the period is from lag −15 to 35 d) in the upper stratosphere, which is almost the opposite tendency compared with $\overline{S}$. The significant discrepancy during SSW events is evident in $\overline{S}$, with negative contributions in the upper stratosphere (Fig. A2) that are possibly due to uncertainties in calculating the eddy transport term, along with uncertainties in the rest of the dynamical terms. A potential source of discrepancy is that Eq. (2) does not account for the effects of numerical diffusion and vertical diffusion due to the gravity wave parameterization in particular; these are presumably non-negligible in the middle to upper stratosphere. As discussed in Brasseur and Solomon (2005), the polar middle stratosphere, as the transition layer, is intricate and requires consideration of various conditions and additional constraints. This is because ozone is chemically controlled above this layer, while below it is dynamically controlled.

During FSW, the anomalous ozone tendency $\overline{\chi}_t$ exhibits notable differences compared to SSW events, particularly in the middle stratosphere, where the FSW ozone tendency is affected by chemical and dynamical process-induced wave–mean flow interactions. In Fig. 9, the negative $\overline{\chi}_t$ anomaly lags from 5 to 15 d in the middle stratosphere, which are attributed to the photochemical effects, partially counteracted (Fig. 9e and h) the positive horizontal eddy transport (Fig. 9b). In the lower stratosphere, the strong anomalous positive tendency $\overline{\chi}_t$ at FSW onset (Fig. 9a) is associated with the dynamical terms, which are horizontal eddy and enhanced vertical advection transports (Fig. 9b and d). In the upper stratosphere, there is no obvious ozone tendency anomaly at FSW onset, which can be explained by the negative contributions of vertical eddy transport (Fig. 9c) counteracted by other terms. The evolutions of TOT and $\overline{S}$ are consistent with $\overline{\chi}_t$ and CHM, respectively, in the lower and middle stratosphere (50–3 hPa) during FSW. In addition, the strong $\overline{\chi}_t$ and CHM around FSW onset emphasize the importance of chemical processes in spring.

There is also remarkable agreement between $\overline{S}$ and CHM (as well as between $\overline{\chi}_{\mathrm{dyn}}$ and DYN) anomalies in the lower mesosphere during the SSW and FSW events displayed in Fig. 8d, h. This can be attributed to the temperature–ozone relation that suggests that, in a region dominated by pure oxygen chemistry, a temperature decrease of 10 K would produce an increase in ozone of about 20 % (Brasseur and Solomon, 2005). Temperature changes will modify all temperature-dependent photochemical rates and hence feedback to the ozone chemistry. As shown in Fig. 1d and h, from lags of 10 to 40 d during SSW events in the lower mesosphere, the negative temperature anomaly is more than 10 K from of lags 10 to 40 d, and the positive ozone VMR anomaly reaches 0.5 ppmv. Ozone anomalies resulting from the negative dynamical transport and chemical production manifest a few days after SSW onset and last for an extended period of 50 d. During FSW events, positive dynamical transport and net chemical loss nearly balance each other out at 0.5 hPa (Fig. A2), leading ozone tendency anomalies to fluctuate around zero.

5.3 Dynamical control of the total column ozone

Many studies have highlighted the significant impact of enhanced propagation of planetary waves in the lower stratosphere on the increase in TCO in winter (Matthias et al., 2013; Shaw and Perlwitz, 2014; Lubis et al., 2017; Safieddine et al., 2020; Matthias et al., 2021), subsequently leading to reduced ozone depletion in springtime (Manney et al., 2020; Lawrence et al., 2020; Schranz et al., 2020). The positive TCO anomalies after SSW events span a period exceeding 40 d when analyzing data from ERA5 and MERRA-2 reanalysis, MLS, or comprehensive GCMs such as WACCM

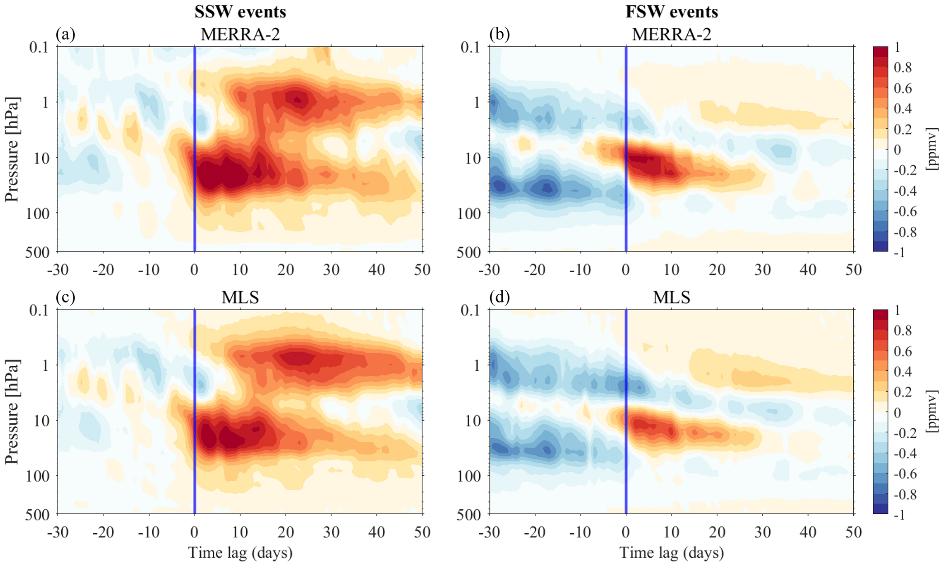

Figure 7. Evolution of the ozone anomalies for the composite of SSW and FSW events as a function of time and pressure averaged over the polar regions (70–90° N) for **(a, b)** MERRA-2 and **(c, d)** MLS.

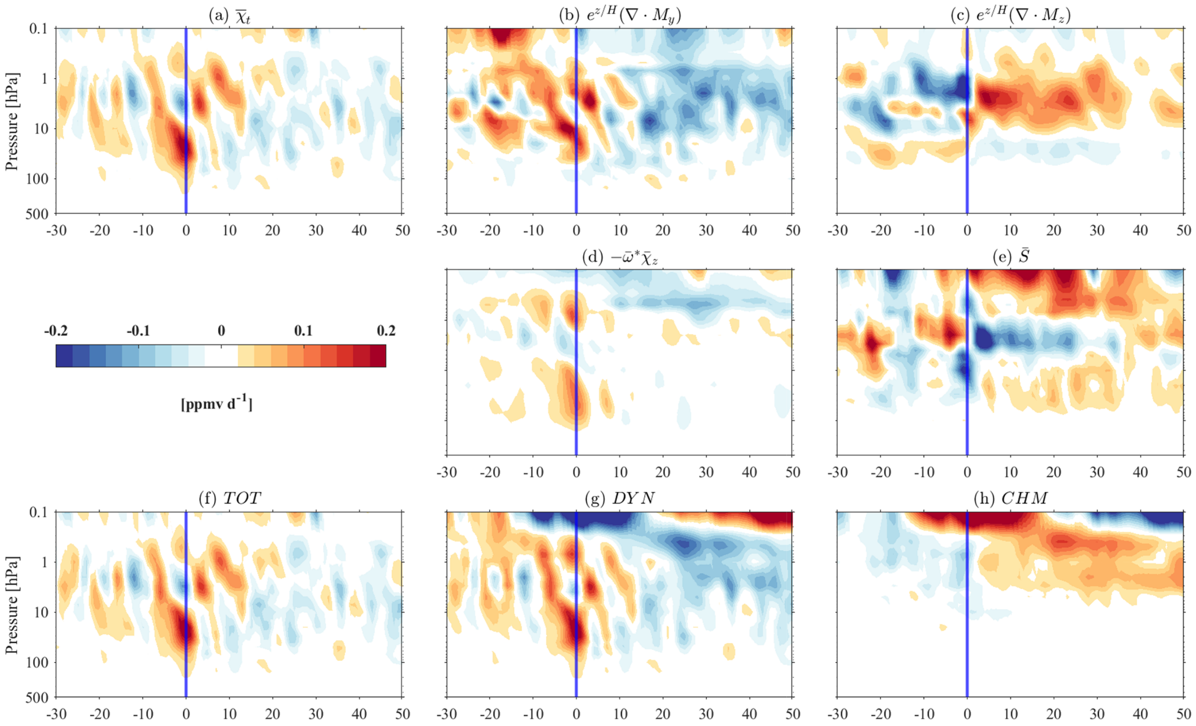

Figure 8. Anomalous ozone tendencies for SSW events as a function of time and pressure averaged over the polar regions (70–90° N) from MERRA-2: calculation of the **(a)** ozone tendency anomaly $\overline{\chi}_{\mathrm{t}}$ due to the dynamical field $\overline{\chi}_{\mathrm{dyn}}$ that is decomposed into the **(b)** horizontal eddy transport effect $e^{z/H}\nabla \cdot M_y$, **(c)** vertical eddy transport effect $e^{z/H}\nabla \cdot M_z$, **(d)** vertical advection transport $-\overline{\omega}^*\overline{\chi}_z$, and **(e)** chemical net $\overline{S}$ chemical field based on Eq. (2). The third row shows **(f)** the TOT, **(g)** the ozone tendency anomaly due to dynamics (DYN), and **(h)** the parameterized chemistry (CHM) based on Eq. (1).

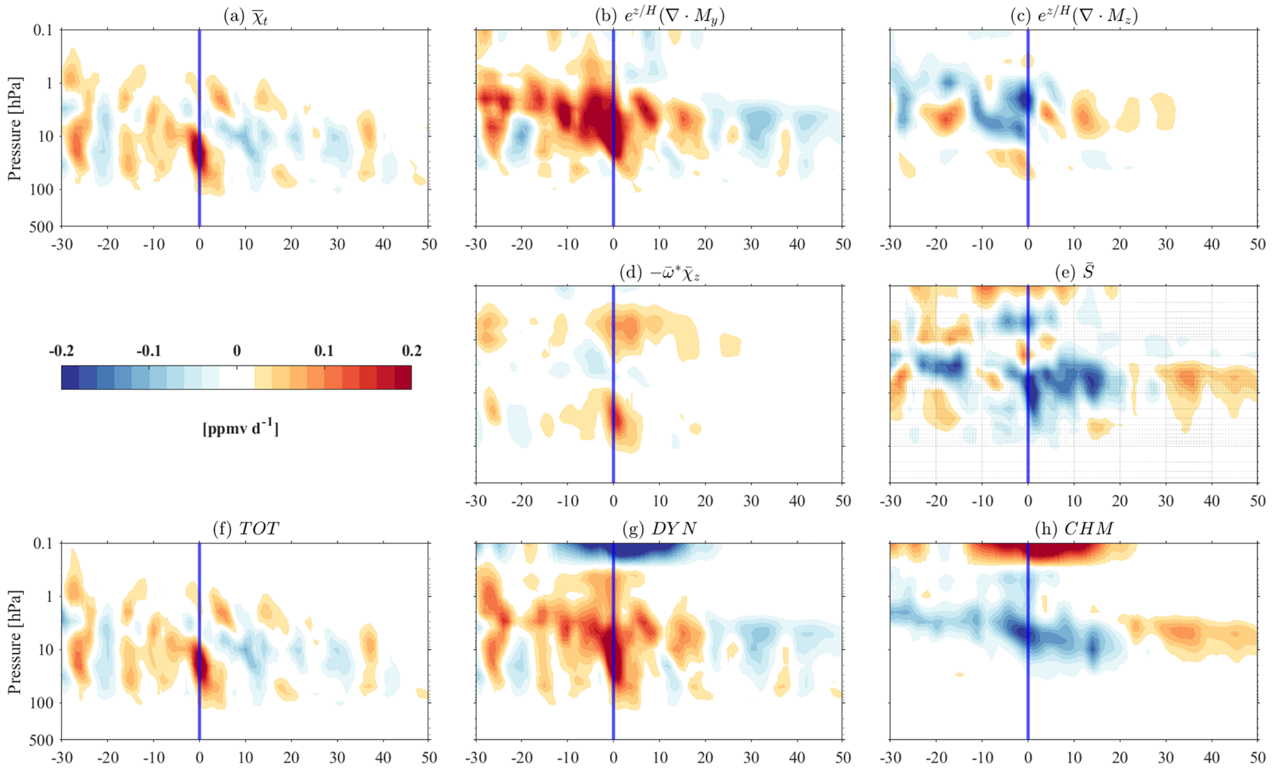

Figure 9. Same as in Fig. 8 but for the FSW composite events.

over the polar regions (de la Cámara et al., 2018b; Safieddine et al., 2020; Bahramvash Shams et al., 2022; Hocke et al., 2023). Robust positive TCO anomalies during early FSW events are influenced by the wave geometry of the FSW (Butler and Domeisen, 2021). Therefore, the dynamical behavior of SSW and FSW events which alter the chemical and dynamical evolution of the polar stratospheric ozone VMRs affects the distribution of TCO over the northern polar region. As TCO is dominated by the lower stratosphere, changes in lower-stratospheric ozone will map directly into TCO.

Quantitatively separating the effects of dynamic and chemical processes on TCO is challenging because polar ozone is similarly affected by each process. Therefore, we focus on the variability caused by dynamical processes in the TCO changes based on the relative contributions of dynamical and chemical processes in Sect. 5.2. We calculate TCO tendency anomalies in the Northern Hemisphere (30–90° N) during SSW and FSW events using MERRA-2 in Fig. 10. We find that enhanced polar TCO close to the SSW and FSW onset is mainly induced by the anomalous horizontal eddy effect and vertical advection transport in the lower stratosphere (at 30 hPa in Fig. 10). In terms of the 450 K level, it turns out that the dynamical processes involved affect the polar TCO tendency anomalies. Figures 10 and A3 indicate that the polar TCO anomalies during SSW and FSW events can be attributed to anomalous dynamical processes.

6 Discussion and conclusions

In this paper, we use MERRA-2 reanalysis data to identify SSW and FSW events by analyzing zonal wind fields and polar temperatures covering the period from 2004 to 2022. We focused on investigating the vertically resolved polar ozone variations during both SSW and FSW events and quantifying their driving mechanisms. The impact of major SSW and early FSW events on ozone in the stratosphere and mesosphere was investigated using microwave radiometer measurements taken by GROMOS-C at Ny-Ålesund, Svalbard (79° N, 12° E). Microwave observations of the daily ozone profiles during SSW and FSW events were retrieved in the stratosphere and lower mesosphere at 20–70 km. GROMOS-C captured the high variability of middle-stratospheric ozone fluctuations, showing a dramatic increase in ozone VMRs after SSW and FSW onset. For validation purposes, local changes in ozone VMRs from MERRA-2 in the stratosphere and mesosphere displayed common features in GROMOS-C and MLS under SSW and FSW conditions. Ozone anomalies are identified throughout the stratosphere and lower mesosphere (from 100 to 0.1 hPa) during SSW and FSW events. Notably, positive ozone VMR anomalies of approximately 1.5 ppmv in the middle stratosphere persisting for 30 d after SSW onset and 20 d after FSW onset have been documented.

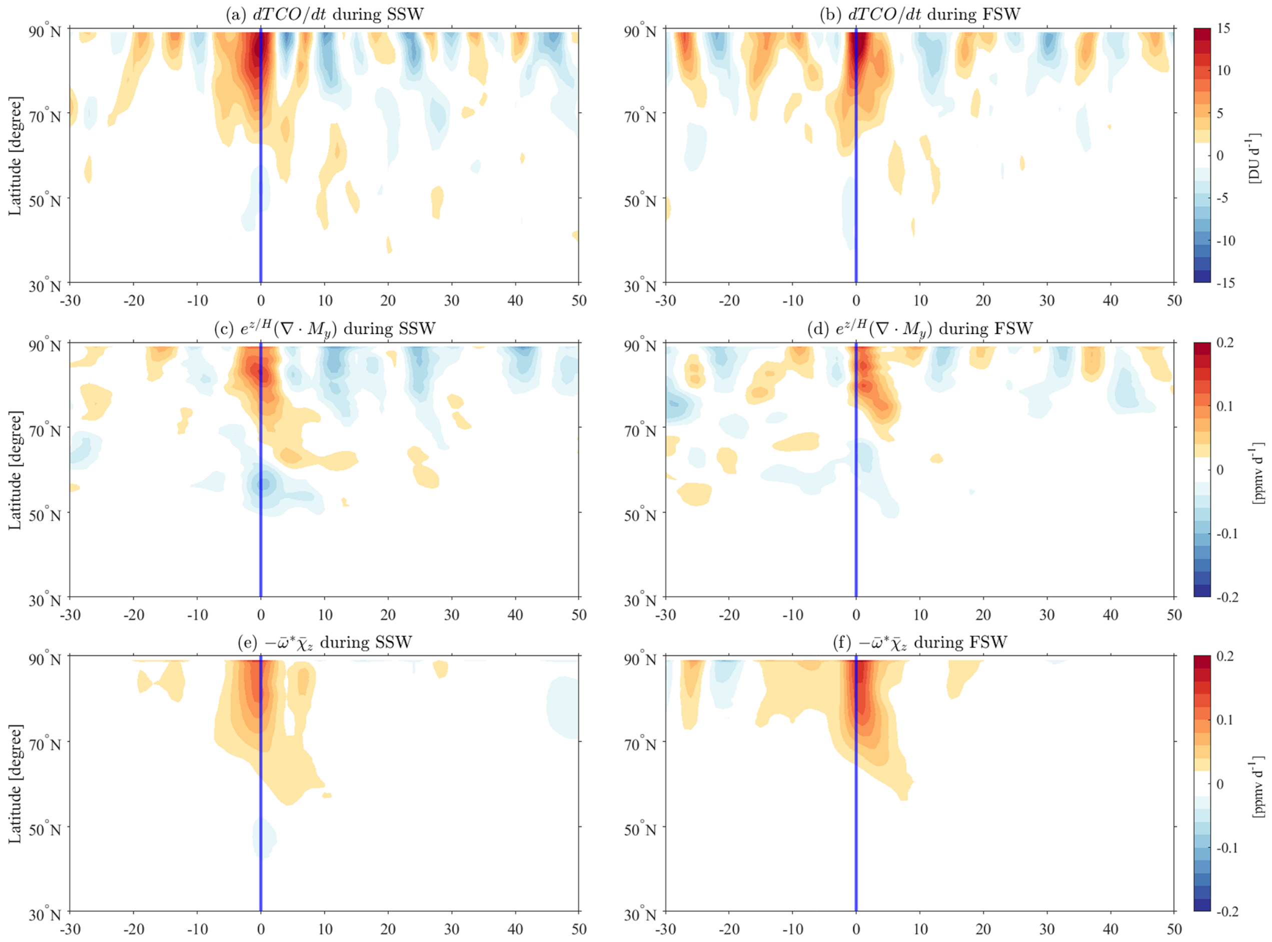

Figure 10. Evolution of the TCO tendency anomalies dO_3/dt (DU d^{-1}), the horizontal eddy effect $e^{z/H}(\nabla \cdot M_y)$, and the vertical advection transport $-\overline{\omega}^*\overline{\chi}_z$ anomalies at 30 hPa (ppmv d^{-1}) for the composite of SSW **(a, c, e)** and FSW **(b, d, f)** events as a function of time and latitude in the Northern Hemisphere.

Qualitative agreement in ozone between MERRA-2 and observations from GROMOS-C and MLS during FSW and SSW events provides confidence in the reliability of MERRA-2 data up to an altitude corresponding to 0.1 hPa for investigating the driving mechanisms of polar ozone dynamics and chemistry. Above 0.1 hPa, MERRA-2 ozone data indicate larger deviations from GROMOS-C and MLS due to the used odd-oxygen family model. In the mesosphere, odd oxygen starts to be dominated by atomic oxygen and no longer by ozone and thus can explain why MERRA-2 exhibits less good agreement with the observations, although MLS ozone is assimilated up to 0.02 hPa in the mesosphere. Based on the TEM budget equation, we rationalize the impact of SSW and FSW events on ozone anomalies by calculating dynamical and chemical terms in Eq. (2) using meteorological variables provided by MERRA-2 reanalysis data.

1. The enhanced transport of ozone into the polar cap on the seasonal scale is attributed to the increased occurrence of SSW events during midwinter in the Northern Hemisphere. However, more ozone chemical loss in springtime than the climatology of the seasonal mean is attributed to more early FSW events (Matthias et al., 2021).

2. The impact of SSW and FSW events on total ozone tendency is shown by the altitude tendencies from the lower to middle stratosphere (from the middle to upper stratosphere and to the lower mesosphere) that change from positive to negative (from negative to positive) close to onset.

3. Positive ozone anomalies larger than 1 ppmv close to SSW onset in the lower and middle stratosphere are attributed to the dynamical processes of the horizontal eddy effect and vertical advection transport, while this response pattern for FSW events is associated with the combined effects of dynamical and chemical terms

reflected by the photochemical effect counteracted partially by positive horizontal eddy transport, in particular in the middle stratosphere.

4. Substantial differences in the chemical fields in the upper stratosphere displaying negative $\overline{S}$ and positive CHM after SSW onset within 30 d are attributed to greater uncertainties in TEM diagnostics, particularly when calculating eddy effects and mean advection transports.

Our results establish a new perspective on the driving mechanisms behind pronounced polar ozone anomalies associated with dynamical and chemical processes in the stratosphere during SSW and FSW events. Although previous studies have shown composite spatial and temporal ozone responses to SSW events in the Arctic (de la Cámara et al., 2018a, b; Hong and Reichler, 2021; Bahramvash Shams et al., 2022; Harzer et al., 2023), we took a more comprehensive approach and higher altitudes up to the lower mesosphere to study the polar ozone anomalies, and we considered not only major SSW events but also early FSW events. The polar ozone response pattern reflects the underlying ozone transport anomalies when viewed over the polar latitude station with a vertically resolved response structure. The ozone response signature during SSW and FSW events in the stratosphere and lower mesosphere can be explained by consecutive counteracting anomalous tendencies associated with eddy-mixing effects and advection transports on daily timescales, as well as chemical production and loss. In particular, these studies showed that weaker midwinter planetary wave forcing in the stratosphere due to weaker upward wave propagation leads to lower spring Arctic temperatures and thus to more ozone destruction in spring. In particular, our results suggest that anomalous ozone tendencies during FSW events in the middle stratosphere can be attributed to the dynamical field counteracted partially by chemical loss. Furthermore, the type of SSW is characterized by anomalous evolution of ozone tendencies in winter, leading to distinct chemistry patterns and variations in the intensity and duration of anomalous transport and mixing properties in the upper stratosphere. In contrast, chemistry contributions during years with FSW events in spring are relatively less pronounced in the upper stratosphere, representing a predominantly smooth transition according to the climatology.

Finally, referring back to a novel aspect of this study involving the relative contributions of dynamical and chemical effects to the anomalous ozone tendency, we found that a significant discrepancy in chemical effects between $\overline{S}$ utilizing TEM diagnostics and CHM from chemistry transport models is observed during SSW events, which is not replicated in FSW events, as shown in Fig. 9e, h. This finding contributes to a growing body of evidence suggesting that the difference is associated with substantial uncertainties in the calculated dynamical terms derived from the MERRA-2 reanalysis for SSW events. However, it is unclear whether the remaining differences only result from the quality of the reanalysis data and substantial anthropogenic ozone-depleting substances in recent decades, indicating that ozone chemistry has become increasingly important in governing climate variability. There have been several studies showing that polar vortex dynamics are key to understanding polar ozone VMRs (Sun et al., 2014; Banerjee et al., 2020; Schranz et al., 2020; Shi et al., 2023). Due to the ban on chlorofluorocarbons (CFCs) that the Montreal Protocol ozone depletion policy was supposed to enforce, a trend reversal in the circulation is expected. Recent studies show such a trend reversal; however, it has not yet been confirmed whether the ozone recovery or the increased carbon dioxide is the cause of the changes in dynamics. Monitoring ozone in the stratosphere and lower mesosphere therefore remains a high priority and is supported by the Global Atmospheric Watch (GAW) program. In addition, we found that the ozone tendency in the lower stratosphere is primarily due to the horizontal eddy effect and vertical advection transport. Thus, we consider the observed variability in zonally averaged TCO in the polar regions for SSW and FSW events from MERRA-2. Dynamical processes in the lower stratosphere dominate TCO variability.

In general, the findings of this study contribute to a more comprehensive interpretation of the observed ozone variability at polar stations, with particular emphasis on the ozone anomaly situation. While existing research has predominantly concentrated on dynamic effects on Arctic ozone (de la Cámara et al., 2018b; Bahramvash Shams et al., 2022; Harzer et al., 2023), our study emphasizes the combined contribution of dynamical and chemical effects to polar ozone anomalies. This is especially evident because the anomalies of polar TCO during SSW and FSW events can be attributed to wave-driven anomalous dynamics. Therefore, understanding the interplay between dynamical and chemical processes during stratospheric extreme events will enhance our comprehension of the connections between middle- and upper-stratospheric dynamics and ozone chemistry. This knowledge is crucial for interpreting the observed vertically resolved pattern of daily variability and better quantifying polar ozone evolution.

Appendix A

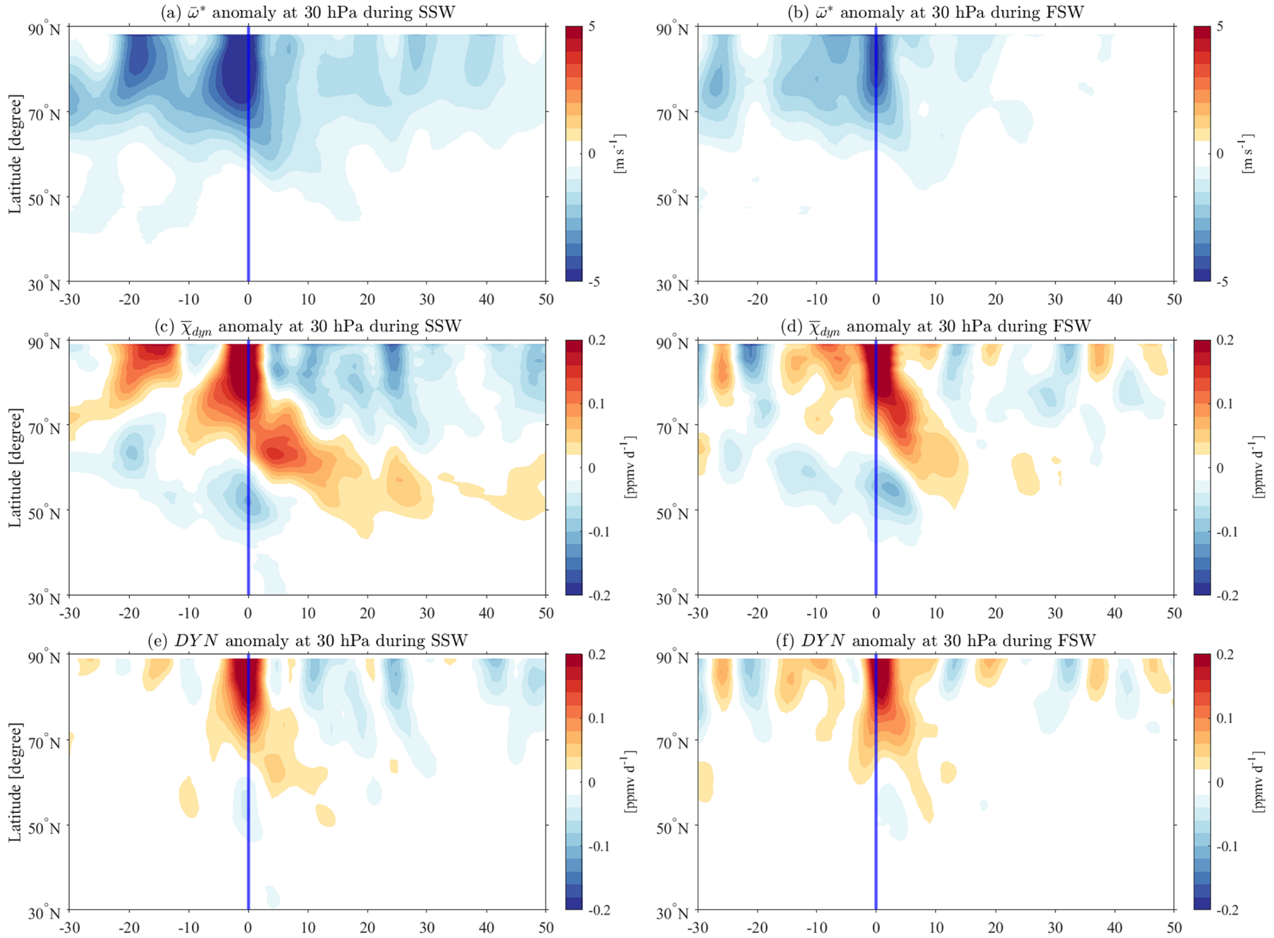
(a) $\bar{\omega}^*$ anomaly at 30 hPa during SSW

(b) $\bar{\omega}^*$ anomaly at 30 hPa during FSW

(c) $\overline{\chi}_{dyn}$ anomaly at 30 hPa during SSW

(d) $\overline{\chi}_{dyn}$ anomaly at 30 hPa during FSW

(e) DYN anomaly at 30 hPa during SSW

(f) DYN anomaly at 30 hPa during FSW

Figure A1. Evolution of the $\overline{\omega}^*$ anomalies dO_3/dt (m s^{-1}) and $\overline{\chi}_{dyn}$ as well as the DYN anomalies at 30 hPa (ppmv d^{-1}) for the composite of SSW **(a, c, e)** and FSW **(b, d, f)** events as a function of time and latitude in the Northern Hemisphere.

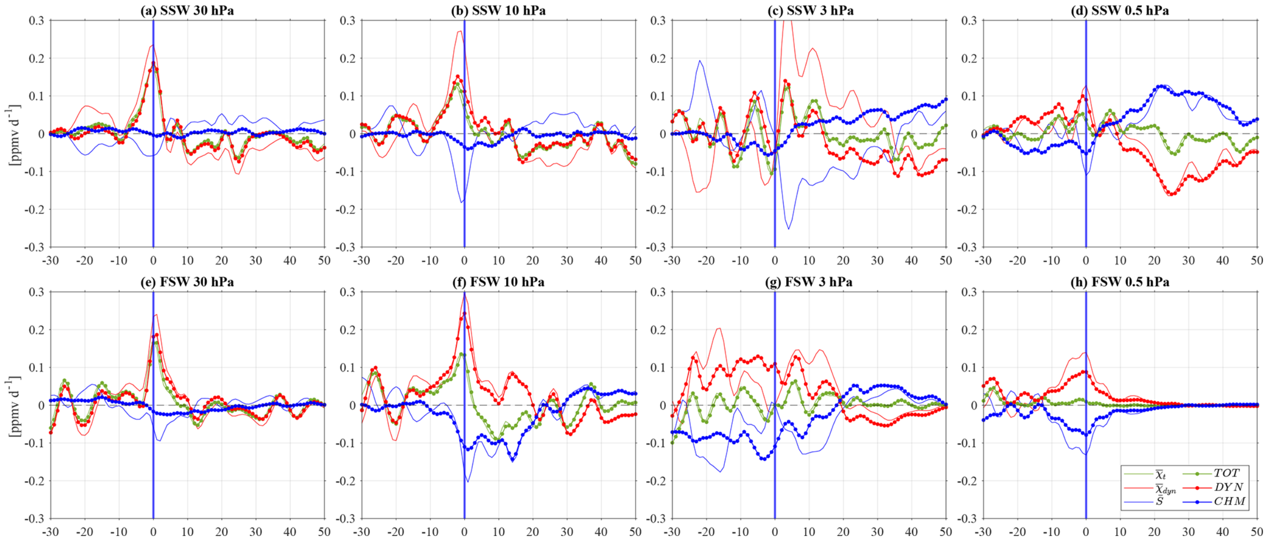

Figure A2. Comparison of the composite evolution of the anomalies of the ozone tendency, dynamical term, and chemical term between Eq. (1) and Eq. (2) at 30, 10, 3, and 0.5 hPa, averaged over 70–90° N for MERRA-2 **(a, b, c, d)** for SSW events and **(e, f, g, h)** for FSW events.

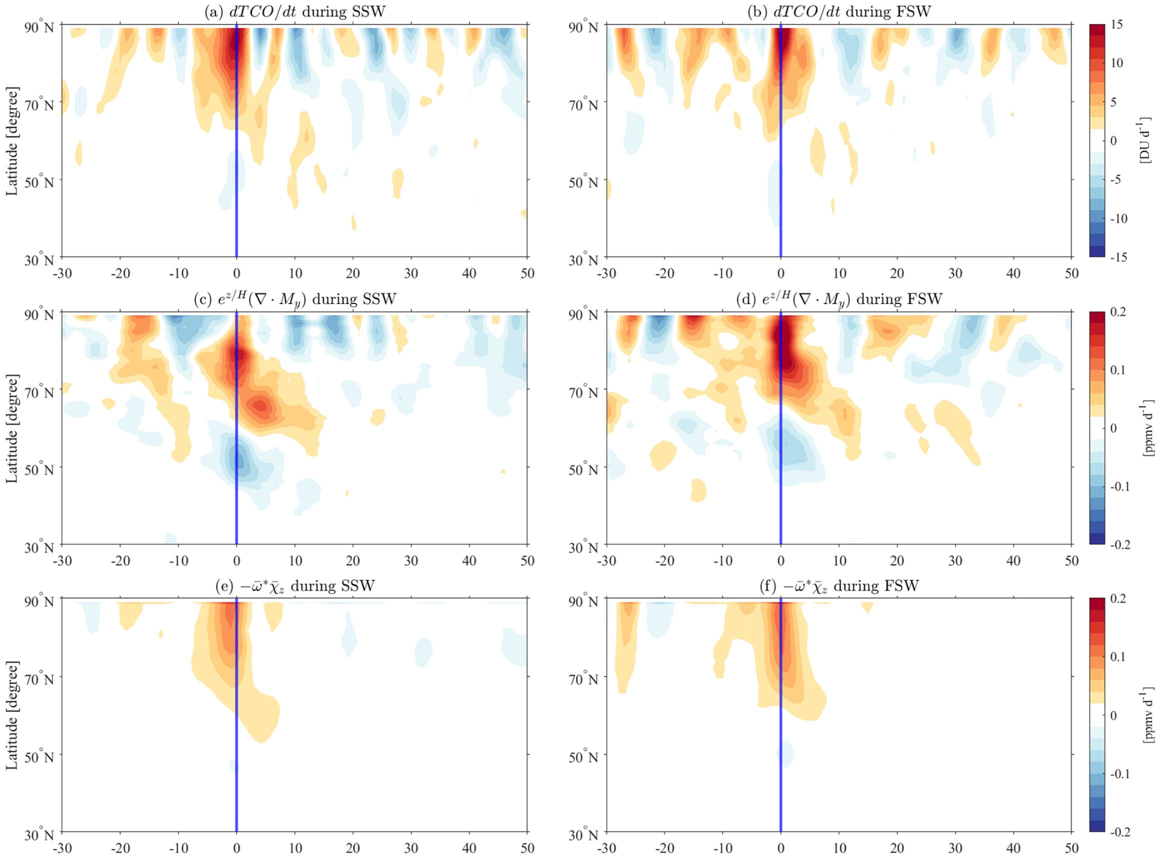

Figure A3. Same as in Fig. 10 but for the pressure level at 20 hPa.

Data availability. The GROMOS-C level-2 data are provided by the Network for the Detection of Atmospheric Composition Change (NDACC) and are available at the NDACC data repository https://www-air.larc.nasa.gov/pub/NDACC/PUBLIC/meta/mwave/ (University of Bern, 2024). The MLS v5 data are available from the NASA Goddard Space Flight Center Earth Sciences Data and Information Services Center (GES DISC) at https://doi.org/10.5067/Aura/MLS/DATA2516 (Schwartz et al., 2020). The MERRA-2 data are provided by NASA at the Modeling and Assimilation Data and Information Services Center (MDISC) and are available at the model level (Global Modeling and Assimilation Office, 2015b) at https://doi.org/10.5067/WWQSXQ8IVFW8, at the pressure level (Global Modeling and Assimilation Office, 2015a) at https://doi.org/10.5067/QBZ6MG944HW0, and for ozone tendency (Global Modeling and Assimilation Office, 2015c) at https://doi.org/10.5067/S0LYTK57786Z.

Author contributions. GSh was responsible for the ground-based ozone measurements with GROMOS-C, performed the data analysis, and prepared the manuscript. ES provided the Aura MLS data. WK helped with the data analysis. GSt designed the concept of the study and contributed to the interpretation of the results. All of the authors discussed the scientific findings and provided valuable feedback for manuscript editing.

Competing interests. The contact author has declared that none of the authors has any competing interests.

Acknowledgements. Guochun Shi, Gunter Stober, and Witali Krochin are members of the Oeschger Center for Climate Change Research. The authors acknowledge NASA's GMAO for providing the MERRA-2 reanalysis data and the Aura MLS team for providing the satellite data. Finally, we thank the two reviewers and the editors for the very helpful comments and suggestions.

Financial support. This research has been supported by the Swiss National Science Foundation (grant no. 200021-200517/1).

Review statement. This paper was edited by Jianzhong Ma and reviewed by three anonymous referees.

References

Albers, J. R. and Birner, T.: Vortex preconditioning due to planetary and gravity waves prior to sudden stratospheric warmings, J. Atmos. Sci., 71, 4028–4054, 2014.

Albers, J. R., Perlwitz, J., Butler, A. H., Birner, T., Kiladis, G. N., Lawrence, Z. D., Manney, G. L., Langford, A. O., and Dias, J.: Mechanisms governing interannual variability of stratosphere-to-troposphere ozone transport, J. Geophys. Res.-Atmos., 123, 234–260, https://doi.org/10.5194/acp-20-12609-2020, 2018.

Andrews, D., Holton, J., and Leovy, C.: Middle Atmosphere Dynamics, International Geophysics, Elsevier Science, ISBN 9780120585762, https://books.google.de/books?id=N1oNurYZefAC (last access: 21 July 2016), 1987.

Bahramvash Shams, S., Walden, V. P., Hannigan, J. W., Randel, W. J., Petropavlovskikh, I. V., Butler, A. H., and de la Cámara, A.: Analyzing ozone variations and uncertainties at high latitudes during sudden stratospheric warming events using MERRA-2, Atmos. Chem. Phys., 22, 5435–5458, https://doi.org/10.5194/acp-22-5435-2022, 2022.

Baldwin, M. P., Ayarzagüena, B., Birner, T., Butchart, N., Butler, A. H., Charlton-Perez, A. J., Domeisen, D. I., Garfinkel, C. I., Garny, H., Gerber, E. P., Hegglin, M. I., Langematz, U., and Pedatella, N. M.: Sudden stratospheric warmings, Rev. Geophys., 59, e2020RG000708, https://doi.org/10.1029/2020RG000708, 2021.

Banerjee, A., Fyfe, J. C., Polvani, L. M., Waugh, D., and Chang, K.-L.: A pause in Southern Hemisphere circulation trends due to the Montreal Protocol, Nature, 579, 544–548, 2020.

Black, R. X. and McDaniel, B. A.: Interannual variability in the Southern Hemisphere circulation organized by stratospheric final warming events, J. Atmos. Sci., 64, 2968–2974, 2007.

Bosilovich, M. G., Akella, S., Coy, L., Cullather, R., Draper, C., Gelaro, R., Kovach, R., Liu, Q., Molod, A., Norris, P., Wargan, K., Chao, W., Reichle, R., Takacs, L., Vikhliaev, Y., Bloom, S., Collow, A., Firth, S., Labows, G., Partyka, G., Pawson, S., Reale, O., Schubert, S. D., and Suarez, M.: MERRA-2: Initial Evaluation of the Climate. Technical Report Series on Global Modeling and Data Assimilation, Tech. Rep. NASA/TM-2015-104606, https://gmao.gsfc.nasa.gov/pubs/docs/Bosilovich785.pdf (last access: 12 July 2016), 2015.

Brasseur, G. and Solomon, S.: Aeronomy of the Middle Atmosphere: Chemistry and Physics of the Stratosphere and Mesosphere, in: Atmospheric and Oceanographic Sciences Library, Springer Netherlands, 2005.

Butler, A. H. and Domeisen, D. I. V.: The wave geometry of final stratospheric warming events, Weather Clim. Dynam., 2, 453–474, https://doi.org/10.5194/wcd-2-453-2021, 2021.

Butler, A. H. and Gerber, E. P.: Optimizing the Definition of a Sudden Stratospheric Warming, J. Climate, 31, 2337–2344, https://doi.org/10.1175/JCLI-D-17-0648.1, 2018.

Butler, A. H., Seidel, D. J., Hardiman, S. C., Butchart, N., Birner, T., and Match, A.: Defining Sudden Stratospheric Warmings, B. Am. Meteorol. Soc., 96, 1913–1928, https://doi.org/10.1175/BAMS-D-13-00173.1, 2015.

Byrne, N. J., Shepherd, T. G., Woollings, T., and Plumb, R. A.: Nonstationarity in Southern Hemisphere climate variability associated with the seasonal breakdown of the stratospheric polar vortex, J. Climate, 30, 7125–7139, 2017.

Charlton, A. J. and Polvani, L. M.: A New Look at Stratospheric Sudden Warmings. Part I: Climatology and Modeling Benchmarks, J. Climate, 20, 449–469, https://doi.org/10.1175/JCLI3996.1, 2007.

de la Cámara, A., Abalos, M., and Hitchcock, P.: Changes in stratospheric transport and mixing during sudden stratospheric warmings, J. Geophys. Res.-Atmos., 123, 3356–3373, 2018a.

de la Cámara, A., Abalos, M., Hitchcock, P., Calvo, N., and Garcia, R. R.: Response of Arctic ozone to sudden stratospheric warmings, Atmos. Chem. Phys., 18, 16499–16513, https://doi.org/10.5194/acp-18-16499-2018, 2018b.

Eriksson, P., Jiménez, C., and Buehler, S. A.: Qpack, a general tool for instrument simulation and retrieval work, J. Quant. Spectrosc. Ra., 91, 47–64, https://doi.org/10.1016/j.jqsrt.2004.05.050, 2005.

Eriksson, P., Buehler, S., Davis, C., Emde, C., and Lemke, O.: ARTS, the atmospheric radiative transfer simulator, version 2, J. Quant. Spectrosc. Ra., 112, 1551–1558, https://doi.org/10.1016/j.jqsrt.2011.03.001, 2011.

Fernandez, S., Murk, A., and Kämpfer, N.: GROMOS-C, a novel ground-based microwave radiometer for ozone measurement campaigns, Atmos. Meas. Tech., 8, 2649–2662, https://doi.org/10.5194/amt-8-2649-2015, 2015.

Friedel, M., Chiodo, G., Stenke, A., Domeisen, D. I. V., and Peter, T.: Effects of Arctic ozone on the stratospheric spring onset and its surface impact, Atmos. Chem. Phys., 22, 13997–14017, https://doi.org/10.5194/acp-22-13997-2022, 2022.

Gelaro, R., McCarty, W., Suárez, M. J., Todling, R., Molod, A., Takacs, L., Randles, C. A., Darmenov, A., Bosilovich, M. G., Reichle, R., Wargan, K., Coy, L., Cullather, R., Draper, C., Akella, S., Buchard, V., Conaty, A., da Silva, A. M., Gu, W., Kim, G.-K., Koster, R., Lucchesi, R., Merkova, D., Nielsen, J. E., Partyka, G., Pawson, S., Putman, W., Rienecker, M., Schubert, S. D., Sienkiewicz, M., and Zhao, B.: The modern-era retrospective analysis for research and applications, version 2 (MERRA-2), J. Climate, 30, 5419–5454, 2017.

Global Modeling and Assimilation Office (GMAO): MERRA-2 inst3_3d_asm_Np: 3d,3-Hourly,Instantaneous,Pressure-Level,Assimilation,Assimilated Meteorological Fields V5.12.4, Goddard Earth Sciences Data and Information Services Center (GES DISC) [data set], Greenbelt, MD, USA, https://doi.org/10.5067/QBZ6MG944HW0, 2015a.

Global Modeling and Assimilation Office (GMAO): MERRA-2 inst3_3d_asm_Nv: 3d,3-Hourly,Instantaneous,Model-Level,Assimilation,Assimilated Meteorological Fields V5.12.4, Goddard Earth Sciences Data and Information Services Center (GES DISC) [data set], Greenbelt, MD, USA, https://doi.org/10.5067/WWQSXQ8IVFW8, 2015b.

Global Modeling and Assimilation Office (GMAO): MERRA-2 tavg3_3d_odt_Np: 3d,3-Hourly,Time-Averaged,Pressure-Level,Assimilation,Ozone Tendencies V5.12.4, Goddard Earth Sciences Data and Information Services Center (GES DISC) [data set], Greenbelt, MD, USA, https://doi.org/10.5067/S0LYTK57786Z, 2015c.

Hardiman, S. C., Butchart, N., Charlton-Perez, A. J., Shaw, T. A., Akiyoshi, H., Baumgaertner, A., Bekki, S., Braesicke, P., Chipperfield, M., Dameris, M., Garcia, R. R., Michou, M., Pawson, S., Rozanov, E., and Shibata, K.: Improved predictability of the troposphere using stratospheric final warmings, J. Geophys. Res.-Atmos., 116, D18113, https://doi.org/10.1029/2011JD015914, 2011.

Harzer, F., Garny, H., Ploeger, F., Bönisch, H., Hoor, P., and Birner, T.: On the pattern of interannual polar vortex–ozone co-variability during northern hemispheric winter, Atmos. Chem. Phys., 23, 10661–10675, https://doi.org/10.5194/acp-23-10661-2023, 2023.

Hocke, K., Sauvageat, E., and Bernet, L.: Response of Total Column Ozone at High Latitudes to Sudden Stratospheric Warmings, Atmosphere, 14, 450, https://doi.org/10.3390/atmos14030450, 2023.

Holton, J. R.: The dynamics of sudden stratospheric warmings, Annu. Rev. Earth Pl. Sc., 8, 169–190, 1980.

Hong, H.-J. and Reichler, T.: Local and remote response of ozone to Arctic stratospheric circulation extremes, Atmos. Chem. Phys., 21, 1159–1171, https://doi.org/10.5194/acp-21-1159-2021, 2021.

Hu, J., Ren, R., and Xu, H.: Occurrence of Winter Stratospheric Sudden Warming Events and the Seasonal Timing of Spring Stratospheric Final Warming, J. Atmos. Sci., 71, 2319–2334, https://doi.org/10.1175/JAS-D-13-0349.1, 2014.

Knowland, K. E., Keller, C. A., Wales, P. A., Wargan, K., Coy, L., Johnson, M. S., Liu, J., Lucchesi, R. A., Eastham, S. D., Fleming, E., Liang, Q., Leblanc, T., Livesey, N. J., Walker, K. A., Ott, L. E., and Pawson, S.: NASA GEOS Composition Forecast Modeling System GEOS-CF v1. 0: Stratospheric Composition, J. Adv. Model. Earth Sy., 14, e2021MS002852, https://doi.org/10.1029/2021MS002852, 2022.

Lawrence, Z. D., Perlwitz, J., Butler, A. H., Manney, G. L., Newman, P. A., Lee, S. H., and Nash, E. R.: The remarkably strong Arctic stratospheric polar vortex of winter 2020: Links to record-breaking Arctic oscillation and ozone loss, J. Geophys. Res.-Atmos., 125, e2020JD033271, https://doi.org/10.1029/2020JD033271, 2020.

Li, Y., Kirchengast, G., Schwaerz, M., and Yuan, Y.: Monitoring sudden stratospheric warmings under climate change since 1980 based on reanalysis data verified by radio occultation, Atmos. Chem. Phys., 23, 1259–1284, https://doi.org/10.5194/acp-23-1259-2023, 2023.

Livesey, N. J., Read, W. G., Froidevaux, L., Lambert, A., Manney, G. L., Pumphrey, H. C., Santee, M. L., Schwartz, M. J., Wang, S., Cofield, R. E., Cuddy, D. T., Fuller, R. A., Jarnot, R. F., Jiang, J. H., Knosp, B. W., Stek, P. C., Wagner, P. A., and Wu, D. L.: EOS MLS Version 3.3 Level 2 data quality and description document, Tech. Rep., JPL D-33509, Jet Propulsion Laboratory, Pasadena, CA, https://mls.jpl.nasa.gov/ (last access: 17 December 2023), 2011.

Lubis, S. W., Silverman, V., Matthes, K., Harnik, N., Omrani, N.-E., and Wahl, S.: How does downward planetary wave coupling affect polar stratospheric ozone in the Arctic winter stratosphere?, Atmos. Chem. Phys., 17, 2437–2458, https://doi.org/10.5194/acp-17-2437-2017, 2017.

Manney, G. L., Livesey, N. J., Santee, M. L., Froidevaux, L., Lambert, A., Lawrence, Z. D., Millán, L. F., Neu, J. L., Read, W. G., Schwartz, M. J., and Fuller, R. A.: Record-low Arctic stratospheric ozone in 2020: MLS observations of chemical processes and comparisons with previous extreme winters, Geophys. Res. Lett., 47, e2020GL089063, https://doi.org/10.1029/2020GL089063, 2020.

Matthias, V., Hoffmann, P., Manson, A., Meek, C., Stober, G., Brown, P., and Rapp, M.: The impact of planetary waves on the latitudinal displacement of sudden stratospheric warmings, Ann. Geophys., 31, 1397–1415, https://doi.org/10.5194/angeo-31-1397-2013, 2013.

Matthias, V., Stober, G., Kozlovsky, A., Lester, M., Belova, E., and Kero, J.: Vertical Structure of the Arctic Spring Transition in the Middle Atmosphere, J. Geophys. Res.-Atmos., 126, e2020JD034353, https://doi.org/10.1029/2020JD034353, 2021.

Minganti, D., Chabrillat, S., Christophe, Y., Errera, Q., Abalos, M., Prignon, M., Kinnison, D. E., and Mahieu, E.: Climatological impact of the Brewer–Dobson circulation on the N_2O budget in WACCM, a chemical reanalysis and a CTM driven by four dynamical reanalyses, Atmos. Chem. Phys., 20, 12609–12631, https://doi.org/10.5194/acp-20-12609-2020, 2020.

Oehrlein, J., Chiodo, G., and Polvani, L. M.: The effect of interactive ozone chemistry on weak and strong stratospheric polar vortex events, Atmos. Chem. Phys., 20, 10531–10544, https://doi.org/10.5194/acp-20-10531-2020, 2020.

Pancheva, D., Mukhtarov, P., Mitchell, N., Merzlyakov, E., Smith, A., Andonov, B., Singer, W., Hocking, W., Meek, C., Manson, A., and Murayama, Y.: Planetary waves in coupling the stratosphere and mesosphere during the major stratospheric warming in 2003/2004, J. Geophys. Res.-Atmos., 113, D12105, https://doi.org/10.1029/2007JD009011, 2008.

Plumb, R. A.: Stratospheric transport, J. Meteorol. Soc. Jpn., Ser. II, 80, 793–809, 2002.

Qin, Y., Gu, S.-Y., Dou, X., Teng, C.-K.-M., and Li, H.: On the westward quasi-8-day planetary waves in the middle atmosphere during arctic sudden stratospheric warmings, J. Geophys. Res.-Atmos., 126, e2021JD035071. https://doi.org/10.1029/2021JD035071, 2021.

Randel, W. J., Boville, B. A., Gille, J. C., Bailey, P. L., Massie, S. T., Kumer, J., Mergenthaler, J., and Roche, A.: Simulation of stratospheric N_2O in the NCAR CCM2: Comparison with CLAES data and global budget analyses, J. Atmos. Sci., 51, 2834–2845, 1994.

Rodgers, C. D.: Inverse methods for atmospheric sounding: theory and practice, Vol. 2, World Scientific, ISBN 9789810227401, 2000.

Safieddine, S., Bouillon, M., Paracho, A.-C., Jumelet, J., Tencé, F., Pazmino, A., Goutail, F., Wespes, C., Bekki, S., Boynard, A., Hadji-Lazaro, J., Coheur, P.-F., Hurtmans, D., and Clerbaux, C.: Antarctic ozone enhancement during the 2019 sudden stratospheric warming event, Geophys. Res. Lett., 47, e2020GL087810, https://doi.org/10.1029/2020GL087810, 2020.

Salby, M. L. and Callaghan, P. F.: Influence of planetary wave activity on the stratospheric final warming and spring ozone, J. Geophys. Res.-Atmos., 112, D20111, https://doi.org/10.1029/2006JD007536, 2007.

Schranz, F., Fernandez, S., Kämpfer, N., and Palm, M.: Diurnal variation in middle-atmospheric ozone observed by ground-based microwave radiometry at Ny-Ålesund over 1 year, Atmos. Chem. Phys., 18, 4113–4130, https://doi.org/10.5194/acp-18-4113-2018, 2018.

Schranz, F., Tschanz, B., Rüfenacht, R., Hocke, K., Palm, M., and Kämpfer, N.: Investigation of Arctic middle-atmospheric dynamics using 3 years of H_2O and O_3 measurements from microwave radiometers at Ny-Ålesund, Atmos. Chem. Phys., 19, 9927–9947, https://doi.org/10.5194/acp-19-9927-2019, 2019.

Schranz, F., Hagen, J., Stober, G., Hocke, K., Murk, A., and Kämpfer, N.: Small-scale variability of stratospheric ozone during the sudden stratospheric warming 2018/2019 observed at Ny-Ålesund, Svalbard, Atmos. Chem. Phys., 20, 10791–10806, https://doi.org/10.5194/acp-20-10791-2020, 2020.

Schwartz, M., Froidevaux, L., Livesey, N., and Read, W.: MLS/Aura Level 2 Ozone (O3) Mixing Ratio V004, Goddard Earth Sciences Data and Information Services Center (GES DISC) [data set], Greenbelt, MD, USA, https://doi.org/10.5067/Aura/MLS/DATA2017, 2015.

Schwartz, M., Froidevaux, L., Livesey, N., and Read, W.: MLS/Aura Level 2 Ozone (O3) Mixing Ratio V005, Goddard Earth Sciences Data and Information Services Center (GES DISC) [data set], Greenbelt, MD, USA, https://doi.org/10.5067/Aura/MLS/DATA2516, 2020.

Shaw, T. A. and Perlwitz, J.: On the control of the residual circulation and stratospheric temperatures in the Arctic by planetary wave coupling, J. Atmos. Sci., 71, 195–206, 2014.

Shi, G., Krochin, W., Sauvageat, E., and Stober, G.: Ozone and water vapor variability in the polar middle atmosphere observed with ground-based microwave radiometers, Atmos. Chem. Phys., 23, 9137–9159, https://doi.org/10.5194/acp-23-9137-2023, 2023.

Smith-Johnsen, C., Orsolini, Y., Stordal, F., Limpasuvan, V., and Pérot, K.: Nighttime mesospheric ozone enhancements during the 2002 southern hemispheric major stratospheric warming, J. Atmos. Sol.-Terr. Phy., 168, 100–108, 2018.

Stober, G., Baumgarten, K., McCormack, J. P., Brown, P., and Czarnecki, J.: Comparative study between ground-based observations and NAVGEM-HA analysis data in the mesosphere and lower thermosphere region, Atmos. Chem. Phys., 20, 11979–12010, https://doi.org/10.5194/acp-20-11979-2020, 2020.

Sun, L., Robinson, W. A., and Chen, G.: The role of planetary waves in the downward influence of stratospheric final warming events, J. Atmos. Sci., 68, 2826–2843, 2011.

Sun, L., Chen, G., and Robinson, W. A.: The role of stratospheric polar vortex breakdown in Southern Hemisphere climate trends, J. Atmos. Sci., 71, 2335–2353, 2014.

Thiéblemont, R., Ayarzagüena, B., Matthes, K., Bekki, S., Abalichin, J., and Langematz, U.: Drivers and surface signal of interannual variability of boreal stratospheric final warmings, J. Geophys. Res.-Atmos., 124, 5400–5417, https://doi.org/10.1029/2018JD029852, 2019.

Tweedy, O. V., Limpasuvan, V., Orsolini, Y. J., Smith, A. K., Garcia, R. R., Kinnison, D., Randall, C. E., Kvissel, O.-K., Stordal, F., Harvey, V. L., and Chandran, A.: Nighttime secondary ozone layer during major stratospheric sudden warmings in specified-dynamics WACCM, J. Geophys. Res.-Atmos., 118, 8346–8358, https://doi.org/10.1002/jgrd.50651, 2013.

University of Bern: https://www-air.larc.nasa.gov/pub/NDACC/PUBLIC/meta/mwave/, last access: 5 September 2024.

Wargan, K., Labow, G., Frith, S., Pawson, S., Livesey, N., and Partyka, G.: Evaluation of the ozone fields in NASA's MERRA-2 reanalysis, J. Climate, 30, 2961–2988, https://doi.org/10.1175/JCLI-D-16-0699.1, 2017.

Wargan, K., Orbe, C., Pawson, S., Ziemke, J. R., Oman, L. D., Olsen, M. A., Coy, L., and Emma Knowland, K.: Recent decline in extratropical lower stratospheric ozone attributed to circulation changes, Geophys. Res. Lett., 45, 5166–5176, https://doi.org/10.1029/2018GL077406, 2018.

Waters, J. W., Froidevaux, L., Harwood, R. S., Jarnot, R. F., Pickett, H. M., Read, W. G., Siegel, P. H., Cofield, R. E., Filipiak, M. J., Flower, D. A., Holden, J. R., Lau, G. K., Livesey, N. J., Manney, G. L., Pumphrey, H. C., Santee, M. L., Wu, D. L., Cuddy, D. T., Lay, R. R., Loo, M. S., Perun, V. S., Schwartz, M. J., Stek, P. C., Thurstans, R. P., Boyles, M. A., Chandra, K. M., Chavez, M. C., Chen, G.-S., Chudasama, B. V., Dodge, R., Fuller, R. A., Girard, M. A., Jiang, J., Jiang, Y., Knosp, B. W., LaBelle, R. C., Lam, J. C., Lee, K., Miller, D., Oswald, J. E., Patel, N. C., Pukala, D. M., Quintero, O., Scaff, D. M., Snyder, W. V., Tope, M. C., Wagner, P. A., and Walch, M. J.: The Earth observing system microwave limb sounder (EOS MLS) on the aura Satellite, IEEE T. Geosci. Remote, 44, 1075–1092, 2006.

6 Radiative effect of ozone and water vapor on mesospheric tides

6.1 Introduction

The anomalies in ozone and water vapor VMR observed during SSW events have been examined to assess their contribution to the atmospheric response, including changes in radiative forcing and dynamical transport in the stratosphere and mesosphere. Moreover, the SSW events also influence the MLT region, including modifications in the propagation and amplitude of atmospheric tides. Therefore, the potential mechanisms linking these tidal variations to changes in radiative forcing and trace gas distributions remain an area of active investigation.

In the following publication, we examine the variability of diurnal, semidiurnal, and terdiurnal tidal amplitudes during and after SSW events in the Arctic MLT region using meteor radar observations from three high-latitude stations Sodankylä (67.37°N, 26.63°E), Tromsø (69.58°N, 19.22°E), and Svalbard (78.99°N, 15.99°E) as well as one station outside the polar vortex located at Collm (51.3°N, 13°E). By integrating ground-based tidal amplitude observations with concurrent variations in ozone and water vapor, we explore how planetary wave activity and associated dynamical changes modulate tidal behavior at polar latitudes. To further understand the radiative contributions of trace gases to tidal variability, we employ simulations from the WACCM-X(SD), focusing on shortwave heating and longwave cooling rates. These observed tidal patterns correlate with ozone-induced radiative changes, suggesting a secondary role of ozone to the tidal amplitudes. In contrast, while water vapor serves as an effective dynamical tracer, its limited radiative influence results in a minimal direct impact on mesospheric tides.

6.2 Publication

The following article has been accepted by *Atmospheric Chemistry and Physics (ACP).*

Citation: Shi, Guochun, Hanli Liu, Masaki Tsutsumi, Njål Gulbrandsen, Alexander Kozlovsky, Dimitry Pokhotelov, Mark Lester, Kun Wu, and Gunter Stober. “New insights into the polar ozone and water vapor, radiative effects, and their connection to the tides in the mesosphere-lower thermosphere during major Sudden Stratospheric Warming events”. In: *EGUsphere* 2024 (2024), pp. 1–33, **Accepted**

DOI: https://egusphere.copernicus.org/preprints/2024/egusphere-2024-3749/

New insights into the polar ozone and water vapor, radiative effects, and their connection to the tides in the mesosphere-lower thermosphere during major Sudden Stratospheric Warming events

Guochun Shi[1,2], Hanli Liu[3], Masaki Tsutsumi[4,5], Njål Gulbrandsen[6], Alexander Kozlovsky[7], Dimitry Pokhotelov[8], Mark Lester[9], Christoph Jacobi[10], Kun Wu[3,*], and Gunter Stober[1,2]

[1]Oeschger Center for Climate Change Research, University of Bern, Bern, Switzerland
[2]Institute of Applied Physics, University of Bern, Bern, Switzerland
[3]High Altitude Observatory, National Center for Atmospheric Research, Boulder, CO, USA
[4]National Institute of Polar Research, Tachikawa, Japan
[5]The Graduate University for Advanced Studies (SOKENDAI), Tokyo, Japan
[6]Tromsø Geophysical Observatory UiT - The Arctic University of Norway, Tromsø, Norway
[7]Sodankylä Geophysical Observatory, University of Oulu, Finland
[8]Potsdam Institute for Climate Impact Research, Member of the Leibniz Association, Potsdam, Germany
[9]Department of Physics and Astronomy, University of Leicester, Leicester, UK
[10]Institute for Meteorology, Leipzig University, Leipzig, Germany
[*]Now: School of Physics and Electronic Sciences, Changsha University of Science and Technology, Changsha, China

Correspondence: Guochun Shi (guochun.shi@unibe.ch)

Abstract. We examine the variability of diurnal (DT), semidiurnal (SDT), and terdiurnal (TDT) tide amplitudes in the Arctic mesosphere and lower thermosphere (MLT) during and after sudden stratospheric warming (SSW) events using meteor radar data at three polar-latitude stations: Sodankylä (67.37°N, 26.63°E), Tromsø (69.58°N, 19.22°E), and Svalbard (78.99°N, 15.99°E) as well as one station outside the polar vortex located at Collm (51.3°N, 13°E). By combining tidal amplitude anomalies with trace gas variations, induced by large-scale dynamical changes caused by the breaking of planetary waves, this study provides new observational insights into the variation of ozone and water vapor, transport, and tides at polar latitudes. We use short-wave (QRS) and long-wave (QRL) radiative heating and cooling rates simulated by the WACCM-X(SD) model to investigate the roles of polar ozone and water vapor in driving mesospheric tidal variability during SSWs in the polar regions. Our analysis reveals distinct tidal responses during SSW events. At the onset of SSWs, a significant negative anomaly in TDT amplitudes in zonal and meridional components is observed, with a decrease of 3 m/s, approximately 25% change compared to the mean TDT amplitude. Meanwhile, SDT shows a positive anomaly of 10 m/s, with changes reaching up to 40% ,indicating an enhancement of tidal amplitude in both components. The DT amplitude exhibits a delayed enhancement, with a positive amplitude anomaly of up to 5 m/s in the meridional wind component, occurring approximately 20 days after the onset of SSWs. A similar, but weaker effect is observed in the zonal wind component, with changes reaching up to 30% in the zonal component and 50% in the meridional wind component. We analyzed the contributions of ozone and water vapor to the short-wave heating and long-wave cooling before, during, and after the onset of SSW events. Our findings suggest that the immediate responses of SDT are most likely driven by dynamical effects accompanied by the radiative effects from ozone. Radiative forcing change during SSW likely plays a secondary role in DT tidal changes, but appears to be important 20 days after the event, particularly during the spring transition. Water vapor acts as a dynamical tracer in the stratosphere and mesosphere but has minimal radiative forcing, resulting in a negligible impact on tidal changes. This study presents the first comprehensive analysis of mesospheric tidal variability in polar regions during sudden stratospheric warmings (SSWs), examining and linking the significant role of trace gases and radiative effects in modulating tidal dynamics.

1 Introduction

Major SSW events are dramatic disruptions of the winter polar stratosphere, characterized by rapid temperature increases and the reversal of the typical westerly winds. These events occur due to the interaction between planetary waves propagating from the troposphere into the stratosphere and the stratospheric mean circulation (Matsuno, 1971; Andrews et al., 1987). This interaction leads to the weakening or splitting of the winter stratospheric polar vortex (Haynes et al., 1991; Matthias et al., 2013), resulting in a circulation reversal, increased downwelling in the polar stratosphere, and a subsequent rise in temperature due to adiabatic heating. SSWs have broad impacts, influencing surface temperature (Davis et al., 2022; Hall et al., 2021), weather patterns in the troposphere (Baldwin et al., 2021; Domeisen et al., 2020), large-scale circulation (Iida et al., 2014), stratospheric transport and composition (de la Cámara et al., 2018; Schranz et al., 2020; Shi et al., 2024), and altering the behavior of atmospheric tides in the MLT regions (Becker, 2017; Zhang et al., 2021; Liu et al., 2022) and up to the ionosphere (Fang et al., 2012; Pedatella and Liu, 2013; Jones Jr. et al., 2020; Günzkofer et al., 2022).

Several observational and numerical studies have established that the occurrence of SSW events influences the tidal variabilities in the MLT across equatorial latitudes (Sridharan et al., 2009; Lima et al., 2012; Jin et al., 2012; Sathishkumar and Sridharan, 2013; Siddiqui et al., 2018; Liu et al., 2021), as well as middle and polar latitudes (Jacobi et al., 1999; Bhattacharya et al., 2004; Hoffmann et al., 2007; Pedatella et al., 2014; Chau et al., 2015; Stober et al., 2020; Liu et al., 2021; Eswaraiah et al., 2018; Hibbins et al., 2019; Zhang et al., 2021; Dempsey et al., 2021; Liu et al., 2022; van Caspel et al., 2023; Dutta et al., 2024). For instance, van Caspel et al. (2023) used a mechanistic tidal model to investigate the response of SDT to the 2013 SSW event and compared their findings with Meteor Radar (MR) wind observations at three stations: CMOR (43.3°N, 80.8°W), Collm (51.3°N, 13.0°E), and Kiruna (67.5°N, 20.1°E). Hibbins et al. (2019) observed an enhancement in the mid-latitude migrating SDT in the MLT regions around 10–17 days after the SSW onset using meteor wind data from the Super Dual Auroral Radar Network (SuperDARN) in the Northern Hemisphere. Dutta et al. (2024) reported an increase in solar SDT amplitude in the polar MLT regions during the boreal SSW event of 2013 and the austral SSW event of 2019. Additionally, Sathishkumar and Sridharan (2013) found a significant enhancement of DT amplitude in the zonal wind and the strength of the equatorial electrojet just before the onset of SSW, with the solar SDT dominating over the DT during the SSW.

Previous studies have suggested that the primary mechanisms driving SDT variability in the MLT during SSW include the modification of tidal amplitudes via propagation of tidal waves (Jin et al., 2012; Eswaraiah et al., 2018; He and Chau, 2019; van Caspel et al., 2023), and the nonlinear interaction between tides and planetary waves (Liu et al., 2010b; Pedatella and Forbes, 2010; Lima et al., 2012; He et al., 2020, 2024). For instance, Lima et al. (2012) demonstrated that the intensified tides and quasi-two-day wave amplitudes at low-latitude observed during a major SSW event are associated with strengthened planetary wave activity in the stratospheric winter of the Northern Hemisphere. Given that the absorption of solar ultraviolet radiation (UV) by stratospheric ozone is the primary source of SDT (Forbes and Garrett, 1978; Lindzen and Chapman, 1969), and that SSWs affect the distribution of stratospheric and mesospheric ozone, changes in ozone density could potentially influence the enhancement of SDT during SSW (Goncharenko et al., 2012; Pedatella et al., 2014; Limpasuvan et al., 2016; Eswaraiah et al., 2018; Stober et al., 2020; van Caspel et al., 2023). Goncharenko et al. (2012) reported that the prolonged increase in tropical ozone density around peak ozone heating rates generated a migrating semidiurnal tide, while circulation changes amplified longitudinal inhomogeneities in ozone distribution, potentially leading to the generation of non-migrating tides. Limpasuvan et al. (2016) suggested that the migrating SDT is globally amplified during the 20–30 day interval following SSW onset, likely due to enhanced stratospheric ozone in the tropics and associated solar heating linked to equatorial upwelling and cooling caused by the SSW. Eswaraiah et al. (2018) studied ozone transport over Antarctica and explored the nonlinear interaction between planetary waves and tides to understand tidal enhancement observed 3 to 4 weeks after the central day of SSWs. Moreover, Siddiqui et al. (2019) utilized WACCM simulations to investigate tidal amplitudes during the 2009 SSW event, highlighting the crucial role of stratospheric ozone variability in modulating semidiurnal solar tidal changes. While the nonlinear interaction between tides and planetary waves is considered a primary cause of SDT enhancement in the MLT region, the impact of stratospheric ozone and water vapor on tidal changes during SSW events has been studied more extensively in tropical regions than in polar regions (Sridharan et al., 2012; Goncharenko et al., 2012; Pedatella and Liu, 2013; Siddiqui et al., 2019). Motivated by the observed links between trace gas variations in tropical regions during SSWs and changes in wave-tidal amplitudes in the MLT, this study aims to explore how trace gases, specifically ozone and water vapor, change in polar regions and their potential influence on tidal amplitudes during SSW events.

This study examines the causes of mesospheric tidal variability in the polar regions during SSWs, specifically focusing on the role of radiative effects from ozone and water vapor. We use long-term MLT wind measurements from MRs at northern polar-latitude stations: Sodankylä (67.37°N, 26.63°E), Tromsø (69.58°N, 19.22°E), and Svalbard (78.99°N, 15.99°E) to analyze the variability of DT, SDT, and TDT in the zonal and meridional wind components compositing 10 major SSW events from 2004 to 2023 and the Collm (51.3°N, 13°E) MR outside the polar vortex as a reference (see in Appendix B). We utilize the short-wave (QRS) heating and long-wave (QRL) cooling rates simulated by the Specified Dynamics (SD) Whole Atmosphere Community Climate Model with thermosphere and ionosphere extension (WACCM-X) to investigate heating and cooling rates associated with ozone and water vapor responses to SSW concerning tidal variations in the MLT region. In the first step, we compare water vapor and ozone anomalies from WACCM-X(SD) with observations to ensure consistency with the observational data before analyzing their role in tidal variability. This study presents a quantification of total radiative forcing changes during SSW events and their close correspondence with ozone and water vapor changes observed at polar latitudes. Previous studies already compared WACCM-X(SD) tides and mean MR winds together with other general circulation models (GCMs) (Stober et al., 2021b). The combined analysis of tidal amplitude anomalies and trace gas variations in the polar regions provides new insights into the factors influencing tidal dynamics during SSWs.

2 Data and Methodology

2.1 Meteor radar data and analysis

Meteor radar observations collected at three stations in high latitudes are located at Svalbard (78.99°N, 15.99°E, from March 2001 to present), Tromsø (69.58°N, 19.22°E, from November 2003 to present), and Sodankylä (67.37°N, 26.63°E, from December 2008 to present) in the Arctic, and Collm (51.3°N, 13°E, from August 2004 to present) in the mid-latitude regions. All systems were almost continuously in operation for measuring zonal and meridional winds in the MLT region with a temporal resolution of 1 h and vertical resolution of 2 km, which uses the same wind retrieval algorithm (Stober et al., 2021a, b). The wind retrieval algorithm is a further development of the wind analysis introduced by Hocking et al. (2001) and Holdsworth et al. (2004). The total tidal amplitude and phases are estimated using the adaptive spectral filter (ASF2D) (Baumgarten and Stober, 2019; Stober et al., 2020; Krochin et al., 2024). The total tides, usually dominated by migrating (DW1, SW2, TW3) tidal components, are obtained using the following function:

$$T(t,z),u(t,z),v(t,z) = T_0(z),u_0(z),v_0(z) + \sum_{n=1}^{3}\left[A_n(z)\sin\left(\frac{2\pi}{P_n}t\right) + B_n(z)\cos\left(\frac{2\pi}{P_n}t\right)\right], \quad (1)$$

where T, u, and v are the temperature, zonal, and meridional winds, respectively. P_n is 8, 12 and 24 h, corresponding to terdiurnal tides (TDT), semidiurnal tides (SDT) and diurnal tides (DT), respectively. A_n and B_n denote the Fourier coefficients for the tidal amplitudes at a given altitude. These coefficients are regularized, assuming certain smoothness of the tidal phase with altitude. The zonal mean zonal and meridional wind and the zonal mean temperature are given by T_0, u_0, and v_0, respectively. The retrieval function also includes longer period waves such as the quasi-two-day wave (QTDW) and stationary planetary waves (Baumgarten and Stober, 2019; Schranz et al., 2020).

2.2 GROMOS-C

GROMOS-C (GRound-based Ozone MOnitoring System for Campaigns) is an ozone microwave radiometer that measures the ozone emission line at 110.836 GHz at Ny-Ålesund, Svalbard (78.99° N, 12° E) since September 2015. It was built by the Institute of Applied Physics at the University of Bern (Fernandez et al., 2015). Measured ozone profiles are retrieved from the ozone spectra with a temporal averaging of 2 hours, leveraging the Atmospheric Radiative Transfer Simulator version-2 (ARTS2; Eriksson et al., 2011) and Qpack2 software (Eriksson et al., 2005) according to the optimal estimation algorithm (Rodgers, 2000). The retrieved ozone profile has a vertical resolution of 10-12 km in the stratosphere and up to 20 km in the mesosphere, covering an altitude range from 23 to 70 km. The measured datasets were used to study the photochemically induced diurnal cycle of ozone in the stratosphere and lower mesosphere (Schranz et al., 2018). The ozone measurements of GROMOS-C have been validated with AURA-MLS and MERRA-2 (Schranz et al., 2020; Shi et al., 2023, 2024). Furthermore, GROMOS-C has proved capable of measuring the tertiary ozone layer above Ny-Ålesund, Svalbard, in winter (Schranz et al., 2018).

2.3 MIAWARA-C

MIAWARA-C (MIddle Atmospheric WAter vapor RAdiometer for Campaigns) is a ground-based microwave radiometer measuring the pressure-broadened rotational emission line of water vapor at the frequency of 22 GHz. The University of Bern built this instrument (Straub et al., 2010) and performed a campaign at Ny-Ålesund, Svalbard (78.99° N, 12° E) since September 2015. MIAWARA-C retrieval, like GROMOS-C, is conducted using the ARTS2 (Eriksson et al., 2011) and QPACK2 software (Eriksson et al., 2005), following the optimal estimation algorithm (Rodgers, 2000). From the measured spectra, the retrieved water vapor profiles cover an altitude range extending from 37 km to 75 km with a time resolution of 2-4 h and a vertical resolution of 12-19 km. MIAWARA-C measurements were validated against MERRA-2 reanalysis, MLS observations, and WACCM simulations, followed by a comprehensive intercomparison (Schranz et al., 2019, 2020; Shi et al., 2023). Moreover, the effective ascent and descent rates of air were estimated using the water vapor from MIAWARA-C as a passive tracer to investigate the dynamics of transport processes in the Arctic middle atmosphere (Straub et al., 2010; Schranz et al., 2019; Shi et al., 2023).

2.4 Aura-MLS

NASA's Earth Observing System (EOS) Microwave Limb Sounder (MLS) instruments on board the Aura spacecraft measure thermal emissions from the limb of Earth's atmosphere. MLS provides comprehensive measurements of vertical profiles of temperature and 15 chemical species from the upper troposphere to the mesosphere, spanning nearly pole-to-pole coverage from 82°S to 82°N (Waters et al., 2006; Schwartz et al., 2008). Aura MLS version 5 Level 2 profile measurements of ozone and water vapor volume mixing ratios (VMR) between August 2004 and December 2022 are used in this study. The pressure range for MLS ozone measurements useful for scientific applications extends from 261 to 0.0215 hPa (16-86km), while for water vapor it ranges from 316 to 0.00215 hPa (10-86km). The MLS water vapor dataset has been compared globally with ground-based microwave radiometers, typically showing values that are 0–10% higher than the profiles obtained from the microwave radiometers in the range of 3–0.03 hPa (Nedoluha et al., 2017). The ozone profiles from MLS and ground-based microwave radiometer measurements agree within 5% in the range of 18–0.04 hPa (Boyd et al., 2007; Bell et al., 2024). Relative differences of ozone and water vapor climatologies at polar stations from Aura-MLS and radiometers agree well, with relative differences mainly within $\pm 7\%$ throughout the middle and upper stratosphere (Shi et al., 2023). In this study, ozone and water vapor profiles are extracted for locations within $\pm 1.2°$ latitude and $\pm 6°$ longitude of Ny-Ålesund, Svalbard, Sodankylä, and Tromsø.

2.5 WACCM-X

The Whole Atmosphere Community Climate Model with thermosphere and ionosphere extension (WACCM-X) is an atmospheric configuration of the NCAR's Community Earth System Model (CESM) that extends into the thermosphere with a model top boundary between 500 and 700 km (Liu et al., 2018). WACCM-X can be run with coupled or prescribed ocean, sea ice, and land components, enabling studies at all atmospheric levels, including thermospheric and ionospheric weather and climate. Physical processes represented in WACCM-X are built upon those in the regular WACCM configuration, which has a model top at 145 km, which in turn is built upon the Community Atmosphere Model (CAM) with its top at the lower stratosphere. The physics of these models is described in Marsh et al. (2013); Gettelman et al. (2019) and Neale et al. (2013). WACCM-X includes an interactive chemistry module that describes the major chemical processes, including ozone and related chemical tracers. Radiative transfer calculations in WACCM-X are based upon those in WACCM3 and described in Liu et al. (2010a).

We performed a climatological run from 2015 to 2023, leveraging the well-established Specified Dynamics mode of the model (WACCM-X(SD)) setup corresponding to the GROMOS-C and MIAWARA-C campaigns. WACCM-X(SD) is a version of WACCM-X whose temperature and winds from the surface to the stratosphere at $\sim$50 km are constrained by the Modern-Era Retrospective Analysis for Research and Applications version 2 (MERRA-2) reanalysis dataset (Gelaro et al., 2017). By nudging with MERRA-2, the model states correspond closely to the actual meteorological state up to the highest nudged altitudes close to the stratopause. The model outputs (winds, temperature, trace gases, QRL, and QRS cooling/heating rates) have a conventional latitude-longitude grid with a horizontal resolution of 1.9 ° × 2.5° and a time resolution of 3 hours. The vertical resolution is the same as WACCM below 0.96 hPa but has been increased to one-quarter scale height above that pressure level. The model top pressure is 4.1×10^{-10} hPa (typically between 500 and 700 km altitude, depending on the solar and geomagnetic activity). The QRS heating rate is primarily governed by ozone and water vapor absorption of radiation at stratospheric altitudes. In the mesosphere, the QRS is affected by atomic oxygen and direct exothermic heating as well as other ionospheric energy sources, such as particle precipitation. In contrast, the presence of carbon dioxide, water vapor, and ozone influences the QRL cooling rate.

2.6 MERRA-2

The Modern-Era Retrospective Analysis for Research and Applications, version 2 (MERRA-2) is a global atmospheric reanalysis produced by NASA's Global Modeling and Assimilation Office (GMAO), using the Goddard Earth Observing System-5 (GEOS-5) atmospheric general circulation model. Covering the period from 1980 to the present, MERRA-2 assimilates a wide range of observational datasets to generate three-dimensional (a horizontal resolution of $0.5° \times 0.625°$ and 72 model levels from the surface to 0.01 hPa) meteorological fields (e.g. zonal and meridional winds, temperature, ozone, and water vapor) with a 3-hourly time resolution. This study uses zonal and meridional wind fields for comparison with WACCM-X(SD) model simulations.

3 Results

3.1 Initial comparison of WACCM-X(SD) and combined Meteor Radar and MERRA-2 fields for SSW 2018/2019

We first evaluate the wind patterns observed by Meteor Radar (MR) + MERRA-2 and WACCM-X(SD) in the stratosphere, mesosphere, and lower thermosphere. Figure 1 illustrates the variability in zonal and meridional wind components above

Tromsø during the winter 2018/2019 SSW event, covering the altitudes from 20 to 100 km. The comparison shows that the combined MERRA-2 and MR winds agree reasonably well with WACCM-X(SD), reflecting even daily features. Zonal winds agree within 2-5 m/s for the overlapping region at 75 km. Climatologically, mean meridional winds are generally weaker and around the zero line; thus, the agreement does not look as good, but the overall magnitude difference is similar within 2-5 m/s. MERRA-2 and MR zonal and meridional winds often show very consistent tidal features and only occasionally some phase difference for individual days. WACCM-X(SD) winds are very similar to MERRA-2 up to the maximum nudging altitude, they start to generate features above that are neither reflected in MERRA-2 nor in the MR winds. These differences are likely due to the decreasing nudging strength with altitude. Additionally, the gravity wave (GW) parameterizations may contribute to these discrepancies by driving the fields away from the observed state (Stober et al., 2021b). In particular, around the SSW there are strong zonal and meridional wind features that are not seen in the observations. We also noticed that the elevated stratopause does not extend beyond 75 km in WACCM-X(SD), but is found up to this height in the combined MR and MERRA-2 wind fields. The formation of the elevated stratopause is accompanied by the reformation of the polar vortex, indicated by the eastward winds that start to intensify at the mesosphere (60–80 km) and gradually descend with time after the SSW event. The GW parameterizations tend to produce or strengthen certain tendencies in the wind fields, resulting in larger deviations of the instantaneous winds, while sustaining most of the large-scale wind patterns. This is in agreement with previous studies targeting the climatological behavior of MLT winds between MR winds and tides in comparison to WACCM-X(SD) (Stober et al., 2021b).

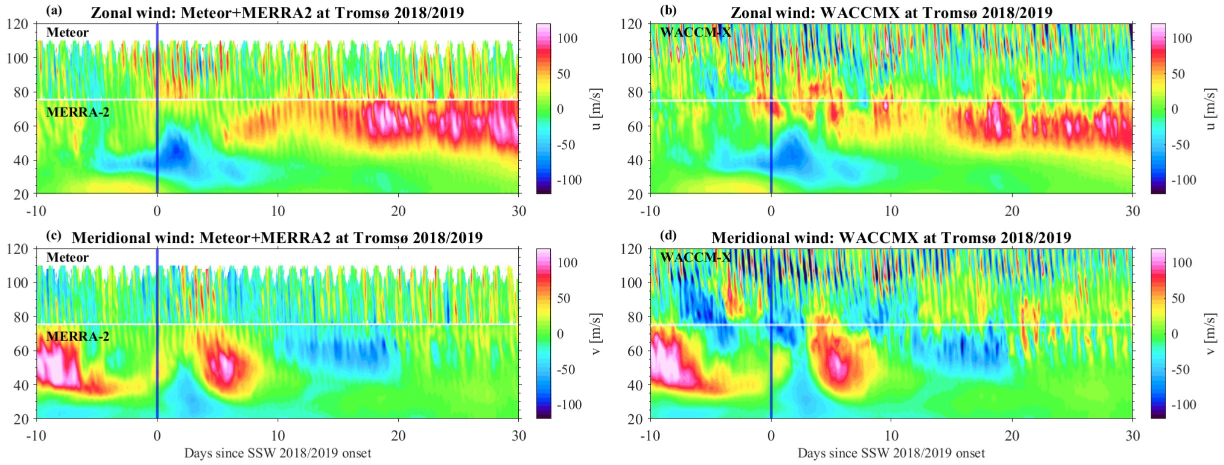

Figure 1. The cross-section of zonal and meridional wind variations at Tromsø (69.58°N, 19.22°E) during the SSW of 2018/2019, derived from (a, c) MR and MERRA-2, (b, d) WACCM-X(SD). The white horizontal line marks the 75 km altitude level. In the left panels, the horizontal line distinguishes meteor radar (upper section) from MERRA-2 (lower section). The vertical blue line denotes the central date of SSW on January 2, 2019.

Furthermore, we present and analyze WACCM-X(SD) fields that are not commonly used but provide essential information to investigate and understand the short-term tidal variability. Figure 2 shows the 3-hourly ozone and water vapor VMR as well as QRL and QRS for the location of Tromsø. The WACCM-X(SD) simulation reflects the exchange of airmasses in the middle atmosphere due to the SSW event. In particular, the sudden intrusion of water vapor into the mesosphere and the increase of ozone in the stratosphere are evident. The large-scale dynamics also directly affect the QRL and, thus, the cooling of the middle atmosphere, resulting in a pronounced double-layer structure with increased cooling rates at around 40 km and above 80 km starting already 10 days before the SSW central day. These changes in the cooling rates are aligned with water vapor anomalies, but given the mean cooling rate of around 0.3 K/day due to water vapor in the mesosphere (Brasseur and Solomon, 2005), its contribution to the QRL cooling rate is negligible. Thus, variations in QRL are more closely aligned with temperature (warming in the stratosphere, cooling in the mesosphere, and warming above) rather than changes in water vapor. For the short-term tidal variability, ozone and short-wave absorption might play a key role. WACCM-X(SD) shows the primary stratospheric ozone layer at 20-50 km, the tertiary ozone layer around 60-70 km, and the secondary ozone layer above 90 km. The secondary ozone layer reflects a strong diurnal modulation and starts to fade toward the spring transition. Furthermore, associated with the large intrusion and exchange of air masses, the secondary ozone layer is disturbed, which starts again about 10 days before the SSW event and restores afterward. These changes are accompanied by a strong response from the QRS. Furthermore, the QRS also reveals a clear signature of a diurnal forcing starting 20-30 days after the SSW, which is related to the slowly descending elevated stratopause and the increased ozone VMR. During this time, after an SSW event, the secondary ozone layer at the MLT almost vanished. Although the 2018/19 SSW event can be considered to be representative of major SSWs, there is a noticeable variability between events. In section 3.2 and 3.3, we present composite analysis for major SSW events concerning the central day and focus on anomalies rather than absolute values.

We also performed a tidal analysis for the SSW 2018/19 event. Therefore, we applied the ASF2D to the MR and WACCM-X(SD) data for the location of Tromsø. Figure 3 shows the SDT anomalies for the zonal and meridional wind components, respectively. The anomaly is calculated by comparing each day's value to the climatological average for the same day across all years from 2015 to 2023. WACCM-X(SD) exhibits a much stronger semidiurnal tidal amplification than can be found in the observations for the horizontal wind. As already seen in the instantaneous winds, WACCM-X(SD) produces additional features at the MLT, which likely also affect the tidal propagation, resulting in a decreased agreement when comparing daily features, while the overall behavior seems to still be reproduced. The comparison for the DT is showcased in Figure 4. The DT appears to be polarized and exhibits much stronger amplitudes in the meridional wind component compared to the zonal wind component. Furthermore, the MR observations as well as WACCM-X(SD) capture a diurnal tidal enhancement starting about 20 days after the SSW. However, the altitude range where this enhancement can be found is more confined below 80 km in WACCM-X(SD), whereas the MR measurements indicate a strong DT up to 100 km. This difference seems to be related to the differences in the altitude coverage of the elevated stratopause presented in Figure 1.

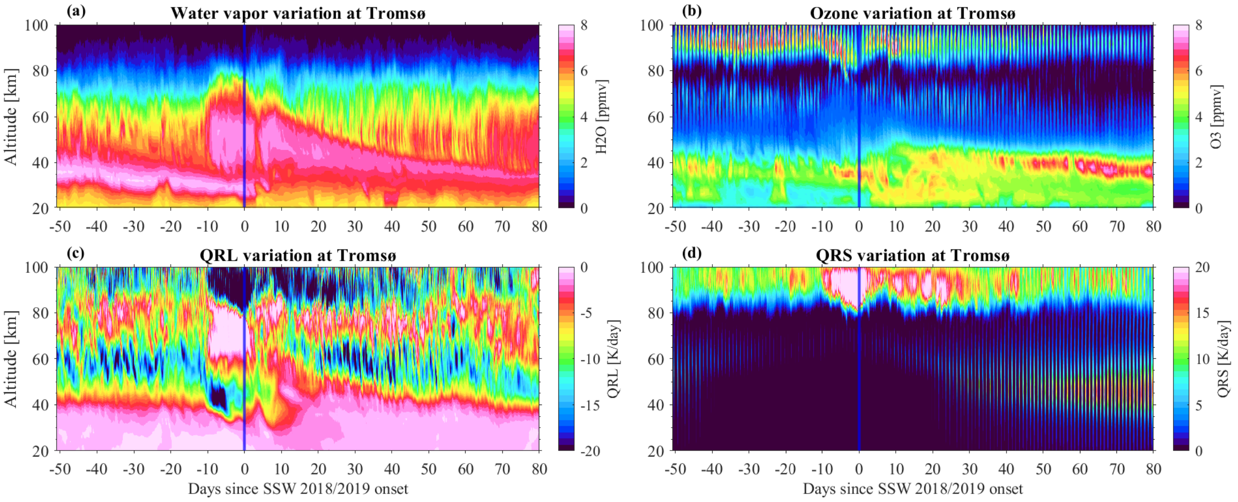

Figure 2. The cross-section of (a) water vapor, (b) ozone, (c) QRL cooling rate, and (d) QRS heating rate variations at Tromsø during the winter SSW of 2018/2019, derived from WACCM-X(SD).

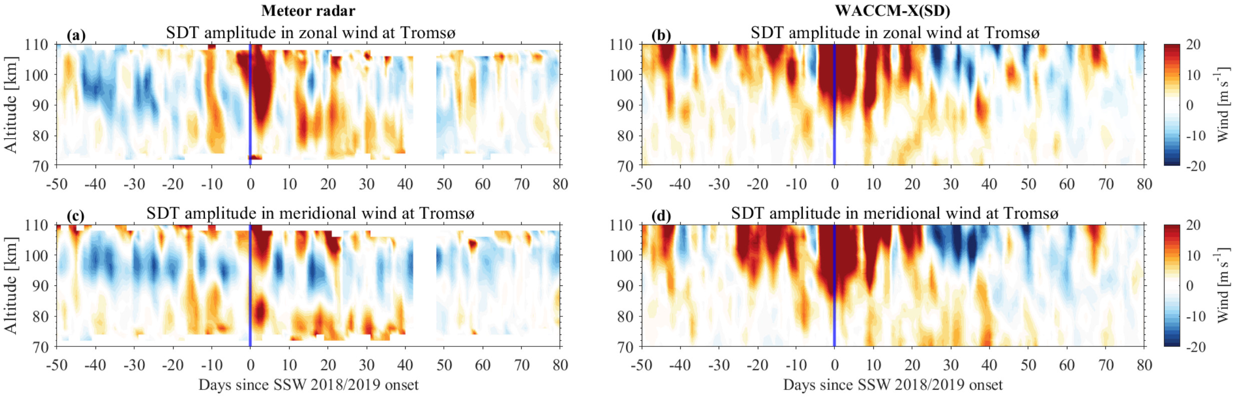

Figure 3. The cross-section of SDT amplitude anomalies in zonal and meridional wind components at Tromsø during the winter SSW of 2018/2019, derived from (a, c) MR and (b, d) WACCM-X(SD).

3.2 Composite analysis of mean wind response during SSWs

To understand the variation of winds and tides before and after SSW, the anomalies of zonal and meridional winds and tidal amplitude are investigated. Figure 5 presents the composite zonal and meridional wind anomalies observed by three MRs at Sodankylä, Tromsø, and Svalbard as a function of time relative to the SSW central date. The central date, as defined in Li et al. (2023) and Butler et al. (2017), corresponds to the onset of SSW, which is identified based on the zonal-mean zonal winds at

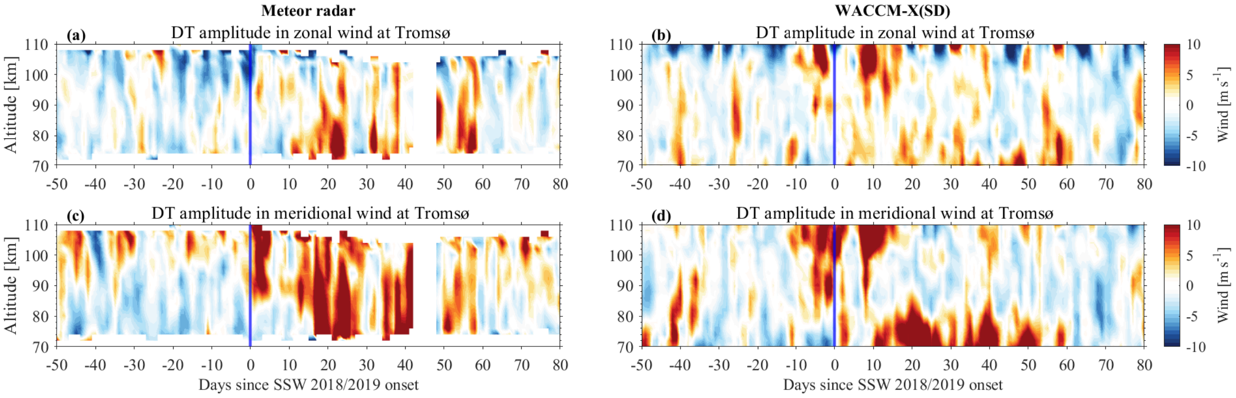

Figure 4. The same as Figure. 3 but for the DT amplitude.

60°N and 10 hPa reversing from westerly to easterly. 10 major SSW events from 2004 to 2023 are analyzed in this study (in Table A1). In the left panel of Figure 5, a reversal of the zonal wind is evident starting about 10 days before the nominal SSW onset according to the mean zonal wind at 10 hPa and 60°N. During this period, the zonal wind becomes westward, with wind reversal anomalies reaching approximately 8 m/s at 80 km altitude.

As we move southward from Svalbard to Tromsø and Sodankylä, the westward winds gradually strengthen after day 0, peaking at around 90 km with anomalies reaching up to 20 m/s. Following the onset of the SSW, eastward winds dominate from 80 to 85 km for approximately 45 days, coincidental with the presence of an elevated stratopause that forms after the stratospheric warming and the reformation of the ’normal’ stratopause towards the spring transition (Manney et al., 2009; Matthias et al., 2021). In contrast, the meridional winds at these polar-latitude stations exhibit greater variability than the zonal winds. Alternating positive and negative wind speed anomalies are observed throughout the entire altitude range, both before and after the SSW onset (from day -50 to day 20), indicating significant large-scale planetary wave activity in the meridional winds before and during the SSW onset and a reduced activity afterward. The polar vortex is reestablished after the SSW, as indicated here by the period of intensified westerly winds, where the planetary waves are rather weak. Planetary wave activity during SSWs plays a crucial role in modulating atmospheric tides (Hibbins et al., 2019; Zhang et al., 2021; van Caspel et al., 2023; Qiao et al., 2024).

3.3 Composite analysis of the mean response of tides during SSW events

The tidal components have been extracted from the zonal and meridional winds observed by meteor radars following the procedure for the mean winds, leveraging the ASF2D analysis during SSW events. Figure 6 shows the composite amplitude anomalies for 10 SSWs of the TDT in the zonal and meridional winds at the three high-latitude stations, while Figures 7 and 8 illustrate the corresponding anomalies for SDT and DT, respectively. The anomalies for SDT and DT observed from WACCM-X(SD) are shown in Appendix A.

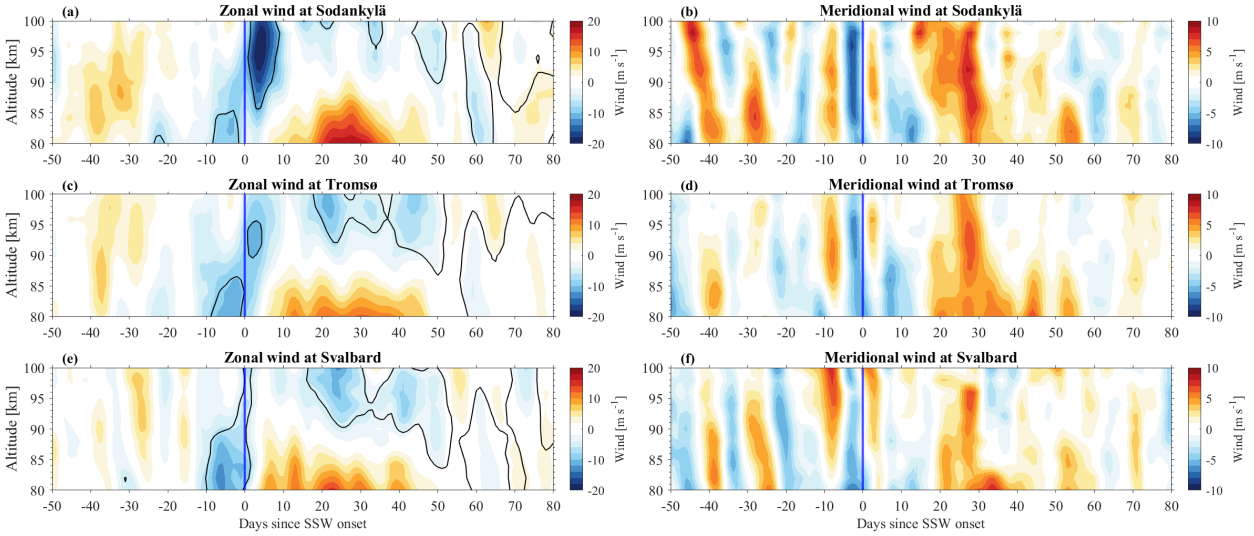

Figure 5. The cross-section of SSW composite (a, c, e) zonal and (b, d, f) meridional wind anomalies observed with three MRs at Sodankylä, Tromsø, and Svalbard over the period from 2004 to 2021, respectively. The vertical blue line represents the central date of the SSW (day 0 of SSW onset). The contours represent zero wind speeds.

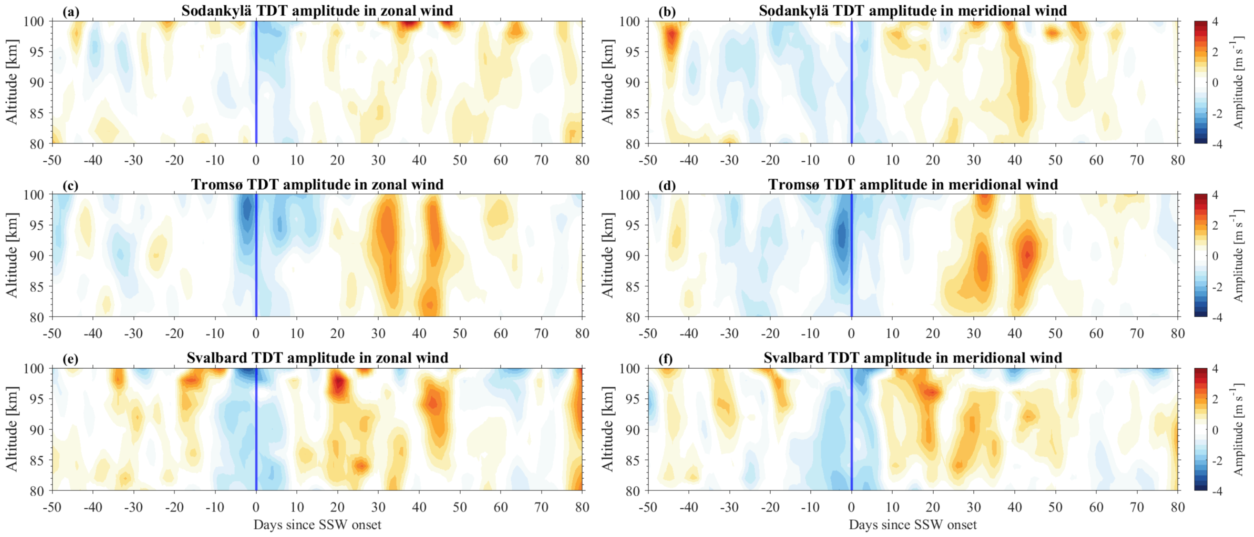

Figure 6. The cross-section of SSW composite TDT amplitude anomalies in the (a, c, e) zonal and (b, d, f) meridional wind components observed with three MRs at Sodankylä, Tromsø, and Svalbard, respectively.

In Figure 6, a pronounced decrease in TDT amplitude is observed within a few days before and after the SSW onset, characterized by a magnitude of up to -3 m/s in both the zonal and meridional wind components. The tidal amplitude changes can be presented as a percentage difference relative to the mean value. This reduction in TDT amplitude (20-30%) suggests a significant suppression of the TDT during the onset phase of SSWs, possibly due to changes in the background wind and temperature conditions that inhibit the propagation of this tidal component. Following this initial suppression, TDT amplitudes start to strengthen approximately 10 days after the SSW onset at Svalbard and Sodankylä and 20 days later at Tromsø, eventually reaching maximum positive anomalies of up to 4 m/s. The recovery and subsequent amplification of the TDT may be attributed to the reformation of the stratopause and the altered wind structure in the MLT region, which facilitates the upward propagation of the tides. Notably, the strength of the TDT amplitude anomaly at Tromsø and Svalbard is stronger than at Sodankylä, indicating potential latitudinal and longitudinal variations in the tidal response to SSWs. These observations align with previous studies that have utilized mechanistic global circulation models (Lilienthal et al., 2018; Lilienthal and Jacobi, 2019) and satellite measurements (Moudden and Forbes, 2013) to discuss the excitation mechanisms of TDT, such as direct solar heating, nonlinear interactions, and gravity wave–tide interactions.

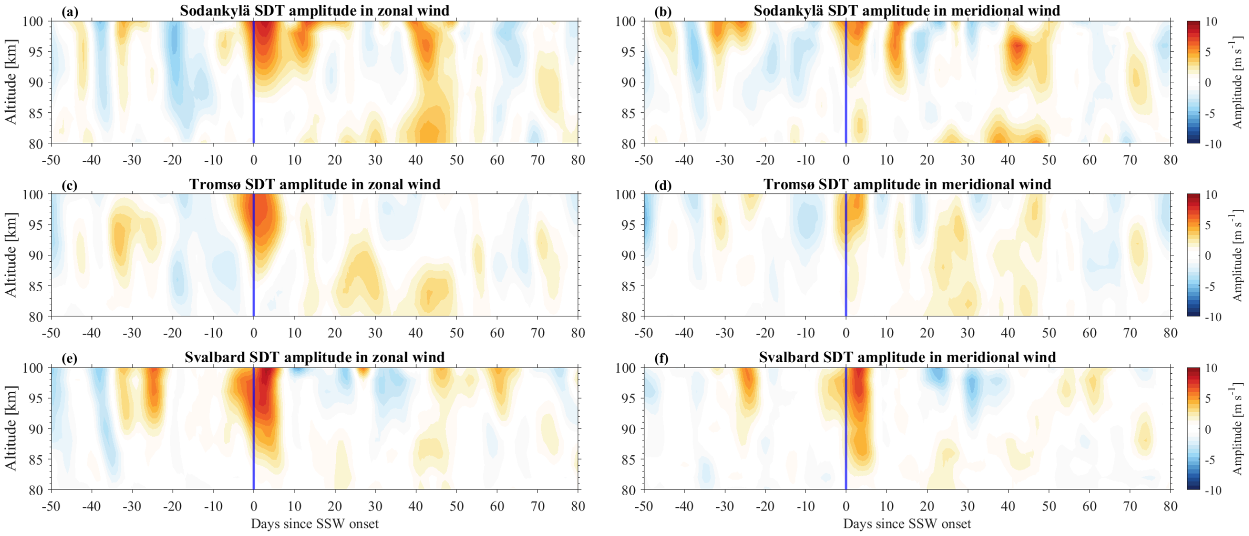

Figure 7. The same as Figure. 6 but for SDT amplitude anomalies.

Figure 7 illustrates that the SDT amplitude anomalies at the three stations, in both wind components, can reach up to 10 m/s (changes with peaks reaching up to 40%) within an altitude range of 90-100 km, persisting for only a few days around the SSW onset. This short-lived but intense enhancement of SDT, particularly in the zonal wind component, indicates a strong and rapid response of the SDT to the dynamical changes induced by the SSW. The pronounced increase in SDT amplitudes suggests that the modification of zonal mean winds during SSW may provide more favorable conditions for the upward propagation of SDT, potentially amplified by interactions with planetary waves. This rapid response is also consistent with the ozone enhancement at equatorial to middle latitudes around the onset of the SSW, as shown by Siddiqui et al. (2019) (in Figure 3b). Overall, the SDT amplitude anomalies are found to be approximately twice as large as those of TDT and DT, highlighting the sensitivity of SDT to SSW-induced disturbances.

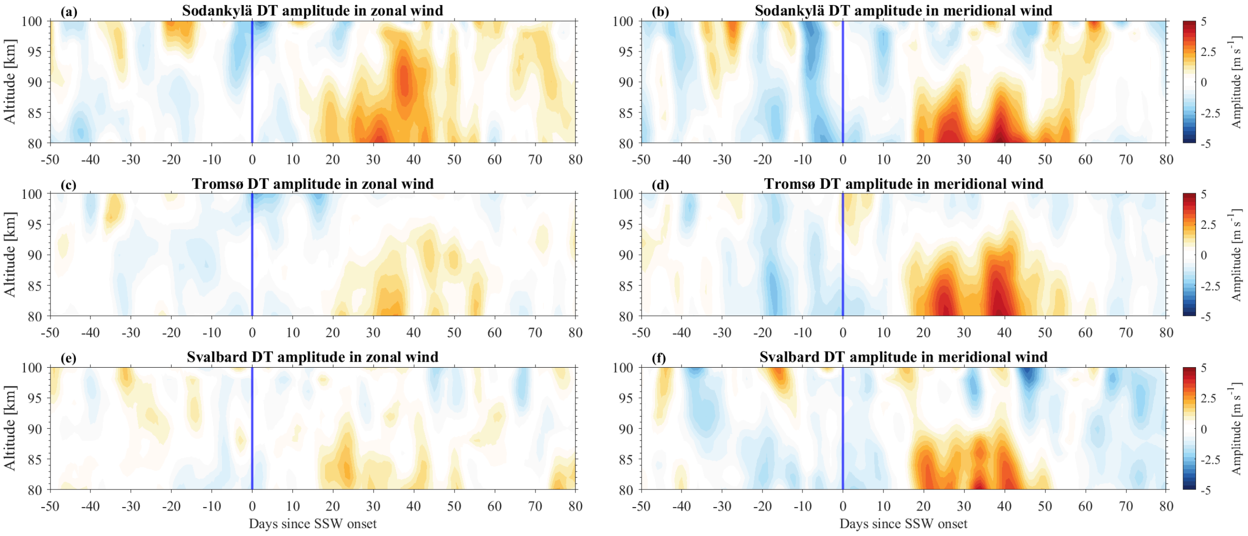

Figure 8. The same as Figure. 6 but for DT amplitude anomalies.

275 Figure 8 shows the DT amplitudes before, during, and after the central date of SSWs. Unlike the TDT and SDT, the DT amplitudes do not exhibit a distinct variation around the SSW onset. However, in both wind components at Sodankylä, Tromsø, and Svalbard, the DT amplitude starts to enhance around 20 days after the SSW onset, reaching a peak nearly 40 days post-SSW. This enhancement in DT amplitude persists for about a month, indicating a delayed response to the SSW. The stronger positive amplitude anomalies are more evident in the meridional wind component than in the zonal wind component. In comparison, the 280 positive amplitude anomaly in the zonal wind component above Tromsø and Svalbard is less pronounced than at Sodankylä, suggesting a latitudinal/longitudinal dependency in the DT response. The DT amplitude changes have magnitudes of the order of 30% in the zonal component and 50% in the meridional component. The delayed enhancement of DT could be linked to the restoration of the stratopause by the gradual descent of an elevated stratopause accompanied by increased ozone VMR and subsequent changes in thermal and dynamical conditions in the upper mesosphere, which may alter the tidal propagation 285 environment and lead to the amplification of the DT.

3.4 Atmospheric composition and radiative processes during SSWs

Trace gases play a crucial role in the energetic and radiative balance in WACCM-X(SD). The modeled long-wave cooling and short-wave heating rates provided by the simulation require a good representation of the trace gas VMR. Therefore, we extracted the WACCM-X(SD) water vapor and ozone fields for all three MR locations and used the retrieved ozone and water vapor VMR from our radiometers MIAWARA-C and GROMOS-C in Ny-Ålesund, Svalbard.

3.4.1 Water vapor

Figure 9 compares MLS and WACCM-X(SD) water vapor VMR anomalies for the entire middle atmosphere. The composite analysis exhibits a similar pattern between the satellite and the model. There is a weak tendency in WACCM-X(SD) to underestimate water vapor anomalies after the SSW event. During the SSW around the central day, larger deviations are only visible above 75 km.

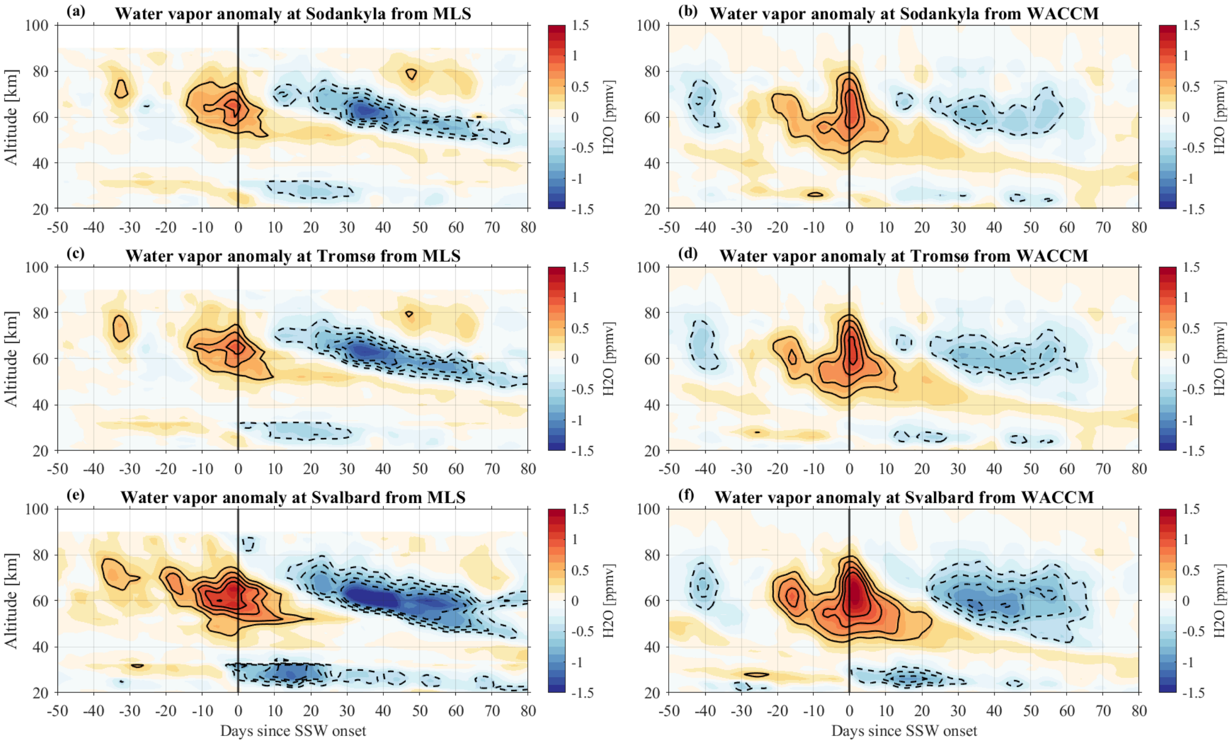

Figure 9. The cross-section of SSW composite water vapor anomalies measured by MLS (a, c, e) and simulated by WACCM-X(SD) (b, d, f) over Sodankylä, Tromsø, and Svalbard. The positive and negative anomalies of water vapor are shown in solid and dashed contours, respectively.

Furthermore, we compared the WACCM-X(SD) reduced water vapor VMRs with the local MIAWARA-C observations from Ny-Ålesund. MIAWARA-C collects spectra during an entire day, whereas MLS only measures at fixed local times above Svalbard. Figure 10 shows MIAWARA-C anomalies from the composite analysis between 2015-2023. The WACCM-X(SD) contours are overlaid and reflect the good agreement for the water vapor anomalies. Composite analysis results in water vapor

VMR changes of about ±1.25 ppmv for SSW events. During the events, the intrusion of water vapor-rich airmasses from the mid-latitudes results in increased water vapor mixing ratios throughout the upper stratosphere up to the mesosphere, reaching altitudes of about 80 km. WACCM-X(SD) reproduces the SSW-related changes in water vapor VMR at the upper stratosphere and mesosphere. This is remarkable considering that the water vapor fields are not nudged and calculated from the interactive chemistry module. This also provides confidence that the calculated QRL cooling rate provides a meaningful model parameter for comparison to the observations.

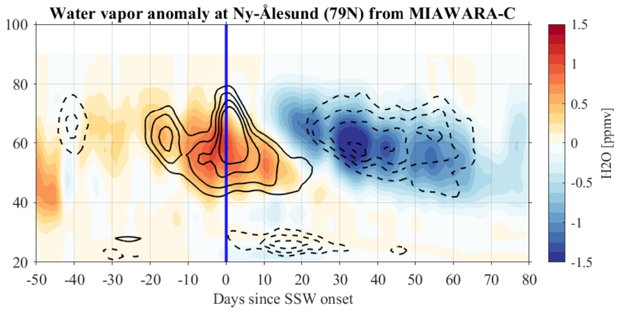

Figure 10. The cross-section of SSW composite water vapor anomalies (color-coded) from ground-based MIAWARA-C microwave radiometer measurements at Ny-Ålesund, Svalbard. The overlaid solid and dashed contours represent positive and negative anomalies of water vapor from WACCM-X(SD) at Svalbard, respectively.

3.4.2 Ozone

Ozone is one of the most crucial trace gases for the excitation of tides. WACCM-X(SD) shows all three ozone layers. The primary layer extends from 20-50 km, the tertiary ozone layer is found at altitudes between 60-80 km, and the secondary ozone layer covers altitudes above 90 km in Figure A2. At polar and high latitudes, WACCM-X(SD) exhibits the highest ozone VMR at the secondary ozone layer, reaching 6-8 ppmv. The tertiary ozone layer takes values between 1-2 ppmv, and the stratospheric ozone reaches about 4 ppmv before the SSW and 5-6 ppmv in the aftermath. Figure 11 presents the ozone anomalies from MLS and WACCM-X(SD) corresponding to three stations during SSWs. The most significant positive ozone anomalies are up to 1.5 ppmv and persist for over 30 days in the middle stratosphere following the SSW onset. In the upper stratosphere and lower mesosphere, positive ozone anomalies persist for approximately two months starting around 10 days after the onset. The persistence of positive ozone anomalies reflects prolonged changes in middle atmospheric circulation following the SSW. The most significant changes in ozone VMR occur in the secondary ozone layer and the stratosphere. The stratospheric ozone anomaly is closely related to the elevated stratopause and lasts up to 70 days after the SSW event. The secondary ozone layer indicates a response around the SSW event, with anomalies reaching a maximum 10-15 days after the SSW. The observed ozone increase reaches up to 1.5 ppmv, which is about 50% of the background value.

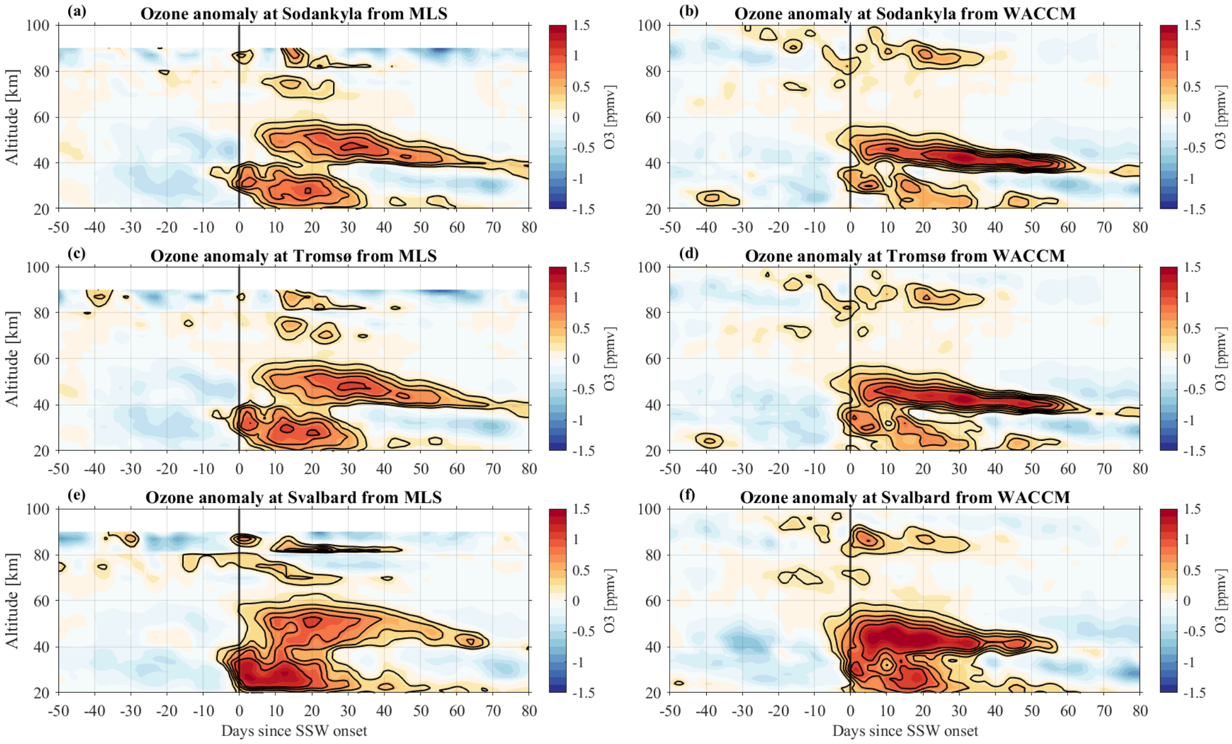

Figure 11. The cross-section of SSW composite ozone anomalies measured by MLS (a, c, e) and simulated by WACCM-X(SD) (b, d, f) over Sodankylä, Tromsø, and Svalbard. The positive anomalies of ozone are shown in solid contours.

We also performed a comparison between WACCM-X(SD), leveraging data reduction, and our local GROMOS-C measurements at Ny-Ålesund, Svalbard. Figure 12 shows in color scale the ozone VMR anomalies from the radiometer, and the WACCM-X(SD) contours are overlaid. The stratospheric ozone anomalies are well-reproduced in WACCM-X(SD), underlining once more the performance of the interactive chemistry module. The differences at altitudes above 75 km are mostly due to the low measurement response of GROMOS-C, as the spectral resolution is no longer sufficient to resolve the ozone Doppler broadened line peak at 142 GHz, thus, the retrieved ozone values start to become dominated by the a priori information taken from a climatology. Specifically, the ozone double-layer structure in the WACCM-X(SD) ozone anomalies that form at the onset of the SSW and last for about two weeks, results in two layers of substantial UV heating. The superposition of these two diurnal tidal waves at the mesosphere may effectively amplify the SDT at high latitudes due to a 12-hour phase offset caused by the different vertical distances both waves have to travel, considering the typical vertical wavelengths of 30-50 km for semidiurnal tides at this latitude (Stober et al., 2021b, 2020). The change in ozone is strongly dependent on altitude and latitude, as shown in the measurements and simulations (Figure 11). With the polar wind reversal during the SSW onset, planetary wave activity in the stratosphere drives anomalous equatorial upwelling and cooling that enhances tropical stratospheric ozone. This

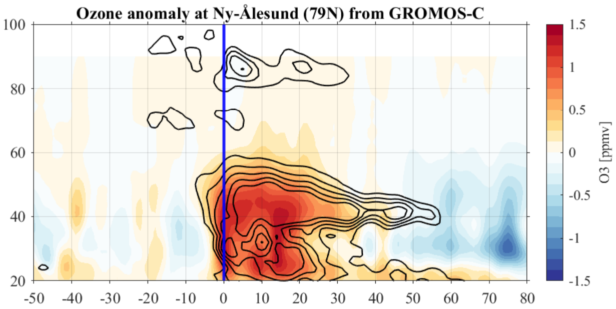

Figure 12. The cross-section of SSW composite water vapor anomalies from ground-based microwave radiometers GROMOS-C at Ny-Ålesund, Svalbard. The overlaid solid contours represent positive anomalies of ozone from WACCM-X(SD) at Svalbard.

is qualitatively consistent with findings from Siddiqui et al. (2019) and Limpasuvan et al. (2016), which show a rapid ozone increase from 20°S to 40°N, and a decrease poleward of 40°N.

3.4.3 QRL cooling and QRS heating rates

Previous studies have identified multiple mechanisms that could contribute to tidal variations during SSW events:

(a) Changes in the zonal mean winds that influence the vertical propagation of tides in the MLT region (Jin et al., 2012; Pedatella et al., 2012; Stober et al., 2020).

(b) Ozone changes (Goncharenko et al., 2012; Eswaraiah et al., 2018; Siddiqui et al., 2019; Mitra et al., 2024).

(c) Nonlinear interactions between stationary planetary waves and tides (Pedatella and Forbes, 2010; Pedatella and Liu, 2013; Qiao et al., 2024).

Performing the composite analysis, we derived QRL and QRS anomalies for all SSW events. These anomalies are shown in Figure 13 for Sodankylä, Tromsø, and Svalbard. There is almost no dependency on latitude in the general morphology of QRL cooling rate anomalies among the three stations. The elevated stratopause reflects reduced cooling rates (reddish color) and increased cooling above. The biggest anomalies and abrupt changes occur directly around and after the central day of the SSW, corresponding to the temperature changes (Figure A1). The QRS heating rate (including effects by ozone) exhibits a more clear stratification. The MLT region (80–100 km) exhibits pronounced positive heating rate anomalies around and shortly after the central date of the SSW, followed by a period of diminished, yet still positive, heating anomalies persisting from approximately 20 to 40 days after the event. Furthermore, the QRS shows a good correspondence to the ozone VMR and captures the diurnal cycle in the stratosphere. During the recovery phase of the stratopause, the QRS shows a characteristic diurnal cycle.

Given the close agreement between all 3 stations, we are going to focus on Tromsø when investigating the absolute QRL and QRS shown in Figure 14. The QRL absolute cooling rate indicates a rather consistent behavior before the SSW, with only a small cooling rate below 40 km and around 80 km altitude. Between these layers, we find cooling rates ranging from -10 to

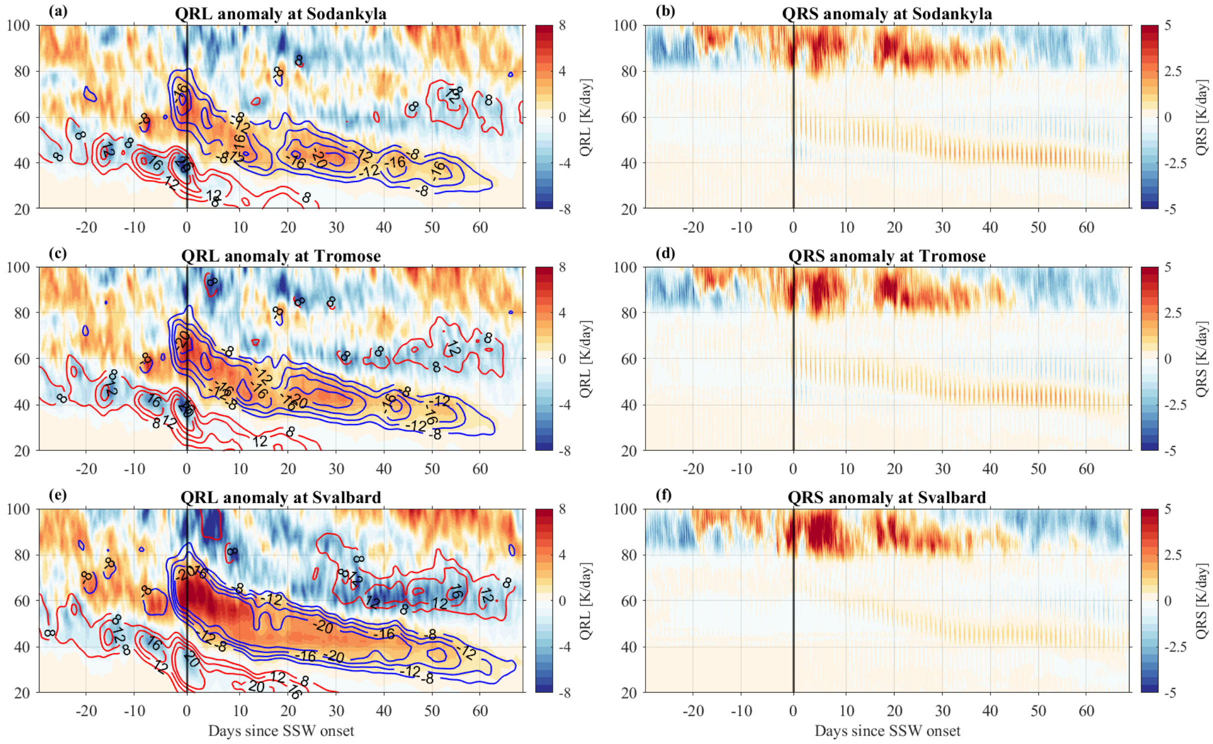

Figure 13. The cross-section of SSW composite QRL cooling (a, c, e) and QRS heating (b, d, f) rate anomalies simulated by WACCM-X(SD) over Sodankylä, Tromsø, and Svalbard. Red contours indicate positive temperature anomalies. Blue contours indicate negative temperature anomalies.

-15 K/day. During the SSW and the first 10-15 days after the SSW event, we find reduced cooling rates from the stratosphere 355 up to 80 km in the MLT. The most extreme QRL value is observed after the central day above 80 km altitude, exceeding the values of -20 k/day. On the other side, the QRS heating aligns with the total ozone VMR at the secondary and primary ozone layers, and a much lower level also in the tertiary ozone layer. The largest QRS values are observed after the central day of the SSW at the MLT, and subsequently in the stratosphere about 20 to 60 days later, when the elevated stratopause reaches again the typical stratospheric altitudes. The QRS values at the MLT and the stratosphere are modulated by a diurnal cycle.

360 For tidal excitation, the QRS plays the most important role in understanding the derived tidal anomalies from the MR. The QRL shows only a large-scale response with characteristic time scales of days during the SSw event. The cooling rates define the large-scale temperature and wind background through which the atmospheric tides have to propagate rather than contribute to the tidal forcing itself. Therefore, we conducted the composite analysis of the water vapor and ozone VMR, as shown in Figure 15. The water vapor VMR shows a characteristic response after the SSW and indicates the presence of an elevated 365 stratopause, and towards the spring, a transition to the summer situation. However, the composite analysis of ozone VMR

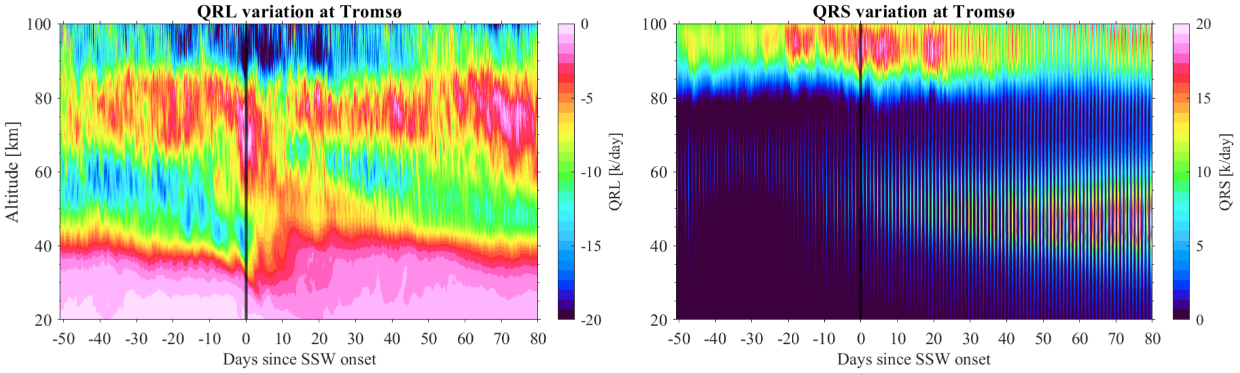

Figure 14. The cross-section of SSW composite QRL and QRS from WACCM-X(SD) at Tromsø.

indicates characteristic diurnal modulations at the stratosphere (30-50km) and at the altitude of the secondary ozone layer. This double-layer structure is mainly responsible for the semidiurnal tidal activity during the winter months at these latitudes. The superposition of the in-situ forced tide at the secondary ozone layer is out of phase with the diurnal tide that was excited at the stratosphere/lower mesosphere and propagates upward. The tidal phase lines shown for the 2018/19 case study reach the MLT region with a 12-hour offset compared to the diurnal heating cycle (see WACCM-X(SD) Figure 1). This coincides with the vertical wavelengths that are found in climatological analysis (Stober et al., 2021b) for these stations. During the SSW, this balance is disturbed, and the secondary ozone layer, together with the elevated stratopause, provides favorable conditions to amplify the SDT. The QRS anomaly shows a pronounced enhancement at the secondary ozone layer that coincides with the time of the semidiurnal tidal amplification and an increased ozone VMR at the stratosphere right after the SSW event. However, WACCM-X(SD) also exhibits a secondary peak of the semidiurnal tides about 20 days before the SSW (Figure A2), which is mostly absent in the observations. Apparently, with the onset of the SSW event, the dynamical conditions in the stratosphere and mesosphere, together with a sufficient ozone VMR at all three ozone layers, provide favorable conditions to cause the semidiurnal tide amplification. Furthermore, WACCM-X(SD) exhibits a fading of the QRS heating 20 days after the SSW event, which is accompanied by reduced semidiurnal tidal activity. During this period, the diurnal tide starts to dominate the observations around 80 km. This diurnal tide seems to be the direct result of the diurnal ozone cycle, which is associated with QRS in the stratosphere. The delayed response of QRS (and consequently DT) in the stratosphere is likely associated with the seasonal increase in solar illumination, as sunlight progressively reaches lower altitudes.

A crucial aspect of marked changes in direct shortwave heating of the stratosphere results from the increased ozone VMR. Therefore, we performed additional analysis by computing the circle of illumination in dependence on altitude. Figure 16 shows a schematic of how to estimate the presence of sunlight for a specific geographic latitude and local time. All calculations are performed using the J2000 reference epoch, and the sun ephemerides are valid for the period from 1950 to 2050 (United States Naval Observatory. Nautical Almanac Office and Nautical Almanac Office (U.S.), 2009). The sun is above the horizon at Svalbard at local noon after the 15th of January in the mesosphere and reaches the stratospheric altitudes towards the end

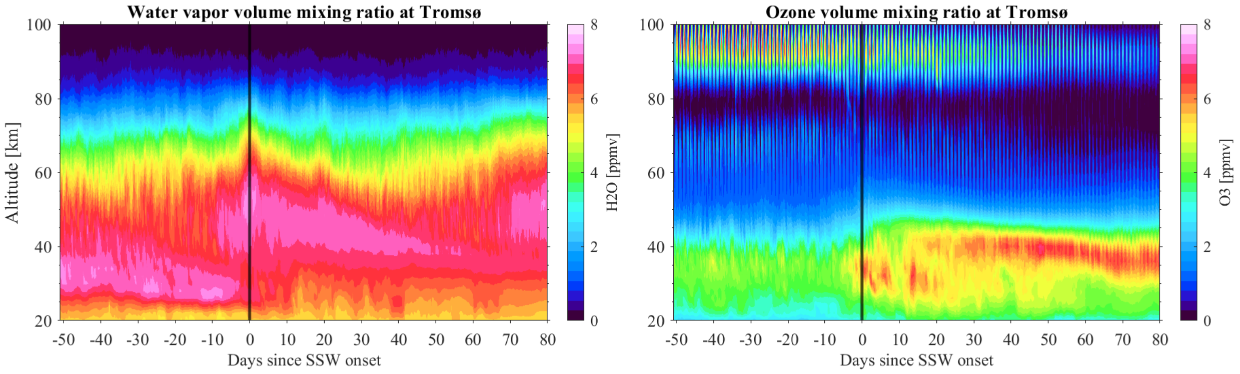

Figure 15. The cross-section of SSW composite of water vapor (left) and ozone (right) VMR anomalies from WACCM-X(SD) at Tromsø.

of January. At Tromsø and Sodankylä, the stratosphere is always illuminated by the sun during noon, although both sites are at latitudes beyond the polar circle and the surface remains in darkness. During midnight, all altitudes remain shadowed by the Earth, and no sunlight reaches the stratosphere or mesosphere. This characteristic diurnal heating results in a pronounced diurnal tide at the stratosphere (Schranz et al., 2018). Thus, the differences in the QRS between Svalbard and the Fennoscandinavian mainland locations are understandable due to the availability of direct sunlight at certain altitudes. We calculated the

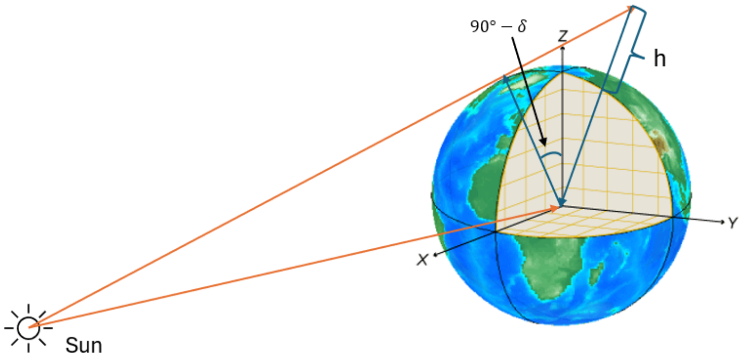

Figure 16. A schematic illustration showing the estimated sunlight presence for a given geographic latitude and local time. The diagram visualizes the variation in sunlight exposure as a function of latitude, highlighting the effects of Earth's rotation and axial tilt on day and night cycles.

circle of illumination height above the latitudes of Sodankylä, Tromsø, and Svalbard for the longitude of the Greenwich meridian, assuming 11:59:59 UTC for the dates listed in Table 1. These numbers are valid for 2023 and depend on the exact solar longitude of the Earth around the sun's orbit. Due to leap years, there are some changes in the exact altitudes between years of a few hundred meters. We show the lowest altitude, the sun will be visible for that latitude at the Greenwich meridian for that

Table 1. Illumination height at 12 UT above the latitudes of Sodankylä, Tromsø, and Svalbard.

Date	Sodankylä (67.37°N)	Tromsø (69.58°N)	Svalbard(78.99°N)
01 Jan	0.14km	4	113km
15 Jan	0	0.23km	77km
31 Jan	0	0	26km
15 Feb	0	0	0
28 Feb	0	0	0

date, around noon (UTC). A zero indicates that the sun reaches the surface. Furthermore, considering the effective sampling volume of more than 400 km in diameter of GROMOS-C and the meteor radars, some parts of the observation volumes are further south and, thus, can collect sunlight at even lower altitudes.

3.5 Diurnal tide amplification and radiative forcing

The amplification of diurnal tides observed 20–40 days after the SSW is closely linked to enhanced radiative forcing, which is closely related to the increased ozone VMR due to the formation of an elevated stratopause, combined with increasing solar radiation toward the end of January. During this period, WACCM-X(SD) exhibits a pronounced diurnal amplitude enhancement around 60-80 km. MR observations reveal a similar amplification, extending 5–10 km higher into the mesosphere. Both model and observations indicate that the meridional wind component shows a stronger enhancement than the zonal component, as shown in Figure 17, which compares MR and WACCM-X(SD) DW1 wind perturbations.

The wind perturbations show clear evidence of vertically propagation tidal modes, as indicated by the vertical phase progression. Notably, DW1 amplitudes in WACCM-X(SD) diminish between 90 and 100 km altitude, precisely the region where the SW2 tide begins to grow significantly. MR observations also display a gradual decrease in DW1 amplitude with height, though the trend is less pronounced than in the model. The DW1 temperature perturbations in WACCM-X(SD) are in good agreement with the meridional wind structure and remain in phase with the QRS heating near 40 km altitude, corresponding to the warm phase of the tide driven by solar forcing. We overlaid the QRS perturbation at the stratosphere onto the wind and temperature contours. Figure 17e compares the QRS and temperature perturbation for the DW1 frequency component averaged between 34-44 km altitude, corresponding to the seed region of the diurnal tidal wave (altitude region before the amplitude grows rapidly). A modest phase offset is apparent between both time series due to the spike-like profile of the QRS and temperature perturbation, in that QRS essentially drops to zero during the night and rises sharply during the day. QRS appears to lead the temperature response. This phase offset may also be influenced by the coarse 3-hour temporal resolution of the WACCM-X(SD) output.

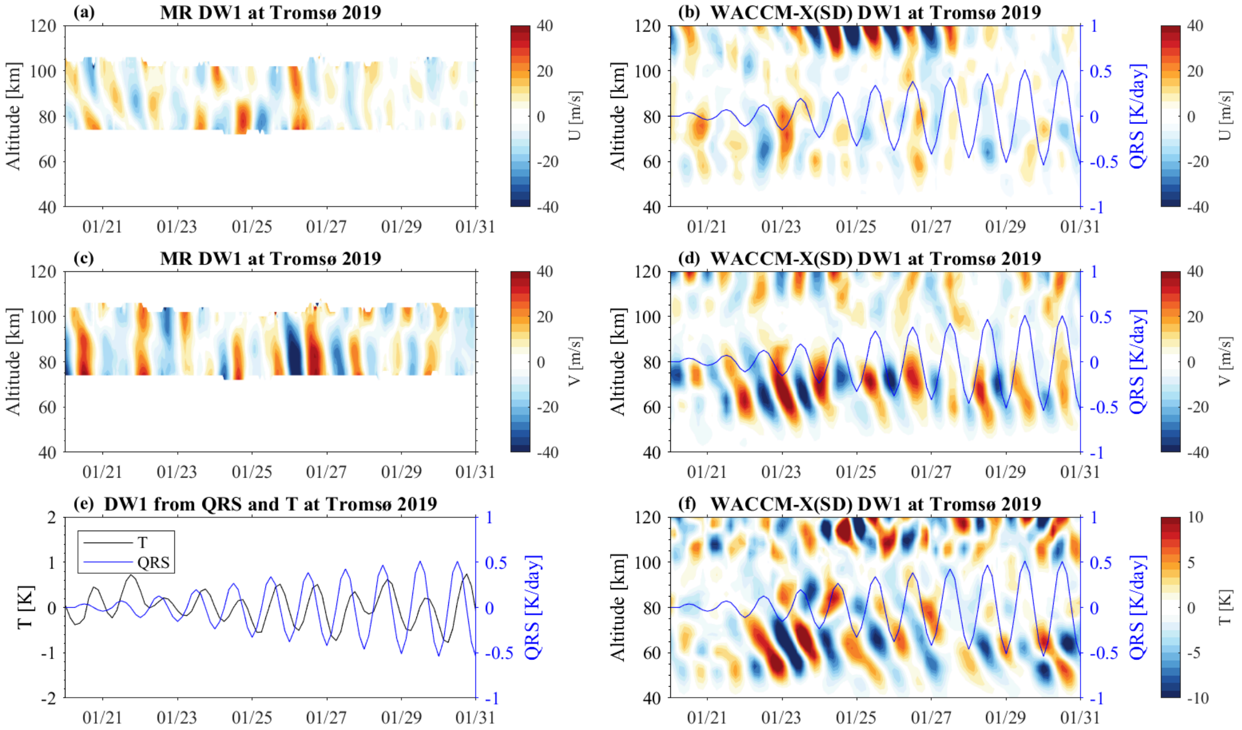

Figure 17. Time series of DW1 zonal and meridional winds, temperature, and QRS perturbations derived using adaptive spectral filtering over Tromsø during 20–40 days following the 2018/19 SSW event. Panels (a) and (c) show results from MR observations, while panels (b), (d), and (f) show results from WACCM-X(SD) simulations. The median values of temperature (black line) and QRS (blue line) perturbations in the stratosphere (34-44 km altitude range) are presented in (e).

3.6 Semidiurnal tide amplification during SSW

The amplification of the semidiurnal tide during SSW events was reported in various previous studies (He et al., 2024; Forbes and Zhang, 2012; He and Chau, 2019), which primarily focused on wind and temperature from observations to investigate this phenomenon. Here, we present a detailed case study comparison between MR observations and WACCM-X(SD) in wind and temperature fields to further investigate semidiurnal tidal behavior. Figure 18 shows the semidurnal tide in zonal and meridional wind perturbations from both MR and WACCM-X(SD), including the temperature fields. Furthermore, we extracted the SW2 spectral band from QRS at mesosphere averaged over the 84–92 km altitude and overlaid it on the WACCM-X(SD) results. Both model and observations exhibit a strong semidiurnal tide throughout most of the winter season above 90-100 km, with a clear vertical phase progression indicative of upward propagation. In MR observations, semidiurnal tide amplification becomes apparent after the onset of the SSW event, whereas in WACCM-X(SD), enhancement begins several days earlier. The simulated tidal amplitudes are also considerably larger than those observed by MR. Notably, both WACCM-X(SD) and MR data

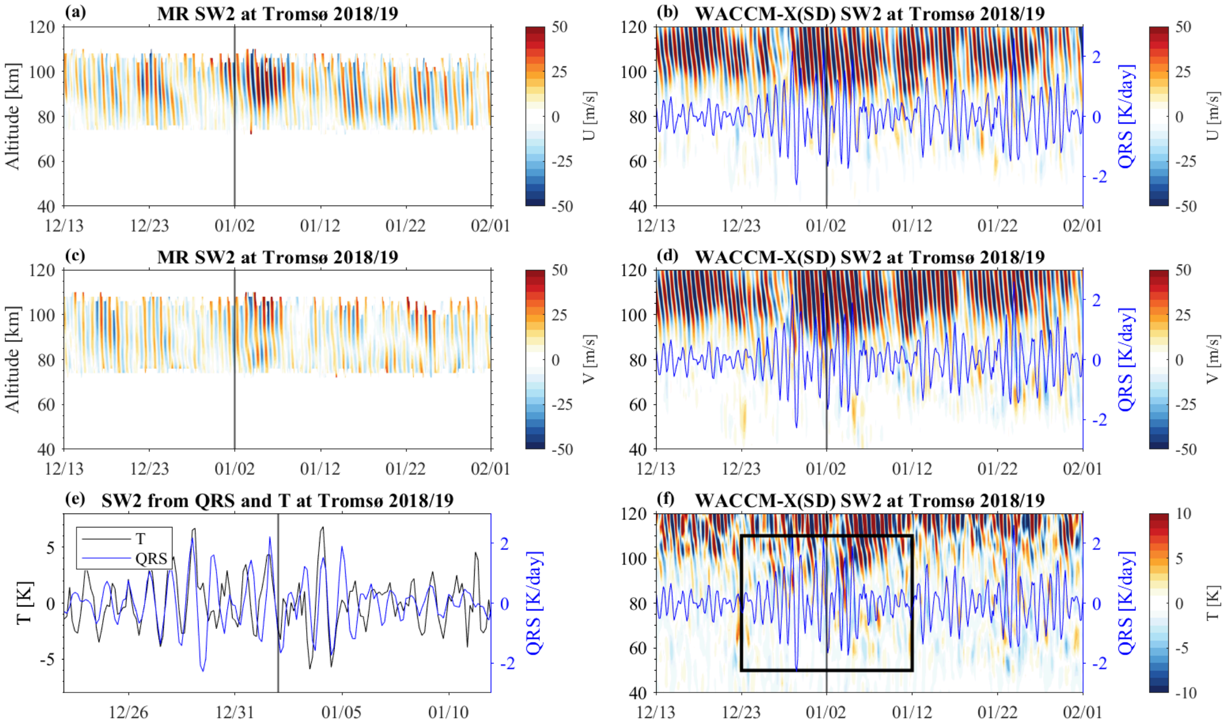

Figure 18. Time series of SW2 zonal and meridional winds, temperature, and QRS perturbations derived using adaptive spectral filtering over Tromsø before 20 days, and after 30 days following the SSW 2018/19 onset. Panels (a) and (c) show results from MR observations, while panels (b), (d), and (f) show results from WACCM-X(SD) simulations. A zoomed-out view of the time series (black solid lines) is shown in panel (f), corresponding to the median values of temperature (black line) and QRS (blue line) perturbations in the mesosphere (84-92 km altitude range) as presented in (e).

display distinct variability in the SW2 tide at multi-day to weekly timescales, which closely resembles modulations observed in the QRS. Filtering the QRS for the semidiurnal spectral contribution exhibits that several bursts of semidiurnal variation agree mostly in the time of their occurrence with an amplified semidiurnal tide in the winds in WACCM-X(SD). However, this coherence is much less visible in the semidiurnal temperature perturbations. Although our spectral analysis of the QRS reveals a semidiurnal variability, the physical mechanism driving this modulation remains uncertain. Nonetheless, such a semidiurnal modulation is beneficial to amplify the semidiurnal tide higher up in the MLT during the SSW.

We further examine the relationship between semidiurnal perturbation in QRS and temperature in Figure 18e. In the tidal amplification region between 82–92 km, the semidiurnal perturbation in QRS reaches approximately 50% of the temperature perturbation and shows even good agreement with periods of enhanced temperature amplitudes. Above this layer, both semidiurnal tidal wind and temperature amplitudes grow rapidly in WACCM-X(SD). MR tidal amplitudes also exhibit increasing magnitude with increasing height, but their amplitude reaches approximately 50% of the WACCM-X(SD).

4 Discussion

This study investigates the amplitude anomalies of DT, SDT, and TDT tides during SSW events using MR data from three polar-latitude stations. The combined analysis of tidal amplitude anomalies and trace gas variations provides new insights into the factors influencing tidal dynamics during SSWs, with a specific focus on the roles of ozone and water vapor. Our analysis of MR data reveals distinct responses of DT, SDT, and TDT during SSW events. Combining observations and model simulation results represents the attempt to explain mesospheric tidal variability in polar regions during SSWs by highlighting the critical roles of trace gases, and short-wave and long-wave radiative heating.

The sun might not be above the horizon all the time during the day, and, hence, the effective short-wave absorption might be smaller, which reduces the magnitude of the diurnal temperature change. In addition, it is important to emphasize that the observed tidal change is part of the global tidal response, and the heating/cooling driving those changes are not confined to winter high latitudes. The observed changes are a proxy for the global change, as discussed in the next paragraph. However, this is not the case for the QRL, which means that the middle atmosphere is dominated by effective daily cooling rates of up to 10 to 20 K/day at the MLT. This cooling of the middle atmosphere defines the large-scale temperature field, and the stratification of the middle atmosphere between the polar and middle latitudes drives the circulation and provides the background condition for the propagation of planetary, tidal, and gravity waves. These dynamic effects further contribute to the energy balance and the vertical coupling between the layers and can reach similar magnitudes to the QRL (see Appendix C).

Furthermore, the WACCM-X(SD) QRL and QRS values result from various processes, with contributions from the radiative effects of ozone and water vapor (see also Liu et al. (2010b) and references therein). Our comparison to these trace gases, thus, provides a proxy for the radiative heating changes. The radiative forcing, summarized, e.g., in Andrews et al. (1987), underlines that ozone is the most important absorber of UV radiation at the stratosphere and lower mesosphere. However, in the MLT region, oxygen and other chemical trace gases, resulting in exothermic heating, become significant. This is important to consider at the MLT, where QRS often indicates a morphology very similar to the ozone VMR, but other chemical reactions and absorbing species already dominate the absolute value, although ozone might affect the reaction rates or VMR of these species as well. This is in particular the case for atomic oxygen.

The enhancement of the diurnal tide 20-40 days after the SSW provides important insights into post/SSW tidal dynamics. This amplification appears to result directly from the increased ozone VMR, associated with the formation of the elevated stratopause. WACCM-X(SD) shows a strong correspondence between the QRS-induced diurnal heating and the diurnal temperature tide at the stratosphere. Although this diurnal tide is supposed to be a trapped mode due to its negative equivalent depth, the WACCM-X(SD) model exhibits a vertical propagation in both temperature and wind perturbations. In the MLT regions (80–90 km), however, the upward-propagating diurnal tide appears to be annihilated and disappears. At these altitudes, the upward propagating diurnal tide is out of phase with the diurnal modulation of the QRS. Thus, heating occurs at heights corresponding to the secondary ozone layer. Given the energy and momentum conservation, the dissipated tidal energy may be transferred to other wave modes or the background mean flow. It is plausible that wave–wave interactions, such as nonlinear wave coupling, could facilitate the generation of secondary tides, potentially contributing to the observed semidiurnal tide amplification. However, a detailed analysis of these processes is beyond the scope of this study.

Non-migrating tides are also affected by SSW events, though they exhibit considerable inter-event variability (Liu et al., 2010b; Miyoshi et al., 2017; Stober et al., 2020). Their forcing seems to depend on the longitudinal difference in the vertical propagation and longitudinal variations of the main absorbing trace gases and the planetary wave activity in the middle atmosphere. In particular, ozone VMR is modulated by the planetary wave activity, which transports ozone-rich airmasses from the mid-latitudes to high latitudes at stratospheric altitudes. Note, however, that we obtain the combined signature of migrating and non-migrating tides from single-station measurements.

We also analyzed observations from the southernmost MR available in the European sector. The Collm MR (51.3°N,13°E) is located at the edge of the polar vortex and, thus, sometimes shows signs of SSW events. As a result, the derived mean winds and tidal anomalies show a morphology similar to that observed at polar and high latitudes. The Collm observations also reflect the enhancement of DT and SDT (see Appendix B1), suggesting a hemispheric impact of these anomalies from polar to the mid-latitudes. A few degrees further south, observations from MIAWARA and GROMOS provide additional insights. Figure B2 shows composite water vapor and ozone VMR for the location at Zimmerwald/Bern (47°N, 7°E), Switzerland. Applying the same composite analysis to the ozone and water vapor measurements from GROMOS and MIAWARA at midlatitudes reveals no discernible signatures associated with the SSW events. This is also reflected in the QRL and QRS anomalies shown in Appendix B3. The QRL and QRS cooling and heating rates indicate a more stratified vertical structure resembling the layering found in the trace gas measurements at the stratosphere and lower mesosphere.

One crucial aspect of the presented analysis is the implementation of the adaptive spectral filter technique, which is designed to infer the short-term tidal variability using an adaptive window length for each tidal mode, performing an onion peeling scheme solving first for the mean wind and diurnal tide and other long-period oscillations, which are later used as background regularization for the higher frequency tidal components (Baumgarten and Stober, 2019; Stober et al., 2020). A critical aspect of the algorithm is that the number of wave cycles determines the window length for each tidal component that is extracted, which in the case of the TDT, SDT, and DT is very short, resulting in a rather wide bandwidth around each tidal frequency; thus, there could be some contamination due to gravity wave activity that falls into this band. The reduction of TDT amplitude during the SSW might be a combined result of a weakening of the tidal generation and changes in GW activity in the stratosphere. A recent study has shown that the polar vortex itself can act as a source of GWs (Vadas et al., 2024), and this source diminishes during the SSW as the polar vortex breaks down.

Our results also confirm the results obtained in van Caspel et al. (2023) using the PRimitive equations In Sigma-coordinates Model (PRISM) tidal model and the Navy Global Environmental Model-High Altitude (NAVGEM-HA) background dynamics to investigate the role of lunar tides relative to the SDT during SSWs. At Svalbard, the lunar tidal amplification should be minimal compared to the mid-latitudes. However, the presented analysis reveals a clear SDT amplification after the onset of the SSW, similar to Tromsø and Sodankylä. This points towards a minor contribution of the lunar tide, considering that lunar tidal potential changes with latitude (Vial and Forbes, 1994; van Caspel et al., 2023). Furthermore, lunar tides are also trapped tidal modes, resulting in a net zero vertical energy flux and requiring a similar mixing effect as proposed above to be amplified (Perkeris resonance). Separating both mechanisms is crucial and requires spectral decomposition on a day-to-day basis. All long window Fourier or wavelet-based methods require phase stability for the selected window length, which is about 21 days to separate a lunar tide from a semidiurnal tide. This assumption is not satisfied considering the day-to-day variability revealed by the adaptive spectral filter (Baumgarten and Stober, 2019; Stober et al., 2020). This underlines that radiative effects (heating/cooling) due to the increase/decrease of trace gases such as ozone play a key role in these short-term amplifications and can further amplify dynamical effects, altering the vertical tidal propagation during SSWs.

5 Conclusions

This study provides a comprehensive quantification of tidal variability and co-located tracer variability by combining observational data with model simulations. It discusses the radiative effects of tracer anomalies on mesospheric tidal variability during SSWs. Our analysis reveals distinct tidal responses to SSWs, characterized by a pronounced enhancement of SDT amplitudes following the onset of these events, while TDT amplitudes exhibit a decrease. The reduction in TDT during SSW likely results from a combination of diminished tidal generation and changes in gravity wave activity, which are strongly influenced by the breakdown of the polar vortex. The DT, in contrast, exhibits a delayed enhancement of amplitude, coinciding with the presence of an elevated stratopause and radiative heating effects driven by stratospheric ozone anomalies, which become prominent 20–30 days after the SSW onset. The observed SDT amplification is likely primarily due to the dynamical effect and modified by radiative heating effects modulated by ozone variability. Our correlation analysis between the semidiurnal tidal perturbation in QRS and temperature at the amplification region suggests that direct radiative absorption plays some role in the observed tidal enhancement. The ozone VMR exhibits distinct diurnal modulations at both the stratospheric ozone layer and the secondary ozone layer, forming a double-layer structure that plays a pivotal role in modulating semidiurnal tidal activity during winter at high latitudes, which leads to a constructive superposition of in situ and propagating DT components resulting in enhanced tidal SDT amplitudes in the MLT region. However, this proposed mechanism requires further investigation and confirmation in future studies.

Radiative processes, including both QRS heating and QRL cooling rates, play a fundamental role in shaping the large-scale temperature structure and atmospheric stratification, thereby modulating the background conditions for planetary, tidal, and gravity wave propagation. The longwave radiative effect dominates cooling processes in the MLT, with daily-averaged cooling rates reaching up to -20 K/day. The dominance of QRL at mesospheric and lower thermospheric altitudes underscores its significance in governing energy balance and vertical coupling processes in the middle atmosphere.

In summary, this study provides new insights into the coupling between trace gas variations, radiative heating, and tidal dynamics in the polar mesosphere during SSWs. Future work should further quantify the isolated radiative effects on tidal generation, potentially through targeted model simulations that distinguish between dynamical and radiative contributions.

Code availability. As a component of the community earth system model, WACCM-X source codes are publicly available at https://www.cesm.ucar.edu/ (NCAR, 2024).

Data availability. MLS v5 data are available from the NASA Goddard Space Flight Center Earth Sciences Data and Information Services Center (GES DISC): https://doi.org/10.5067/Aura/MLS/DATA2516 (Schwartz et al., 2020). The MR data can be obtained upon request from the instrument PIs. The 3-hourly WACCM-X simulation output is archived on NCAR's archive repository and can be obtained upon request from Guochun Shi. The GROMOS-C and MIAWARA-C level 2 data are provided by the Network for the Detection of Atmospheric Composition Change and are available at https://www-air.larc.nasa.gov/pub/NDACC/PUBLIC/meta/mwave/ (University of Bern, 2024). NOAA CSL: Chemistry & Climate Processes: SSWC, https://csl.noaa.gov/groups/csl8/sswcompendium/majorevents.html, (last access: October 2024).

Author contributions. GShi was responsible for the WACCM-X simulations, performed the data analysis, and prepared the manuscript. GStober contributed to the interpretation of the results. NG, MT, CJ, and AK provided MR data. HL and KW provided their technical assistance in setting up the WACCM-X simulations, and DP supported data reduction. All of the authors provided valuable feedback for manuscript editing.

Competing interests. The contact author has declared that none of the authors has any competing interests.

Acknowledgements. Guochun Shi and Gunter Stober are members of the Oeschger Center for Climate Change Research. We acknowledge the PIs for maintaining radar operations. We also thank Douglas Kinnison for helpful discussions and Joe McInerney for his technical assistance in setting up the WACCM-X simulations. Guochun Shi would like to acknowledge travel support provided by the High Altitude Observatory Visitor Committee. We thank the Aura/MLS team and NASA/JPL for providing the Microwave Limb Sounding measurements, with the level 2 data set available through the Aura Validation Data Center. Christoph Jacobi acknowledges the support of the IAP Kühlungsborn, Germany, for their support in the maintenance of the Collm radar. This research was supported by the International Space Science Institute (ISSI) in Bern, through ISSI International Team project # 23-580 "Meteors and phenomena at the boundary between Earth's atmosphere and outer space". National Center for Atmospheric Research is a major facility sponsored by the National Science Foundation under Cooperative Agreement No. 1852977.

Financial support. This research has been supported by the Swiss National Science Foundation (grant no. 200021-200517/1) and STFC UK grant (ST/W00089X/1). This research employed data from instruments supported by the Research Council of Norway under the project Svalbard Integrated Arctic Earth Observing System—Infrastructure Development of the Norwegian node (SIOS-InfraNor, Project No. 269927). The operation of MIAWARA-C and GROMOS-C is supported by AWIPEV under grant AWIPEV_0023.

Appendix A: Tidal amplitudes from WACCM-X(SD)

Appendix B: Mean winds and tidal amplitudes at mid-latitude station

Table A1. Dates of major SSW events were used for the composite in this study.

Number	Winters	SSW central date
1	2005/2006	21 Jan 2006
2	2006/2007	24 Feb 2007
3	2007/2008	22 Feb 2008
4	2008/2009	24 Jan 2009
5	2009/2010	09 Feb 2010
6	2012/2013	06 Jan 2013
7	2017/2018	12 Feb 2018
8	2018/2019	02 Jan 2019
9	2020/2021	03 Jan 2021
10	2022/2023	16 Feb 2023

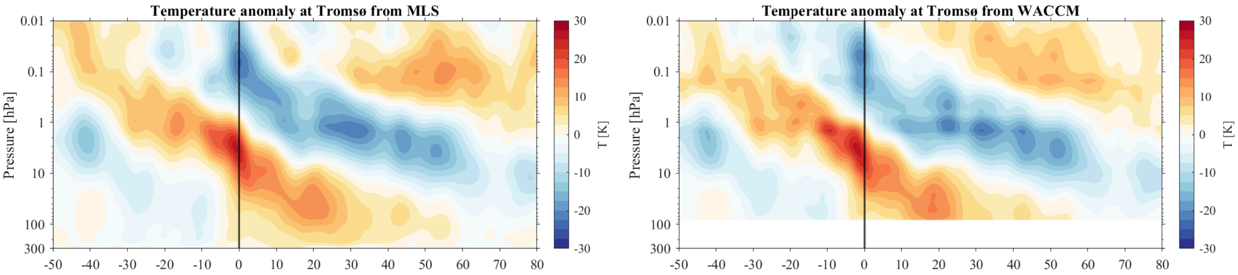

Figure A1. The cross-section of SSW composite temperature anomalies at Tromsø from MLS and WACCM-X(SD).

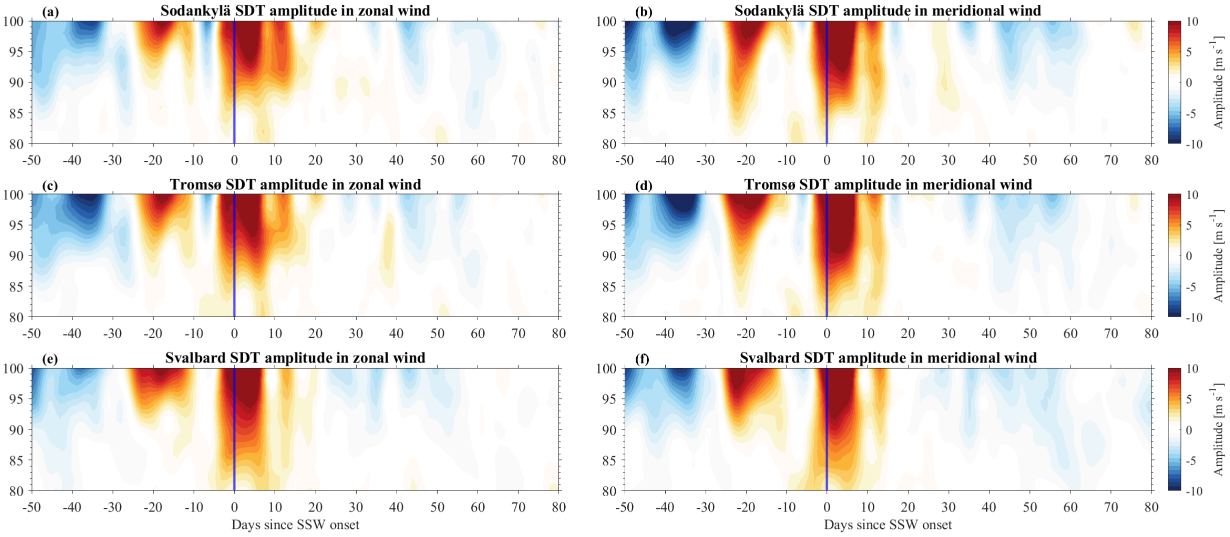

Figure A2. The same as Figure. 7 but for WACCM-X(SD).

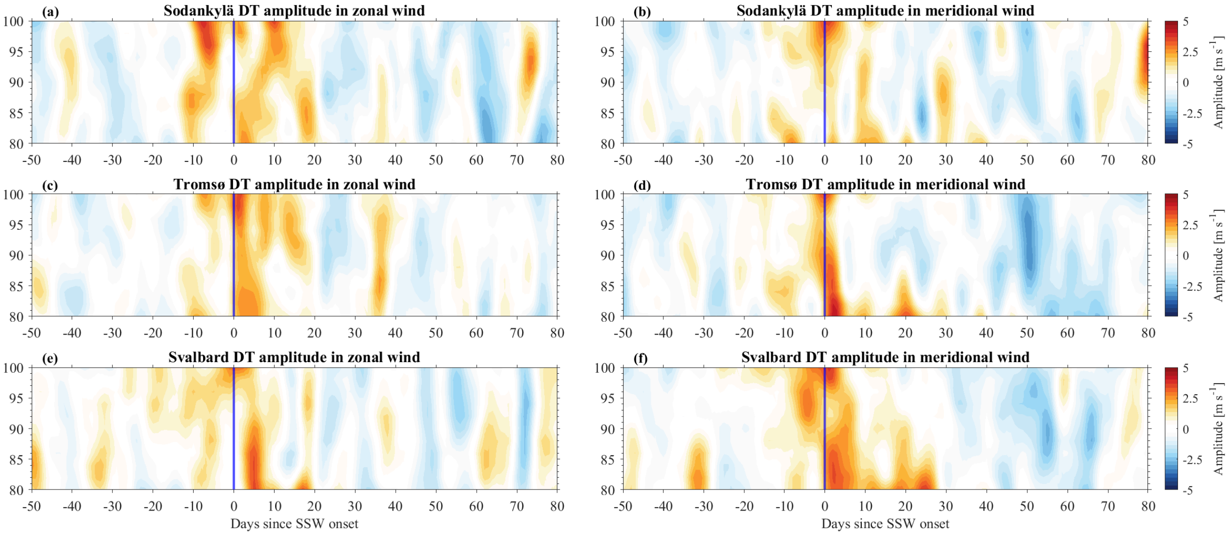

Figure A3. The same as Figure. 8 but for WACCM-X(SD).

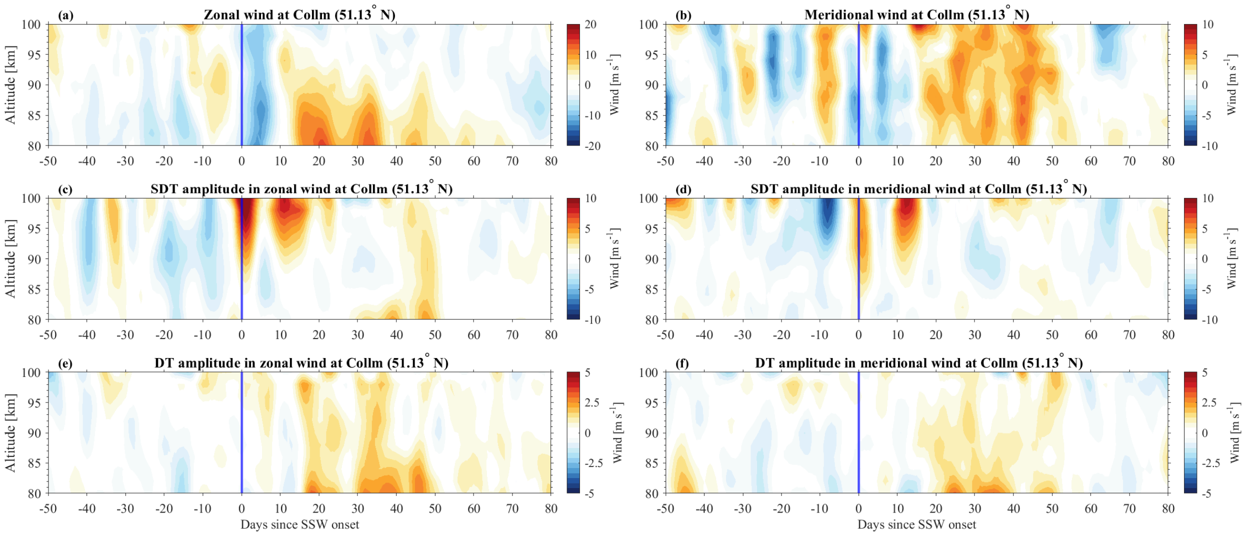

Figure B1. The cross-section of SSW composite wind anomaly, SDT and DT amplitude anomalies in the zonal (left panels) and meridional (right panels) wind components observed with MR at Collm (51.13°N, 13.01°E).

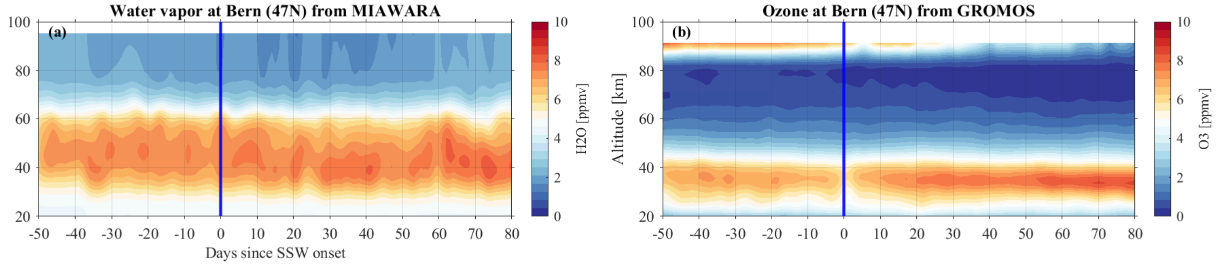

Figure B2. The cross-sections of SSW composite water vapor and ozone from ground-based microwave radiometers GROMOS and MIAWARA at Bern (47°N, 7°E).

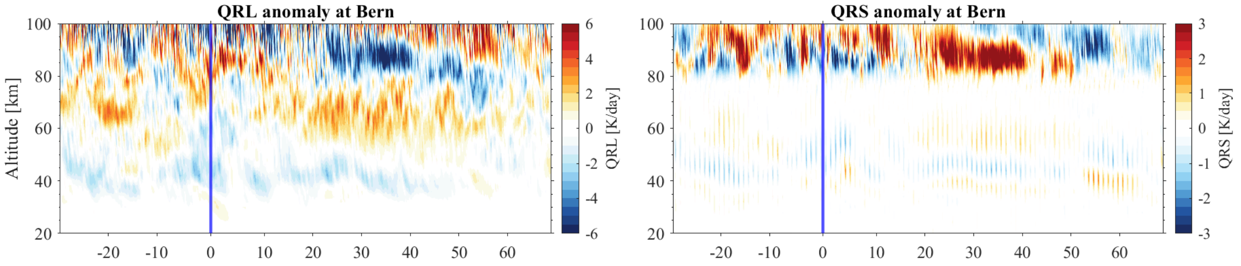

Figure B3. The cross-sections of SSW composite QRL and QRS anomalies from WACCM-X(SD) at Bern (47°N, 7°E).

Appendix C: Dynamic effects

To better understand these processes, we calculate dynamical heating and cooling rates associated with the air motion in the Arctic region (65-90°N), along with the long-wave cooling and short-wave heating rates from a diagnostic viewpoint, as shown in Figure C1. The dynamic rates associated with meridional and vertical motions according to the transformed Eulerian mean framework described by equations 3.5.1 in Andrews et al. (1987) are calculated as follows:

$$Q_{dyn} = -[\overline{v}^* \frac{\partial \overline{T}}{\partial y} + \overline{\omega}^* (\frac{HN^2}{R} + \frac{\partial \overline{T}}{\partial z})] \tag{C1}$$

where $\overline{T}$ is the zonally averaged deviation from the global mean temperature, $\frac{\partial \overline{T}}{\partial z}$ represents the temperature gradient, and $\frac{HN^2}{R}$ represents the global mean static stability. Q_{dyn} is the dynamic heating/cooling rate. The $\overline{v}^*$ and $\overline{\omega}^*$ are the residual meridional and vertical winds.

The results indicate that anomalous vertical descent, as shown in Figure C2, causes adiabatic heating in the stratosphere around 10 hPa before the SSW onset, which is only minimally offset by QRL radiative cooling, making the process nearly adiabatic. The upward branch of the enhanced circulation, on the other hand, leads to dynamical cooling in the mesosphere, minimally offset by a reduction in QRL. Although the dynamical heating/cooling term Q_{dyn} dominates in the stratosphere and mesosphere (Figure C1a), the radiative effects from QRL and QRS (Figure C2b, c) play a crucial role in shaping the evolution of the thermal structure of the middle atmosphere. The residual vertical wind is calculated at each time step using Equation 3.5.1b in Andrews et al. (1987). In the middle stratosphere before day 0, a negative $\overline{\omega}^*$ indicates downwelling, resulting in dynamic heating due to enhanced descent. In the mesosphere at onset, a positive $\overline{\omega}^*$ signifies upwelling, leading to dynamic cooling associated with increased ascent.

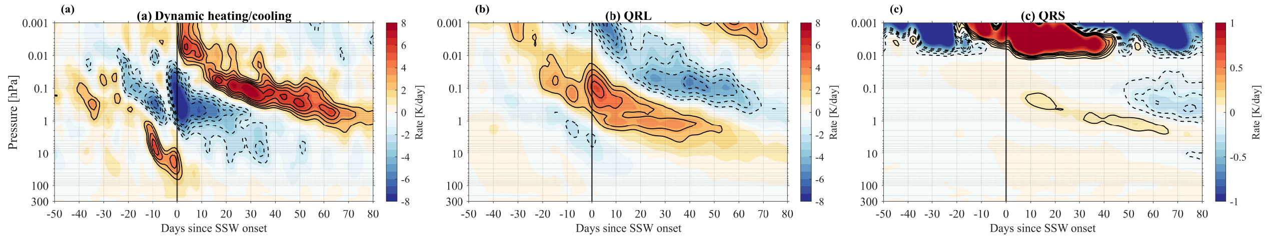

Figure C1. The cross-section of the anomaly of dynamic heating/cooling (Q_{dyn}), QRL, and QRS heating rates averaged over 65-90°N from WACCM-X data.

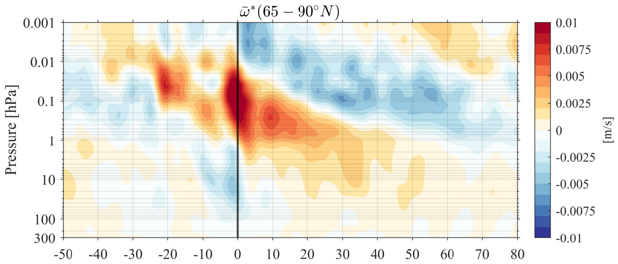

Figure C2. The cross-section of $\overline{\omega}^*$ anomaly during SSW compiste.

References

Andrews, D., Holton, J., and Leovy, C.: Middle Atmosphere Dynamics, International Geophysics, Elsevier Science, 1987.

Baldwin, M. P., Ayarzagüena, B., Birner, T., Butchart, N., Butler, A. H., Charlton-Perez, A. J., Domeisen, D. I., Garfinkel, C. I., Garny, H., Gerber, E. P., et al.: Sudden stratospheric warmings, Reviews of Geophysics, 59, e2020RG000 708, 2021.

Baumgarten, K. and Stober, G.: On the evaluation of the phase relation between temperature and wind tides based on ground-based measurements and reanalysis data in the middle atmosphere, Annales Geophysicae, 37, 581–602, https://doi.org/10.5194/angeo-37-581-2019, 2019.

Becker, E.: Mean-Flow Effects of Thermal Tides in the Mesosphere and Lower Thermosphere, Journal of the Atmospheric Sciences, 74, 2043 – 2063, https://doi.org/10.1175/JAS-D-16-0194.1, 2017.

Bell, A., Sauvageat, E., Stober, G., Hocke, K., and Murk, A.: Developments on a 22GHz Microwave Radiometer and Reprocessing of 13-Year Time Series for Water Vapour Studies, EGUsphere, 2024, 1–20, https://doi.org/10.5194/egusphere-2024-2474, 2024.

Bhattacharya, Y., Shepherd, G., and Brown, S.: Variability of atmospheric winds and waves in the Arctic polar mesosphere during a stratospheric sudden warming, Geophysical Research Letters, 31, 2004.

Boyd, I. S., Parrish, A. D., Froidevaux, L., Von Clarmann, T., Kyrölä, E., Russell III, J. M., and Zawodny, J. M.: Ground-based microwave ozone radiometer measurements compared with Aura-MLS v2. 2 and other instruments at two Network for Detection of Atmospheric Composition Change sites, Journal of Geophysical Research: Atmospheres, 112, 2007.

Brasseur, G. P. and Solomon, S.: Aeronomy of the middle atmosphere: Chemistry and physics of the stratosphere and mesosphere, vol. 32, Springer Science & Business Media, 2005.

Butler, A. H., Sjoberg, J. P., Seidel, D. J., and Rosenlof, K. H.: A sudden stratospheric warming compendium, Earth System Science Data, 9, 63–76, 2017.

Chau, J., Hoffmann, P., Pedatella, N., Matthias, V., and Stober, G.: Upper mesospheric lunar tides over middle and high latitudes during sudden stratospheric warming events, Journal of Geophysical Research: Space Physics, 120, 3084–3096, 2015.

Davis, N., Richter, J., Glanville, A., Edwards, J., and LaJoie, E.: Limited surface impacts of the January 2021 sudden stratospheric warming, Nature communications, 13, 1136, 2022.

de la Cámara, A., Abalos, M., Hitchcock, P., Calvo, N., and Garcia, R. R.: Response of Arctic ozone to sudden stratospheric warmings, Atmospheric Chemistry and Physics, 18, 16 499–16 513, https://doi.org/10.5194/acp-18-16499-2018, 2018.

Dempsey, S. M., Hindley, N. P., Moffat-Griffin, T., Wright, C. J., Smith, A. K., Du, J., and Mitchell, N. J.: Winds and tides of the Antarctic mesosphere and lower thermosphere: One year of meteor-radar observations over Rothera (68 S, 68 W) and comparisons with WACCM and eCMAM, Journal of Atmospheric and Solar-Terrestrial Physics, 212, 105 510, 2021.

Domeisen, D. I., Grams, C. M., and Papritz, L.: The role of North Atlantic–European weather regimes in the surface impact of sudden stratospheric warming events, Weather and Climate Dynamics, 1, 373–388, 2020.

Dutta, R., Sridharan, S., and Sinha, P.: Signature of sudden stratospheric warming in the pole and its antipode, Journal of Geophysical Research: Space Physics, 129, e2023JA032 285, 2024.

Eriksson, P., Jiménez, C., and Buehler, S. A.: Qpack, a general tool for instrument simulation and retrieval work, Journal of Quantitative Spectroscopy and Radiative Transfer, 91, 47–64, https://doi.org/https://doi.org/10.1016/j.jqsrt.2004.05.050, 2005.

Eriksson, P., Buehler, S., Davis, C., Emde, C., and Lemke, O.: ARTS, the atmospheric radiative transfer simulator, version 2, Journal of Quantitative Spectroscopy and Radiative Transfer, 112, 1551–1558, https://doi.org/https://doi.org/10.1016/j.jqsrt.2011.03.001, 2011.

Eswaraiah, S., Kim, Y. H., Lee, J., Ratnam, M. V., and Rao, S.: Effect of Southern Hemisphere sudden stratospheric warmings on Antarctica mesospheric tides: First observational study, Journal of Geophysical Research: Space Physics, 123, 2127–2140, 2018.

Fang, T.-W., Fuller-Rowell, T., Akmaev, R., Wu, F., Wang, H., and Anderson, D.: Longitudinal variation of ionospheric vertical drifts during the 2009 sudden stratospheric warming, Journal of Geophysical Research: Space Physics, 117, 2012.

Fernandez, S., Murk, A., and Kämpfer, N.: GROMOS-C, a novel ground-based microwave radiometer for ozone measurement campaigns, atmospheric measurement techniques, 8, 2649–2662, 2015.

Forbes, J. M. and Garrett, H. B.: Thermal excitation of atmospheric tides due to insolation absorption by O3 and H2O, Geophysical Research Letters, 5, 1013–1016, 1978.

Forbes, J. M. and Zhang, X.: Lunar tide amplification during the January 2009 stratosphere warming event: Observations and theory, Journal of Geophysical Research: Space Physics, 117, 2012.

Gelaro, R., McCarty, W., Suárez, M. J., Todling, R., Molod, A., Takacs, L., Randles, C. A., Darmenov, A., Bosilovich, M. G., Reichle, R., et al.: The modern-era retrospective analysis for research and applications, version 2 (MERRA-2), Journal of climate, 30, 5419–5454, 2017.

Gettelman, A., Mills, M. J., Kinnison, D. E., Garcia, R. R., Smith, A. K., Marsh, D. R., Tilmes, S., Vitt, F., Bardeen, C. G., McInerny, J., Liu, H.-L., Solomon, S. C., Polvani, L. M., Emmons, L. K., Lamarque, J.-F., Richter, J. H., Glanville, A. S., Bacmeister, J. T., Phillips, A. S., Neale, R. B., Simpson, I. R., DuVivier, A. K., Hodzic, A., and Randel, W. J.: The Whole Atmosphere Community Climate Model Version 6 (WACCM6), Journal of Geophysical Research: Atmospheres, 124, 12 380–12 403, https://doi.org/https://doi.org/10.1029/2019JD030943, 2019.

Goncharenko, L., Coster, A., Plumb, R. A., and Domeisen, D. I.: The potential role of stratospheric ozone in the stratosphere-ionosphere coupling during stratospheric warmings, Geophysical Research Letters, 39, 2012.

Günzkofer, F., Pokhotelov, D., Stober, G., Liu, H., Liu, H.-L., Mitchell, N. J., Tjulin, A., and Borries, C.: Determining the Origin of Tidal Oscillations in the Ionospheric Transition Region With EISCAT Radar and Global Simulation Data, Journal of Geophysical Research: Space Physics, 127, e2022JA030 861, https://doi.org/https://doi.org/10.1029/2022JA030861, e2022JA030861 2022JA030861, 2022.

Hall, R. J., Mitchell, D. M., Seviour, W. J., and Wright, C. J.: Tracking the stratosphere-to-surface impact of sudden stratospheric warmings, Journal of Geophysical Research: Atmospheres, 126, e2020JD033 881, 2021.

Haynes, P., McIntyre, M., Shepherd, T., Marks, C., and Shine, K. P.: On the “downward control” of extratropical diabatic circulations by eddy-induced mean zonal forces, Journal of the Atmospheric Sciences, 48, 651–678, 1991.

He, M. and Chau, J. L.: Mesospheric semidiurnal tides and near-12 h waves through jointly analyzing observations of five specular meteor radars from three longitudinal sectors at boreal midlatitudes, Atmospheric Chemistry and Physics, 19, 5993–6006, 2019.

He, M., Chau, J. L., Forbes, J. M., Thorsen, D., Li, G., Siddiqui, T. A., Yamazaki, Y., and Hocking, W. K.: Quasi-10-day wave and semidiurnal tide nonlinear interactions during the Southern Hemispheric SSW 2019 observed in the Northern Hemispheric mesosphere, Geophysical Research Letters, 47, e2020GL091 453, 2020.

He, M., Forbes, J. M., Stober, G., Jacobi, C., Li, G., Liu, L., and Xu, J.: Nonlinear Interactions of Planetary-Scale Waves in Mesospheric Winds Observed at 52°N Latitude and Two Longitudes, Geophysical Research Letters, 51, e2024GL110 629, https://doi.org/https://doi.org/10.1029/2024GL110629, e2024GL110629 2024GL110629, 2024.

Hibbins, R., Espy, P. J., Orsolini, Y., Limpasuvan, V., and Barnes, R.: SuperDARN observations of semidiurnal tidal variability in the MLT and the response to sudden stratospheric warming events, Journal of Geophysical Research: Atmospheres, 124, 4862–4872, 2019.

Hocking, W., Fuller, B., and Vandepeer, B.: Real-time determination of meteor-related parameters utilizing modern digital technology, Journal of Atmospheric and Solar-Terrestrial Physics, 63, 155–169, 2001.

Hoffmann, P., Singer, W., Keuer, D., Hocking, W., Kunze, M., and Murayama, Y.: Latitudinal and longitudinal variability of mesospheric winds and temperatures during stratospheric warming events, Journal of Atmospheric and Solar-Terrestrial Physics, 69, 2355–2366, 2007.

Holdsworth, D. A., Reid, I. M., and Cervera, M. A.: Buckland Park all-sky interferometric meteor radar, Radio Science, 39, n/a–n/a, https://doi.org/10.1029/2003RS003014, rS5009, 2004.

Iida, C., Hirooka, T., and Eguchi, N.: Circulation changes in the stratosphere and mesosphere during the stratospheric sudden warming event in January 2009, Journal of Geophysical Research: Atmospheres, 119, 7104–7115, 2014.

Jacobi, C., Portnyagin, Y. I., Solovjova, T., Hoffmann, P., Singer, W., Fahrutdinova, A., Ishmuratov, R., Beard, A., Mitchell, N., Muller, H., et al.: Climatology of the semidiurnal tide at 52–56 N from ground-based radar wind measurements 1985–1995, Journal of Atmospheric and Solar-Terrestrial Physics, 61, 975–991, 1999.

Jin, H., Miyoshi, Y., Pancheva, D., Mukhtarov, P., Fujiwara, H., and Shinagawa, H.: Response of migrating tides to the stratospheric sudden warming in 2009 and their effects on the ionosphere studied by a whole atmosphere-ionosphere model GAIA with COSMIC and TIMED/SABER observations, Journal of Geophysical Research: Space Physics, 117, 2012.

Jones Jr., M., Siskind, D. E., Drob, D. P., McCormack, J. P., Emmert, J. T., Dhadly, M. S., Attard, H. E., Mlynczak, M. G., Brown, P. G., Stober, G., Kozlovsky, A., Lester, M., and Jacobi, C.: Coupling From the Middle Atmosphere to the Exobase: Dynamical Disturbance Effects on Light Chemical Species, Journal of Geophysical Research: Space Physics, 125, e2020JA028 331, https://doi.org/https://doi.org/10.1029/2020JA028331, e2020JA028331 10.1029/2020JA028331, 2020.

Krochin, W., Murk, A., and Stober, G.: Thermal tides in the middle atmosphere at mid-latitudes measured with a ground-based microwave radiometer, Atmospheric Measurement Techniques, 17, 5015–5028, https://doi.org/10.5194/amt-17-5015-2024, 2024.

Li, Y., Kirchengast, G., Schwaerz, M., and Yuan, Y.: Monitoring sudden stratospheric warmings under climate change since 1980 based on reanalysis data verified by radio occultation, Atmospheric Chemistry and Physics, 23, 1259–1284, 2023.

Lilienthal, F. and Jacobi, C.: Nonlinear forcing mechanisms of the terdiurnal solar tide and their impact on the zonal mean circulation, Annales Geophysicae Discusses, pp. 1–18, 2019.

Lilienthal, F., Jacobi, C., and Geißler, C.: Forcing mechanisms of the terdiurnal tide, Atmospheric Chemistry and Physics, 18, 15 725–15 742, 2018.

Lima, L., Alves, E., Batista, P., Clemesha, B., Medeiros, A., and Buriti, R.: Sudden stratospheric warming effects on the mesospheric tides and 2-day wave dynamics at 7 S, Journal of Atmospheric and Solar-Terrestrial Physics, 78, 99–107, 2012.

Limpasuvan, V., Orsolini, Y. J., Chandran, A., Garcia, R. R., and Smith, A. K.: On the composite response of the MLT to major sudden stratospheric warming events with elevated stratopause, Journal of Geophysical Research: Atmospheres, 121, 4518–4537, 2016.

Lindzen, R. S. and Chapman, S.: Atmospheric tides, Space science reviews, 10, 3–188, 1969.

Liu, G., Lieberman, R. S., Harvey, V. L., Pedatella, N. M., Oberheide, J., Hibbins, R. E., Espy, P. J., and Janches, D.: Tidal variations in the mesosphere and lower thermosphere before, during, and after the 2009 sudden stratospheric warming, Journal of Geophysical Research: Space Physics, 126, e2020JA028 827, 2021.

Liu, G., Janches, D., Ma, J., Lieberman, R. S., Stober, G., Moffat-Griffin, T., Mitchell, N. J., Kim, J.-H., Lee, C., and Murphy, D. J.: Mesosphere and lower thermosphere winds and tidal variations during the 2019 Antarctic sudden stratospheric warming, Journal of Geophysical Research: Space Physics, 127, e2021JA030 177, 2022.

Liu, H., Foster, B. T., Hagan, M. E., McInerney, J. M., Maute, A., Qian, L., Richmond, A. D., Roble, R. G., Solomon, S. C., Garcia, R. R., Kinnison, D., Marsh, D. R., Smith, A. K., Richter, J., Sassi, F., and Oberheide, J.: Thermosphere extension of the Whole Atmosphere Community Climate Model, Journal of Geophysical Research: Space Physics, 115, https://doi.org/10.1029/2010ja015586, 2010a.

Liu, H.-L., Wang, W., Richmond, A., and Roble, R.: Ionospheric variability due to planetary waves and tides for solar minimum conditions, Journal of Geophysical Research: Space Physics, 115, 2010b.

Liu, H.-L., Bardeen, C. G., Foster, B. T., Lauritzen, P., Liu, J., Lu, G., Marsh, D. R., Maute, A., McInerney, J. M., Pedatella, N. M., Qian, L., Richmond, A. D., Roble, R. G., Solomon, S. C., Vitt, F. M., and Wang, W.: Development and Validation of the Whole Atmosphere Community Climate Model With Thermosphere and Ionosphere Extension (WACCM-X 2.0), Journal of Advances in Modeling Earth Systems, 10, 381–402, https://doi.org/10.1002/2017MS001232, 2018.

Manney, G. L., Schwartz, M. J., Krüger, K., Santee, M. L., Pawson, S., Lee, J. N., Daffer, W. H., Fuller, R. A., and Livesey, N. J.: Aura Microwave Limb Sounder observations of dynamics and transport during the record-breaking 2009 Arctic stratospheric major warming, Geophysical Research Letters, 36, 2009.

Marsh, D. R., Mills, M. J., Kinnison, D. E., Lamarque, J.-F., Calvo, N., and Polvani, L. M.: Climate change from 1850 to 2005 simulated in CESM1 (WACCM), Journal of climate, 26, 7372–7391, 2013.

Matsuno, T.: A dynamical model of the sudden stratospheric warming phenomenon, J. Atmos. Sci, 28, 1479–1494, 1971.

Matthias, V., Hoffmann, P., Manson, A., Meek, C., Stober, G., Brown, P., and Rapp, M.: The impact of planetary waves on the latitudinal displacement of sudden stratospheric warmings, Annales Geophysicae, 31, 1397–1415, https://doi.org/10.5194/angeo-31-1397-2013, 2013.

Matthias, V., Stober, G., Kozlovsky, A., Lester, M., Belova, E., and Kero, J.: Vertical Structure of the Arctic Spring Transition in the Middle Atmosphere, Journal of Geophysical Research: Atmospheres, 126, e2020JD034 353, https://doi.org/https://doi.org/10.1029/2020JD034353, e2020JD034353 2020JD034353, 2021.

Mitra, G., Guharay, A., and Paulino, I.: Signature of a zonally symmetric semidiurnal tide during major sudden stratospheric warmings and plausible mechanisms: a case study, Scientific Reports, 14, 23 806, 2024.

Miyoshi, Y., Pancheva, D., Mukhtarov, P., Jin, H., Fujiwara, H., and Shinagawa, H.: Excitation mechanism of non-migrating tides, Journal of Atmospheric and Solar-Terrestrial Physics, 156, 24–36, https://doi.org/https://doi.org/10.1016/j.jastp.2017.02.012, 2017.

Moudden, Y. and Forbes, J.: A decade-long climatology of terdiurnal tides using TIMED/SABER observations, Journal of Geophysical Research: Space Physics, 118, 4534–4550, 2013.

Neale, R. B., Richter, J., Park, S., Lauritzen, P. H., Vavrus, S. J., Rasch, P. J., and Zhang, M.: The mean climate of the Community Atmosphere Model (CAM4) in forced SST and fully coupled experiments, Journal of Climate, 26, 5150–5168, 2013.

Nedoluha, G. E., Kiefer, M., Lossow, S., Gomez, R. M., Kämpfer, N., Lainer, M., Forkman, P., Christensen, O. M., Oh, J. J., Hartogh, P., et al.: The SPARC water vapor assessment II: intercomparison of satellite and ground-based microwave measurements, Atmospheric chemistry and physics, 17, 14 543–14 558, 2017.

Pedatella, N. and Forbes, J.: Evidence for stratosphere sudden warming-ionosphere coupling due to vertically propagating tides, Geophysical Research Letters, 37, 2010.

Pedatella, N. and Liu, H.-L.: The influence of atmospheric tide and planetary wave variability during sudden stratosphere warmings on the low latitude ionosphere, Journal of Geophysical Research: Space Physics, 118, 5333–5347, 2013.

Pedatella, N., Liu, H.-L., Richmond, A., Maute, A., and Fang, T.-W.: Simulations of solar and lunar tidal variability in the mesosphere and lower thermosphere during sudden stratosphere warmings and their influence on the low-latitude ionosphere, Journal of Geophysical Research: Space Physics, 117, 2012.

Pedatella, N., Raeder, K., Anderson, J., and Liu, H.-L.: Ensemble data assimilation in the whole atmosphere community climate model, Journal of Geophysical Research: Atmospheres, 119, 9793–9809, 2014.

Qiao, Z., Liu, A. Z., Pedatella, N., Stober, G., Reid, I. M., Fuentes, J., and Adami, C. L.: Evidence for SSW triggered Q6DW-tide and Q6DW-gravity wave interactions observed by meteor radars at 30 S, Geophysical Research Letters, 51, e2023GL108 066, 2024.

Rodgers, C. D.: Inverse methods for atmospheric sounding: theory and practice, vol. 2, World scientific, 2000.

Sathishkumar, S. and Sridharan, S.: Lunar and solar tidal variabilities in mesospheric winds and EEJ strength over Tirunelveli (8.7 N, 77.8 E) during the 2009 major stratospheric warming, Journal of Geophysical Research: Space Physics, 118, 533–541, 2013.

Schranz, F., Fernandez, S., Kämpfer, N., and Palm, M.: Diurnal variation in middle-atmospheric ozone observed by ground-based microwave radiometry at Ny-Ålesund over 1 year, Atmospheric Chemistry and Physics, 18, 4113–4130, https://doi.org/10.5194/acp-18-4113-2018, 2018.

Schranz, F., Tschanz, B., Rüfenacht, R., Hocke, K., Palm, M., and Kämpfer, N.: Investigation of Arctic middle-atmospheric dynamics using 3 years of H_2O and O_3 measurements from microwave radiometers at Ny-Ålesund, Atmospheric Chemistry and Physics, 19, 9927–9947, https://doi.org/10.5194/acp-19-9927-2019, 2019.

Schranz, F., Hagen, J., Stober, G., Hocke, K., Murk, A., and Kämpfer, N.: Small-scale variability of stratospheric ozone during the sudden stratospheric warming 2018/2019 observed at Ny-Ålesund, Svalbard, Atmospheric chemistry and physics, 20, 10 791–10 806, 2020.

Schwartz, M., Froidevaux, L., Livesey, N., and Read, W.: MLS/Aura Level 2 Ozone (O3) Mixing Ratio V005, Greenbelt, MD, USA, Goddard Earth Sciences Data and Information Services Center (GES DISC), https://doi.org/10.5067/Aura/MLS/DATA2516, 2020.

Schwartz, M. J., Lambert, A., Manney, G. L., Read, W. G., Livesey, N. J., Froidevaux, L., Ao, C. O., Bernath, P. F., Boone, C. D., Cofield, R. E., Daffer, W. H., Drouin, B. J., Fetzer, E. J., Fuller, R. A., Jarnot, R. F., Jiang, J. H., Jiang, Y. B., Knosp, B. W., Krüger, K., Li, J.-L. F., Mlynczak, M. G., Pawson, S., Russell III, J. M., Santee, M. L., Snyder, W. V., Stek, P. C., Thurstans, R. P., Tompkins, A. M., Wagner, P. A., Walker, K. A., Waters, J. W., and Wu, D. L.: Validation of the Aura Microwave Limb Sounder temperature and geopotential height measurements, Journal of Geophysical Research: Atmospheres, 113, https://doi.org/https://doi.org/10.1029/2007JD008783, 2008.

Shi, G., Krochin, W., Sauvageat, E., and Stober, G.: Ozone and water vapor variability in the polar middle atmosphere observed with ground-based microwave radiometers, Atmospheric Chemistry and Physics, 23, 9137–9159, https://doi.org/10.5194/acp-23-9137-2023, 2023.

Shi, G., Krochin, W., Sauvageat, E., and Stober, G.: Ozone anomalies over the polar regions during stratospheric warming events, Atmospheric Chemistry and Physics, 24, 10 187–10 207, 2024.

Siddiqui, T., Maute, A., and Pedatella, N.: On the importance of interactive ozone chemistry in Earth-system models for studying mesosphere-lower thermosphere tidal changes during sudden stratospheric warmings, Journal of Geophysical Research: Space Physics, 124, 10 690–10 707, 2019.

Siddiqui, T. A., Maute, A., Pedatella, N., Yamazaki, Y., Lühr, H., and Stolle, C.: On the variability of the semidiurnal solar and lunar tides of the equatorial electrojet during sudden stratospheric warmings, in: Annales Geophysicae, vol. 36, pp. 1545–1562, Copernicus Publications Göttingen, Germany, 2018.

Sridharan, S., Sathishkumar, S., and Gurubaran, S.: Variabilities of mesospheric tides and equatorial electrojet strength during major stratospheric warming events, in: Annales Geophysicae, vol. 27, pp. 4125–4130, Copernicus Publications Göttingen, Germany, 2009.

Sridharan, S., Sathishkumar, S., and Gurubaran, S.: Variabilities of mesospheric tides during sudden stratospheric warming events of 2006 and 2009 and their relationship with ozone and water vapour, Journal of atmospheric and solar-terrestrial physics, 78, 108–115, 2012.

Stober, G., Baumgarten, K., McCormack, J. P., Brown, P., and Czarnecki, J.: Comparative study between ground-based observations and NAVGEM-HA analysis data in the mesosphere and lower thermosphere region, Atmospheric Chemistry and Physics, 20, 11 979–12 010, 2020.

Stober, G., Kozlovsky, A., Liu, A., Qiao, Z., Tsutsumi, M., Hall, C., Nozawa, S., Lester, M., Belova, E., Kero, J., Espy, P. J., Hibbins, R. E., and Mitchell, N.: Atmospheric tomography using the Nordic Meteor Radar Cluster and Chilean Observation Network De Meteor Radars: network details and 3D-Var retrieval, Atmospheric Measurement Techniques, 14, 6509–6532, https://doi.org/10.5194/amt-14-6509-2021, 2021a.

Stober, G., Kuchar, A., Pokhotelov, D., Liu, H., Liu, H.-L., Schmidt, H., Jacobi, C., Baumgarten, K., Brown, P., Janches, D., et al.: Interhemispheric differences of mesosphere–lower thermosphere winds and tides investigated from three whole-atmosphere models and meteor radar observations, Atmospheric chemistry and physics, 21, 13 855–13 902, 2021b.

Straub, C., Murk, A., and Kämpfer, N.: MIAWARA-C, a new ground based water vapor radiometer for measurement campaigns, Atmospheric Measurement Techniques, 3, 1271–1285, 2010.

United States Naval Observatory. Nautical Almanac Office and Nautical Almanac Office (U.S.): Astronomical Almanac for the Year 2010 and Its Companion, the Astronomical Almanac Online, Astronomical Almanac for the Year, U.S. Government Printing Office, 2009.

Vadas, S. L., Becker, E., Bossert, K., Hozumi, Y., Stober, G., Harvey, V. L., Baumgarten, G., and Hoffmann, L.: The Role of the Polar Vortex Jet for Secondary and Higher-Order Gravity Waves in the Northern Mesosphere and Thermosphere During 11–14 January 2016, Journal of Geophysical Research: Space Physics, 129, e2024JA032 521, https://doi.org/https://doi.org/10.1029/2024JA032521, e2024JA032521 2024JA032521, 2024.

van Caspel, W. E., Espy, P., Hibbins, R., Stober, G., Brown, P., Jacobi, C., and Kero, J.: A case study of the solar and lunar semidiurnal tide response to the 2013 sudden stratospheric warming, Journal of Geophysical Research: Space Physics, 128, e2023JA031 680, 2023.

Vial, F. and Forbes, J.: Monthly simulations of the lunar semi-diurnal tide, Journal of Atmospheric and Terrestrial Physics, 56, 1591–1607, https://doi.org/https://doi.org/10.1016/0021-9169(94)90089-2, 1994.

Waters, J. W., Froidevaux, L., Harwood, R. S., Jarnot, R. F., Pickett, H. M., Read, W. G., Siegel, P. H., Cofield, R. E., Filipiak, M. J., Flower, D. A., Holden, J. R., Lau, G. K., Livesey, N. J., Manney, G. L., Pumphrey, H. C., Santee, M. L., Wu, D. L., Cuddy, D. T., Lay, R. R., Loo, M. S., Perun, V. S., Schwartz, M. J., Stek, P. C., Thurstans, R. P., Boyles, M. A., Chandra, K. M., Chavez, M. C., Chen, G.-S., Chudasama, B. V., Dodge, R., Fuller, R. A., Girard, M. A., Jiang, J., Jiang, Y., Knosp, B. W., LaBelle, R. C., Lam, J. C., Lee, K., Miller, D., Oswald, J. E., Patel, N. C., Pukala, D. M., Quintero, O., Scaff, D. M., Snyder, W. V., Tope, M. C., Wagner, P. A., and Walch, M. J.: The Earth observing system microwave limb sounder (EOS MLS) on the aura Satellite, IEEE Transactions on Geoscience and Remote Sensing, 44, 1075–1092, 2006.

Zhang, J., Limpasuvan, V., Orsolini, Y. J., Espy, P. J., and Hibbins, R. E.: Climatological westward-propagating semidiurnal tides and their composite response to sudden stratospheric warmings in SuperDARN and SD-WACCM-X, Journal of Geophysical Research: Atmospheres, 126, e2020JD032 895, 2021.

7 Conclusions and Outlook

Conclusions

This thesis investigates the variability of ozone and water vapor in the Arctic middle atmosphere and their radiative effects on the mesospheric dynamics, leveraging long-term ground-based microwave radiometer observations from GROMOS-C and MIAWARA-C at Ny-Ålesund, Svalbard. By integrating these measurements with satellite datasets (MLS), reanalysis (MERRA-2), meteor radar observations, and simulations from the WACCM-X(SD) model, the work provides new insights into the dynamic and chemical processes modulating the Arctic stratosphere and mesosphere.

Firstly, we establish the long-term climatology and interannual variability of ozone and water vapor at polar latitudes. The comparison of ground-based data with satellite and reanalysis datasets reveals that ground-based radiometers effectively capture seasonal and interannual variations in both trace gases. Notably, the interhemispheric comparison highlights stronger variability in the Northern Hemisphere, reflecting more active polar dynamics. Vertical transport velocities derived from water vapor further support the seasonal evolution of the polar vortex and the residual circulation, offering a robust tool for diagnosing hemispheric asymmetries in atmospheric transport.

Secondly, we explore the evolution of ozone anomalies during major SSW and early final warming SSW events. Using ground-based, satellite, and reanalysis datasets, the study quantifies the contributions of dynamical and chemical processes to ozone anomalies. During SSW events, the analysis shows that ozone increases throughout the stratosphere and lower mesosphere and is largely driven by enhanced horizontal eddy transport and vertical advection. For early final warming SSW events, the anomalies reflect a more complex interplay between photochemical loss and dynamical transport, presenting the variability of the polar middle atmosphere during transitional periods. These results deepen our understanding of the comprehension of the connections between ozone and dynamic and chemical variability during polar stratospheric disturbances.

Thirdly, we connect the radiative forcing of ozone and water vapor to mesospheric tidal variability during SSW events, using a combination of WACCM-X(SD) model simulations and meteor radar data. The study reveals distinct tidal amplitude anomalies in diurnal, semidiurnal, and terdiurnal components during and after SSW onset, with the radiative effects of ozone playing a significant role in modulating these tides. Water vapor, while important as a dynamical tracer, shows limited direct radiative impact. The results highlight the coupling between radiatively driven processes and wave–mean flow interactions in the Arctic MLT during dynamically disturbed periods.

Together, these studies address the crucial role of continuous observations at high latitudes in advancing our understanding of middle atmospheric variability. Ground-based microwave radiometry proves to be a powerful tool for tracking both short-term events and long-term trends in key atmospheric trace gases. Moreover, the integration of observational and modeling approaches enhances our ability to diagnose and attribute changes in the Arctic atmosphere, particularly in response to extreme dynamical events.

Outlook

Building upon the findings of this thesis, several promising research directions are as follows:

The continued operation of GROMOS-C and MIAWARA-C will strengthen the climatological baseline for Arctic ozone and water vapor, enabling more effective assessments of long-term trends and their links to climate variability and change.

Building on the observed feedback between ozone and atmospheric dynamics, future work might explore the role of ozone variability in modulating the QBO and its teleconnections with polar stratospheric processes.

To better understand the coupling between chemical composition and wave dynamics, radiative transfer calculations for GCMs could be refined by incorporating more realistic trace gas distributions derived from high-resolution observations.

The impact of SSW-induced ozone anomalies on surface weather and climate remains an open question. Future studies could investigate how radiative and chemical feedback in the middle atmosphere propagate downward to affect tropospheric circulation patterns.

As the Arctic continues to warm, assessing whether and how the frequency and intensity of SSW, and related chemical anomalies change over time is critical. The combined use of observations and chemistry-climate models will be vital in quantifying such changes and their implications for the Arctic and global climate.

In conclusion, this thesis not only advances our understanding of Arctic middle atmospheric processes but also is the groundwork for future interdisciplinary studies focused on atmospheric composition, dynamics, and their evolving role in the Earth’s climate system.

Bibliography

Alexander, M. J. et al. “Recent Developments in Gravity-Wave Effects in Climate Models and the Global Distribution of Gravity-Wave Momentum Flux from Observations and Models”. In: *Quarterly Journal of the Royal Meteorological Society* (July 20, 2010), n/a–n/a. ISSN: 00359009, 1477870X.

Amos, Matt et al. “Projecting ozone hole recovery using an ensemble of chemistry–climate models weighted by model performance and independence”. In: *Atmospheric Chemistry and Physics* 20.16 (2020), pp. 9961–9977.

Anderson, James G et al. “Stratospheric ozone over the United States in summer linked to observations of convection and temperature via chlorine and bromine catalysis”. In: *Proceedings of the National Academy of Sciences* 114.25 (2017), E4905–E4913.

Andrews, D.G., J.R. Holton, and C.B. Leovy. *Middle Atmosphere Dynamics.* International Geophysics. Elsevier Science, 1987. ISBN: 9780120585762.

Andrews, DG and ME McIntyre. “Generalized Eliassen-Palm and Charney-Drazin theorems for waves on axismmetric mean flows in compressible atmospheres”. In: *Journal of Atmospheric Sciences* 35.2 (1978), pp. 175–185.

Ayarzagüena, Blanca and Encarna Serrano. “Monthly characterization of the tropospheric circulation over the Euro-Atlantic area in relation with the timing of stratospheric final warmings”. In: *Journal of Climate* 22.23 (2009), pp. 6313–6324.

Bahramvash Shams, S. et al. “Analyzing ozone variations and uncertainties at high latitudes during sudden stratospheric warming events using MERRA-2”. In: *Atmospheric Chemistry and Physics* 22.8 (2022), pp. 5435–5458.

Bailey, SM et al. “A multi tracer analysis of thermosphere to stratosphere descent triggered by the 2013 Stratospheric Sudden Warming”. In: *Geophysical Research Letters* 41.14 (2014), pp. 5216–5222.

Baldwin, Mark P, Blanca Ayarzagüena, et al. “Sudden stratospheric warmings”. In: *Reviews of Geophysics* 59.1 (2021), e2020RG000708.

Baldwin, Mark P and Timothy J Dunkerton. “Stratospheric harbingers of anomalous weather regimes”. In: *Science* 294.5542 (2001), pp. 581–584.

Baldwin, Mark P, David B Stephenson, et al. “Stratospheric Memory and Skill of Extended-Range Weather Forecasts.” In: *Science* 301 (August 2003), pp. 636–640. ISSN: 0036-8075.

Banerjee, Antara et al. “Stratospheric water vapor: an important climate feedback”. In: *Climate Dynamics* 53 (2019), pp. 1697–1710.

Bates, David R and Marcel Nicolet. “Atmospheric hydrogen”. In: *Publications of the Astronomical Society of the Pacific* 62.366 (1950), pp. 106–110.

Baumgarten, Kathrin and Gunter Stober. “On the evaluation of the phase relation between temperature and wind tides based on ground-based measurements and reanalysis data in the middle atmosphere”. In: *Annales Geophysicae.* Vol. 37. 4. Copernicus Publications Göttingen, Germany. 2019, pp. 581–602.

Beard, AG et al. “Non-linear interactions between tides and planetary waves resulting in periodic tidal variability”. In: *Journal of Atmospheric and Solar-Terrestrial Physics* 61.5 (1999), pp. 363–376.

Becker, Erich. “Dynamical Control of the Middle Atmosphere”. In: *Space Science Reviews* 168 (2012), pp. 283–314. ISSN: 0038-6308.

Bernet, Leonie et al. “Trends of atmospheric water vapour in Switzerland from ground-based radiometry, FTIR and GNSS data”. In: *Atmospheric Chemistry and Physics Discussions* 2020 (2020), pp. 1–39.

Bey, Isabelle et al. “Global modeling of tropospheric chemistry with assimilated meteorology: Model description and evaluation”. In: *Journal of Geophysical Research: Atmospheres* 106.D19 (2001), pp. 23073–23095.

Bhattacharya, Yajnavalkya, GG Shepherd, and S Brown. “Variability of atmospheric winds and waves in the Arctic polar mesosphere during a stratospheric sudden warming”. In: *Geophysical Research Letters* 31.23 (2004).

Birner, Thomas and John R Albers. “Sudden stratospheric warmings and anomalous upward wave activity flux”. In: *Sola* 13.Special_Edition (2017), pp. 8–12.

Black, Robert X and Brent A McDaniel. “Interannual variability in the Southern Hemisphere circulation organized by stratospheric final warming events”. In: *Journal of the Atmospheric Sciences* 64.8 (2007), pp. 2968–2974.

Blanc, Elisabeth et al. “Middle atmosphere variability and model uncertainties as investigated in the framework of the ARISE project”. In: *Infrasound Monitoring for Atmospheric Studies: Challenges in Middle Atmosphere Dynamics and Societal Benefits* (2019), pp. 845–887.

Brasseur, Guy P and Susan Solomon. “Composition and chemistry”. In: *Aeronomy of the Middle Atmosphere: Chemistry and Physics of the Stratosphere and Mesosphere* (2005), pp. 265–442.

Brewer, AW. “Evidence for a world circulation provided by the measurements of helium and water vapour distribution in the stratosphere”. In: *Quarterly Journal of the Royal Meteorological Society* 75.326 (1949), pp. 351–363.

Buehler, Stefan A. et al. “ARTS, the Atmospheric Radiative Transfer Simulator - Version 2.2, the planetary toolbox edition”. eng. In: *Geoscientific Model Development* 11.4 (Apr. 2018), pp. 1537–1556. ISSN: 1991-959X.

Butchart, Neal. “The Brewer-Dobson circulation”. In: *Reviews of geophysics* 52.2 (2014), pp. 157–184.

Butler, Amy H, Andrew Charlton-Perez, et al. “Predictability of Northern Hemisphere final stratospheric warmings and their surface impacts”. In: *Geophysical Research Letters* 46.17-18 (2019), pp. 10578–10588.

Butler, Amy H and Daniela IV Domeisen. “The wave geometry of final stratospheric warming events”. In: *Weather and Climate Dynamics* 2.2 (2021), pp. 453–474.

Calisesi, Y et al. “The Stratospheric Ozone Monitoring Radiometer SOMORA: first validation results”. In: *Proc. of the Sixth European Symposium on Stratospheric Ozone, ed.: European Commission.* 2002.

Calisesi, Yasmine. “The stratospheric ozone monitoring radiometer SOMORA: NDSC application document”. In: *IAP Res. Rep* 11 (2003), pp. 53–54.

Cámara, A. de la et al. “Response of Arctic ozone to sudden stratospheric warmings”. In: *Atmospheric Chemistry and Physics* 18.22 (2018), pp. 16499–16513.

Caspel, Willem E. van et al. “A Case Study of the Solar and Lunar Semidiurnal Tide Response to the 2013 Sudden Stratospheric Warming”. In: *Journal of Geophysical Research: Space Physics* 128.9 (2023), e2023JA031680.

Cen, Yetao et al. “Suppressed migrating diurnal tides in the mesosphere and lower thermosphere region during El Niño in northern winter and its possible mechanism”. In: *Atmospheric Chemistry and Physics* 22.12 (2022), pp. 7861–7874.

Chane-Ming, Fabrice et al. “Vertical short-scale structures in the upper tropospheric and lower stratospheric temperature and ozone at la Réunion Island (20.8° S 55.3° E)”. In: *Journal of Geophysical Research: Atmospheres* 105.D22 (2000), pp. 26857–26870.

Charlton, Andrew J. and Lorenzo M. Polvani. “A New Look at Stratospheric Sudden Warmings. Part I: Climatology and Modeling Benchmarks”. In: *Journal of Climate* 20.3 (2007), pp. 449–469.

Charlton, Andrew James, A. Oneill, et al. “Sensitivity of Tropospheric Forecasts to Stratospheric Initial Conditions”. In: (2004), pp. 1771–1792.

Charney, Jule G and PG Drazin. “Propagation of planetary-scale disturbances from the lower into the upper atmosphere”. In: *The Atmosphere—A Challenge: The Science of Jule Gregory Charney*. Springer, 1990, pp. 295–321.

Charney, Jule G and Philip G Drazin. “Propagation of planetary-scale disturbances from the lower into the upper atmosphere”. In: *Journal of Geophysical Research* 66.1 (1961), pp. 83–109.

Chau, JL et al. “Upper mesospheric lunar tides over middle and high latitudes during sudden stratospheric warming events”. In: *Journal of Geophysical Research: Space Physics* 120.4 (2015), pp. 3084–3096.

Chipperfield, MP. “New version of the TOMCAT/SLIMCAT off-line chemical transport model: Intercomparison of stratospheric tracer experiments”. In: *Quarterly Journal of the Royal Meteorological Society: A journal of the atmospheric sciences, applied meteorology and physical oceanography* 132.617 (2006), pp. 1179–1203.

Clancy, Todd and Duane Muhleman. “Ground-Based Microwave Spectroscopy of the Earth’s Stratosphere and Mesosphere”. In: Janssen, Michael A. *Atmospheric Remote Sensing by Microwave Radiometry*. Wiley Series in Remote Sensing. New York: Wiley, 1993. ISBN: 978-0-471-62891-0.

Cohen, Yann et al. “Interpol-IAGOS: a new method for assessing long-term chemistry–climate simulations in the UTLS based on IAGOS data, and its application to the MOCAGE CCMI REF-C1SD simulation”. In: *Geoscientific Model Development* 14.5 (2021), pp. 2659–2689.

Corti, Thierry et al. “The impact of cirrus clouds on tropical troposphere-to-stratosphere transport”. In: *Atmospheric Chemistry and Physics* 6.9 (2006), pp. 2539–2547.

Coy, Lawrence, Stephen Eckermann, and Karl Hoppel. “Planetary wave breaking and tropospheric forcing as seen in the stratospheric sudden warming of 2006”. In: *Journal of the atmospheric sciences* 66.2 (2009), pp. 495–507.

Davis, Sean M et al. “The role of tropical upwelling in explaining discrepancies between recent modeled and observed lower-stratospheric ozone trends”. In: *Atmospheric Chemistry and Physics* 23.5 (2023), pp. 3347–3361.

De Mazière, Martine et al. “The Network for the Detection of Atmospheric Composition Change (NDACC): history, status and perspectives”. In: *Atmospheric Chemistry and Physics* 18.7 (2018), pp. 4935–4964.

De Wachter, Evelyn et al. “The seoul water vapor radiometer for the middle atmosphere: Calibration, retrieval, and validation”. In: *IEEE transactions on geoscience and remote sensing* 49.3 (2010), pp. 1052–1062.

Degenstein, Douglas Arthur et al. “Observations of an extended mesospheric tertiary ozone peak”. In: *Journal of atmospheric and solar-terrestrial physics* 67.15 (2005), pp. 1395–1402.

Dessler, Andrew E and Steven C Sherwood. “A matter of humidity”. In: *Science* 323.5917 (2009), pp. 1020–1021.

Deuber, Beat et al. “Middle Atmospheric Water Vapour Radiometer (MIAWARA): Validation and first results of the LAPBIAT Upper Tropospheric Lower Stratospheric Water Vapour Validation Project (LAUTLOS-WAVVAP) campaign”. In: *Journal of Geophysical Research: Atmospheres* 110.D13 (2005).

Dobson, Gordon Miller Bourne. “Origin and distribution of the polyatomic molecules in the atmosphere”. In: *Proceedings of the Royal Society of London. Series A. Mathematical and Physical Sciences* 236.1205 (1956), pp. 187–193.

Domeisen, Daniela IV, Amy H Butler, and Andrew J Charlton-Perez. “The role of the stratosphere in sub-seasonal to seasonal prediction”. In: *Newsletter n 54 January 2020* (2020), p. 14.

Domeisen, Daniela IV, Lantao Sun, and Gang Chen. “The role of synoptic eddies in the tropospheric response to stratospheric variability”. In: *Geophysical research letters* 40.18 (2013), pp. 4933–4937.

Dubé, Kimberlee et al. “Upper-stratospheric temperature trends: new results from the Optical Spectrograph and InfraRed Imager System (OSIRIS)”. In: *Atmospheric Chemistry and Physics* 24.22 (2024), pp. 12925–12941.

Dunkerton, Timothy. “On the mean meridional mass motions of the stratosphere and mesosphere”. In: *Journal of Atmospheric Sciences* 35.12 (1978), pp. 2325–2333.

Dutta, Reetambhara, S Sridharan, and PR Sinha. “Signature of sudden stratospheric warming in the pole and its antipode”. In: *Journal of Geophysical Research: Space Physics* 129.3 (2024), e2023JA032285.

Eliassen, Arnt. “On the transfer of energy in stationary mountain waves.” In: *Geofys. Publ.* 22 (1961), pp. 1–23.

Eriksson, Patrick, SA Buehler, et al. “ARTS, the atmospheric radiative transfer simulator, version 2”. In: *Journal of Quantitative Spectroscopy and Radiative Transfer* 112.10 (2011), pp. 1551–1558.

Eriksson, Patrick, Mattias Ekström, et al. “Efficient forward modelling by matrix representation of sensor responses”. In: *International Journal of Remote Sensing* 27.9 (2006), pp. 1793–1808.

Eriksson, Patrick, Carlos Jiménez, and Stefan A Buehler. “Qpack, a general tool for instrument simulation and retrieval work”. In: *Journal of Quantitative Spectroscopy and Radiative Transfer* 91.1 (2005), pp. 47–64.

Eyring, Veronika et al. “Overview of IGAC/SPARC Chemistry-Climate Model Initiative (CCMI) community simulations in support of upcoming ozone and climate assessments”. In: *SPARC newsletter* 40.Januar (2013), pp. 48–66.

Fejer, BG et al. “Enhanced lunar semidiurnal equatorial vertical plasma drifts during sudden stratospheric warmings”. In: *Geophysical Research Letters* 38.21 (2011).

Fernández, Susana, Axel Murk, and Niklaus Kämpfer. “GROMOS-C, a novel ground-based microwave radiometer for ozone measurement campaigns”. In: *Atmospheric Measurement Techniques* 8 (2015), pp. 2649–2662.

Forbes, J. M., X. Zhang, et al. “Tidal Variability in the Ionospheric Dynamo Region”. In: *Journal of Geophysical Research: Space Physics* 113.A2 (2008). ISSN: 2156-2202.

Forbes, Jeffrey M. “Middle atmosphere tides”. In: *Journal of atmospheric and terrestrial physics* 46.11 (1984), pp. 1049–1067.

Forbes, Jeffrey M and Henry B Garrett. “Theoretical studies of atmospheric tides”. In: *Reviews of Geophysics* 17.8 (1979), pp. 1951–1981.

Friedel, M., G. Chiodo, A. Stenke, D. I. V. Domeisen, and T. Peter. “Effects of Arctic ozone on the stratospheric spring onset and its surface impact”. In: *Atmospheric Chemistry and Physics* 22.21 (2022), pp. 13997–14017.

Friedel, Marina, Gabriel Chiodo, Andrea Stenke, Daniela IV Domeisen, Stephan Fueglistaler, et al. “Springtime arctic ozone depletion forces northern hemisphere climate anomalies”. In: *Nature Geoscience* 15.7 (2022), pp. 541–547.

Friedel, Marina, Gabriel Chiodo, Timofei Sukhodolov, et al. “Weakening of springtime Arctic ozone depletion with climate change”. In: *Atmospheric Chemistry and Physics* 23.17 (2023), pp. 10235–10254.

Fueglistaler, S et al. “Tropical tropopause layer”. In: *Reviews of Geophysics* 47.1 (2009).

Garcia, Rolando R et al. “Modification of the gravity wave parameterization in the Whole Atmosphere Community Climate Model: Motivation and results”. In: *Journal of the Atmospheric Sciences* 74.1 (2017), pp. 275–291.

Garfinkel, Chaim I et al. “Influence of the El Niño–Southern Oscillation on entry stratospheric water vapor in coupled chemistry–ocean CCMI and CMIP6 models”. In: *Atmospheric Chemistry and Physics* 21.5 (2021), pp. 3725–3740.

Gelaro, Ronald et al. “The modern-era retrospective analysis for research and applications, version 2 (MERRA-2)”. In: *Journal of climate* 30.14 (2017), pp. 5419–5454.

Gettelman, A et al. “The whole atmosphere community climate model version 6 (WACCM6)”. In: *Journal of Geophysical Research: Atmospheres* 124.23 (2019), pp. 12380–12403.

Goncharenko, LP et al. “Unexpected connections between the stratosphere and ionosphere”. In: *Geophysical Research Letters* 37.10 (2010).

Graf, M. et al. “Compact and lightweight mid-infrared laser spectrometer for balloon-borne water vapor measurements in the UTLS”. In: *Atmospheric Measurement Techniques* 14.2 (2021), pp. 1365–1378.

Hagan, ME. “Comparative effects of migrating solar sources on tidal signatures in the middle and upper atmosphere”. In: *Journal of Geophysical Research: Atmospheres* 101.D16 (1996), pp. 21213–21222.

Hagan, ME, RG Roble, and J Hackney. “Migrating thermospheric tides”. In: *Journal of Geophysical Research: Space Physics* 106.A7 (2001), pp. 12739–12752.

Hagen, Jonas et al. “WIRA-C: a compact 142-GHz-radiometer for continuous middle-atmospheric wind measurements”. In: *Atmospheric Measurement Techniques* 11.9 (2018), pp. 5007–5024.

Harari, Ohad et al. “Influence of Arctic stratospheric ozone on surface climate in CCMI models”. In: *Atmospheric Chemistry and Physics* 19.14 (2019), pp. 9253–9268.

Held, Isaac M, Mingfang Ting, and Hailan Wang. “Northern winter stationary waves: Theory and modeling”. In: *Journal of climate* 15.16 (2002), pp. 2125–2144.

Hibbins, R. E. et al. “SuperDARN Observations of Semidiurnal Tidal Variability in the MLT and the Response to Sudden Stratospheric Warming Events”. In: *Journal of Geophysical Research: Atmospheres* 124.9 (2019), pp. 4862–4872.

Hocking, WK, B Fuller, and B Vandepeer. “Real-time determination of meteor-related parameters utilizing modern digital technology”. In: *Journal of Atmospheric and Solar-Terrestrial Physics* 63.2-3 (2001), pp. 155–169.

Hoffmann, P et al. “Latitudinal and longitudinal variability of mesospheric winds and temperatures during stratospheric warming events”. In: *Journal of Atmospheric and Solar-Terrestrial Physics* 69.17-18 (2007), pp. 2355–2366.

Holdsworth, David A., Iain M. Reid, and Manuel A. Cervera. “Buckland Park all-sky interferometric meteor radar”. In: *Radio Science* 39.5 (2004). RS5009, n/a–n/a. ISSN: 1944-799X.

Holton, James R. “The dynamics of sudden stratospheric warmings”. In: *Annual Review of Earth and Planetary Sciences, Vol. 8, p. 169* 8 (1980), p. 169.

– “The influence of gravity wave breaking on the general circulation of the middle atmosphere”. In: *Journal of Atmospheric Sciences* 40.10 (1983), pp. 2497–2507.

Holton, James R et al. “Stratosphere-troposphere exchange”. In: *Reviews of geophysics* 33.4 (1995), pp. 403–439.

Hong, H.-J. and T. Reichler. “Local and remote response of ozone to Arctic stratospheric circulation extremes”. In: *Atmospheric Chemistry and Physics* 21.2 (2021), pp. 1159–1171.

Hu, Jinggao, Rongcai Ren, and Haiming Xu. “Occurrence of winter stratospheric sudden warming events and the seasonal timing of spring stratospheric final warming”. In: *Journal of the Atmospheric Sciences* 71.7 (2014), pp. 2319–2334.

Huang, Rong-hui and K Gambo. “The response of a hemispheric multi-level model atmosphere to forcing by topography and stationary heat sources (I) Forcing by topography”. In: *Journal of the Meteorological Society of Japan. Ser. II* 60.1 (1982), pp. 78–92.

– “The response of a hemispheric multi-level model atmosphere to forcing by topography and stationary heat sources in summer”. In: *Journal of the Meteorological Society of Japan. Ser. II* 61.4 (1983), pp. 495–509.

Hubert, Daan et al. “Ground-based assessment of the bias and long-term stability of 14 limb and occultation ozone profile data records”. In: *Atmospheric measurement techniques* 9.6 (2016), pp. 2497–2534.

Jacobi, Ch et al. “Climatology of the semidiurnal tide at 52–56 N from ground-based radar wind measurements 1985–1995”. In: *Journal of Atmospheric and Solar-Terrestrial Physics* 61.13 (1999), pp. 975–991.

Jiang, Jonathan H et al. “An assessment of upper troposphere and lower stratosphere water vapor in MERRA, MERRA2, and ECMWF reanalyses using Aura MLS observations”. In: *Journal of Geophysical Research: Atmospheres* 120.22 (2015), pp. 11–468.

Joshi, MM and GS Jones. “The climatic effects of the direct injection of water vapour into the stratosphere by large volcanic eruptions”. In: *Atmospheric Chemistry and Physics* 9.16 (2009), pp. 6109–6118.

Kawatani, Yoshio, Jae N Lee, and Kevin Hamilton. “Interannual variations of stratospheric water vapor in MLS observations and climate model simulations”. In: *Journal of the Atmospheric Sciences* 71.11 (2014), pp. 4072–4085.

Keckhut, Philippe et al. “An evaluation of uncertainties in monitoring middle atmosphere temperatures with the ground-based lidar network in support of space observations”. In: *Journal of Atmospheric and Solar-Terrestrial Physics* 73.5-6 (2011), pp. 627–642.

Kiehl, JT and Susan Solomon. “On the radiative balance of the stratosphere”. In: *Journal of Atmospheric Sciences* 43.14 (1986), pp. 1525–1534.

Kim, Young-Joon, Stephen D. Eckermann, and Hye-Yeong Chun. “An Overview of the Past, Present and Future of Gravity-wave Drag Parametrization for Numerical Climate and Weather Prediction Models”. In: *Atmosphere-Ocean* 41.1 (Mar. 2003), pp. 65–98.

KLEY, Dieter. “SPARC assessment of upper tropospheric and stratospheric water vapour”. In: *WCRP 113 WMO/TD SPARC Report* 1043 (2000).

Lawrence, Zachary D et al. “The remarkably strong Arctic stratospheric polar vortex of winter 2020: Links to record-breaking Arctic oscillation and ozone loss”. In: *Journal of Geophysical Research: Atmospheres* 125.22 (2020), e2020JD033271.

– “The remarkably strong Arctic stratospheric polar vortex of winter 2020: Links to record-breaking Arctic oscillation and ozone loss”. In: *Journal of Geophysical Research: Atmospheres* 125.22 (2020), e2020JD033271.

Le Pichon, A. et al. “Comparison of Co-Located Independent Ground-Based Middle Atmospheric Wind and Temperature Measurements with Numerical Weather Prediction Models”. In: *Journal of Geophysical Research: Atmospheres* 120.16 (2015), pp. 8318–8331. ISSN: 2169-8996.

Le Texier, H, S Solomon, and RR Garcia. “The role of molecular hydrogen and methane oxidation in the water vapour budget of the stratosphere”. In: *Quarterly Journal of the Royal Meteorological Society* 114.480 (1988), pp. 281–295.

Lee, Jae N et al. “Aura Microwave Limb Sounder observations of the polar middle atmosphere: Dynamics and transport of CO and H2O”. In: *Journal of Geophysical Research: Atmospheres* 116.D5 (2011).

Lieberman, RS, DA Ortland, and ES Yarosh. “Climatology and interannual variability of diurnal water vapor heating”. In: *Journal of Geophysical Research: Atmospheres* 108.D3 (2003).

Limpasuvan, Varavut et al. “On the composite response of the MLT to major sudden stratospheric warming events with elevated stratopause”. In: *Journal of Geophysical Research: Atmospheres* 121.9 (2016), pp. 4518–4537.

Lindzen, R. S. “Turbulence and stress owing to gravity wave and tidal breakdown”. In: *Journal of Geophysical Research: Oceans* 86.C10 (1981), pp. 9707–9714.

Lindzen, Richard S. “Tides and Gravity Waves in the Upper Atmosphere”. In: *Mesospheric Models and Related Experiments*. Ed. by G. Fiocco. Vol. 25. Dordrecht: Springer Netherlands, 1971, pp. 122–130.

Lindzen, Richard S. and Sydney Chapman. “Atmospheric Tides”. In: *Space Science Reviews* 10.1 (Oct. 1969), pp. 3–188. ISSN: 1572-9672.

Liu, Guiping, Diego Janches, et al. “Mesosphere and lower thermosphere winds and tidal variations during the 2019 Antarctic sudden stratospheric warming”. In: *Journal of Geophysical Research: Space Physics* 127.3 (2022), e2021JA030177.

Liu, H.-L. “Variability and predictability of the space environment as related to lower atmosphere forcing”. In: *Space Weather* 14.9 (2016), pp. 634–658.

Liu, Han-Li, Charles G Bardeen, et al. “Development and validation of the whole atmosphere community climate model with thermosphere and ionosphere extension (WACCM-X 2.0)”. In: *Journal of Advances in Modeling Earth Systems* 10.2 (2018), pp. 381–402.

Livesey, NJ et al. *EOS MLS Version 4.2 x Level 2 data quality and description document (Revision E).* Tech. rep. Tech. rep., JPL, http://mls. jpl. nasa. gov/data/datadocs. php (last access …, 2018.

Lobsiger, E. “Ground-Based Microwave Radiometry to Determine Stratospheric and Mesospheric Ozone Profiles”. In: *Journal of Atmospheric and Terrestrial Physics* 49.5 (May 1, 1987), pp. 493–501. ISSN: 0021-9169.

Lu, Xian et al. “Latitudinal double-peak structure of stationary planetary wave 1 in the austral winter middle atmosphere and its possible generation mechanism”. In: *Journal of Geophysical Research: Atmospheres* 123.20 (2018), pp. 11–551.

Madden, Roland A. “Observations of large-scale traveling Rossby waves”. In: *Reviews of Geophysics* 17.8 (1979), pp. 1935–1949.

Mak, Mankin. *Atmospheric dynamics.* Cambridge University Press, 2011.

Manney, Gloria L, Nathaniel J Livesey, et al. “Record-low Arctic stratospheric ozone in 2020: MLS observations of chemical processes and comparisons with previous extreme winters”. In: *Geophysical Research Letters* 47.16 (2020), e2020GL089063.

Manney, Gloria L, Luis F Millán, et al. “Signatures of anomalous transport in the 2019/2020 Arctic stratospheric polar vortex”. In: *Journal of Geophysical Research: Atmospheres* 127.20 (2022), e2022JD037407.

Manney, Gloria L, Michelle L Santee, et al. “Siege in the southern stratosphere: Hunga Tonga-Hunga Ha’apai water vapor excluded from the 2022 Antarctic polar vortex”. In: *Geophysical Research Letters* 50.14 (2023), e2023GL103855.

Marsh, Daniel, Anne Smith, et al. “The existence of a tertiary ozone maximum in the high-latitude middle mesosphere”. In: *Geophysical Research Letters* 28.24 (2001), pp. 4531–4534.

Marsh, Daniel R, Michael J Mills, et al. “Climate change from 1850 to 2005 simulated in CESM1 (WACCM)”. In: *Journal of climate* 26.19 (2013), pp. 7372–7391.

Matsuno, Taroh. “A dynamical model of the stratospheric sudden warming”. In: *Journal of Atmospheric Sciences* 28.8 (1971), pp. 1479–1494.

– “Vertical propagation of stationary planetary waves in the winter Northern Hemisphere”. In: *Journal of Atmospheric Sciences* 27.6 (1970), pp. 871–883.

Matsuzaka, Yukihiko et al. “Thin-film balloon for high altitude observation”. In: *Advances in Space Research* 26.9 (2000), pp. 1365–1368.

Matthias, V., A. Dörnbrack, and G. Stober. “The extraordinarily strong and cold polar vortex in the early northern winter 2015/2016”. In: *Geophysical Research Letters* 43.23 (2016), pp. 12, 287–12, 294.

McKenna, Daniel S et al. “A new Chemical Lagrangian Model of the Stratosphere (CLaMS) 1. Formulation of advection and mixing”. In: *Journal of Geophysical Research: Atmospheres* 107.D16 (2002), ACH–15.

McLandress, Charles. “The seasonal variation of the propagating diurnal tide in the mesosphere and lower thermosphere. Part II: The role of tidal heating and zonal mean winds”. In: *Journal of the Atmospheric Sciences* 59.5 (2002), pp. 907–922.

Mitra, Gourav et al. “Investigation on the MLT tidal variability during September 2019 minor sudden stratospheric warming”. In: *Advances in Space Research* 71.1 (2023), pp. 869–882.

Mohanakumar, K. “Structure and composition of the lower and middle atmosphere”. In: *Stratosphere Troposphere Interactions: An Introduction* (2008), pp. 1–53.

Moreira, L et al. “Trend analysis of the 20-year time series of stratospheric ozone profiles observed by the GROMOS microwave radiometer at Bern”. In: *Atmospheric chemistry and physics* 15.19 (2015), pp. 10999–11009.

Müllemann, Arno and Franz-Josef Lübken. “Horizontal Winds in the Mesosphere at High Latitudes”. In: *Advances in Space Research* 35.11 (Jan. 2005), pp. 1890–1894. ISSN: 02731177.

Murata, I et al. “Measurements of stratospheric ozone with a balloon-borne optical ozone sensor”. In: *International Journal of Remote Sensing* 30.15-16 (2009), pp. 3961–3966.

Murtagh, Donal et al. “An overview of the Odin atmospheric mission”. In: *Canadian Journal of Physics* 80.4 (2002), pp. 309–319.

Nair, Prijitha J et al. “Relative drifts and stability of satellite and ground-based stratospheric ozone profiles at NDACC lidar stations”. In: *Atmospheric Measurement Techniques* 5.6 (2012), pp. 1301–1318.

Nassar, Ray et al. “ACE-FTS measurements across the edge of the winter 2004 Arctic vortex”. In: *Geophysical research letters* 32.15 (2005).

Neale, Richard B et al. “Description of the NCAR community atmosphere model (CAM 5.0)”. In: *NCAR Tech. Note Ncar/tn-486+ STR* 1.1 (2010), pp. 1–12.

Nedoluha, Gerald E, R Michael Gomez, et al. “A comparison of middle atmospheric water vapor as measured by WVMS, EOS-MLS, and HALOE”. In: *Journal of Geophysical Research: Atmospheres* 112.D24 (2007).

Nedoluha, Gerald E., Richard M. Bevilacqua, et al. “Ground-Based Measurements of Water Vapor in the Middle Atmosphere”. In: *Journal of Geophysical Research: Atmospheres* 100.D2 (1995), pp. 2927–2939. ISSN: 2156-2202.

Orsolini, Yvan J et al. “Descent from the polar mesosphere and anomalously high stratopause observed in 8 years of water vapor and temperature satellite observations by the Odin Sub-Millimeter Radiometer”. In: *Journal of Geophysical Research: Atmospheres* 115.D12 (2010).

Pancheva, D. “Non-linear interaction of tides and planetary waves in the mesosphere and lower thermosphere: observations over Europe”. In: *Physics and Chemistry of the Earth, Part C: Solar, Terrestrial & Planetary Science* 26.6 (2001), pp. 411–418.

Pancheva, D et al. “Planetary waves in coupling the stratosphere and mesosphere during the major stratospheric warming in 2003/2004”. In: *Journal of Geophysical Research: Atmospheres* 113.D12 (2008).

Pedatella, Nicholas M, Jorge Luis Chau, et al. “Solar flare effects on 150-km echoes observed over Jicamarca: WACCM-X simulations”. In: *Geophysical Research Letters* 46.20 (2019), pp. 10951–10958.

Pedatella, NM, H-L Liu, et al. “Simulations of solar and lunar tidal variability in the mesosphere and lower thermosphere during sudden stratosphere warmings and their influence on the low-latitude ionosphere”. In: *Journal of Geophysical Research: Space Physics* 117.A8 (2012).

Pogoreltsev, AI et al. “Planetary waves in coupling the lower and upper atmosphere”. In: *Journal of Atmospheric and Solar-Terrestrial Physics* 69.17-18 (2007), pp. 2083–2101.

Qin, Yusong et al. “On the westward quasi-8-day planetary waves in the middle atmosphere during arctic sudden stratospheric warmings”. In: *Journal of Geophysical Research: Atmospheres* 126.19 (2021), e2021JD035071.

Rao, Jian and Chaim I Garfinkel. “The strong stratospheric polar vortex in March 2020 in subseasonal to seasonal models: Implications for empirical prediction of the low Arctic total ozone extreme”. In: *Journal of Geophysical Research: Atmospheres* 126.9 (2021), e2020JD034190.

Rao, Jian, Chaim I Garfinkel, et al. “The Southern Hemisphere minor sudden stratospheric warming in September 2019 and its predictions in S2S models”. In: *Journal of Geophysical Research: Atmospheres* 125.14 (2020), e2020JD032723.

Rao, Jian, Rongcai Ren, et al. “The stratospheric sudden warming event in February 2018 and its prediction by a climate system model”. In: *Journal of Geophysical Research: Atmospheres* 123.23 (2018), pp. 13–332.

Read, William G et al. “The clear-sky unpolarized forward model for the EOS Aura Microwave Limb Sounder (MLS)”. In: *IEEE Transactions on Geoscience and Remote Sensing* 44.5 (2006), pp. 1367–1379.

Riggin, Dennis M and Ruth S Lieberman. “Variability of the diurnal tide in the equatorial MLT”. In: *Journal of Atmospheric and Solar-Terrestrial Physics* 102 (2013), pp. 198–206.

Roberts, B. C. and M. F. Larsen. “Structure function analysis of chemical tracer trails in the mesosphere-lower thermosphere region”. In: *Journal of Geophysical Research: Atmospheres* 119.11 (2014), pp. 6368–6375.

Rodgers, Clive D. *Inverse methods for atmospheric sounding: theory and practice*. Vol. 2. World scientific, 2000.

Rossby, Carl-G et al. “Relation between variations in the intensity of the zonal circulation of the atmosphere and the displacements of the permanent centers of action atmosphere and the displacements of the permanent centers of action”. In: (1939).

Rüfenacht, R., G. Baumgarten, et al. “Intercomparison of Middle-Atmospheric Wind in Observations and Models”. In: *Atmospheric Measurement Techniques* 11.4 (2018), pp. 1971–1987.

Rüfenacht, Rolf, Gerd Baumgarten, et al. “Intercomparison of middle-atmospheric wind in observations and models”. In: *Atmospheric Measurement Techniques* 11.4 (2018), pp. 1971–1987.

Rüfenacht, Rolf, Niklaus Kämpfer, and Axel Murk. “First middle-atmospheric zonal wind profile measurements with a new ground-based microwave Doppler-spectro-radiometer”. In: *Atmospheric Measurement Techniques* 5.11 (2012), pp. 2647–2659.

Salawitch, Ross J et al. “Twenty questions and answers about the ozone layer: 2018 Update”. In: *World Meteorological Organization* (2019).

Salby, Murry L and Patrick F Callaghan. “Influence of planetary wave activity on the stratospheric final warming and spring ozone”. In: *Journal of Geophysical Research: Atmospheres* 112.D20 (2007).

Sander, SP et al. *Chemical kinetics and photochemical data for use in atmospheric studies: evaluation number 15*. Pasadena, CA: Jet Propulsion Laboratory, California Institute of Technology, 2010.

Scheiben, Dominik et al. “Observations of middle atmospheric H2O and O3 during the 2010 major sudden stratospheric warming by a network of microwave radiometers”. In: *Atmospheric chemistry and physics* 12.16 (2012), pp. 7753–7765.

Schneider, M and F Hase. “Ground-based FTIR water vapour profile analyses”. In: *Atmospheric Measurement Techniques* 2.2 (2009), pp. 609–619.

Schön, Martin et al. “Case studies of the wind field around Ny-Ålesund, Svalbard, using unmanned aircraft”. In: *Polar Research* 41 (2022).

Schranz, Franziska, Susana Fernandez, et al. “Diurnal variation in middle-atmospheric ozone observed by ground-based microwave radiometry at Ny-Ålesund over 1 year”. In: *Atmospheric Chemistry and Physics* 18.6 (2018), pp. 4113–4130.

Schranz, Franziska, Jonas Hagen, et al. “Small-scale variability of stratospheric ozone during the sudden stratospheric warming 2018/2019 observed at Ny-Ålesund, Svalbard”. In: *Atmospheric chemistry and physics* 20.18 (2020), pp. 10791–10806.

Schranz, Franziska, Brigitte Tschanz, et al. “Investigation of Arctic middle-atmospheric dynamics using 3 years of H2O and O3 measurements from microwave radiometers at Ny-Ålesund”. In: *Atmospheric Chemistry and Physics* 19.15 (2019), pp. 9927–9947.

Schwartz, Michael J, William G Read, and WV Snyder. “Polarized radiative transfer for Zeeman-split oxygen lines in the EOS MLS forward model”. In: *IEEE Trans. Geosci. Remote Sens* 44.5 (2006), pp. 1182–1191.

Shaw, Tiffany A, Judith Perlwitz, and Nili Harnik. “Downward wave coupling between the stratosphere and troposphere: The importance of meridional wave guiding and comparison with zonal-mean coupling”. In: *Journal of Climate* 23.23 (2010), pp. 6365–6381.

Shepherd, MG, SR Beagley, and VI Fomichev. “Stratospheric warming influence on the mesosphere/lower thermosphere as seen by the extended CMAM”. In: *Annales geophysicae*. Vol. 32. 6. Copernicus Publications Göttingen, Germany. 2014, pp. 589–608.

Shi, Guochun, Xiong Hu, et al. “Case study on stratospheric and mesospheric concentric gravity waves generated by deep convection”. In: *Earth and Planetary Physics* 5.1 (2021), pp. 79–89.

Shi, Guochun, Witali Krochin, et al. “Ozone and water vapor variability in the polar middle atmosphere observed with ground-based microwave radiometers”. In: *Atmospheric Chemistry and Physics* 23.16 (2023), pp. 9137–9159.

– “Ozone anomalies over the polar regions during stratospheric warming events”. In: *Atmospheric Chemistry and Physics* 24.17 (2024), pp. 10187–10207.

Shi, Guochun, Hanli Liu, et al. “New insights into the polar ozone and water vapor, radiative effects, and their connection to the tides in the mesosphere-lower thermosphere during major Sudden Stratospheric Warming events”. In: *EGUsphere* 2024 (2024), pp. 1–33.

Sigmond, M. et al. “Enhanced Seasonal Forecast Skill Following Stratospheric Sudden Warmings”. In: *Nature Geoscience* 6.2 (Feb. 2013), pp. 98–102. ISSN: 1752-0894, 1752-0908.

Siskind, David E et al. “Case studies of the mesospheric response to recent minor, major, and extended stratospheric warmings”. In: *Journal of Geophysical Research: Atmospheres* 115.D3 (2010).

Smith, Anne K, Patrick J Espy, et al. “Spatial and temporal structure of the tertiary ozone maximum in the polar winter mesosphere”. In: *Journal of Geophysical Research: Atmospheres* 123.8 (2018), pp. 4373–4389.

Smith, Anne K and Daniel R Marsh. “Processes that account for the ozone maximum at the mesopause”. In: *Journal of Geophysical Research: Atmospheres* 110.D23 (2005).

Smith, Anne K. “Global Dynamics of the MLT”. In: *Surveys in Geophysics* 33.6 (2012), pp. 1177–1230. ISSN: 1573-0956.

Smith, Karen L and Richard K Scott. “The role of planetary waves in the tropospheric jet response to stratospheric cooling”. In: *Geophysical Research Letters* 43.6 (2016), pp. 2904–2911.

Solomon, S et al. “Tracer transport by the diabatic circulation deduced from satellite observations”. In: *Journal of Atmospheric Sciences* 43.15 (1986), pp. 1603–1617.

Song, Yucheng and Walter A Robinson. “Dynamical mechanisms for stratospheric influences on the troposphere”. In: *Journal of the atmospheric sciences* 61.14 (2004), pp. 1711–1725.

Sonnemann, GR, M Grygalashvyly, and U Berger. “Autocatalytic water vapor production as a source of large mixing ratios within the middle to upper mesosphere”. In: *Journal of Geophysical Research: Atmospheres* 110.D15 (2005).

Steinbrecht, W et al. “Ozone and temperature trends in the upper stratosphere at five stations of the Network for the Detection of Atmospheric Composition Change”. In: *International journal of remote sensing* 30.15-16 (2009), pp. 3875–3886.

Stober, G., K. Baumgarten, et al. “Comparative study between ground-based observations and NAVGEM-HA analysis data in the mesosphere and lower thermosphere region”. In: *Atmospheric Chemistry and Physics* 20.20 (2020), pp. 11979–12010.

Stober, G., Ch. Jacobi, et al. “Meteor Radar Temperatures over Collm (51.3°N, 13°E)”. In: *Advances in Space Research* 42.7 (2008), pp. 1253–1258. ISSN: 0273-1177.

Stober, G., V. Matthias, et al. “Exceptionally Strong Summer-like Zonal Wind Reversal in the Upper Mesosphere during Winter 2015/16”. In: *Annales Geophysicae* 35.3 (2017), pp. 711–720.

Stober, Gunter, Ales Kuchar, et al. “Interhemispheric differences of mesosphere–lower thermosphere winds and tides investigated from three whole-atmosphere models and meteor radar observations”. In: *Atmospheric chemistry and physics* 21.18 (2021), pp. 13855–13902.

Stober, Gunter, Alan Liu, et al. “Identifying gravity waves launched by the Hunga Tonga–Hunga Ha apai volcanic eruption in mesosphere/lower-thermosphere winds derived from CONDOR and the Nordic Meteor Radar Cluster”. In: *Annales Geophysicae*. Vol. 41. 1. 2023, pp. 197–208.

Stober, Gunter, Sharon L Vadas, et al. “Gravity waves generated by the Hunga Tonga–Hunga Ha apai volcanic eruption and their global propagation in the mesosphere/lower thermosphere observed by meteor radars and modeled with the High-Altitude general Mechanistic Circulation Model”. In: *Atmospheric Chemistry and Physics* 24.8 (2024), pp. 4851–4873.

Straub, C., A. Murk, and N. Kämpfer. “MIAWARA-C, a new ground based water vapor radiometer for measurement campaigns”. In: *Atmospheric Measurement Techniques* 3.5 (2010), pp. 1271–1285.

Straub, Corinne, Brigitte Tschanz, et al. “Transport of mesospheric H2O during and after the stratospheric sudden warming of January 2010: observation and simulation”. In: *Atmospheric chemistry and physics* 12.12 (2012), pp. 5413–5427.

Straus, David M and J Shukla. “A comparison of a GCM simulation of the seasonal cycle of the atmosphere with observations part II: Stationary waves and transient fluctuations”. In: *Atmosphere-Ocean* 26.4 (1988), pp. 575–607.

Summers, Michael E et al. “Discovery of a water vapor layer in the Arctic summer mesosphere: Implications for polar mesospheric clouds”. In: *Geophysical research letters* 28.18 (2001), pp. 3601–3604.

Tateno, Satoshi and Kaoru Sato. “A study of inertia-gravity waves in the middle stratosphere based on intensive radiosonde observations”. In: *Journal of the Meteorological Society of Japan. Ser. II* 86.5 (2008), pp. 719–732.

Tegtmeier, Susann et al. “SPARC Data Initiative: A comparison of ozone climatologies from international satellite limb sounders”. In: *Journal of Geophysical Research: Atmospheres* 118.21 (2013), pp. 12–229.

Thiéblemont, Rémi et al. “Drivers and surface signal of interannual variability of boreal stratospheric final warmings”. In: *Journal of Geophysical Research: Atmospheres* 124.10 (2019), pp. 5400–5417.

Thompson, David WJ, Jason C Furtado, and Theodore G Shepherd. “On the tropospheric response to anomalous stratospheric wave drag and radiative heating”. In: *Journal of the atmospheric sciences* 63.10 (2006), pp. 2616–2629.

Tschanz, B., C. Straub, et al. “Validation of middle-atmospheric campaign-based water vapour measured by the ground-based microwave radiometer MIAWARA-C”. In: *Atmospheric Measurement Techniques* 6.7 (2013), pp. 1725–1745.

Tschanz, Brigitte and Niklaus Kämpfer. “Signatures of the 2-day wave and sudden stratospheric warmings in Arctic water vapour observed by ground-based microwave radiometry”. In: *Atmospheric Chemistry and Physics* 15.9 (2015), pp. 5099–5108.

Tsuda, Toshitaka and Susumu Kato. “Diurnal non-migrating tides excited by a differential heating due to land-sea distribution”. In: *Journal of the Meteorological Society of Japan. Ser. II* 67.1 (1989), pp. 43–55.

Tweedy, Olga V et al. “Nighttime secondary ozone layer during major stratospheric sudden warmings in specified-dynamics WACCM”. In: *Journal of Geophysical Research: Atmospheres* 118.15 (2013), pp. 8346–8358.

Van Malderen, Roeland et al. “Fifty years of balloon-borne ozone profile measurements at Uccle, Belgium: a short history, the scientific relevance, and the achievements in understanding the vertical ozone distribution”. In: *Atmospheric Chemistry and Physics* 21.16 (2021), pp. 12385–12411.

Vigouroux, C et al. “Evaluation of tropospheric and stratospheric ozone trends over Western Europe from ground-based FTIR network observations”. In: *Atmospheric Chemistry and Physics* 8.23 (2008), pp. 6865–6886.

Volland, Hans. *Atmospheric Tidal and Planetary Waves*. Springer Science & Business Media, Dec. 6, 2012. 358 pp. ISBN: 978-94-009-2861-9.

Von Zahn, U and U Berger. “Persistent ice cloud in the midsummer upper mesosphere at high latitudes: Three-dimensional modeling and cloud interactions with ambient water vapor”. In: *Journal of Geophysical Research: Atmospheres* 108.D8 (2003).

Walterscheid, RL. “Dynamical cooling induced by dissipating internal gravity waves”. In: *Geophysical Research Letters* 8.12 (1981), pp. 1235–1238.

Wang, Mingcheng, Qiang Fu, et al. “Stratosphere-Troposphere Exchanges of Air Mass and Ozone Concentrations From ERA5 and MERRA2: Annual-Mean Climatology, Seasonal Cycle, and Interannual Variability”. In: *Journal of Geophysical Research: Atmospheres* 128.24 (2023), e2023JD039270.

Wang, Wuke, Jin Hong, et al. “Zonally asymmetric influences of the quasi-biennial oscillation on stratospheric ozone”. In: *Atmospheric Chemistry and Physics* 22.20 (2022), pp. 13695–13711.

Waters, Joe William et al. “The Earth observing system microwave limb sounder (EOS MLS) on the aura Satellite”. In: *IEEE Transactions on Geoscience and Remote Sensing* 44 (2006), pp. 1075–1092.

Wing, Robin et al. “Lidar temperature series in the middle atmosphere as a reference data set–Part 2: Assessment of temperature observations from MLS/Aura and SABER/TIMED satellites”. In: *Atmospheric Measurement Techniques* 11.12 (2018), pp. 6703–6717.

Wu, Peng et al. “Ground-based remote sensing of atmospheric water vapor using high-resolution FTIR spectrometry”. In: *Remote Sensing* 15.14 (2023), p. 3484.

Xu, Jingyuan et al. “Large amounts of water vapor were injected into the stratosphere by the Hunga Tonga–Hunga Ha’apai volcano eruption”. In: *Atmosphere* 13.6 (2022), p. 912.

Yang, Chengyun et al. “The effect of the Madden-Julian oscillation on the mesospheric migrating diurnal tide: A study using SD-WACCM”. In: *Geophysical Research Letters* 45.10 (2018), pp. 5105–5114.

Yiğit, Erdal and Alexander S Medvedev. “Internal wave coupling processes in Earth’s atmosphere”. In: *Advances in Space Research* 55.4 (2015), pp. 983–1003.

Yu, Yueyue et al. “On the linkage among strong stratospheric mass circulation, stratospheric sudden warming, and cold weather events”. In: *Monthly Weather Review* 146.9 (2018), pp. 2717–2739.

Zängl, Günther et al. “The ICON (ICOsahedral Non-hydrostatic) modelling framework of DWD and MPI-M: Description of the non-hydrostatic dynamical core”. In: *Quarterly Journal of the Royal Meteorological Society* 141.687 (2015), pp. 563–579.

Zhang, Jiarong et al. “Climatological westward-propagating semidiurnal tides and their composite response to sudden stratospheric warmings in SuperDARN and SD-WACCM-X”. In: *Journal of Geophysical Research: Atmospheres* 126.3 (2021), e2020JD032895.

List of publications

Publications

- **Shi, Guochun**, Hanli Liu, Masaki Tsutsumi, Njål Gulbrandsen, Alexander Kozlovsky, Dimitry Pokhotelov, Mark Lester, Kun Wu, and Gunter Stober. "New insights into the polar ozone and water vapor, radiative effects, and their connection to the tides in the mesosphere-lower thermosphere during major Sudden Stratospheric Warming events". In: *EGUsphere* 2024 (2024), pp. 1–33
- **Shi, Guochun**, Witali Krochin, Eric Sauvageat, and Gunter Stober. "Ozone anomalies over the polar regions during stratospheric warming events". In: *Atmospheric Chemistry and Physics* 24.17 (2024), pp. 10187–10207
- **Shi, Guochun**, Witali Krochin, Eric Sauvageat, and Gunter Stober. "Ozone and water vapor variability in the polar middle atmosphere observed with ground-based microwave radiometers". In: *Atmospheric Chemistry and Physics* 23.16 (2023), pp. 9137–9159
- Gunter Stober, Sharon L Vadas, Erich Becker, Alan Liu, Alexander Kozlovsky, Diego Janches, Zishun Qiao, Witali Krochin, **Shi, Guochun**, Wen Yi, et al. "Gravity waves generated by the Hunga Tonga–Hunga Ha apai volcanic eruption and their global propagation in the mesosphere/lower thermosphere observed by meteor radars and modeled with the High-Altitude general Mechanistic Circulation Model". In: *Atmospheric Chemistry and Physics* 24.8 (2024), pp. 4851–4873
- Gunter Stober, Alan Liu, Alexander Kozlovsky, Zishun Qiao, Witali Krochin, **Shi, Guochun**, Johan Kero, Masaki Tsutsumi, Njål Gulbrandsen, Satonori Nozawa, et al. "Identifying gravity waves launched by the Hunga Tonga–Hunga Ha apai volcanic eruption in mesosphere/lower-thermosphere winds derived from CONDOR and the Nordic Meteor Radar Cluster". In: *Annales Geophysicae*. Vol. 41. 1. 2023, pp. 197–208
- **Shi, Guochun**, Xiong Hu, ZhiGang Yao, WenJie Guo, MingChen Sun, and XiaoYan Gong. "Case study on stratospheric and mesospheric concentric gravity waves generated by deep convection". In: *Earth and Planetary Physics* 5.1 (2021), pp. 79–89

Online

The list of publications is available online: https://orcid.org/0000-0002-2160-0449

Selected Talks

- **Guochun Shi** and Gunter Stober: Ozone and water vapor variability during sudden stratospheric warming and its connection to mesospheric tides, *Microwave and Atmospheric Physics Seminar*, Bern, Switzerland, 15 November 2024.
- **Guochun Shi**, Eric Sauvageat, Hanli Liu, and Gunter Stober: Explore stratospheric and lower mesospheric ozone variability across the middle to polar latitudes using ground-based microwave radiometers, *Quadrennial Ozone Symposium 2024*, Boulder, USA, 15–19 July 2024.
- **Guochun Shi**, Alexander Kozlovsky, Njål Gulbrandsen, Masaki Tsutsumi, Kun Wu, and Gunter Stober: Ozone anomalies over the Arctic during major sudden stratospheric warming events and their relation to mesospheric dynamics, *The 28th IUGG General Assembly 2023*, Berlin, Germany, 11–20 July 2023.
- **Guochun Shi** and Gunter Stober: Analyzing ozone variability at northern polar latitude during sudden stratospheric warming events using a ground-based microwave radiometer, *EGU General Assembly 2023*, Vienna, Austria, 23–28 April 2023.
- **Guochun Shi** and Gunter Stober: Ozone and water vapor variability in the middle atmosphere observed with ground-based microwave radiometers at Ny-Ålesund, Svalbard (79°N, 12°E), *Microwave and Atmospheric Physics Seminar*, Bern, Switzerland, 09 December 2022.

Selected Posters

- **Guochun Shi**, Hanli Liu, Alexander Kozlovsky, Njål Gulbrandsen, Dimitry Pokhotelov, Mark Lester, Masaki Tsutsumi, Kun Wu, and Gunter Stober: Polar ozone anomalies, radiative effects, and their connection to mesospheric tidal dynamics during extreme events, EGU General Assembly 2025, Vienna, Austria, 27 April–2 May 2025.
- **Guochun Shi**, Hanli Liu, Alexander Kozlovsky, Njål Gulbrandsen, Dimitry Pokhotelov, Mark Lester, Masaki Tsutsumi, Kun Wu, and Gunter Stober: Comparative analysis of middle atmosphere composition and mesosphere-lower thermosphere tidal changes during sudden stratospheric warming events, American Geophysical Union (AGU) 2024, Washington, D.C, USA, 9-13 December 2024.
- **Guochun Shi**, Hanli Liu, Witali Krochin, Masaki Tsutsumi, Njål Gulbrandsen, and Gunter Stober: Variability of middle atmospheric polar ozone and its effects on Arctic mesospheric tides, EGU General Assembly 2024, Vienna, Austria, 14–19 April 2024.
- **Guochun Shi**, Witali Krochin, Axel Murk, and Gunter Stober: Ozone and water vapor variability in the 2019/2020 Arctic stratospheric polar vortex compared to climatology, Swiss Geoscience Meeting 2022, Lausanne, Switzerland, 18-29 November 2022.
- **Guochun Shi**, Witali Krochin, and Gunter Stober: Stratospheric ozone variability driven by planetary waves at polar latitudes, Swiss Remote Sensing 2022, Ascona, Switzerland, May 1-4, 2022.

Acknowledgements

First and foremost, I would like to express my heartfelt gratitude to my advisor, **Gunter Stober**, for his invaluable guidance and unwavering support throughout my PhD journey. I feel truly fortunate and honored to have been his PhD student—an experience I will always cherish as one of the most rewarding in my life.

I am also deeply thankful to my family for their constant support and unconditional love. Their belief in me has been a steady source of strength and motivation along the way.

I would also like to thank myself—for never giving up and for continuing to grow. I will keep striving to become the best version of myself.

Lastly, I am grateful to everyone I have met along this journey.

As the Chinese saying goes: "***To read ten thousand books and travel ten thousand miles — the greatest truths are the simplest.***" This PhD journey has been a reflection of that philosophy—uniting knowledge, experience, and simplicity in pursuit of understanding.

Erklärung

gemäss Art. 18 PromR Phil.-nat. 2019

Name/Vorname:	Guochun Shi
Matrikelnummer:	10-113-843
Studiengang:	Physik Bachelor ☐ Master ☐ Dissertation ☒
Titel der Arbeit:	Investigate the variability of polar ozone and water vapor in the middle atmosphere and their impacts on the mesospheric dynamics
Leiter der Arbeit:	PD. Dr. Gunter Stober

Ich erkläre hiermit, dass ich diese Arbeit selbständig verfasst und keine anderen als die angegebenen Quellen benutzt habe. Alle Stellen, die wörtlich oder sinngemäss aus Quellen entnommen wurden, habe ich als solche gekennzeichnet. Mir ist bekannt, dass andernfalls der Senat gemäss Artikel 36 Absatz 1 Buchstabe r des Gesetzes über die Universität vom 5. September 1996 und Artikel 69 des Universitätsstatuts vom 7. Juni 2011 zum Entzug des Doktortitels berechtigt ist. Für die Zwecke der Begutachtung und der Überprüfung der Einhaltung der Selbständigkeitserklärung bzw. der Reglemente betreffend Plagiate erteile ich der Universität Bern das Recht, die dazu erforderlichen Personendaten zu bearbeiten und Nutzungshandlungen vorzunehmen, insbesondere die Doktorarbeit zu vervielfältigen und dauerhaft in einer Datenbank zu speichern sowie diese zur Überprüfung von Arbeiten Dritter zu verwenden oder hierzu zur Verfügung zu stellen.

Bern, April 15, 2025